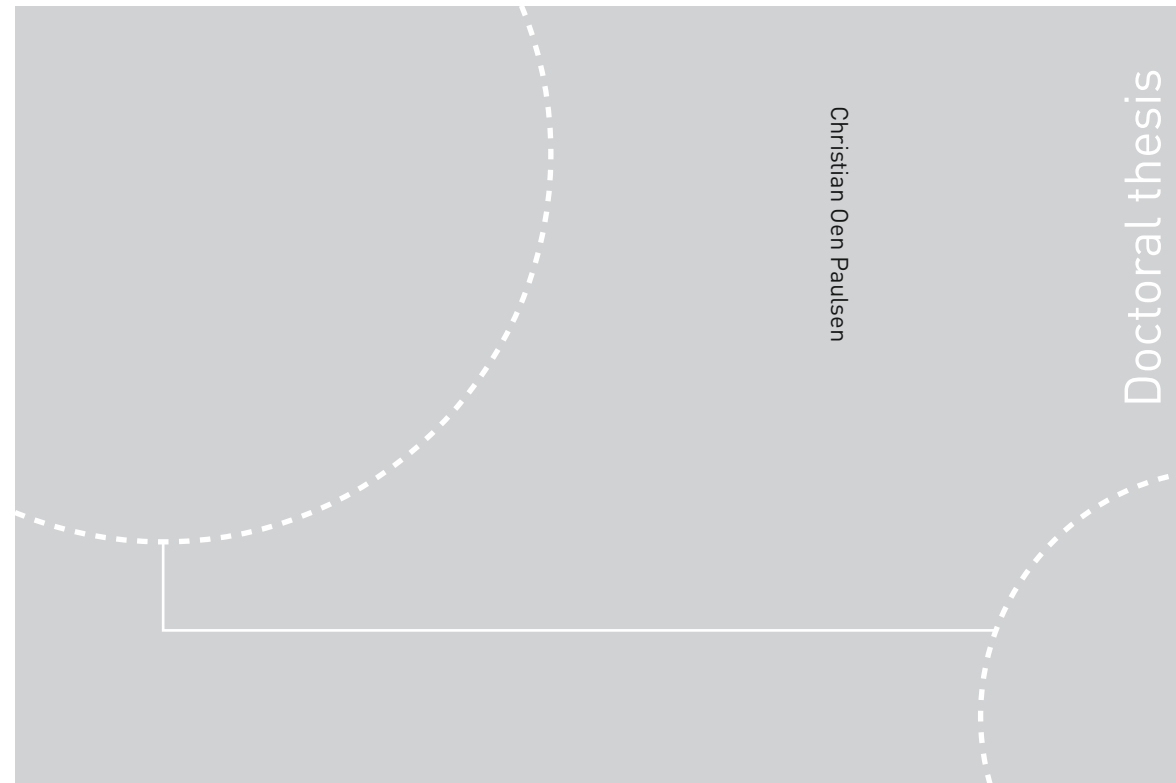


ISBN 978-82-326-4146-8 (printed ver.)  
ISBN 978-82-326-4147-5 (electronic ver.)  
ISSN 1503-8181



# Experimental Characterization of Two-Phase Steels

Christian Oen Paulsen

# Experimental Characterization of Two-Phase Steels

Thesis for the Degree of Philosophiae Doctor

Trondheim, October 2019

Norwegian University of Science and Technology  
Faculty of Natural Sciences  
Department of Materials Science and Engineering



Norwegian University of  
Science and Technology



**NTNU**

Norwegian University of Science and Technology

Thesis for the Degree of Philosophiae Doctor

Faculty of Natural Sciences

Department of Materials Science and Engineering

© Christian Oen Paulsen

ISBN 978-82-326-4146-8 (printed ver.)

ISBN 978-82-326-4147-5 (electronic ver.)

ISSN 1503-8181

Doctoral theses at NTNU, 2019:275

Printed by NTNU Grafisk senter

# Preface

The work presented in this thesis has been carried out primarily at the Department of Materials Science and Engineering (IMA) at Norwegian University of Science and Technology (NTNU). The exception being the period between May 2017 and September 2018. May 2017 to June 2017 was spent at the School of Materials at the University of Manchester in Manchester, England. The period July 2017 to August 2018 was spent at the Department of Civil Engineering and Engineering Mechanics at Columbia University in New York, NY, USA.

This thesis focuses on investigating and characterizing two-phase steels using *in-situ* scanning electron microscope (SEM) techniques. One of the main deliverables from this work has been to establish an experimental technique to perform digital imaging correlation (DIC) analysis on images acquired during an *in-situ* SEM tensile tests at IMA. Further, this technique has been verified and used on different steels. This thesis consists of ten main chapters and two appendices. Chapter 1 is the introduction and Chapters 2 and 3 present the theoretical background and the experimental methods used, respectively. Chapter 4 and 5 further investigate and verify our experimental technique. During the Chapters 6-9, four different investigations are presented. Finally, Chapter 10 summarizes the thesis, concludes the work, and recommends future work.

In Chapter 2.2, the theoretical basis of DIC is presented. This chapter is based on the thesis of Fagerholt [1] and is partly written by Dr. Egil Fagerholt at the Department of Structural Engineering (KT), NTNU, as part of the published article [2]. The numerical model in Chapter 7 was performed with the assistance of Dr. Torodd Berstad at KT, NTNU. Further, in Chapter 9 the modeling work were performed by Dr. Afaf Saai at SINTEF Materials and Nanotechnology.

A total of two peer-reviewed journal articles are published as part of this thesis [2, 3]. The published articles are attached in Appendix A and Appendix B. Also, the author has presented work in a total of four conferences [4–7].

In addition to the work presented in this thesis, the thesis author has been involved in a study related to ballistic perforation resistance of additive manufactured aluminum plates [8]. The principal investigator on this article was Dr. Martin Kristoffersen at KT, NTNU. In this publication, the microstructural investigation was carried by the thesis author.

# Abstract

This thesis consists of several *in-situ* scanning electron microscope (SEM) tensile test studies of different two-phase steels. Three different two-phase steels have been investigated: a NVE36 plate steel, a dual-phase (DP) plate steel, and a super duplex stainless steel (SDSS) from a pipe. In each of these steels, one phase is ferrite and the second is pearlite, martensite and austenite, respectively. The interactions between the two phases in the microstructure have been investigated by utilizing recent advances in scanning electron microscope (SEM) *in-situ* tensile testing in combination with digital image correlation (DIC), electron backscatter diffractions (EBSD) and SEM micrographs acquired using secondary electron imaging.

A main part of the Ph.D. work had concerned the establishment of an experimental technique to create contrast when imaging a specimen surface in an SEM. Here, a polished specimen is coated with a continuous gold layer using a gold sputter coater. This continuous layer is then remodeled by placing the specimen on a hot plate with a gas flowing across the surface. The result is a specimen surface covered in random gold speckles. This technique is based on what was first presented by Di Gioacchino and Quinta da Fonseca [9] and Orozco-Caballero et al. [10] and tailored to the resources available at the Department of Materials Science and Engineering, Norwegian University of Technology and Science (NTNU). Using this technique, the goal was to create a pattern on different two-phase steel specimens with sufficient contrast when imaging at large magnifications in an SEM. A representative area of the tested specimen containing this pattern was then recorded throughout an *in-situ* SEM tensile test. The in-house DIC software eCorr [11] then analyzed the resulting image series. The result is a strain map with a spatial resolution capable of resolving strains at a sub-grain level.

Throughout this work, several studies were undertaken in order to verify the technique and methods used. First, a study on the effect of heat treatment on the steels investigated was conducted. Second, the DIC results were verified by comparing the grain rotations measured in DIC and EBSD. Third, two different speckled patterns were compared to highlight differences and advantages with different speckled patterns applied to create contrast for DIC. Finally, a series of investigations were undertaken using *in-situ* SEM tensile testing. These tests were performed on a NVE36 two-phase steel, four different DP steels and an SDSS.

This thesis has the following outline: first, some background on relevant theories is given. These topics are SEM, DIC, steel microstructure and behavior and numerical models. Second, a description of the experimental equipment and techniques used in this thesis are described. Also, specimen preparation and the different steels tested are presented. Third, two chapters are investigating the validity of the measurements and the effect of the specimen preparation on the materials. Then four different studies are presented where all the results from the thesis work will be given and discussed. Finally, the last chapter will summarize this thesis, make concluding remarks and provide some suggestions for future work. At the end of the thesis, two peer-reviewed articles published based on this work are attached.

# Acknowledgement

Throughout this Ph.D. work my supervisors have been Associate Professor Ida Westermann at the Department of Materials Science and Engineering (IMA), Norwegian University of Science and Technology (NTNU) and Professor Tore Børvik at the Department of Structural Engineering (KT), NTNU. Their continuous support, guidance, and encouragement throughout this work are highly appreciated.

In addition to residing at IMA, NTNU, part of this work has taken place working at two additional locations. These were the School of Materials at the University of Manchester in Manchester, England and the Department of Civil Engineering and Engineering Mechanics at Columbia University in New York, NY, USA. I want to thank Professor João Quinta da Fonseca and Professor Jacob Fish for hosting me in respectively, Manchester and New York during these stays.

The experimental work in this thesis has been carried out at the laboratories at IMA, NTNU. The assistance of the laboratory staff is acknowledged, in particular, Dr. Sergey Khromov, who provided support with the scanning electron microscope (SEM) and the *in-situ* SEM tensile test stage. Also, Dr. Egil Fagerholt at KT, NTNU, Dr. Torodd Berstad at KT, NTNU and Dr. Afaf Saai at SINTEF Materials and Nanotechnology have contributed to this thesis, and their contributions are highly appreciated.

Finally, I would like to thank my wife, Anastasia Paulsen, and my parents for their encouragement and continued support throughout my Ph.D. work.



# Contents

<b>Preface</b>	<b>iii</b>
<b>Abstract</b>	<b>v</b>
<b>Acknowledgements</b>	<b>vii</b>
<b>Contents</b>	<b>ix</b>
<b>List of Tables</b>	<b>xv</b>
<b>List of Figures</b>	<b>xvii</b>
<b>List of Abbreviations</b>	<b>xxi</b>
<b>List of Symbols</b>	<b>xxiii</b>
<b>1 Introduction</b>	<b>1</b>
1.1 Background . . . . .	1
1.2 Previous Work . . . . .	3
1.2.1 Digital Image Correlation . . . . .	3
1.2.2 Two-Phase Steel <i>in-situ</i> SEM Investigations . . . . .	4



1.3	Scope . . . . .	6
1.4	Outline . . . . .	6
<b>2</b>	<b>Theoretical Background</b>	<b>7</b>
2.1	Scanning Electron Microscope . . . . .	7
2.1.1	Imaging in an SEM . . . . .	7
2.1.2	Secondary Electrons . . . . .	11
2.1.3	Backscatter Electrons . . . . .	11
2.1.4	Electron Backscatter Diffraction . . . . .	12
2.2	Digital Image Correlation . . . . .	16
2.2.1	Theoretical Background . . . . .	16
2.2.2	Digital Image Correlation in SEM . . . . .	19
2.2.3	Gold Remodeling . . . . .	20
2.3	Steels . . . . .	21
2.3.1	Crystal Structures and Slip Systems . . . . .	21
2.3.2	Dislocations and Damage Mechanisms . . . . .	26
2.3.3	TMP, Alloying, and Formation of Intermetallics . . . . .	29
2.3.4	Influence of Temperature . . . . .	31
2.4	Stress and Strain . . . . .	36
2.5	Constitutive Relations . . . . .	37
2.5.1	Voce . . . . .	37
2.5.2	Taylor Equation and Bergström Model . . . . .	41
<b>3</b>	<b>Experimental Procedures</b>	<b>43</b>
3.1	Tensile Testing Using <i>in-situ</i> SEM Stage . . . . .	43
3.2	Electron Backscatter Diffraction Acquisition . . . . .	46
3.3	Gold Remodeling . . . . .	47

3.4	Materials . . . . .	52
3.4.1	NVE36 Two Phase-Steel . . . . .	52
3.4.2	2507 Super Duplex Stainless Steel . . . . .	53
3.4.3	Dual-Phase Steel . . . . .	55
<b>4</b>	<b>Effect of Heat Treatment on Different Steels</b>	<b>59</b>
4.1	Material Characterization . . . . .	59
4.2	Results . . . . .	61
4.3	Discussion . . . . .	65
4.4	Concluding Remarks . . . . .	66
<b>5</b>	<b>Verifying the <i>in-situ</i> DIC</b>	<b>69</b>
5.1	Experimental . . . . .	70
5.1.1	Specimen Preparation and Data Acquisition . . . . .	70
5.1.2	Extracting Grain Rotation . . . . .	71
5.2	Results . . . . .	72
5.3	Discussion . . . . .	74
5.4	Concluding Remarks . . . . .	76
<b>6</b>	<b>Comparing <i>in-situ</i> DIC Speckled Pattern</b>	<b>77</b>
6.1	Experimental . . . . .	78
6.1.1	Etched Surface . . . . .	78
6.1.2	Gold Speckled Surface . . . . .	78
6.2	Experimental Results on Etched Specimen . . . . .	80
6.3	Experimental Results on Gold Speckled Specimen . . . . .	86
6.4	Discussion . . . . .	92
6.5	Concluding remarks . . . . .	96

<b>7</b>	<b>A Numerical Study of NVE36</b>	<b>99</b>
7.1	Tensile Tests Recorded With a Macro Lens . . . . .	99
7.1.1	Experimental Setup . . . . .	99
7.1.2	Experimental Results . . . . .	100
7.2	Numerical Simulations . . . . .	106
7.2.1	Constitutive Relation . . . . .	106
7.2.2	Identification of Material Constants . . . . .	106
7.2.3	Numerical Model . . . . .	108
7.2.4	Numerical Results . . . . .	109
7.3	Discussion . . . . .	112
7.4	Concluding Remarks . . . . .	112
<b>8</b>	<b>Investigating DP Steels Using <i>in-situ</i> SEM DIC and FE Simulations</b>	<b>113</b>
8.1	Experimental . . . . .	114
8.2	Experimental results . . . . .	116
8.2.1	Microstructure Characterization . . . . .	116
8.2.2	DIC Investigation . . . . .	119
8.3	Finite Element Model . . . . .	125
8.4	Discussion . . . . .	127
8.5	Concluding Remarks . . . . .	130
<b>9</b>	<b>Low-Temperature Study of SDSS Containing <math>\sigma</math>-Phase</b>	<b>133</b>
9.1	Experimental . . . . .	134
9.2	Results . . . . .	135
9.2.1	Tensile Testing . . . . .	135
9.2.2	Microstructure Evolution . . . . .	139
9.3	Discussion . . . . .	142

9.4 Concluding Remarks . . . . .	145
<b>10 Summary, Conclusions and Recommendations</b>	<b>147</b>
10.1 Summary . . . . .	147
10.2 Concluding Remarks . . . . .	150
10.3 Recommendations for Further Work . . . . .	152
<b>References</b>	<b>155</b>
<b>Appendix A</b>	<b>173</b>
<b>Appendix B</b>	<b>199</b>



# List of Tables

3.1	SEM Parameters Used During EBSD Acquisition of SDSS . . . .	46
3.2	Parameters Used During Electropolishing . . . . .	46
3.3	Gold Sputter Coater Settings . . . . .	47
3.4	Experimental Settings for Gold Remodeling . . . . .	49
3.5	SEM Setting for BSE Imaging of Gold Speckle Pattern . . . . .	51
3.6	Chemical Composition of NVE36 . . . . .	53
3.7	Chemical Composition of SDSS . . . . .	54
3.8	Microstructure Statistics of SDSS . . . . .	54
3.9	Chemical Composition of DP Steels . . . . .	56
3.10	Phase Composition and Average Grain Size of DP Steels . . . . .	56
4.1	Heat Treatment Matrix for the Different Steels . . . . .	60
5.1	The Grain Rotation From EBSD and DIC . . . . .	74
6.1	Microstructure Measurements Before and After Heat Treatment .	93
7.1	Material Constants Used in Simulation of NVE36 . . . . .	107

8.1	Local Strains in Martensite and Ferrite in Different DP Steels . . .	124
9.1	Heat Treatment and Amount of $\sigma$ -Phase in SDSS . . . . .	135

# List of Figures

1.1	Path For Modeling Steels . . . . .	3
2.1	Interaction Volume in SEM Specimen . . . . .	8
2.2	Raster Scanning in SEM . . . . .	9
2.3	An illustration of the Electron Beam . . . . .	10
2.4	Everhart-Thornley Detector . . . . .	12
2.5	Bragg Reflection . . . . .	13
2.6	Electron Backscatter Diffraction Pattern . . . . .	14
2.7	Tilted EBSD Specimen . . . . .	15
2.8	Iron-Carbon Phase Diagram . . . . .	22
2.9	BCC and FCC unit cells . . . . .	23
2.10	Ferrite–Pearlite Microstructure . . . . .	24
2.11	BCT unit cell . . . . .	24
2.12	FCC Slip Systems . . . . .	25
2.13	Illustration of an Edge Dislocation . . . . .	26
2.14	Illustration of an Edge Dislocation Propagating . . . . .	27
2.15	Illustration of a Screw Dislocation . . . . .	28



2.16	Heat Treatment of DP Steels . . . . .	30
2.17	Effect of Alloying Elements in Ferrite and Austenite . . . . .	31
2.18	Fe-Ni-Cr Phase Diagram . . . . .	32
2.19	TTT Diagram for Formation of Intermetallics in Duplex Steels . .	33
2.20	Formation of $\sigma$ -Phase . . . . .	34
2.21	Ductile-to-Brittle Transition Temperature . . . . .	35
2.22	Engineering Tensile Test Curve and True Tensile Test Curve . . .	37
2.23	Influence of Parameters on the Voce Equation . . . . .	38
3.1	Tensile Test Stage for <i>in-situ</i> SEM Testing . . . . .	44
3.2	Specimen Geometry for <i>in-situ</i> SEM Tensile Testing . . . . .	45
3.3	Cold Finger for <i>in-situ</i> SEM Tensile Testing . . . . .	45
3.4	Gold Remodeling in a Water Atmosphere . . . . .	48
3.5	Gold Remodeling in an Argon/Styrene Atmosphere . . . . .	48
3.6	BSE Image of Gold Speckles . . . . .	50
3.7	Image Acquisition of a Large Area in SEM . . . . .	51
3.8	Micrograph of NVE36 . . . . .	52
3.9	NVE36 Cut From Plate . . . . .	53
3.10	SDSS Microstructure and Location of Specimen . . . . .	55
3.11	DP500, DP600, DP800 and DP980 Microstructure . . . . .	57
4.1	Grain Size Before and After Heat Treatment . . . . .	61
4.2	Hardness Values Before and After Heat Treatment . . . . .	62
4.3	Phase Composition Before and After Heat Treatment . . . . .	63
4.4	Tensile Test Curves Before and After Heat Treatment . . . . .	64
5.1	IPF Maps From Before and After Deformation in a SDSS . . . . .	72
5.2	Rotation Map From DIC . . . . .	73

5.3	IQ Maps From Before and After Deformation in a SDSS . . . . .	75
6.1	Recorded Area of NVE36 . . . . .	79
6.2	Tensile Test Curve From <i>in-situ</i> Experiment on Notched Specimen	80
6.3	Micrographs From Etched Specimen . . . . .	82
6.4	DIC Strain Field From Etched Microstructure . . . . .	83
6.5	Local Strain Evolution in Etched Specimen . . . . .	84
6.6	Grain Used for Local Strain Measurements on Etched Specimen .	85
6.7	Micrographs From Gold Specimen . . . . .	87
6.8	DIC Maps from Gold Specimen . . . . .	88
6.9	Phase Map and DIC Map of the Gold Specimen . . . . .	89
6.10	Local Strain Measurements in Gold Specimen . . . . .	90
6.11	Grain Used for Local Strain Measurements for Gold Specimen . .	90
6.12	Comparing Strain Field of Equal Mesh Size . . . . .	91
6.13	Effect of heat Treatment on NVE36 . . . . .	93
6.14	Local Strain Evolution Compared . . . . .	96
7.1	Measured Engineering Tensile Curve for the Smooth Specimen . .	101
7.2	Measured Strain Field in Smooth Specimen Tested in Air . . . . .	102
7.3	Propagation of Lüders Bands During the Tensile Test . . . . .	104
7.4	Measured Strain Fields in Notched Specimen Tested in Air . . . .	105
7.5	Measured Versus Fitted True Stress–Plastic Strain Curves . . . . .	107
7.6	Numerical Models of Smooth and Notched Specimen Geometries	109
7.7	Simulated Strain Field in the Smooth Specimen . . . . .	110
7.8	Measured Versus Simulated Force-Displacement Curves . . . . .	110
7.9	Simulated Strain Field in the Notched Specimen . . . . .	111
8.1	Definition of $L_\alpha$ and $L_{\alpha'}$ . . . . .	116

8.2	Engineering Stress–Strain Curves for DP Steels . . . . .	117
8.3	Correlation Between Tensile Data and Fraction Martensite . . . . .	118
8.4	Comparing Properties of DP Steels . . . . .	118
8.5	Phase Map and DIC Map of DP500 . . . . .	119
8.6	Phase Map and DIC Map of DP600 . . . . .	120
8.7	Phase Map and DIC Map of DP800 . . . . .	121
8.8	Crack in DP800 Microstructure . . . . .	121
8.9	Phase Map and DIC Map of DP980 . . . . .	122
8.10	Damage in DP980 . . . . .	123
8.11	Local Strain Measurements for DP800 Specimen . . . . .	124
8.12	Phase Map and RVE of DP800 . . . . .	126
8.13	Strain Map from FE Analysis and DIC of DP800 . . . . .	127
9.1	Tensile Test Curves From the <i>in-situ</i> Tensile Test on SDSS . . . . .	136
9.2	$\chi$ -Phase in SDSS . . . . .	137
9.3	Fracture Surfaces From SDSS With Different Amounts of $\sigma$ -Phase . . . . .	138
9.4	Micro-Crack in $\sigma$ -Phase in SDSS . . . . .	140
9.5	Micrographs of Cracks Formed in the $\sigma$ -Phase . . . . .	140
9.6	Cracks in $\sigma$ -Phase Recorded With EBSD . . . . .	141
9.7	Grain Orientation Spread Curves in SDSS . . . . .	142

# List of Abbreviations

AE	Absorbed Electrons
BCC	Body Centered Cubic
BCT	Body Centered Tetragonal
BSE	Backscatter Electrons
CASA	Center for Advanced Structural Analysis
CCD	Charge Coupled Device
CD	Circumferential Direction
DIC	Digital Image Correlation
DOF	Degrees of Freedom
DP	Dual Phase
DSS	Duplex Stainless Steel
DVC	Digital Volume Correlation
EBSD	Electron Backscatter Diffraction
EBSP	Electron Backscatter Diffraction Pattern
ETD	Everhart-Thornley Detector
FCC	Face Centered Cubic

FE	Finite Element
GOS	Grain Orientation Spread
GS	Grain Size
HRDIC	High Resolution Digital Image Correlation
IMA	Department of Materials Science and Engineering
IPF	Inverse Pole Figure
IQ	Image Quality
KT	Department of Structural Engineering
LD	Length Direction
ND	Normal Direction
NTNU	Norwegian University of Science and Technology
RD	Rolling Direction
ROI	Region of Interest
RVE	Representative Volume Element
SDSS	Super Duplex Stainless Steel
SE	Secondary Electrons
SEM	Scanning Electron Microscope
SFI	Sentre for Forskningsdrevet Innovasjon
SSD	Sum of Squared Differences
TD	Transverse Direction
TMP	Thermo Mechanical Process
TTT	Time Temperature Transformation
UMAT	User-Defined Subroutine
UTS	Ultimate Tensile Strength
ZNSSD	Zero-Mean Normalized Sum of Squared Differences

# List of Symbols

$\sigma_0$	Yield Stress	MPa
$R(p)$	Work-Hardening as a Function of Plastic Strain	MPa
$\varphi(\hat{\sigma})$	Yield Surface	MPa
$q_1, q_2, q_3, k_s$	Parameters in the Gurson Model	
$\epsilon_f$	Fracture Strain	
$\sigma^*$	Triaxiality	
$\mu$	Lode Parameter	
$i$	probe current	
$\eta$	Fraction Backscatter Electrons	
$\delta$	Secondary Electron Coefficient	
$Z$	Atomic Number	
$\lambda$	Wave Length of Electrons in Braggs Law	m
$\theta$	Bragg Angle	
$d$	Interplanar Spacing in Braggs Law	m
$n$	Order of Reflection in Braggs Law	

$I_r$	Reference Image	
$I_c$	Current Image	
$\mathbf{X}$	Image Coordinates in Reference Configuration	
$\mathbf{u}$	Displacement Field	
$\mathbf{u}'$	Displacement Since Previous Image	
$\mathbf{x}'$	Image Coordinates in Current Configuration	
$\mathbf{F}$	Deformation Gradient Matrix	
$\mathbf{U}$	Displacement Matrix	
$\mathbf{R}$	Rotation Matrix	
$t$	Time	
$\mathbf{C}$	Cauchy-Green Deformation Tensor	
$\mu$	Principal Stretch	
$\mathbf{n}$	Direction of the Principal Stretch	
$\varepsilon$	Logarithmic Principal Strain	
$\alpha$	Ferrite	
$\alpha'$	Martensite	
$\gamma$	Austenite	
$\sigma$	Sigma Intermetallic Phase	
$\chi$	Chi Intermetallic Phase	
$E$	Young's Modulus	MPa
$L$	Current Gauge Length	m
$L_0$	Original Gauge Length	m
$A$	Current Area	m <sup>2</sup>

---

$A_0$	Original Area	$\text{m}^2$
$e$	Engineering Strain	
$s$	Engineering Stress	MPa
$\varepsilon$	True Strain	
$\sigma$	True Stress	MPa
$\varepsilon^P$	True Plastic Strain	
$\theta$	Hardening Coefficient in Voce Equation	MPa
$\sigma_{eq}$	Equivalent Stress	MPa
$\sigma_Y$	Yield Stress	MPa
$Q$	Saturation Stress in Voce Equation	MPa
$\sigma_{Y,\alpha}$	Yield Stress of Ferrite	MPa
$\sigma_{Y,\alpha'}$	Yield Stress of Martensite	MPa
$C_{\alpha'}$	Carbon Content in Martensite	
$C_{total}$	Total Carbon Content	
$Q_{\alpha'}$	Saturation Stress of Martensite	MPa
$n_{\alpha'}$	Hardening coefficient of Martensite	MPa
$V_{\alpha'}$	Volume Fraction of Martensite	
$H_\alpha, n_\alpha$	Fitting Parameters for Ferrite	
$a, b, C_0, q$	Fitting Parameters for Martensite	
$\beta$	Dynamic Recovery Coefficient	
$\varepsilon_{tr}^P$	Plastic Strain at Transition from Stage III to IV	
$\sigma_{tr}$	Stress at Transition from Stage III to IV	MPa
$\theta_\alpha$	Initial Hardening Rate for Ferrite	MPa



$\theta_{IV}$	Hardening Rate in Stage IV	MPa
$\alpha$	Dislocation Hardening Constant	
$\mu$	Shear Modulus	MPa
$\rho(\varepsilon)$	Dislocation Density	m <sup>-2</sup>
$\sigma_{int}$	Friction Stress	MPa
$\sigma_{def}$	Work Hardening Flow Stress	MPa
$\Omega$	Dynamic Recovery Coefficient	
$b$	Burgers Vector	m
$f(\varepsilon)$	Active Volume Fraction of Ferrite	
$f_1$	Initial Active Volume Fraction of Ferrite	
$f_0$	Total Amount of Ferrite	
$f_m$	Volume Fraction Martensite	
$K_r$	Recovery Rate	
$L$	Dislocation Mean Free Path	m
$M_T$	Taylor Constant	
$s(\varepsilon)$	Dislocation Mean Free Path	m
$s_0$	Final Value of Dislocation Mean Free Path	m
$s_1$	Start Value of Dislocation Mean Free Path	m
$r, k$	Rate Constant	
$L_\alpha$	Free Path of Ferrite	m
$L_{\alpha'}$	Linear Size of Martensite	m
$V_{\alpha'}$	Volume Fraction of Martensite	
$P_L$	Number of Interceptions per Unit Length	/m

# Chapter 1

## Introduction

### 1.1 Background

In all structural materials, the microstructure will be heterogeneous at various scales, and the mechanical properties will strongly depend on the local variations and the thermomechanical history of the material. Steels with a two-phase microstructure are such materials and are commonly used by the industry. In such steels, the properties of the soft ferrite are combined with a second harder phase, to achieve a good combination of mechanical properties [12]. Knowing the local strain field at the grain scale is an important premise in order to understand the relationship between the microstructure, microstructural constituents, and the elastoplastic response. Elastic deformations are reversible, meaning that the material returns to its original shape when the applied loads are released. Conversely, plastic deformations are irreversible, introducing non-reversible changes and damage to the material. During plastic deformation, typically micro-void formation and growth or micro-cracking are the dominating damaging mechanisms leading to fracture [13]. Thus, a thorough understanding of these processes is important in the design of steel structures.

Two-phase steel is a category of steels where the microstructure consists of two different crystal structures. This is typically a combination of ferrite and one of the following phases: austenite, martensite or bainite. A ferrite-pearlite steel follows the metastable Fe-Fe<sub>3</sub>C phase diagram. Bainitic and martensitic structures are obtained when quenching at sufficient cooling rates, while austenite is retained at room temperature by adding alloying elements. By combining two different phases, with different properties, the resulting steel will have properties from both phases. As an example, steels with a ferritic and martensitic microstructure (termed dual-

phase (DP) steels) will have greater strength than ferritic steels and greater ductility than martensitic steels. By altering the phase composition, different strength and ductility combinations are achieved. Other important considerations are the alloying content, corrosion properties, and cost, in addition to the mechanical properties.

In order to further develop two-phase steels, it is desirable to develop a modeling framework for these materials. Such a framework is being worked on at several research institutes, one of them being the Center for Advanced Structural Analysis (CASA) at the Norwegian University of Science and Technology (NTNU) [14]. Here, one of the goals is to reduce the need for mechanical testing when developing new alloys and characterizing DP steels using a multiscale framework. The idea of this multiscale framework follows the path shown in Figure 1.1. First, the chemical composition and thermal history of the DP steel investigated are entered into a nano-mechanical model. From this, the yield stress,  $\sigma_0$ , and the work-hardening as a function of plastic strain,  $R(p)$ , are obtained for the material and used to calibrate a standard plasticity model. The sum of these two equals the plastic region of the stress-strain curve. Second, microstructure information (volume fraction of each phase, grain size distribution, average constituent size, etc.) is added to a micromechanical DP model. This model subjects a representative volume element (RVE) to many different stress states, and from this the yield surface,  $\varphi(\hat{\sigma})$ , is calculated. Third, the stress-strain curve and yield surface obtained are used in unit cell modeling to calibrate a porous plasticity model, in most cases the Gurson model [15–17]. The parameters  $q_1, q_2, q_3, k_s$  are modeling constants in the Gurson model calibrated during the unit cell modeling. In order to have damage evolution in the microstructure, a localization analysis is performed combining the standard plasticity model and the porous plasticity model in step four. Here, the white part in Figure 1.1 is the area modeled by the standard plasticity model and the dark band is modeled using the porous plasticity model. From this analysis, localization of damage is introduced in the model. As a result, the fracture strain,  $\epsilon_f$ , is obtained as a function of stress states, which are described by the triaxiality,  $\sigma^*$ , and the Lode parameter,  $\mu$ . The final result is a virtual calibration of a structural component using continuum modeling with a minimum of mechanical tests.

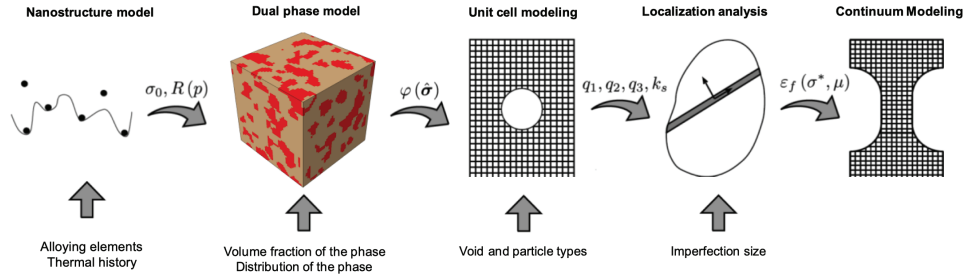


**Figure 1.1:** The different stages in virtual modeling DP steel. From alloying content, thermal history, phase composition, particle information and imperfection size, a continuum model of a structural component can be created from this virtual laboratory. This figure is provided courtesy of SFI-CASA at NTNU.

## 1.2 Previous work

### 1.2.1 Digital image correlation (DIC)

DIC is a non-contact measuring technique that performs an analysis of images acquired during a mechanical test. From this analysis, it is possible to calculate displacements and local strains within the recorded area. In order to correlate the images and track points on the surface, a speckle pattern is required. This pattern is key and may be achieved by several different methods. These methods are dependent on the required resolution, specimen surface, and image acquisition. As an example, for a uniaxial tensile test on an arbitrary metal, recorded using a digital camera, a speckled pattern is achieved by applying a black and white spray paint on to the surface.

Peters and Ranson [18] published one of the earliest papers on the use of DIC in mechanical testing and later others further developed the technique [19–25]. Today, DIC is an established measuring technique with several commercial systems for mechanical testing available [26–29], and since 2010 more than 3,000 articles<sup>1</sup> have been published using DIC. Within these publications, there is a diverse use of DIC. It is used as a virtual extensometer during a tensile test on plane specimen [30] (2D-DIC), to evaluate the neck shape of notched round-bar specimens during tensile test [31] (3D-DIC), to measure deflection during blast loading [32] (3D-DIC) and more. As a further development of DIC, X-ray tomography data are used in digital volume correlation (DVC) to get 3D strain maps from within the specimen. This technique was utilized by Buljac et al. [33] and by Buljac et al. [34] on different

<sup>1</sup>Articles were identified by searching Scopus with the following query string: TITLE-ABS-KEY(digital image correlation) AND (DIC) AND PUBYEAR > 2009 AND PUBYEAR < 2020 AND (LIMIT-TO ( DOCTYPE, "ar" ) ).

aluminum alloys. The alloys had a machined notch, and this notch was loaded stepwise. After each loading step radiographs were collected in a synchrotron. From these radiographs 3D volumes were reconstructed and from the series of volumes collected during the *in-situ* tensile tests a DVC analysis was performed. As a result, the crack growth and void nucleation within the tensile specimen could be investigated with a 3D perspective. Recently, the DIC technique has caught interest for images acquired with an SEM [35]. All that is required for DIC is an image series of the desired region containing a speckled pattern with sufficient contrast. In an SEM the images are acquired at a much larger magnification compared to images recorded using conventional digital cameras. One challenge during SEM imaging is to apply a speckle pattern and image acquisition. An early work combining DIC with SEM images was performed by Allais et al. [36]. They developed a technique using a micro-grid to measure the local strains in a DP steel. This micro-grid consisted of several hundred gold dots. These were deposited on the surface using a microelectrolithographic technique. This resulted in a spatial resolution of 0.5  $\mu\text{m}$  - 1  $\mu\text{m}$ . Several other techniques have been utilized over the years to study the local straining of microstructures, including, but not limited to: etching, surface deposition, creation of micro-grids using electron beam lithography [9, 37–49]. Recent advances in *in-situ* SEM DIC is the ability to achieve higher spatial resolution in the DIC strain field. A successful technique has been to apply a gold speckled pattern on a polished surface. For instance, Orozco-Caballero et al. [10] achieved a spatial resolution of 44 nm in their strain fields using this technique.

### 1.2.2 Two-phase steel *in-situ* SEM investigations

One of the first studies using *in-situ* SEM tensile testing was performed by Porter et al. [50]. Here, two steels with a pearlitic microstructure was investigated. The difference between the two steels was the interlaminar spacing in the pearlite. This study described the difference in deformation behavior of a coarse pearlite structure versus a fine pearlite structure. Building on their work, Sidhom et al. [51] combined *in-situ* SEM tensile testing with electron backscatter detector (EBSD) to correlate the observations with the different grain orientations. The conclusion from both these investigations was that the coarse pearlite has a more brittle behavior than the fine pearlite during tensile deformation. As a result, the plastically induced damage was found to be delayed by incorporating a fine pearlitic structure compared to a coarser pearlite structure.

Recently there have been several studies investigating DP steels using *in-situ* SEM techniques [47–49]. Tasan et al. [49] investigated two types of microstructural bands from rolled two phased steel. One continuous hard band of martensite and one discontinuous softer band of pearlite. The hard band was from a DP600 plate, and the discontinuous softer band was created by heating the same DP600

plate at 1050°C and cooling by air. During the heat treatment, the martensite was transformed into austenite at 1050°C before transforming into pearlite during cooling. The bands from these steels were investigated by performing an *in-situ* SEM tensile test on the etched microstructure. Secondary electron (SE) images were acquired during the tensile test, and these were subsequently used for a DIC analysis. In the specimen with a continuous microstructural band, the shear bands were forced to propagate through the band of martensite. As a consequence, the shear band cuts through the narrowest section. For the discontinuous bands of pearlite, the shear bands propagated naturally across the gaps within the band, thereby delaying early damage initiation.

Super duplex stainless steel (SDSS) is a two-phase steel consisting of roughly 50% ferrite and 50% austenite. This steel contains a large amount of alloying elements in order to achieve superior corrosion properties. The main elements are Cr (25%), Ni (7%) and Mo (3.5%). During production, SDSS is annealed at 1050°C. While cooling after the heat treatment, precipitation of intermetallic phases ( $\sigma$ ,  $\chi$ ,  $\pi$  and  $R$ ) may occur. The precipitation and effects of these have been studied in several journal articles [52–55]. From these studies, it is clear that the precipitation of intermetallic phases has a deteriorating effect on both mechanical properties and corrosion properties. An *in-situ* SEM study by Elstad [56] investigated the intermetallics effect on the microstructure. The microstructure was recorded with EBSD before and after a tensile test. The EBSD results from this study showed that the grain orientation gradients in the deformed specimen increased with the presence of  $\sigma$ -phase in the microstructure. Also, the austenite seemed to accommodate more deformation than ferrite during the tensile test. A different *in-situ* SEM study on duplex steels was conducted by Wang et al. [57]. Here, the effects of the long-term thermal aging on the deformation and fracture mechanism of casting duplex stainless steels were investigated. These were thermally aged up to 10,000 hours at 400°C. During this aging process a spinodal decomposing occurs where the ferrite separates into a Fe-rich ferrite and a Cr-rich ferrite. As a result, there will be a fluctuation of hardness in the ferrite with the amplitude gradually increasing during the aging [58]. Wang et al. [57] showed that the effect of this decomposition would result in the alteration of the crack initiation sites from the second phase particles in austenite and  $\delta/\gamma$  interface to the glide steps in ferrite. The fracture mechanism will change from the ductile fracture to the cleavage fracture in ferrite and the quasi-cleavage fracture in austenite.

### 1.3 Scope

A total of three types of two-phase steels have been investigated in this thesis. These are a ferritic-pearlitic steel, a ferritic-austenitic steel, and ferritic-martensitic steels. The interactions between the two phases in the microstructure have been investigated by utilizing recent advances in SEM *in-situ* tensile testing. An important part of this thesis has been to establish an experimental technique, combining *in-situ* SEM tensile testing with DIC at NTNU. This technique includes preparing the specimens for electron backscatter diffraction (EBSD) analysis, acquiring an EBSD scan, applying a speckled pattern for DIC, performing *in-situ* tensile test, acquire suitable images for DIC during the tensile test and analyzing the images in a DIC software. The resulting data from such a test is a detailed strain map of the microstructure on a sub-grain scale, including information from the microstructure obtained by EBSD. In addition, information from this EBSD characterization will contribute with experimental data to the first two steps in the virtual laboratory (Figure 1.1) and verifying the modeling sequence for DP steels.

Throughout this work, several studies were undertaken in order to verify the technique and methods used. First, a study on the effect of heat treatment on the steels investigated was conducted. Second, the DIC results were verified by comparing the grain rotations measured in DIC and EBSD. Third, two different speckled patterns were compared to highlight differences and advantages with different speckled patterns applied for DIC. Finally, a series of investigations were undertaken using *in-situ* SEM tensile testing. These tests were performed on a NVE36 two-phase steel, DP steels and an SDSS.

### 1.4 Outline

This thesis has the following outline: first, some background on relevant theories are given. These topics are SEM, DIC, steel microstructure and behavior, and numerical models. Second, a description of the experimental equipment and techniques used in this thesis are described. Also, specimen preparation and the different steels tested are presented. Third, two chapters are investigating the validity of the measurements and the effect of sample preparation on the specimens. Then four different studies are presented where all the results from the thesis work will be given and discussed. Finally, the last chapter will summarize this thesis, make concluding remarks and provide some suggestions for future work. In addition, two published journal articles are attached in the appendix.

## Chapter 2

# Theoretical background

This chapter will present the current state of the art and relevant theory for this thesis. First, the mechanics of a scanning electron microscope (SEM) and the imaging techniques used during this work are presented. Second, the digital image correlation (DIC) technique will be described. Third, a section on micromechanics of steels is given, focusing on crystal structures, damage mechanisms, forming processes and influence of temperature. Also, a section describing the different strain and stress measurements used throughout this thesis and how they are related is given. Finally, the fundamentals related to the constitutive relations used during numerical simulations are presented.

### 2.1 Scanning electron microscope

#### 2.1.1 Imaging in an SEM

An SEM focuses an electron beam on to the specimen placed in a vacuum chamber. The electron beam is emitted from an electron gun, going through a series of electromagnetic lenses which focus and control the beam. Typically, the beam has an energy ranging from 0.2 keV to 40 keV with a beam spot size of approximately 0.4 nm to 5 nm [59, 60]. The electrons in the beam interact with a volume beneath the specimen surface. This volume is known as the interaction volume. As a result of this interaction, there is an elastic and inelastic scattering of electrons, emission of electromagnetic radiation and transmitted electrons, as illustrated in Figure 2.1. How deep the electrons penetrate below the surface ranges from 100 nm up to 5  $\mu\text{m}$  depending on the material and electron beam energy [59, 60]. Different signals provide different information about the specimen. One type of detector typically captures one type of signal from which one type of image is created. As a consequence, one SEM has many detectors.



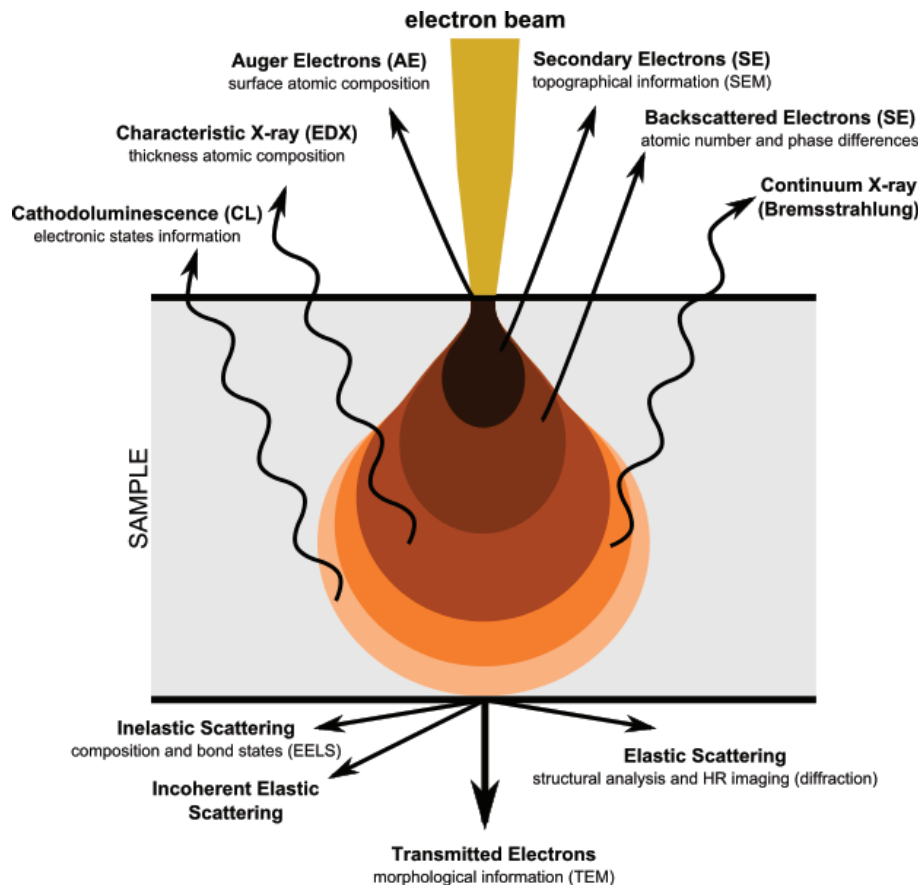


**Figure 2.1:** An illustration of the interaction volume. Straight lines are electrons emitted and the curved lines are electromagnetic radiation. The image is taken from [61] and is available under Public License [62].

During image acquisition, the electron beam scans a user selected area in a raster manner. This means that the beam scans the area row-by-row (most common) or column-by-column. The former is illustrated in Figure 2.2. The SEM operator controls the scanning speed. Lower scanning speed means that more time is spent on each point of the area increasing the signal-to-noise ratio (time spent at each pixel in the image is termed dwell time). Then, each pixel in the image will be loaded at different times. As a consequence, with a frame rate of 6 s, the first pixel will be loaded 6 s earlier than the last. Normally this will not influence the final image since the specimen is stationary during the acquisition process. However, during acquisition, imaging artifacts are always present. These artifacts are grouped into three categories [35]:

1. Non-random, time-independent spatial distortions
2. Non-random, time-dependent image distortions (drift-induced)
3. Random, time-dependent distortion

Artifact (1) occurs since no magnetic lens is perfect. As a consequence, there will be some spherical aberrations or astigmatism [60], similar to effects seen in optical systems. Artifact (2) is a result of the scanning in SEM imaging. Longer dwell time (time spent acquiring each pixel) leads to larger drift [35]. The sources of artifact (3) are not fully understood. However, reports relate the issue to specimen charging, electromagnetic field fluctuation, and environmental factors [35]. All these distortions are generally small (in the order of nm [35]), but at higher magnifications, small errors will have a more significant influence on the image. Even though these artifacts may not be visible to the human eye, they will still be captured by a DIC analysis. As a result, the final strain field from a DIC analysis will contain artifacts from the microscope imaging process.

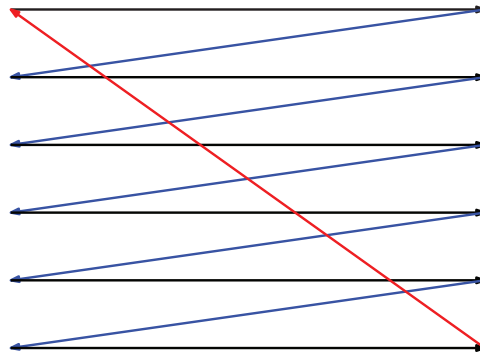


**Figure 2.2:** A schematic of the raster scanning process. Typically goes from left to right, row-by-row, from top to bottom, before starting over.

The four major parameters when it comes to SEM imaging are accelerating voltage, convergence angle, probe current and spot size. In Figure 2.3 these parameters are illustrated. The accelerating voltage is a user-controlled setting and is the voltage applied on the electron gun to emit the electron beam. The convergence angle is the angle between the spot size and where the electrons exit the electron column. This value is controlled by the condenser lenses, objective lenses, aperture size, and working distance. Here the former two are given by the microscope specifications, and the latter two are user settings. The probe current is the number of electrons impacting the specimen per unit time. A higher accelerating voltage and larger aperture size increase the probe current. The spot size is the diameter of the electron

beam interacting with the specimen and is the theoretical resolution limit of the resulting image. This diameter is dependent on the accelerating voltage (a lower voltage equals a smaller spot size), aperture size (a smaller aperture size equals a smaller spot size) and working distance (a shorter working distance equals a smaller spot size). In addition, the working distance is in many instances limited by the presence of detectors in the vacuum chamber and the specimen dimensions.

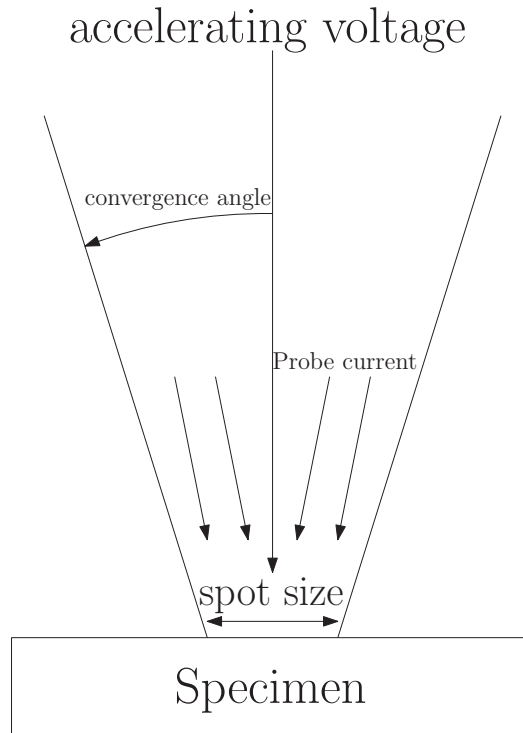


**Figure 2.3:** An illustration showing the electron beam impacting a specimen. The meaning of the parameters accelerating voltage, convergence angle, probe current and spot size are labelled.

The effects of these four variables (accelerating voltage, convergence angle, spot size, and aperture size) are summarized in the probe current. A larger probe current gives more signal and data. However, at larger magnifications, the image would be less detailed. In addition, a large probe current can damage or contaminate the specimen surface. Conversely, a smaller probe current provides less damage and signal, but more details. When considering a specimen with no charging, the probe current is defined as [60]

$$i = i_{SE} + i_{BSE} + i_{AE} \quad (2.1)$$

where  $i$  is the probe current,  $i_{SE}$  is the current from the secondary electrons (SE),  $i_{BSE}$  is the current from the backscatter electrons (BSE) and  $i_{AE}$  is the current from the absorbed electrons (AE). Assuming that both the SE and BSE are a fraction of the incoming electrons the total equation then becomes

$$i = \delta \cdot i + \eta \cdot i + i_{AE} \quad (2.2)$$

where  $\delta$  is the fraction of SE, often set to 0.1 when the accelerating voltage is 20 kV, and  $\eta$  is the fraction of BSE and is a function of the atomic number ( $Z$ ) given by Equation 2.3. In addition, the microscope can measure the absorbed electrons. As a result, the probe current can be estimated from Equation 2.2 by utilizing the empirical relationship in Equation 2.3.

$$\eta = -0.0254 + 0.016 \cdot Z - 1.86 \cdot 10^{-4} \cdot Z^2 + 8.3 \cdot 10^{-7} \cdot Z^3 \quad (2.3)$$

### 2.1.2 Secondary electrons

SE are low energy signals (<50 eV [59]) inelastically scattered and emitted from the very top of the interaction volume (seen in Figure 2.2). This signal provides information about the surface topography. After SE exit the specimen surface, they are collected by an Everhart-Thornley detector (ETD) [63]. This detector can collect both SE signals and BSE signals. However, it is mostly used to detect SE, since there are more efficient BSE detectors available [59] (described in Chapter 2.1.3). A schematic representation of an ETD is presented in Figure 2.4. The Faraday cage surrounding the front of the detector has a charge in the range +50 to +200 V to attract SE. At the tip, there is a scintillator (a material re-emitting absorbed energy in the form of light) with an even greater charge (typically +10 kV) compared to the Faraday Cage. As a result, most of the SE interacts the scintillator, converting the energy from SE into light. From here, this light is guided to a photocathode. The photocathode converts the light from the scintillator into an amplified electrical signal which in turn is further amplified. This signal is a two-dimensional intensity distribution, which converts into a pixel in the final image. The specimen topography will result in different levels of SE emitted from the surface. As a result, there is different brightness in different areas based on topography.

### 2.1.3 Backscatter electrons

In contrast to SE, BSE are high energy signals (with approximately 90% of the energy compared to the incoming electron beam) elastically scattered from the sample [59, 65]. These electrons typically penetrate a few atom layers deep, which

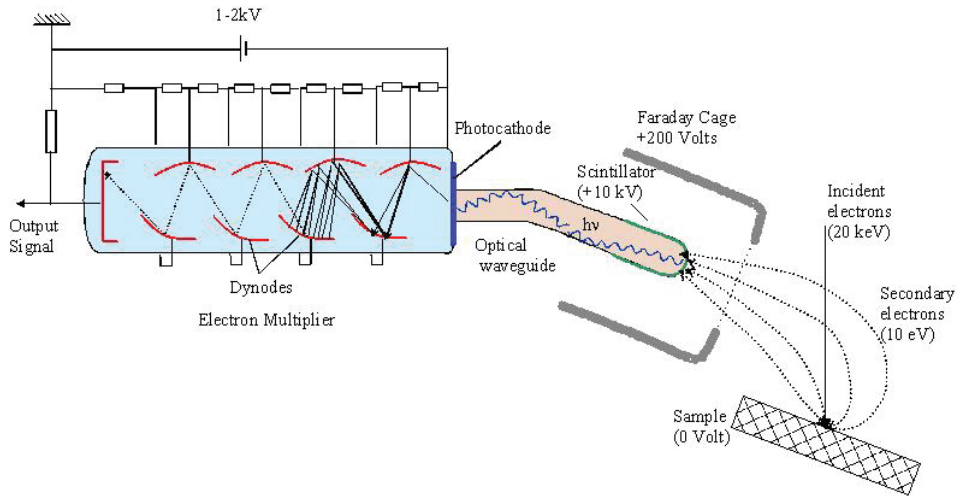


**Figure 2.4:** A schematic representation of an Everhart-Thornley detector. The image is in the public domain, available at [64].

is deeper beneath the surface compared to SE (see Figure 2.1). Most of the BSE signal is reflected out from the specimen with a low angle between the electron beam and BSE (assuming a flat specimen surface). For this reason, the BSE detector is placed above the sample, in a circle concentric around the electron beam. There are two types of BSE detectors: a scintillator-photomultiplier type similar to the SE detector described in Chapter 2.1.2 or a solid-state silicon type where the latter is more common and ten times more efficient [60]. The solid-state type is a silicon semiconductor, where it takes a certain amount of energy before a signal is created. This barrier helps to filter out lower energy signals (e.g., SE) enhancing the signal-to-noise ratio.

BSE signals are highly dependent on the atomic number of the specimen [59]. Materials with a higher atomic number will return more BSE-signal and appear brighter in the image. A larger difference in atomic number gives greater contrast difference in the image. As a result, BSE imaging is also often referred to as atomic-number-contrast imaging or Z-contrast imaging.

#### 2.1.4 Electron backscatter diffraction

An additional feature of BSE is to obtain diffraction patterns from the material. This technique is called Electron Backscatter Diffraction (EBSD). From these diffraction patterns, crystallographic information is extracted from the material. The incoming electron beam will impact the specimen surface, and BSE are reflected onto the EBSD detector. This setup is shown in Figure 2.5. This detector

consists of a phosphor screen and a charge-coupled-device (CCD) camera. The incoming BSE will hit the phosphor screen, and the light from this will be converted to electrical signals by the CCD camera [65]. The reflected BSE will have different intensities, depending on the interactions between the incoming beam and the atomic planes. As a result, the recorded BSE signal consists of different bands. The resulting pattern is seen in Figure 2.6 and is termed electron backscatter diffraction pattern (EBSP) or Kikuchi pattern. From the characteristics of these patterns, the crystal structures and grain orientations can be obtained. During the acquisition of EBSP, the specimen is tilted in order to increase the fraction of BSE signal emitted from the surface. As mentioned in Chapter 2.1.3, BSE are elastically scattered from the specimen surface. The energy of the scattered signal will decrease as a function of the distance it has to travel inside the material before leaving the specimen. When tilting the specimen, this distance is decreased. As a consequence, the BSE signal from a tilted specimen will be greater compared to a non-tilted specimen. This is illustrated in Figure 2.7. The optimal tilting angle for modern, commercial EBSD systems is found to be  $70^\circ$  [60, 65].

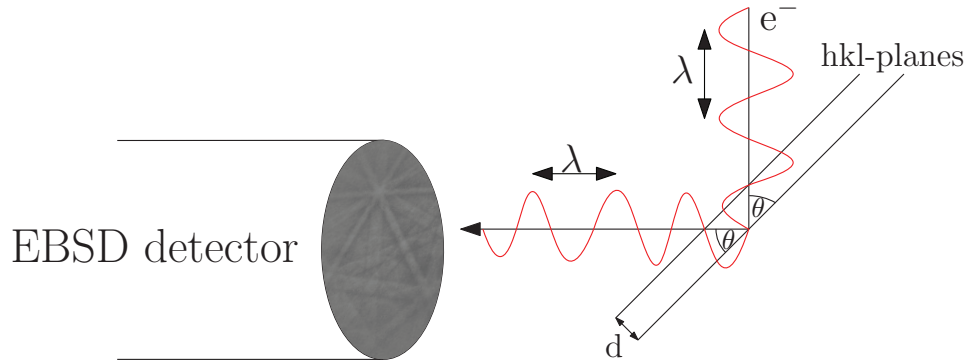


**Figure 2.5:** A schematic representation of the setup for EBSD acquisition. The electron beam interacts with the tilted specimen, and the backscatter diffraction patterns are recorded by a CCD camera located behind a phosphor screen. Electrons from the incoming beam are reflected, fulfilling Bragg's law. Here,  $d$  is atomic plane spacing,  $\theta$  is the angle between the atom plane and the reflected BSE signal and  $\lambda$  is the wavelength of electrons in the electron beam.

The width of the bands seen in the EBSP in Figure 2.6 is equal to two times the Bragg angle  $\theta$ . Following Bragg's law, the interplanar spacing  $d$  can then be found as:

$$2 \cdot d \cdot \sin(\theta) = n \cdot \lambda \quad (2.4)$$

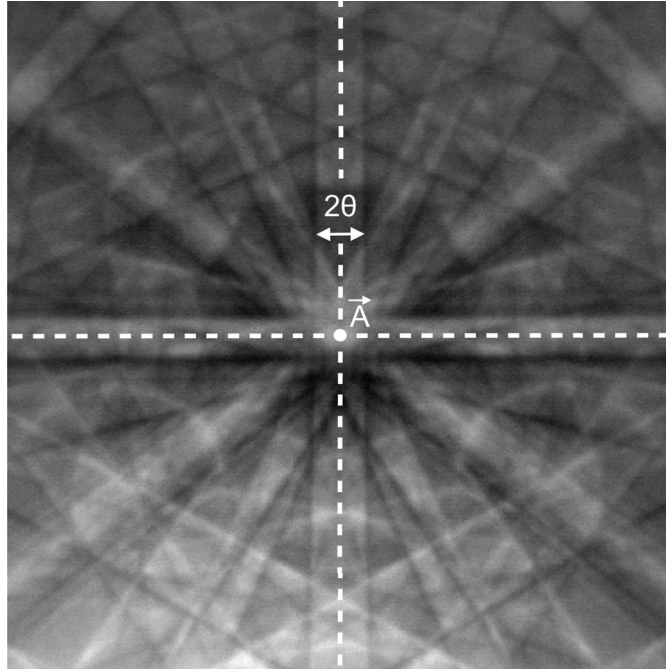


**Figure 2.6:** EBSP with labels indicating the planar spacing for a plane and the cross section between two planes. The image is adapted from [66] and is available under Public License [67].

where  $n$  is the order of reflection and  $\lambda$  is the wavelength of the electrons in the electron beam and is a function of the accelerating voltage applied [65]. The meaning of  $d$ ,  $\theta$  and  $\lambda$  is illustrated in Figure 2.5. Reflected electrons fulfilling Bragg's law will have more energy compared to reflected electrons which do not fulfill Bragg's law. As a consequence, Bragg reflected electrons appear brighter in the EBSP. Each band corresponds to a crystal plane with a width of  $2 \cdot \theta$  as shown in Figure 2.6. The angle between the different bands seen in the EBSP corresponds to the angle between the planes. Where the planes meet, labeled  $\vec{A}$  in the figure, represents the direction of a zone axis [60]. The position of the planes (or bands) in the pattern corresponds to the crystallographic orientation [65, 68]. By comparing the acquired Kikuchi patterns with a database of known and indexed patterns, the acquired patterns are indexed to provide crystallographic information from each pattern in the scanned area.

EBSP are collected in a selected area with a given step size. As a practical example, a scanned area of  $500 \mu\text{m} \times 500 \mu\text{m}$ , with a step size  $1 \mu\text{m}$  will contain 250 000 EBSP. If the step size is halved, the number of patterns is squared. After being

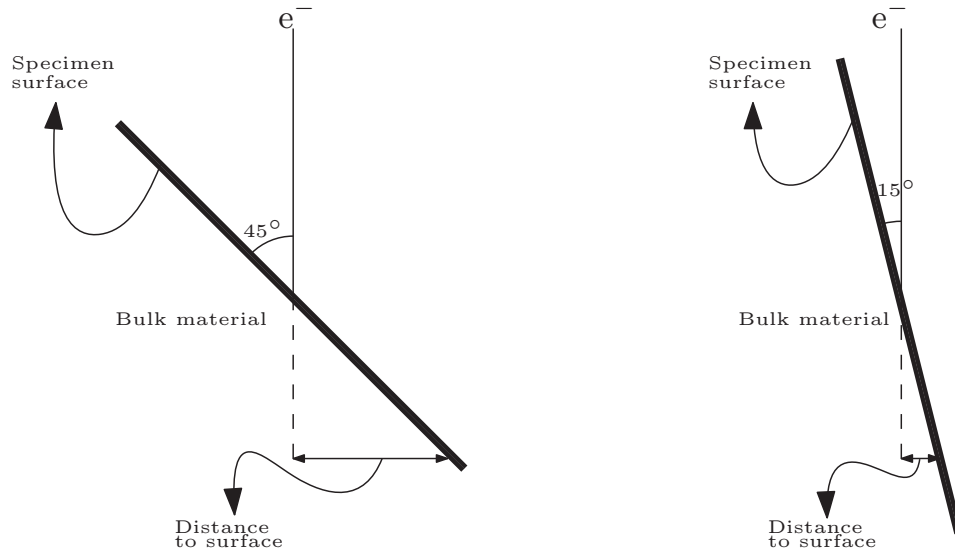


**Figure 2.7:** An illustration of how the tilting angle influences the distance BSE signals have to travel from inside the bulk material before escaping the surface. An increased distance will reduce the BSE signal strength.

collected, each pattern is matched with a database and indexed, returning crystal structure and orientation. After the patterns are indexed, the scanned area is ready for post-processing. During the post-processing, it is possible to extract several types of data. Some common features to extract is texture, average grain size, grain size distribution, phase composition, and misorientation profiles.



## 2.2 Digital image correlation

### 2.2.1 Theoretical background

Digital Image Correlation (DIC) has become a well-established tool for full-field displacement and strain measurements during mechanical testing. Various formulations of DIC exist in the literature, where the principle of optical flow forms the basis for the technique. The traditional formulation of DIC (see e.g., Sutton et al. [19]) is the subset-based formulation, where subsets are optimized individually. In contrast, the finite-element (FE) formulation of DIC proposed by Besnard et al. [23] is a global approach where the parameters describing the displacement field are solved in a single global procedure. FE-DIC uses a mesh of two-dimensional elements to describe the displacement field, and the degrees-of-freedom (DOF) of the elements are optimized for each image in the series. Various types of elements have been investigated in the literature (see e.g., Réthoré et al. [25]) and the technique is in principle independent of the choice of the element type. However, Q4 elements (elements with four nodes and eight DOF) seems to be the most used. In the following section, the most relevant details and equations are presented for the FE-DIC approach applied in this study. However, the reader is referred to Fagerholt [1] for a complete mathematical description.

During a mechanical test, a region of interest (ROI) is recorded with a digital camera at a certain frequency. This image series is then used for the subsequent analysis. The first image is the undeformed reference image  $I_r$ . An image at the deformed stage  $I_c$  (current configuration) is compared to the reference state in the DIC algorithm. The image coordinates are given by  $\mathbf{X} = (X, Y)$ , and the displacement is given by  $\mathbf{u} = (u, v)$ . Bold variables denote the variable being a vector. The basic assumption is "conservation of optical flow", i.e., the coordinates in the current image  $I_c(\mathbf{X} + \mathbf{u})$  is equal to a displacement field  $\mathbf{u}(\mathbf{X})$  added to the reference image  $I_r(\mathbf{X})$ . The "conservation of optical flow" yields

$$I_c(\mathbf{X} + \mathbf{u}(\mathbf{X})) = I_r(\mathbf{X}) \quad (2.5)$$

The displacement field  $\mathbf{u}(\mathbf{X})$  consists of a known part  $\mathbf{u}'(\mathbf{X})$  (displacement field from previous image) and a small unknown part  $\Delta\mathbf{u}(\mathbf{X})$  (displacement since previous image) such that the new displacement field for the current image becomes  $\mathbf{u}(\mathbf{X}) = \mathbf{u}'(\mathbf{X}) + \Delta\mathbf{u}(\mathbf{X})$ . When inserting the initially known coordinate in the current configuration  $\mathbf{x}' = \mathbf{X} + \mathbf{u}'$ , and the unknown incremental part of the displacement,  $\Delta\mathbf{u}$ , into Equation 2.5, this becomes

$$I_c(\mathbf{X} + \mathbf{u}'(\mathbf{X})) = I_c(\mathbf{x}') = I_r(\mathbf{X} - \Delta \mathbf{u}(\mathbf{X})) \quad (2.6)$$

The incremental part of the displacement is here subtracted from the reference configuration coordinates  $\mathbf{X}$  at the right-hand side of the equation. The unknown part,  $\Delta \mathbf{u}$ , is found by minimizing a correlation function  $F$  based on the difference in grayscale values between the reference image  $I_r$  and the current image  $I_c$ .  $F$  is used as the objective function in the Newton-Raphson optimization. The sum of squares (SSD) of the grayscale difference within the elements is defined by

$$F = \sum_{i \in \Omega} (I_r(\mathbf{X}_i) - I_c(\mathbf{x}_i))^2 \quad (2.7)$$

Solving the minimizing function in Equation 2.7 by inserting the expression in Equation 2.6, the deformation field increment,  $\Delta \mathbf{u}(\mathbf{X})$ , can be found. The increment is then added to the displacement field in the previous state, and  $\mathbf{u}(\mathbf{X})$  for the current state is obtained.

From the principle of optical flow, DIC assumes all images in a series to be a transformed version of the reference image, where the transformation is given by the displacement field. Thus, effects like gray-scale pixel noise (or signal-to-noise ratio), light variations, propagating cracks, etc., causes increasing residuals in the DIC optimization process and pose challenges to the algorithm. The pixel noise must be considered in the design and setup of the experiment, concerning the choice of camera, lighting conditions, room temperature and similar. In the analysis stage, it is possible to increase the element size to overcome a high noise level, with the downside of losing resolution in the displacement field measurements. Temporal changes in the ambient lighting conditions during the test may be optimized by a normalization of the pixel gray values. Here, an elementwise normalization based on both mean and variance of the gray-scale values is applied, i.e., using a zero-mean normalized sum of squared differences (ZNSSD) criterion [35]. Updating of reference images in the DIC algorithm acts as a reset of gray-scale value residuals and can be used when the appearance of the specimen surface has deviated significantly from the reference image. Reference updates may be challenging and should, in general, be reduced to a minimum because errors in the displacement field are accumulated, as discussed in Tang et al. [69].

Local strain at the nodes is calculated as principal logarithmic strains at element level (see e.g., [70]). First, the deformation gradient  $\mathbf{F} = \mathbf{F}(\mathbf{X}, t) = \mathbf{1} + \partial \mathbf{u} / \partial \mathbf{X}$  is found from the measured two-dimensional displacement field  $\mathbf{u} = \mathbf{u}(\mathbf{X}, t)$  for a particular location  $\mathbf{X}$  and time  $t$ . The right Cauchy-Green tensor is then calculated as

$$\mathbf{C} = \mathbf{F}^T \mathbf{F} \quad (2.8)$$

The principal stretches,  $\mu_i, i = 1, 2$  are found by solving the eigenvalue problem for the right Cauchy-Green tensor

$$(\mu_i^2 \mathbf{1} - \mathbf{C}) \mathbf{n}_i = \mathbf{0} \quad (2.9)$$

where the vectors  $\mathbf{n}_i$  gives the direction of the principal stretches  $\mu_i$ . The in-plane logarithmic principal strains  $\varepsilon_i = \varepsilon_i(\mathbf{X}, t)$  are finally found as

$$\varepsilon_i = \ln(\mu_i), i = 1, 2 \quad (2.10)$$

The index  $i$  is arranged so that  $\varepsilon_1 > \varepsilon_2$ . In this work, the major logarithmic principal strain  $\varepsilon_i$  is used for visualization of strain fields, but is also used to access the local maximum strain within a DIC element.

Most strains in this study are referred to as average engineering strains. These strains are calculated using virtual extensometers in the DIC software, defined as a vector between two material points in the DIC mesh. The average engineering strain ( $\bar{e}_{DIC}$ ) is then calculated as

$$\bar{e}_{DIC} = \sum_{i=1}^N e_{DIC_i}, \quad e_{DIC_i} = \frac{\Delta L}{L_0} \quad (2.11)$$

where  $L_0$  is the initial length of the virtual extensometer (vector), and  $\Delta L$  is the change in length of the virtual extensometer (vector).

Using polar decomposition, it is possible to separate the deformation gradient,  $\mathbf{F}$ , into a component that stretches the space along a set of orthogonal axes, and a rotation (with possible reflection) represented by  $\mathbf{U}$  and  $\mathbf{R}$ , respectively, in Equation 2.12.

$$\mathbf{F} = \mathbf{R} \cdot \mathbf{U} \quad (2.12)$$

The deformation gradient  $\mathbf{F}$ , the rotation  $\mathbf{R}$  and the displacement  $\mathbf{U}$  is defined by

$$\begin{aligned}
\mathbf{F} &= \begin{pmatrix} F_{11} & F_{12} \\ F_{21} & F_{22} \end{pmatrix} \\
\mathbf{R} &= \begin{pmatrix} \cos(\theta) & -\sin(\theta) \\ \sin(\theta) & \cos(\theta) \end{pmatrix} \\
\mathbf{U} &= \begin{pmatrix} U_{11} & U_{12} \\ U_{21} & U_{22} \end{pmatrix}
\end{aligned} \tag{2.13}$$

From this it is possible to isolate and extract the rotations of the material surface and represent them using the DIC software using Equation 2.14.

$$\mathbf{R} = \mathbf{F} \cdot \mathbf{U}^{-1} \tag{2.14}$$

### 2.2.2 Digital image correlation in scanning electron microscope

Using an SEM, it is possible to record high-resolution images with high magnification. These images can be correlated using DIC to get strain fields which can resolve the slip bands within grains (see e.g., [9, 10, 71–73]). A challenge is to have a speckled pattern suitable for DIC analysis. Several different approaches are taken, depending on the desired resolution. Allais et al. [36] developed a technique using a micro-grid to measure the local strains in a dual-phase (DP) steel. This micro-grid consisted of several hundred gold dots. These were deposited on the surface using a microelectrolithographic technique. The technique is briefly described here and is based on Appendix A in Allais et al. [36]. First, the surface is covered with a thin layer of an electro-sensitive resin. To polymerize the resin, it was cured for 30 minutes at 140°C. The desired pattern is drawn using the SEM electron beam. This irradiation lowers the molecular weight of the resin, making it easily soluble. After the dotted pattern is created, the resin inside the dots is dissolved using a solvent, before a gold layer is applied to the sample surface. Finally, the remaining resin is dissolved using a different solvent, leaving only the dotted gold micro-grid pattern on the surface. The displacement of the gold dots during an *in-situ* SEM tensile test was used to calculate the strain field in the microstructure. The resulting spatial resolution was 0.5 - 1  $\mu\text{m}$ . Several other techniques have been utilized over the years to study the local straining of a microstructure, including, but not limited to: etching, surface deposition and creation of micro-grids using electron beam lithography [9, 37, 38, 44, 46].

One technique not mentioned above is to use secondary electron images of the microstructure. These images can then be correlated to find local strain values and distributions. The technique relies on using the variation of gray-scale values in the

recorded micrographs without any adaptations (such as adding a micro-grid or a speckled pattern). The features in the microstructure (grain boundaries, particles, different phases, etc.) are used as reference points for the subsequent DIC analysis. Using the microstructure of the specimen to correlate images was first shown by Kang et al. [74] and later by others [39–43, 45, 49]. Ghadbeigi et al. [42] compared results from DIC using the microstructure as a reference to the micro-grid method. The results were quantitatively similar for the two techniques, demonstrating the reliability of using the microstructure directly for the DIC analysis. Banerjee et al. [45] correlated SEM topography images based on micrographs to investigate the local strain variations in a grain of high strength steel. The applied global strain in that study was 8.3%, but locally, inside a grain, strain values as high as 150% were observed. Other grains were found to have a local average strain value of 1.9%. In the study by Kang et al. [74], a micrograph was acquired for every 3-5% of macroscopic strain and then loaded into a DIC software and correlated to obtain the microscopic strain field.

Recent advances in *in-situ* SEM-DIC is the ability to get higher spatial resolution. For instance, Orozco-Caballero et al. [10] have achieved a spatial resolution of 44 nm in their strain fields. This fine resolution is accomplished by using a refined method developed by Di Gioacchino and Quinta da Fonseca [9]. Here, the specimen surface is coated with a 50 nm - 100 nm thick continuous gold layer. Then the specimen is heated in a water vapor atmosphere at 300 °C. This technique is described in detail in Chapter 3.3. The final result is a gold speckled pattern with fine dispersion, covering the specimen surface. Also, since gold has atomic number 79, it is much heavier magnesium ( $Z = 12$ ), aluminum ( $Z = 13$ ), titanium ( $Z = 22$ ) and iron ( $Z = 26$ ). As a result, the gold speckled pattern will provide great contrast between the specimen surface and the gold particles in an SEM-BSE image, providing excellent conditions for DIC analysis. In the study of Orozco-Caballero et al. [10], the resulting strain field in a magnesium alloy is capable of resolving slip bands within grains, quantifying the strain ratio between these bands, grain boundaries, and the overall average strain.

### 2.2.3 Gold remodeling

When the continuous gold layer is remodeled into a random speckled pattern, gas is flowing across the surface of the heated specimen. During this process, there are several stages from a continuous film to an island structure, and these are explained in detail in references [75–82]. First, hillocks form on the surface. The driving force for this formation is the relief of thermal stresses [79]. Second, pores in the film start to grow and eventually joins together. As a result, the hillocks continue to grow [75, 79, 81]. Finally, as the hillocks continue to grow the film has depleted the hillocks turning them into islands and a final random gold speckled pattern is obtained.

## 2.3 Steels

### 2.3.1 Crystal structures and slip systems

Steel is defined as iron with between 0.008 and 2.14 wt.% carbon added [83]. If more carbon is added to iron, it is termed cast iron. However, the carbon content rarely exceeds 1 wt.%, and in this work, only steels with less than 0.2 wt.% carbon will be considered. The advantage of this is to retain the formability and weldability of the material. In Figure 2.8 the metastable phase diagram for Fe-Fe<sub>3</sub>C is shown. This gives the different phases of steel obtained at different temperatures and carbon content with no other elements added and low cooling rates. When considering the metastable phase diagram in Figure 2.8 with no addition of carbon, the first phase to form during solidification, at 1538°C, is  $\delta$ -ferrite. In  $\delta$ -ferrite the atoms are arranged to create a body-centered cubic (BCC) crystal structure (illustrated in Figure 2.9(a)). This is stable between 1538°C and 1394°C. At 1394°C the  $\delta$ -ferrite transforms into austenite ( $\gamma$ ). Austenite has face-centered-cubic (FCC) crystal structure (illustrated in Figure 2.9(b)). Upon further cooling,  $\alpha$ -ferrite is formed at 912°C.  $\alpha$ -ferrite, as the  $\delta$ -ferrite, also has a BCC crystal structure and is the stable phase of iron at room temperature. In this work  $\alpha$ -ferrite will be referred to as ferrite, as this is the only ferritic phase being considered. When adding small amounts of carbon, a constituent named pearlite will be present at room temperature. Pearlite is a constituent consisting of a lamella structure, with alternating layers of ferrite and cementite (Fe<sub>3</sub>C). An illustration of the ferrite-pearlite microstructure is given in Figure 2.10. In the left half of the figure is a ferrite grain and in the right half is the pearlite grain, with the black line being the grain boundary.

As seen in Figure 2.8, an essential difference between austenite and ferrite, is their ability to dissolve carbon. A ferritic structure can maximum contain 0.022 wt.% of carbon before cementite starts to precipitate, resulting in the lamellar pearlite structure seen in Figure 2.10. In contrast, austenite can dissolve a maximum of 2.14 wt.% of carbon (at 1147°C). It is this difference in solubility of carbon which is exploited in order to harden steel. Usually, during the cooling process, there is enough time for the carbon to diffuse within the austenite and ferrite structure in order to precipitate carbides or have a phase transformation into pearlite. However, if a steel is kept at an elevated temperature, in the austenitic region of the phase diagram, and subsequently quenched, there would be no time for diffusion to take place. As a result, a metastable structure called martensite is formed. The formation of martensite takes place by deforming the austenite FCC lattice into a body-centered-tetragonal (BCT) crystal structure (illustrated in Figure 2.11). In a BCT unit cell, the lattice parameter of the a-axis is not equal to the lattice parameter of the c-axis. However, in martensite, the c-axis is only slightly longer in order to

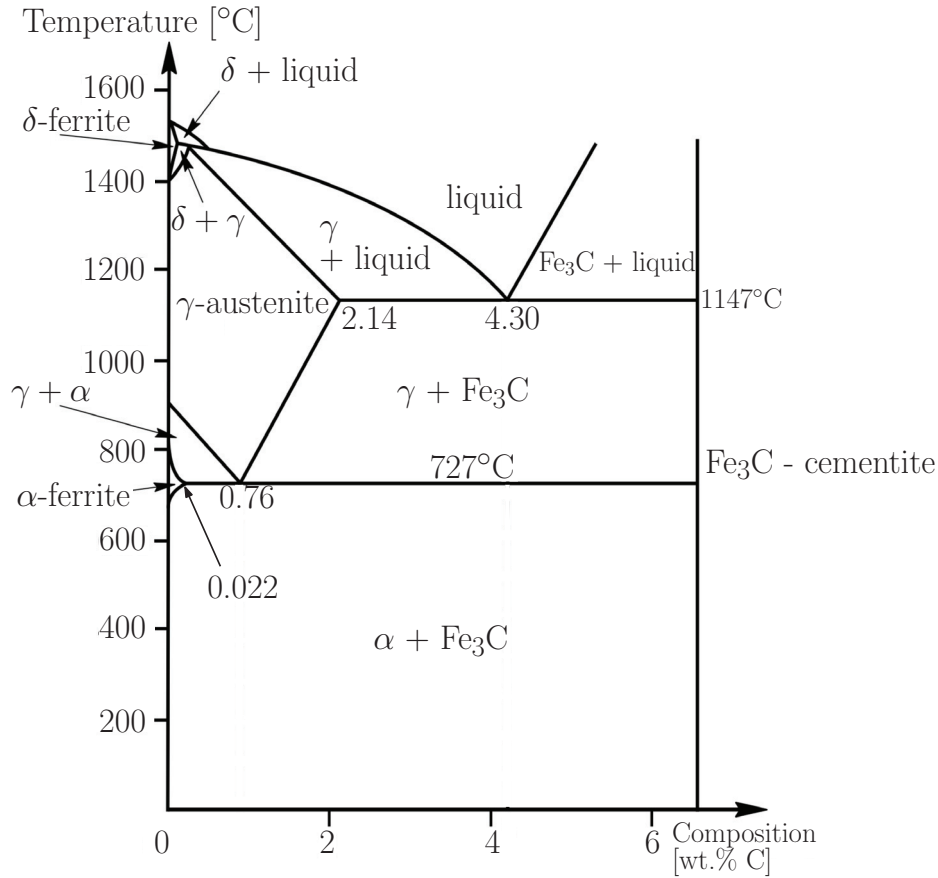


**Figure 2.8:** The iron-carbon phase diagram. Illustrating at which temperature and composition the different phases are stable.

accommodate the carbon atom and therefore it is worth noting that the illustration in Figure 2.11 is exaggerated in the case of martensite. The  $c/a$  ratio is given by Equation 2.15 [86]. During the transformation, the material is exposed to a volume expansion and large shear forces [86]. The resulting structure is hard and brittle. For that reason, it is often tempered after quenching in order to relax some of the internal stresses and make the material more formable. A typical steel containing martensite is dual-phase (DP) steels. These steels contain ferrite and martensite, and in these steels, martensite provides strength and ferrite provide ductility.

$$\frac{c}{a} = 1 + 0.045 \text{ wt.\% C} \quad (2.15)$$

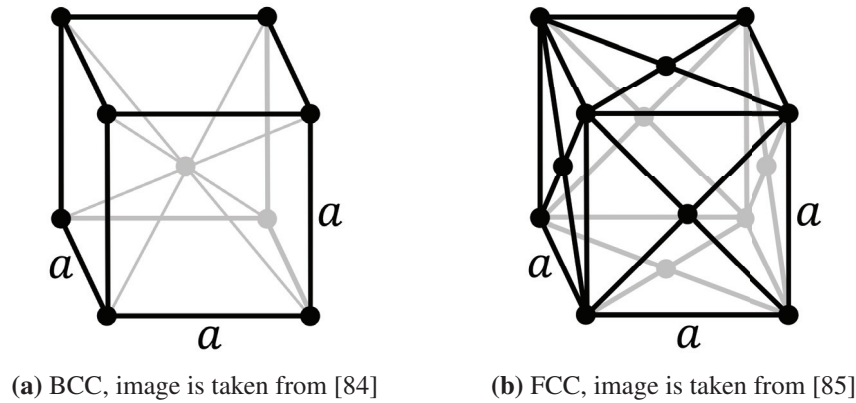


**Figure 2.9:** An illustration of the unit cell of BCC and FCC. The images are available under Public License [67].

The FCC crystal structure is a closely packed structure, meaning that the atoms are stacked in such fashion to minimize empty space. In an FCC crystal, 74% of the space is occupied by atoms. Conversely, for a BCC crystal this is 68% [83]. In addition, there are 12 slip systems associated with the FCC crystal. Slip systems include a slip plane and a slip direction. A slip plane is a plane, within the crystal structure, where the atoms are most densely packed. A slip direction is the most densely packed direction in the slip plane. For FCC the most densely packed plane is the  $\{111\}$ -family of planes. Within these planes, the  $[110]$ -directions are where the atoms are most densely packed. This is illustrated in Figure 2.12. From this figure, it is possible to see that this slip plane is the most densely packed with six atoms in the plane. Also, the slip directions are the most densely packed directions with three atoms. However, for BCC it is a little more complicated. There are a total of three slip planes,  $\{110\}$ ,  $\{211\}$  and  $\{321\}$ . For each of them, the slip direction is in the  $[111]$ -family. This corresponds to 12, 12 and 24 slip systems, respectively, meaning that it has a total of 48 slip systems [83]. However, since the structure is not a closely packed structure, there is a larger barrier (compared to FCC) for a slip to occur for these systems. Despite this fact, due to a large number of slip systems active in BCC and FCC structures, metals having these crystal structures will be quite ductile [83]. Martensite and cementite, on the other hand, are very hard and brittle phases. Martensite has carbon atoms locked into place within the BCC structure, and cementite has an orthorhombic crystal structure with iron and carbon atoms.



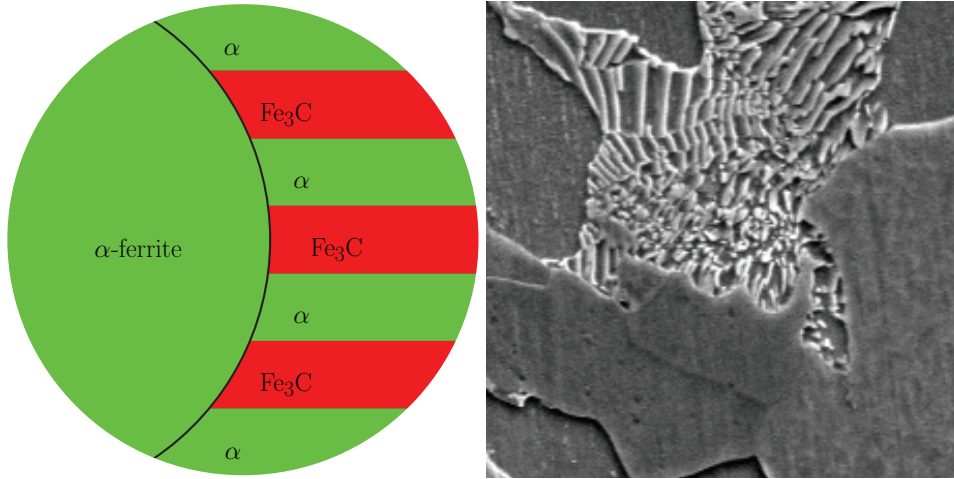


**Figure 2.10:** The ferrite–pearlite microstructure illustrated. Pearlite has a lamellae structure with alternating layers of cementite and ferrite. To the left is a graphical representation. Here, the black line is the grain boundary, with the left grain being ferrite and the right being pearlite. To the right is a micrograph with the cementite being the white lamellae.

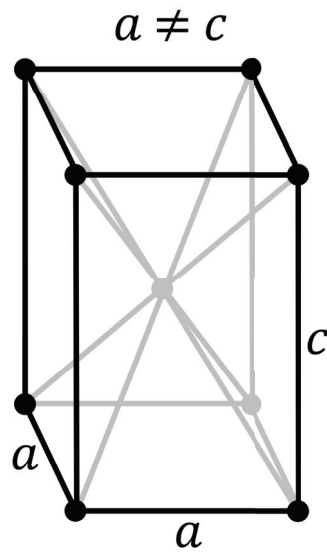


**Figure 2.11:** An illustration of the BCT unit cell. This is the unit cell for martensite. However, in martensite the ratio between  $a$  and  $c$  are not as extreme as illustrated here. The  $c/a$  ratio is given in Equation 2.15 and from here it can be seen that  $a \approx c$  in low carbon steels. The image is taken from [87] and is available under Public License [67].

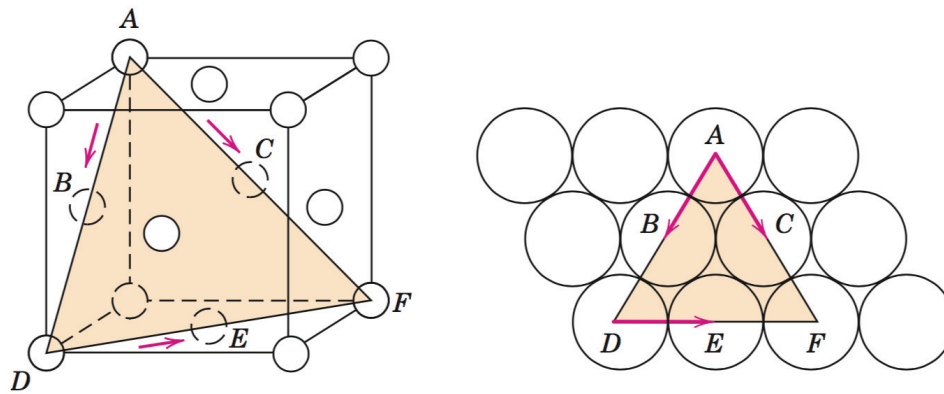


**Figure 2.12:** An illustration of the slip systems in the FCC unit cell. To the left is the  $\{111\}$  plane shown, with the slip directions marked. To the right is the plane from the left, seen from above, with the slip directions marked. The image is taken from [83].

### 2.3.2 Dislocations and damage mechanisms

The movement of dislocations [13] causes nearly all aspects of plastic deformation in metals. Dislocations are line defects moving through the metal when subjected to external loading, causing slip of crystals. There are two types of dislocations, edge dislocations and screw dislocations. The simplest type is the edge dislocation, and this is illustrated in Figure 2.13. Above the dislocation line, there is an extra insert half plane, and below it, there is a dislocation line running through the lattice. To accommodate this extra insert half plane, there is tension in the region above the dislocation line. Conversely, below the dislocation line, there is compression. Above and below this region, the lattice is unaffected by the dislocation. The movement of the dislocation line is illustrated in Figure 2.14. The structure is subjected to shear stress, and the dislocation line wants to move. It moves by breaking the atomic bonds in front of its path (atomic plane B in the figure). When the line has passed plane B, the bottom half of the plane form new bonds with plane A. Now, the top half of plane B is acting as the inserted half plane. This continues until it reaches the surface and here a step in the surface will be created. This process is termed slip, and in densely packed planes, the dislocations can move with fewer obstacles. As a result, the closely packed atomic planes in structures are termed slip planes. The Burgers vector, labeled  $b$  in the figure, is pointing in the slip direction and its length is the slip length from one dislocation.

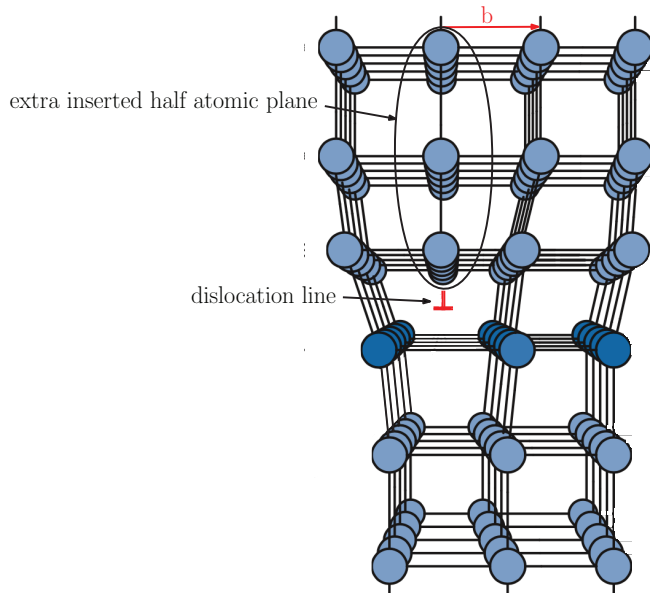


**Figure 2.13:** An illustration of an edge dislocation. The image is adapted from [83].

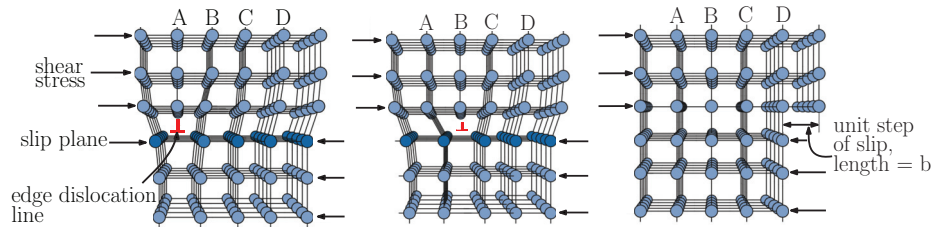


**Figure 2.14:** An illustration of an edge dislocation propagation through a metal. The image is adapted from [83].

The second type of dislocations is screw dislocations. These also produce a slip in the same direction, with the same length as the Burgers vector. However, the screw dislocation moves perpendicular to the shear direction. For an edge dislocation, this movement is parallel to the applied shear stress. A screw dislocation midway, moving through a crystal, is illustrated in Figure 2.15. The applied shear stress is parallel to the dislocation line and Burgers vector. The dislocation moves perpendicular to these. When a dislocation has passed through the lattice, a slip is created. The resulting slip for a screw dislocation is identical to a slip created by an edge dislocation, and after the dislocation has passed, there is no way of telling them apart. In reality, all dislocations will be a mixed dislocation, with having partially screw and edge components [13].

All metals contain some amount of dislocations. These are introduced during solidification and plastic deformation. The dislocation density (length of dislocations per unit volume, giving the unit  $\text{m}^{-2}$ ) in a carefully solidified material will be in the order of  $10^6 \text{ m}^{-2}$ . However, a highly deformed metal will have a dislocation density in the order of  $10^{13} \text{ m}^{-2}$  [83]. The cumulative effect of slip due to dislocations is the main source of plastic deformation in metals. When a material is subjected to a load, the dislocations start to move, and the dislocation density increases. The dislocations then start to interact with each other and the material in general. This is when a material gets stronger during deformation and is termed work-hardening. Two dislocations traveling in the same plane with parallel Burgers vectors can either repulse each other or attract each other. If the dislocations are identical, i.e., the Burgers vectors have the same sign, the compression field around the dislocation will interact with the compression field around the other dislocation. Also, the two tension fields will also interact, and as a result, the two dislocations will repel each other. Conversely, if the Burgers vectors are of opposite sign, the compression side of one dislocation will interact with the tension side of the other dislocation, and as a result, the dislocations will annihilate each other and leave a perfect crystal [83].

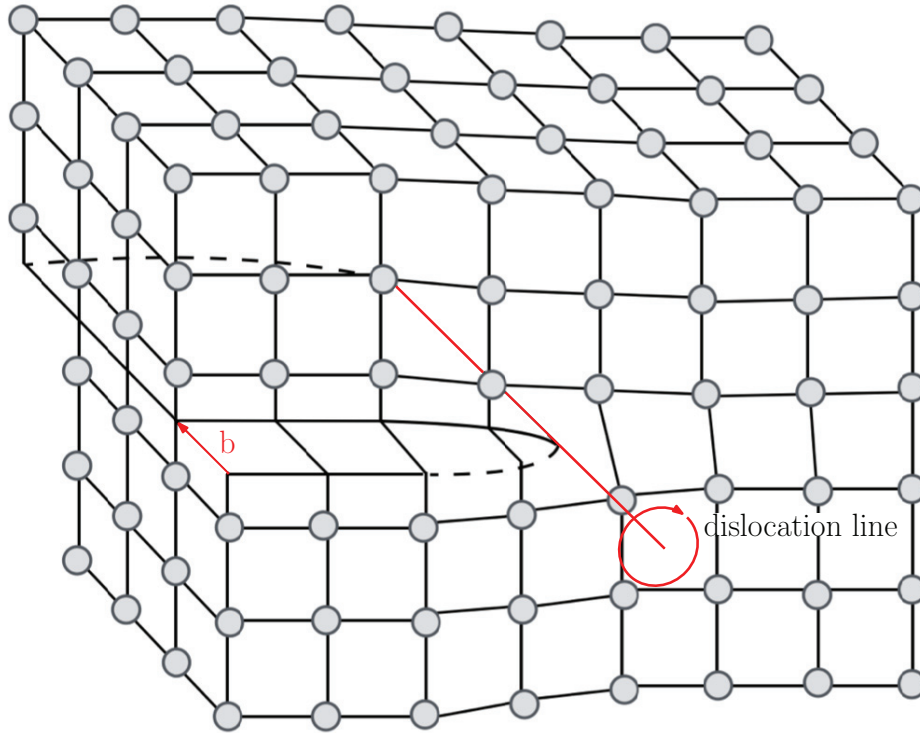


**Figure 2.15:** An illustration of a screw dislocation. Here, the dislocation moves from the left to the right, resulting in the lattice being shifted in the direction of the Burgers vector ( $b$ ). This distance is the slip length, and its length is the length of  $b$ . The image is adapted from [83].

However, in most cases interactions will obstruct the movement of the dislocations, resulting in a strengthening of the material. In addition to the interaction between dislocations, dislocations will interact with solute atoms and vacancies in the lattice. These interactions and the fact that the dislocation density increases during deformation lead to work hardening of metals.

In the material, some obstacles, like grain boundaries and secondary phases, will act as barriers on the dislocations. As a result, dislocations will pile up, leading to a high concentration of stress on the leading dislocation in the pileup. The increased stress can lead to yielding on the other side of the barrier or nucleate a crack at the barrier [13].

### 2.3.3 Thermomechanical processing, the effect of alloying, and formation of intermetallic phases

It is possible to tailor steel properties by adding different alloying elements and altering the heat treatment. From this, a wide range of microstructures can be achieved. One microstructure discussed above, in Chapter 2.3.1, is martensite. This phase is obtained by quenching austenite, avoiding diffusion and forcing the excess carbon into a BCT structure. The resulting structure is a hard and strong material. DP steels are steels with a microstructure consisting of both ferrite and martensite. The amount of each phase varies, depending on the amount of austenite before quenching, cooling rates, and alloying elements. A DP steel with a large fraction of martensite will have a high ultimate tensile strength (UTS), but less ductility. Conversely, a steel consisting mostly of ferrite and some martensite will have a greater ductility, but a lower UTS. In order to achieve this microstructure with both ferrite and martensite present, a method called thermo-mechanical processing (TMP) is used [88]. First, the steel is cold rolled to achieve the desired grain size. Here the microstructure consists of elongated ferrite grains and pearlite. Second, the alloy is heated to the intercritical  $\alpha + \gamma$  region in the phase diagram (see Figure 2.8), at a temperature between 750°C and 900°C. During the heating, the ferrite will recrystallize before it starts to transform into austenite. The microstructure will then consist of ferrite and austenite where the ratio depends on temperature and alloying content. For example, a temperature of 800°C would result in a microstructure containing 10-20% austenite, depending on the composition. Third, after the intercritical annealing, the steel is quenched transforming all the austenite into martensite. Finally, the last heat treatment step is tempering. This is done in order to reduce some of the internal residual stresses due to the martensitic transformation during quenching. The final structure is then a steel with both ferrite and martensite present, where the amount of martensite depends on the amount of austenite before quenching, the temperature where quenching starts and the alloying. This heat treatment process is shown in Figure 2.16. A typical use for DP steels is energy absorbing components in car body parts.

In addition to heat treatment, adding alloying elements is a common approach to tailor the microstructure to improve properties. For instance, by adding a minimum of 10.5% of Cr, steels become stainless. Different elements will also stabilize different phases. Typically, elements with a BCC crystal structure (Cr and Mo) will stabilize other BCC phases, in this case, ferrite. This is illustrated in Figure 2.17(a). Here, ferrite stabilizing elements are added, and as a consequence, the austenite region ( $\gamma$ ) contracts and the region where ferrite occurs is greatly expanded. Conversely, elements with an FCC crystal structure will promote the formation of FCC. An example of this is Ni. By adding sufficient amounts of Ni to steel,

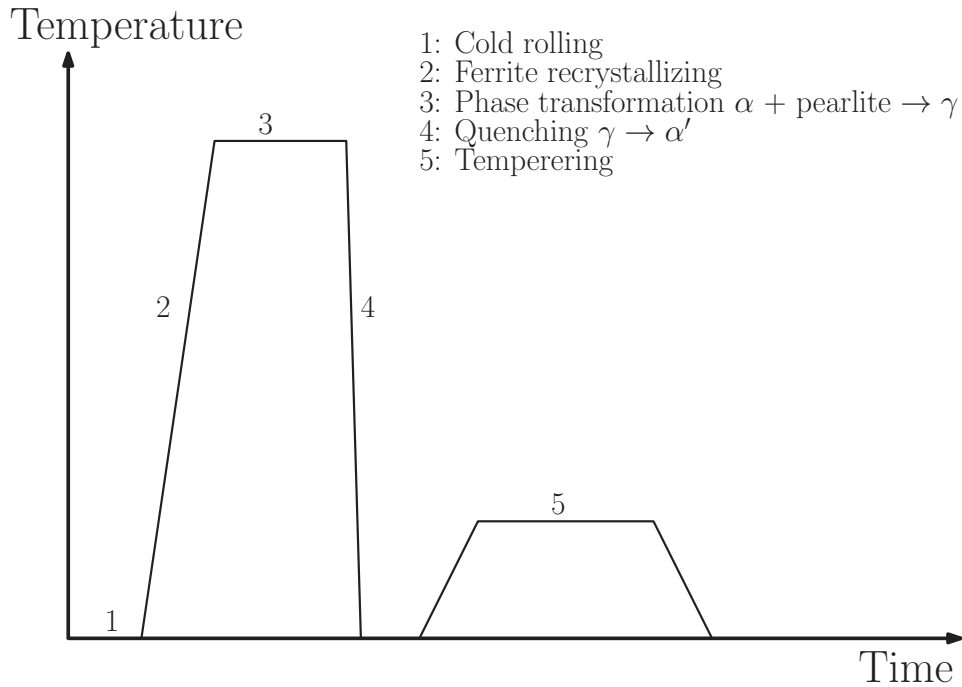


**Figure 2.16:** The heat treatment for DP steels. Starting with a cold rolled microstructure consisting of ferrite and pearlite. An example from the SSAB plant in Borlänge perform the heat treatment cycle in approximately 10 minutes [89]. Here, the intercritical annealing in 3 takes place at 800°C for two minutes and the tempering in 5 at 200°C for two minutes.

it is possible to have stable austenite at room temperature, as shown in Figure 2.17(b). Other elements stabilizing austenite at room temperature is N, which has the added benefit of increasing the resistance to pitting and crevice corrosion and is an effective solid solution strengthening element. This knowledge is the basis when making duplex stainless steels (DSS). DSS is a stainless steel with a microstructure consisting of ferrite and austenite. It was developed to have excellent corrosion properties, while still having sufficient strength and toughness. This is achieved by adding a minimum of 20% of Cr and a 1-4% of Mo, both of which are ferrite stabilizer. Ni is added as an austenite stabilizer, and it is also improving the material's toughness. The ternary phase diagram of Fe-Ni-Cr with 65% Fe is shown in Figure 2.18. For DSS the goal is to achieve a ferrite and austenite microstructure which is in the  $\alpha + \gamma$  region in Figure 2.18. This is obtained by adding roughly 25% Cr and 7% Ni. Other elements are also added, but the amounts of Cr, Mo, N, and Ni is a characteristic feature of DSS.

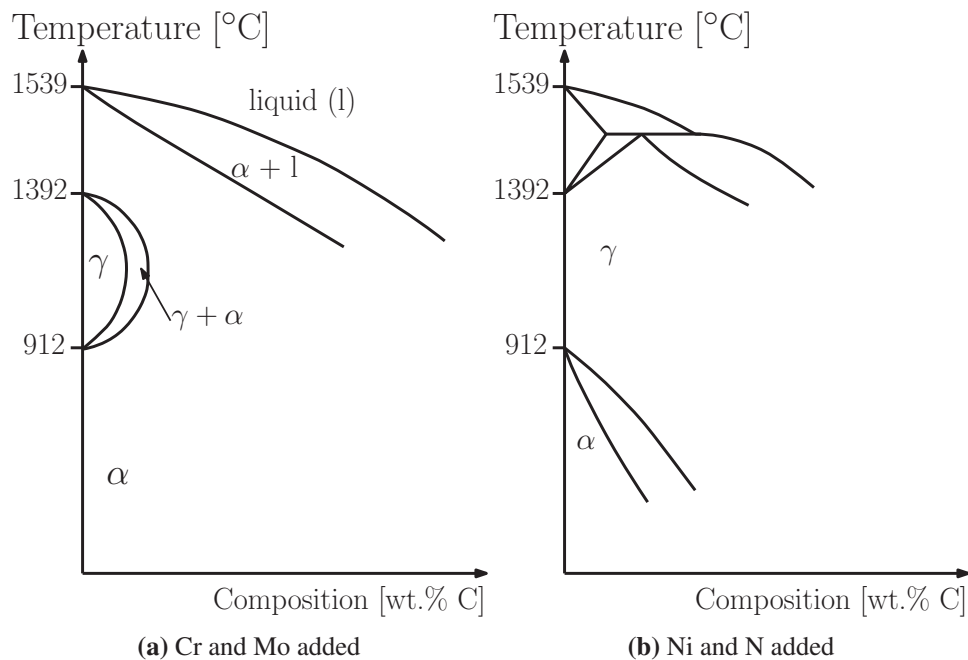


**Figure 2.17:** Effect of alloying elements on austenite and ferrite. **(a)** By adding Cr and Mo the austenite region contracts. **(b)** Conversely, adding Ni and N the austenite region expands and can be made stable at room temperature. The figure is adapted from [90].

TMP produces DSS similarly as for DP steels. However, DSS contains more alloying elements. First, the steel is cold rolled to achieve the desired grain size. Second, it is heated to the intercritical region (typically 1150°C) where it is recrystallized and obtain a microstructure of austenite and ferrite. The goal is to have 50% of each phase present. Finally, cooling to room temperature has to occur sufficiently fast to avoid the formation of intermetallic phases. Also, due to the amount of alloying elements, the austenite will not transform to ferrite or martensite. The heat treatment profile of DSS will be similar to the profile for DP steels shown in Figure 2.16 without the tempering after cooling.

### 2.3.4 Influence of temperature

A consequence of all the alloying elements in DSS is an increased risk of forming intermetallic phases like  $\chi$  and  $\sigma$ . These form in the temperature interval of 650-950°C after only a few minutes, as illustrated in the time-temperature-transformation (TTT)-diagram in Figure 2.19. If the cooling rate is not sufficiently fast after the intercritical annealing or welding, intermetallic phases as the  $\sigma$ -phase will form.



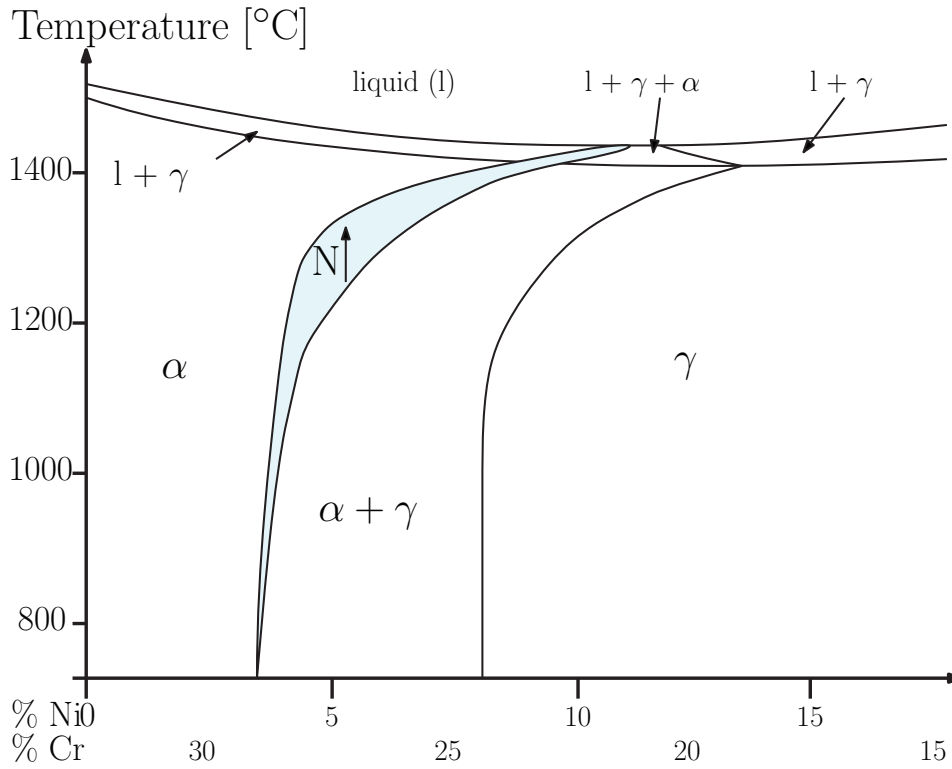


**Figure 2.18:** The ternary phase diagram of Fe-Ni-Cr, with 65% Fe. The desired area for DSS is in the  $\alpha + \gamma$  region. By adding N, the  $\alpha + \gamma$  region is expanded. The figure is adapted from [91]

The  $\chi$ -phase precipitates on ferrite-ferrite grain boundaries and occurs before the  $\sigma$ -phase [92, 93]. In addition, the  $\chi$ -phase is a metastable phase, consumed during  $\sigma$ -phase precipitation [93].  $\sigma$ -phase typically forms on ferrite-austenite boundaries but can also form on ferrite-ferrite boundaries. The  $\sigma$ -phase forms in the temperature range 675°C - 900°C. After 10 min at 850°C, small amounts of  $\sigma$ -phase will start to precipitate [54, 55, 94].  $\sigma$ -phase has a body-centered tetragonal crystal structure with the lattice parameters  $a = 8.8 \text{ \AA}$  and  $c = 4.55 \text{ \AA}$ , while the  $\chi$ -phase has a body-centered cubic crystal structure with lattice parameter  $a = 8.8 \text{ \AA}$  [95]. The lattice parameters of both are significantly larger than the  $2.87 \text{ \AA}$  and  $3.65 \text{ \AA}$  for ferrites and austenite, respectively [96, 97]. The chemical composition of  $\sigma$ -phase includes, in addition to Fe, approximately 30-60% Cr and 4-10% Mo. The  $\chi$ -phase differs from  $\sigma$ -phase with a higher Mo content and a lower content of Cr [92]. As a result, since  $\chi$ -phase has a higher atomic weight it is possible to distinguish it from  $\sigma$ -phase in a scanning electron microscope (SEM) using Z-contrast. In such an image the  $\chi$ -phase will

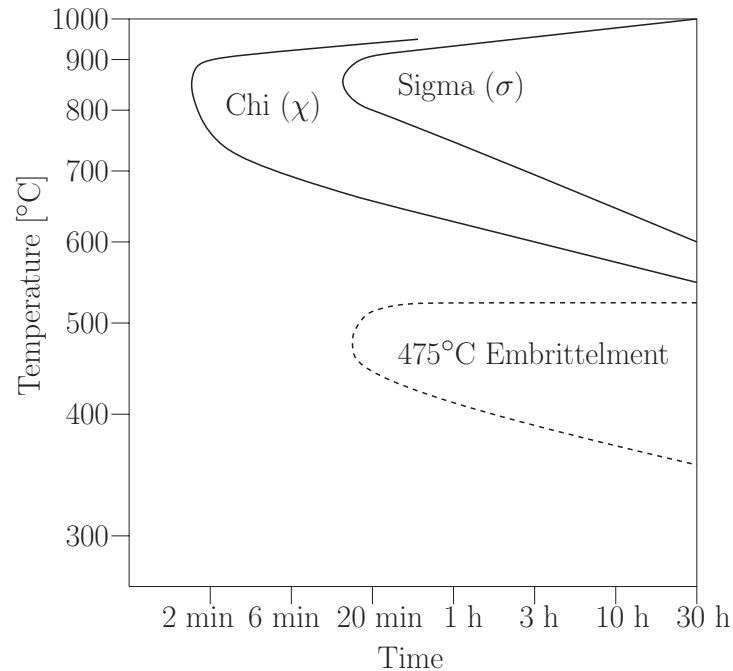


**Figure 2.19:** This TTT-diagram illustrate the time it takes for intermetallics to form at different temperatures. After only 2 min at 850°C, the  $\chi$ -phase starts to precipitate. The figure is adapted from [55].

appear brighter. Since Cr and Mo are stabilizing elements for ferrite, the  $\sigma$ -phase and  $\chi$ -phase will form at the expense of ferrite. Following the eutectoid reaction  $\alpha \rightarrow \sigma + \gamma$  or  $\alpha \rightarrow \chi + \gamma$ , an increase in the austenite phase will also occur [55, 92]. The surrounding area will be depleted of Cr and Mo, which are important elements for corrosion protection and as a consequence, leaving the material exposed. This is especially troublesome in super duplex stainless steels (SDSS) since these are mostly selected to operate in areas requiring a corrosion resistance superior to DSS. The formation of  $\sigma$ -phase is illustrated in Figure 2.20. Here, the dashed line indicates the former grain boundary between ferrite and austenite.

A study by Børvik et al. [52] looked into the low-temperature effect of  $\sigma$ -phase in DSS. In this work, it was found that the temperature had a minor effect on the tensile ductility while increasing the amount of  $\sigma$ -phase in the structure considerably reduced the toughness. Another study by Kim et al. [98] investigated the low-temperature mechanical behavior of SDSS containing  $\sigma$ -phase. Here, the material was tested in a universal tensile test machine, equipped with a sub-zero chamber. After the specimens were tested, the microstructure was investigated, comparing

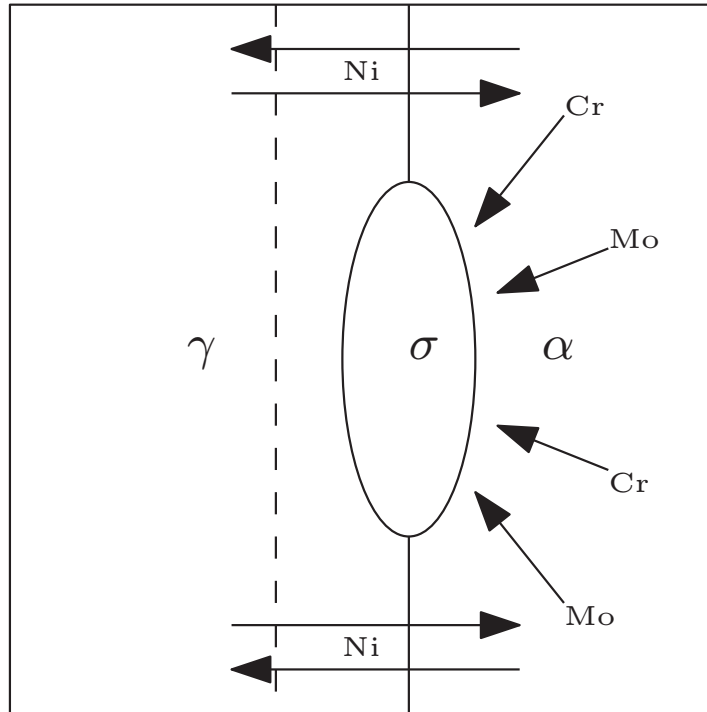


**Figure 2.20:** The  $\sigma$ -phase typically forms on the grain boundary between ferrite and austenite, at the expense of ferrite. The solid line is the new grain boundary and the dashed line is the old, before formation of  $\sigma$ -phase. The figure is adapted from [55].

the amount of  $\sigma$ -phase present with microcrack length. Microcracks were found to have propagated through the entire  $\sigma$ -phase, relating the crack length to the size of  $\sigma$ -phase inclusions. As in Børvik et al. [52], the influence of temperature was observed to be minor. Also, in the tensile tests performed at  $-50^{\circ}\text{C}$ , no strain-induced martensite was produced.

Some materials have a ductile behavior at room temperature, but at lower temperatures a brittle behavior is exhibited. For ferritic steels, there is a sharp transition from ductile to brittle behavior. Conversely, austenitic steels will have an increased ductility at lower temperatures. This is related to the crystal structure of the material, with ferrite being BCC and austenite being FCC. However, the phenomenon is not fully understood, but there are two main theories. The first theory concerns the slip systems in BCC crystals. Even though there are more slip systems available in BCC crystals, the atomic planes are not as closely packed as in FCC structures, creating a barrier for the dislocations to move at the slip planes [99]. The second theory is based on interstitial impurities. Since BCC is not a closely packed structure, there

will be more space for interstitial atoms, making it more likely for them to be in BCC crystals. Interstitial atoms pin down dislocations, making them immobile at lower temperatures [100].

A common way of measuring the ductile-to-brittle transition temperature is by doing a series of impact tests at different temperatures. This test is called a Charpy V-notch test [101]. In this test, a notched specimen is placed in the path of a hammer attached at the end of a pendulum. This hammer breaks the specimen in a single strike, and the energy absorbed by the specimen is recorded. The curves in Figure 2.21, the impact energy from a Charpy impact test at different temperatures for different strength materials are shown. The top curve is for FCC materials, which do not have any ductile-to-brittle transition [13]. The middle curve gives a more traditional low strength steel BCC material. Here, there is a ductile-to-brittle transition, where at a certain temperature the material will exhibit a pure brittle behavior. During the transition, the material fracture toughness goes down. Knowledge of this transition temperature is essential in design of steel structures. A poorly designed material may have a ductile-to-brittle transition at room temperature. The lower curve is for high strength materials ( $\sigma_{yield} > E/150$ ). These materials have a very low notch toughness and as a consequence, a brittle fracture can occur for all temperatures [13, 102].

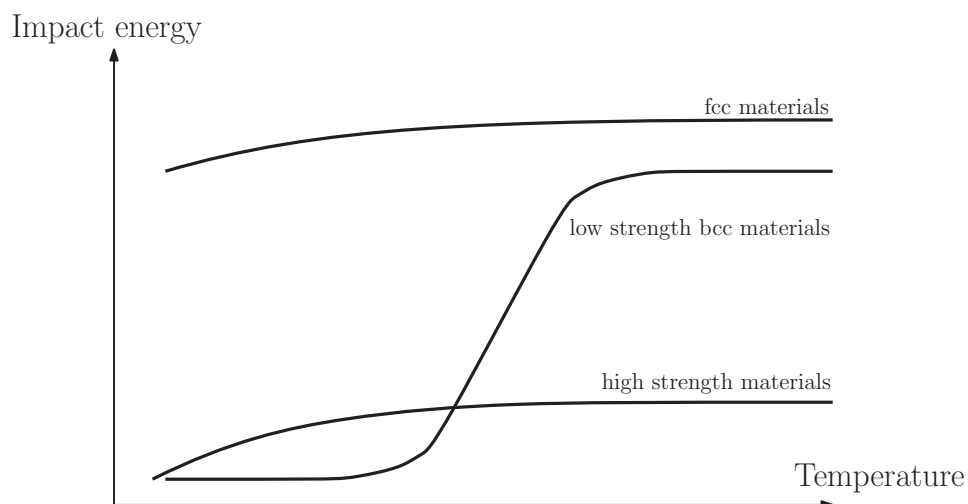


**Figure 2.21:** Illustration of the theoretical temperature-transition curve for different materials. This figure is adapted from Dieter [13].

## 2.4 Stress and strain

Considering a standard tensile test of a steel with the shape of a bar. The steel specimen is then fixed at one end and pulled in the other. During this test, the force and displacement are measured. An engineering stress-strain curve can be constructed from these measurements. Engineering stress is defined as

$$s = \frac{F}{A_0} \quad (2.16)$$

where  $F$  is force measured by a load cell and  $A_0$  the original cross-section area of the specimen. This is the average longitudinal stress in the tensile specimen. The engineering strain is defined as

$$e = \frac{\Delta L}{L_0} = \frac{L - L_0}{L_0} \quad (2.17)$$

Here,  $L_0$  is the original gauge length of the specimen and  $L$  is the current gauge length. The engineering stress-strain curve has the same shape as the force-displacement curve, with a different scale. However, the engineering stress-strain curve does not give a correct description of the deformation progress as it is only based on original dimensions. In order to get the true stress and true strain, the calculations have to be based on current dimensions. In Figure 2.22 the difference between the true curve and engineering curve is illustrated. The true strain is then defined as [13]

$$\varepsilon = \int_{L_0}^L \frac{dL}{L} = \ln \frac{L}{L_0} \Rightarrow \varepsilon = \ln(e + 1) \quad (2.18)$$

from this, it follows (assuming no volume change and homogeneous distribution of strain along the gauge length)

$$\sigma = \frac{F}{A} = \frac{F}{A_0}(e + 1) \Rightarrow \sigma = s(e + 1) \quad (2.19)$$

These equations are valid until the onset of necking. After necking the true stress and true strain should be based on actual area measurements since the stress state on the neck is triaxial.

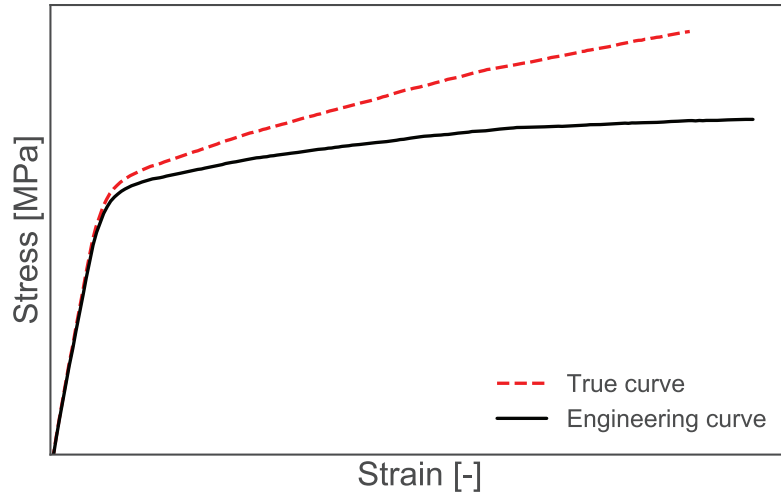


**Figure 2.22:** An illustration of the difference between the engineering tensile test curve and the true tensile test curve. The curves are calculated from force-displacement data from a flat tensile specimen using Equation 2.16-2.19.

True stress and strain make the force and displacement measurements independent of dimensions. Conversely, the engineering stress and strain values are based on original measurements and not current. This means that tensile specimen with a short gauge length will typically have larger engineering strain values compared to a specimen with a long gauge length. To truly compare two materials, either true tensile test data must be used, or specimens tested with the same geometry and dimensions can be compared using engineering tensile test data.

## 2.5 Constitutive relations

### 2.5.1 Voce

For steel and aluminum structures (BCC and FCC materials) it has been shown experimentally that the stress-strain relationship is well described by the Voce hardening rule [103–106]

$$\sigma_{eq} = \sigma_Y + \sum_{i=1}^N Q_i \left( 1 - \exp \left( -\frac{\theta_i}{Q_i} \varepsilon_{eq}^P \right) \right) \quad (2.20)$$

where  $\sigma_{eq}$  is the equivalent stress,  $\sigma_Y$  is the yield stress of the material and  $\varepsilon_{eq}^P$  is the equivalent plastic strain. The yield stress is experimentally found in the tensile test or fitted to the measured stress-strain curve. When the exponential expression in the brackets is going towards zero, the maximum value of the equation is achieved. The hardening parameters  $Q_i$  and  $\theta_i$  are respectively the initial hardening rate and the saturated value of the hardening term  $i$ . The different parameters are found by a direct calibration to the measured stress-strain curve until necking using the method of least squares or by inverse modeling of the tensile test, and the importance of the different parameters are illustrated in Figure 2.23 for  $N = 1$ .

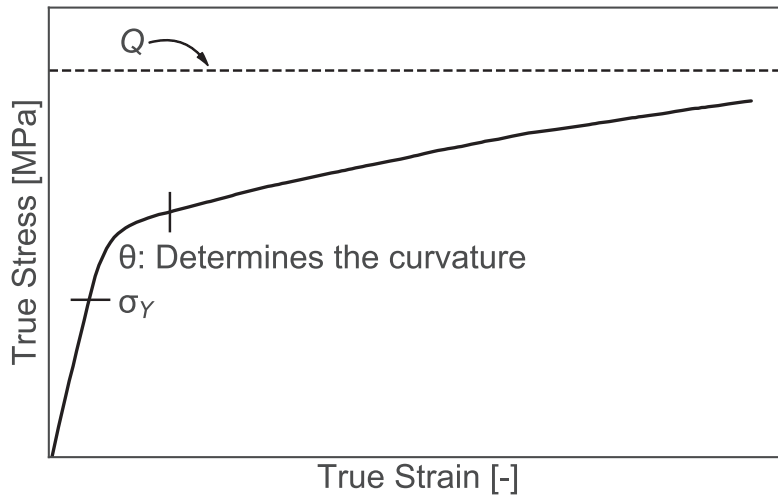


**Figure 2.23:** The influence of the parameters in the Voce equation is illustrated.  $Q$  is the saturation stress and  $\theta$  gives the work-hardening rate of the material. Also, the yield stress of the material,  $\sigma_Y$ , is labelled.

In Saai et al. [104], the Voce equation was used with  $N = 2$  to predict the stress-strain curve for a DP steel. The Voce equation was used to describe the collective tensile behavior of both martensite and ferrite. However, in Pierman et al. [107] the Voce equation was used with  $N = 1$ , and it was only used to describe the martensitic ( $\alpha'$ ) phase. As a result, the equation was reduced to

$$\sigma_{eq,\alpha'} = \sigma_{Y\alpha'} + Q_{\alpha'} (1 - \exp(-\varepsilon_{eq}^P n_{\alpha'})) \quad (2.21)$$

Here,  $\sigma_{Y,\alpha'}$  is described by the equation

$$\sigma_{Y,\alpha'} = 300 + 1000C_{\alpha'}^{1/3} \quad (2.22)$$

where  $C_{\alpha'}$  is the carbon content in the martensitic phase, which is related to the total carbon content ( $C_{total}$ ) and volume fraction of martensite ( $V_{\alpha'}$ )

$$C_{\alpha'} = \frac{C_{total}}{V_{\alpha'}} \quad (2.23)$$

assuming no solubility of carbon in ferrite, which is a reasonable assumption. Ferrite can resolve a maximum of 0.022 wt.% of carbon.  $Q_{\alpha'}$  is described by the equation

$$Q_{\alpha'} = \frac{1}{\theta_{\alpha'}} \left[ a + \frac{bC_{\alpha'}}{1 + \left( \frac{C_{\alpha'}}{C_0} \right)^q} \right] \quad (2.24)$$

where  $a$ ,  $b$ ,  $C_0$ ,  $q$  are fitting parameters and  $C_{\alpha'}$  is a physical parameter. The fitting parameters were fitted to specimens with 100% martensite. Similarly, to Equation 2.20,  $n_{\alpha'}$  represent the hardening coefficient, in this case for martensite.

In [107], the ferrite ( $\alpha$ ) is described by a Swift-type equation

$$\sigma_{\alpha} = \sigma_{Y,\alpha} (1 + H_{\alpha} \varepsilon^P)^{n_{\alpha}} \quad (2.25)$$

where  $\sigma_{Y,\alpha}$ ,  $H_{\alpha}$ , and  $n_{\alpha}$  are fitting parameters, fitted to DP specimens containing 15% martensite. The fitted parameters in both ferrite and martensite are kept constant for all grades of steel in the work of Pierman et al. [107], only changing the total carbon content and volume fraction of martensite in Equation 2.23.

In a study similar to Pierman et al. [107] by Lai et al. [108], also investigating DP steels, the same constitutive equations were used for martensite (Equation 2.21 - 2.24). Lai et al. used the same constants as Pierman et al. and kept them constant for all grades of steel, only changing  $C_{\alpha'}$ . The ferrite was, in contrast to Pierman et al. [107], described by the two equations shown in Equation 2.26. The first stage (Equation 2.26a) is described by a Voce type equation, without a series expansion, similar to the martensite. This stage is stage III of strain hardening and is characterized by a decreasing strain hardening rate with increasing strain [109]. Stage I and II describes the elastic-plastic transition in the initial part of the



stress-strain curve and are not considered here. The second stage (Equation 2.26b) of ferrite deformation in the model by Lai et al. is a Power law-type equation and is equivalent to stage IV of strain hardening. This stage is added to avoid saturation of the flow stress, at large strains, since this was not observed in the experimental tests [109]. Stage IV is the strain hardening stage where large plastic strains occur at a low constant strain hardening rate.

$$\sigma_{\alpha} = \sigma_{Y,\alpha} + \frac{\theta_{\alpha}}{\beta} (1 - \exp(-\beta \varepsilon^P)) \quad \text{for } \sigma_{\alpha} \leq \sigma_{tr} \quad (2.26a)$$

$$\sigma_{\alpha} = \sigma_{tr} + \theta_{IV} (\varepsilon^P - \varepsilon_{tr}^P) \quad \text{for } \sigma_{\alpha} > \sigma_{tr} \quad (2.26b)$$

Here  $\sigma_{Y,\alpha}$  is the yield strength of the material,  $\theta_{\alpha}$  is the initial hardening rate and  $\beta$  is the dynamic recovery coefficient. Equation 2.26a is valid during stage III strain hardening. The upper limit of this range, when it transitions to stage IV, is denoted  $\sigma_{tr}$ . When the values of the flow stress exceed this value, Equation 2.26b is the governing equation for the ferritic phase.  $\sigma_{tr}$  and  $\varepsilon_{tr}^P$  is given by

$$\sigma_{tr} = \sigma_{Y,\alpha} + \frac{\theta_{\alpha} - \theta_{IV}}{\beta} \quad (2.27)$$

and

$$\varepsilon_{tr}^P = \frac{1}{\beta} \ln \frac{\theta_{\alpha}}{\theta_{IV}} \quad (2.28)$$

In Equation 2.26b, 2.27 and 2.28  $\theta_{IV}$  appears. This is the constant hardening rate in stage IV. The parameters in these equations describing the ferrite phase,  $\sigma_{Y,\alpha}$ ,  $\theta_{\alpha}$ ,  $\beta$  and  $\theta_{IV}$ , are identified using an inverse modeling procedure. In the work by Lai et al.  $\theta_{IV}$  was kept constant for all grades of steel, while the other three parameters were fitted to each steel type.

During the initial stages of the study by Lai et al. [108], the tensile test curves were fitted using only Equation 2.26a, without accounting for stage IV hardening. These results consistently gave an early onset of necking compared to the experimental data. When accounting for stage IV hardening with Equation 2.26b the onset of necking was postponed, with little impact on the initial deformation.

### 2.5.2 Taylor equation and Bergström model

Another method of describing tensile test curves is a Taylor-type equation. The original Taylor model is given by [110]

$$\sigma(\varepsilon) = \sigma_{int} + \sigma_{def} = \sigma_{int} + \alpha\mu b\sqrt{\rho(\varepsilon)} \quad (2.29)$$

where  $\sigma_{int}$  is the friction stress and  $\sigma_{def}$  is the work-hardening component of the flow stress. Here,  $\alpha$  is the dislocation hardening constant,  $\mu$  is the shear modulus,  $b$  is the Burgers vector, and  $\rho(\varepsilon)$  is the dislocation density, as a function of strain. A version of this equation was used by Ramazani et al. [111], based on the work by Rodriguez and Gutierrez [112]. The equation used by Ramazani was

$$\sigma_{eq}(\varepsilon) = \sigma_0 + \Delta\sigma + \alpha M_T \mu \sqrt{b} \sqrt{\frac{1 - \exp(-M_T k_r \varepsilon_{eq})}{k_r L}} \quad (2.30)$$

where  $\sigma_0$  describes the strengthening contribution from elements in solid solution following

$$\begin{aligned} \sigma_0 = & 77 + 750 (\% \text{ P}) + 60 (\% \text{ Si}) + 80 (\% \text{ Cu}) + 45 (\% \text{ Ni}) \\ & + 60 (\% \text{ Cr}) + 80 (\% \text{ Mn}) + 11 (\% \text{ Mo}) + 5000 (\% \text{ N}_{\text{solid solution}}) \end{aligned} \quad (2.31)$$

Further,  $\Delta\sigma$  is the strengthening contribution from the carbon in solid solution given as

$$\Delta\sigma = 5000 \times (\% \text{ C}_{\text{solid solution}})^\alpha \quad \text{for ferrite} \quad (2.32a)$$

$$\Delta\sigma = 3065 \times (\% \text{ C}_{\text{solid solution}})^{\alpha'} - 161 \quad \text{for martensite} \quad (2.32b)$$

The final term of Equation 2.30 describes the strain hardening of the material where  $M_T$  is the Taylor constant,  $k_r$  is the recovery rate and  $L$  is the dislocation mean free path.  $\alpha$ ,  $\mu$ ,  $b$  and  $M_T$  are known material constants.  $k_r$  and  $L$  are microstructural characteristics, identified by inverse modeling in martensite. In ferrite, these are based on the grain size. The dislocation mean free path is assumed equal to the average grain size,  $L = d_\alpha$ , and the recovery rate is given by  $k_r = 10^{-5}/d_\alpha$ .

In the work of Bergström et al. [113], a Taylor-type equation was also used to describe DP steel. However, here the dislocation density,  $\rho(\varepsilon)$ , in Equation 2.29 is described by the differential equation

$$\frac{d\rho}{d\varepsilon} = \frac{1}{f(\varepsilon)} \left[ \frac{M_T}{b \cdot s(\varepsilon)} - \Omega\rho \right] \quad (2.33)$$

where  $M_T$  is the Taylor constant,  $b$  is the burgers vector,  $\Omega$  is a strain-independent material constant representing dynamic recovery.  $f(\varepsilon)$  is the strain dependent volume fraction and  $s(\varepsilon)$  is the strain dependence of the dislocation mean free path given respectively by

$$f(\varepsilon) = f_0 + (f_1 - f_0) \exp(-r\varepsilon) \quad (2.34)$$

and

$$s(\varepsilon) = s_0 + (s_1 - s_0) \exp(-k\varepsilon) \quad (2.35)$$

Here,  $f_1$  is the initial active volume fraction of ferrite taking part in the deformation process and  $f_0$  is the total amount of ferrite.  $r$  is a rate constant, controlling the rate of ferrite active as a function of the plastic strain.  $s_0$  is the final value of dislocation mean free path,  $s_1$  is the start value of dislocation mean free path and  $k$  is a rate constant, controlling the rate of progress, and serves the same purpose as  $r$  in Equation 2.34.

Equation 2.29 and 2.33 - 2.35 gives the Bergström model [113]. In Bergström et al. [113] these equations were fitted to the true stress-strain curve of several DP steels, keeping the following parameters constant:  $\mu = 80000$  MPa,  $b = 2.5 \cdot 10^{-10}$  m,  $M_T = 2$ ,  $\alpha = 0.5$  and  $\Omega = 5$ . When solving the differential equation (Equation 2.33), an initial dislocation density,  $\rho_0$ , is required. This was kept constant for all grades, i.e.,  $\rho_0 = 1.5 \cdot 10^{14}$  m<sup>-2</sup>. The total amount of martensite,  $f_m$ , was measured from SEM secondary electron images. The relationship between ferrite and martensite content is given by  $f_0 = 1 - f_m$ . All remaining parameters ( $f_1$ ,  $r$ ,  $s_0$ ,  $s_1$ ,  $k$  and  $\sigma_{int}$ ) were identified from an inverse modeling procedure.

In the study of Bergström et al. [113], four steels were investigated, namely DP500, DP600, DP800 and DP980. For all fitted curves, a mean error was calculated, with the largest mean discrepancy between model and experimental values being 0.105 MPa. From this, it can be said to be an accurate fit for all grades. In addition, a strong correlation between yield strength and volume fraction of martensite, as well as between ultimate tensile strength and volume fraction martensite were found. Both exhibited a linear relationship with  $R^2 = 0.94$  and  $0.98$ , respectively. The same linear relationship was found between the friction stress,  $\sigma_{int}$ , and the martensite volume fraction, with  $R^2 = 0.97$ .

## Chapter 3

# Experimental procedures

In this chapter the experimental equipment, methods and materials used in this thesis are outlined. First, the *in-situ* scanning electron microscope (SEM) tensile stage equipment will be presented. Second, the gold remodeling procedure is described. Finally, details about the different materials are given, with a description of properties and preparation methods used.

### 3.1 Tensile testing using *in-situ* SEM stage

The experimental work in this thesis is based on *in-situ* tensile testing in SEM. The *in-situ* device used is shown in Figure 3.1. This is a spindle-driven device, with the outer dimensions 155 mm × 95 mm × 45 mm. The device is placed inside the vacuum chamber, where it is mounted on top of the SEM stage after removal of the rotation unit. It consists of a rigid frame with two gripping cross-heads, where one is movable, and the other one is fixed. An electrical direct current motor drives the movable cross-head. During testing, the displacement and load transducers record the elongation and applied force, respectively. Additional modules for the device can be mounted to provide other deformation modes, such as compression and bending. For further reading and previous use of the *in-situ* SEM device, the reader is referred to [114, 115].

As seen in Figure 3.1, the specimen needs a specific geometry to fit into the stage. In this thesis, two types of geometries have been used, i.e., specimens with a smooth gauge length and notched. These geometries are displayed in Figure 3.2, where all measures are in mm. All materials will have one of these geometries, and the only difference between samples will be the thickness. The thickness is selected according to the materials ultimate tensile strength (UTS), to avoid to exceed the

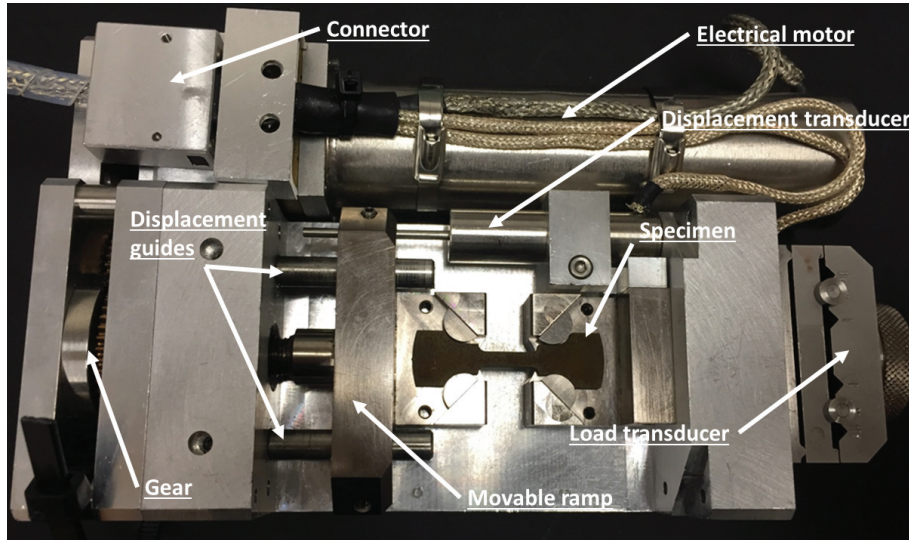


**Figure 3.1:** Image showing the *in-situ* SEM tensile test device.

maximum load capacity of the stage at 5000 N. As a result, specimens from stronger materials will be thinner compared to a weaker material. All specimens were spark eroded from a larger section to a thickness of either 1 mm or 2 mm depending on the strength of the specimen. This section was either from a plate or a pipe wall. More specific details about specimen preparation are given later.

During an *in-situ* SEM tensile test a selected area is recorded with a series of images of the deforming microstructure. These images are recorded using either secondary electron (SE) imaging, backscatter electron (BSE) imaging or electron backscatter electron diffraction (EBSD) imaging mode. Image series from the two former modes can be loaded into the digital image correlation (DIC) software and correlated to obtain a local strain field of the recorded area. In addition, it is possible to cool the specimen during an *in-situ* SEM tensile test. When performing sub-zero experiments a cold finger is attached to the specimen as shown in Figure 3.3. This cold finger is made from 99.99% Cu. They are attached to the specimen, through the microscope door, into a dewar filled with liquid N. The blue and white wires seen in Figure 3.3 are thermocouples. It is placed between the screw-head and specimen throughout the experiments. In this work the temperature was measured to be in the interval  $-35^{\circ}\text{C}$  and  $-45^{\circ}\text{C}$  for all specimens. However, the fluctuations in temperature are assumed to be due to the variable thermal resistance between the thermocouples and specimen. During loading, the specimen would move, and the thermocouples could change their position to no longer be placed between the screw-head and specimen. The temperature is assumed constant and reported as  $-40^{\circ}\text{C}$  in this work.



are in mm.

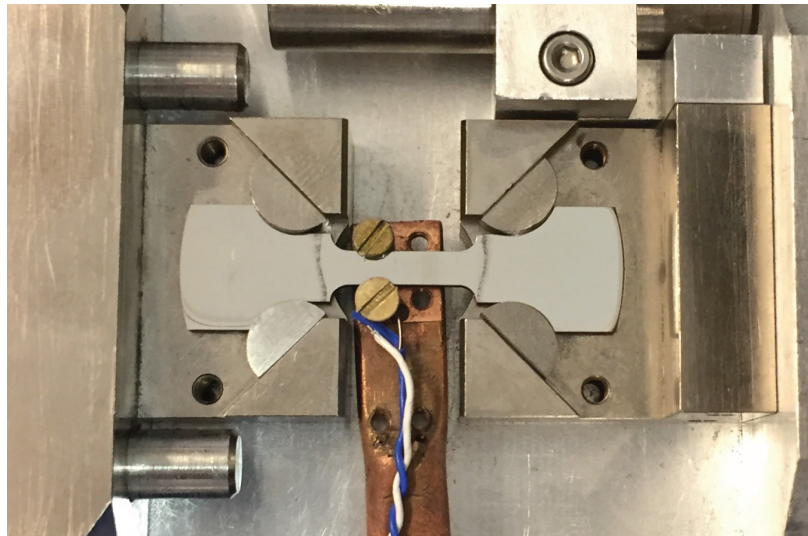


**Figure 3.3:** Cold finger attached to the specimen with thermocouples placed between the screw-head and specimen.

### 3.2 Electron backscatter diffraction acquisition.

The microscope used during EBSD acquisition was a Field Emission SEM Zeiss Ultra 55 Limited Edition with a NORDIF UF-1100 EBSD detector, with the microscope settings given in Table 3.1. In order to remove the deformation layer at the surface and expose the underlying structure of the material, two separate methods were used. In both methods, the specimen is ground and polished until 1  $\mu\text{m}$ . The first method is used for super duplex stainless steels (SDSS) and uses electropolishing to remove the final deformation layer. A LectroPol from Struers, with the settings in Table 3.2 was utilized for the electropolishing. The second method is used for steels where the two phases have a large difference in hardness. Here, the final polishing step is vibration polishing using a VibroMet2 from Buehler for 16 hours. In the vibration polisher, there is a suspension with pH 8 containing  $\text{SiO}_2$  particles with a size of 0.02  $\mu\text{m}$ . Finally, after the final polishing step, all specimens were rinsed in an ultrasonic bath with acetone for 5 min to obtain a clean surface finish.

**Table 3.1:** SEM parameters used during EBSD acquisition.

Parameter	Setting
Acceleration Voltage [kV]	20
Working distance [mm]	24.6–25.4
Tilt angle [ $^\circ$ ]	70
Aperture size [ $\mu\text{m}$ ]	300
Probe current [nA]	65–70

**Table 3.2:** Parameters used during the electropolishing.

Parameter	Setting
Electrolyte	Struers A2
Voltage [V]	20
Time [s]	15
Temperature [ $^\circ\text{C}$ ]	22



### 3.3 Gold remodeling

In order to enable high-resolution DIC, gold remodeling has been essential to produce the speckled pattern for DIC analysis. To obtain the gold nanoparticle speckled pattern the experimental set-up proposed by Di Gioacchino and Quinta da Fonseca [9] was used. This section is based on the experimental technique described in [9] and subsequent articles by the same research group [10, 71, 73, 116, 117]. First, the specimen has to be prepared for use in SEM, removing the deformation layer from the surface. Second, the polished surface is coated with gold, creating a thin continuous layer. Here, an Edwards S150B sputter coater was used to coat the surface. The setting used to obtain this result is summarized in Table 3.3. Finally, in order to get this gold layer to remodel into particles, the gold-coated specimen is placed on a heat source with heated gas flowing across the surface. For stainless materials, which could withstand 300°C for 60 min, water vapor is used. In Figure 3.4 the experimental setup for the remodeling process with water vapor is shown. Here, a beaker filled with water (vapor source) is placed in the center of a hotplate surrounded by gold-coated specimens. On top, covering both the specimens and the vapor source is a larger beaker, acting like a dome. This dome is slightly lifted to secure flow of steam over the specimen surface and avoid any build up of pressure.

**Table 3.3:** Settings used when coating the specimen with gold.

Parameter	Setting
Current [mA]	40
Voltage [kV]	0.5
Time [min]	3-4
Pressure [mbar]	7.8

If the material corrodes in the water vapor atmosphere or if it is affected by the higher temperature, a similar approach can be used with a lower temperature of 180°C. Here, a mixture of argon and styrene gas is used as the flow medium. The setup is similar to one for water vapor, but here the argon and styrene gas have to mix before being guided into the chamber with the specimen, as illustrated in Figure 3.5. The hot plate where the specimen is placed is located inside a desiccator to create an atmosphere without oxygen. This to prevent corrosion. Also, by doing this, the argon/styrene fumes are contained. In Table 3.4 the differences between the two methods are highlighted. Most notably is the difference in time and temperature.



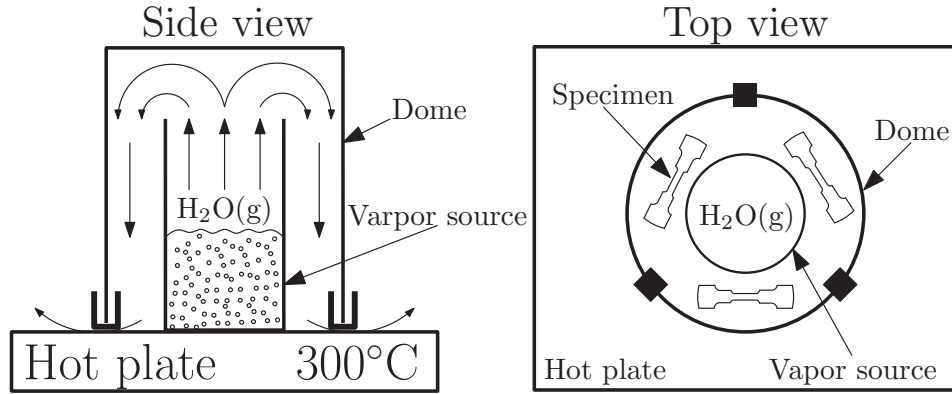


**Figure 3.4:** Experimental setup for gold remodeling in a water vapor atmosphere.

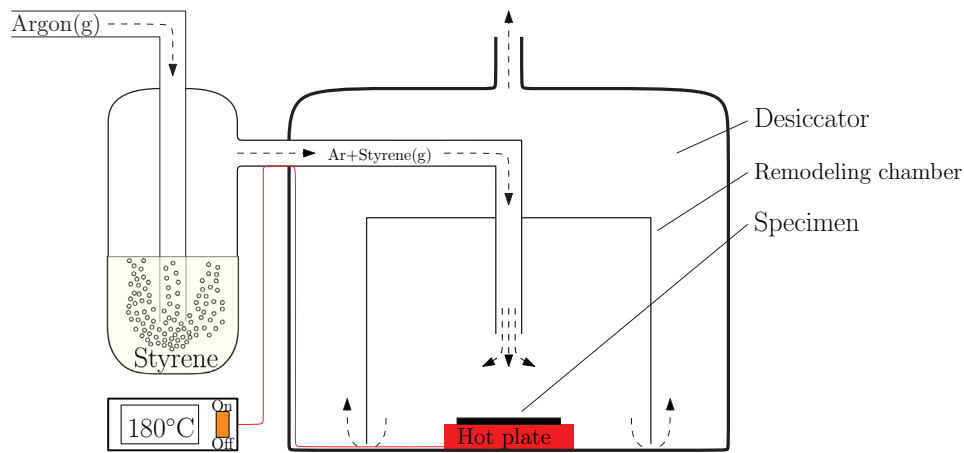


**Figure 3.5:** Experimental setup for gold remodeling in an argon/styrene atmosphere. Argon gas flows into a gas washing bottle filled with styrene. From here a mixture of argon and styrene is guided into a remodeling chamber placed inside a desiccator. Inside the remodeling chamber the specimen is placed on top of a hot plate. The temperature of the hot plate is set by the control box on the outside of the desiccator.

During the time the specimen is in the remodeling chamber, the gold layer will transform from a continuous layer to randomly distributed nanoparticles. This process is explained in further detail in Chapter 2.2.3. When imaged in SEM using BSE imaging mode, this speckled pattern will provide excellent contrast between the specimen and gold particles. As a result, a very high spatial resolution is achieved in the strain field obtained from DIC.

**Table 3.4:** Experimental settings for gold remodeling.

Setting	Vapor	Ar/styrene
Time	1 hour	96 hours
Temperature	300°C	180°C
Gold layer thickness	70 nm	50 nm

The field of view of the acquired BSE image is dependent on the speckle size. In order to ensure a good quality speckle pattern for DIC, each speckle should be covered by a minimum of 3–4 pixels in the image, but preferably twice that amount [35]. An excellent gold speckled pattern on a SDSS can be seen in Figure 3.6. Here the speckles are random, clearly defined as white speckles, and the area between the speckles is black. The average speckle size is  $35 \text{ pixel}^2$  or  $0.0012 \mu\text{m}^2$ . Depending on the size of the speckles the horizontal field of view will typically be between 10–15  $\mu\text{m}$ . However, these images will not be a representative area for most materials. To overcome this, an area is mapped by acquiring images in a grid pattern, and merged, as illustrated in Figure 3.7. By doing this, a larger area of the microstructure can be imaged. Here, the limiting factor is acquisition time, electron beam stability and final image file size. As an example, if the horizontal field of view for each frame is 11.5  $\mu\text{m}$ , and a horizontal field of view of 160  $\mu\text{m}$  is required to achieve a representative area of the microstructure, the number of frames required will then be  $16 \text{ frames} \times 16 \text{ frames} = 256 \text{ frames}$ . This is including a 20% overlapping area required for the stitching procedure. In addition, each frame takes roughly 1.5 min to collect (depending on acquisition settings) and between each captured frame a stage settle time is set to a minimum of 15 seconds. Then the total collection time for one loading step will be close to 7.5 hours. This is challenging when considering beam stability and resulting image file size. 256 images stitched together to one image will result in an image file size of about 1 gigabyte, which is inconvenient for data processing. Also, each test will include one mapped area for each loading step, and in each test, there are several loading steps. For this reason, one tensile test will occupy the microscope for days. The only way to overcome this issue is to map a smaller area or increase the speckle size. Both of these approaches will reduce the amount of data acquired during a test.

After the acquisition, a set of images are obtained which needs to be stitched together into one single image before the DIC analysis. This stitching process was performed using a plugin to the open source software ImageJ [118–120]. To ensure good correlation while stitching, the precision of the grid collection is essential. The stage movement is controlled by external software, collecting the images row-by-row. If a 20% overlap is selected and the horizontal field of view is 15  $\mu\text{m}$ , then the stage movement needs to be precise to 3  $\mu\text{m}$  to secure an overlapping area. In addition, having stage settling time

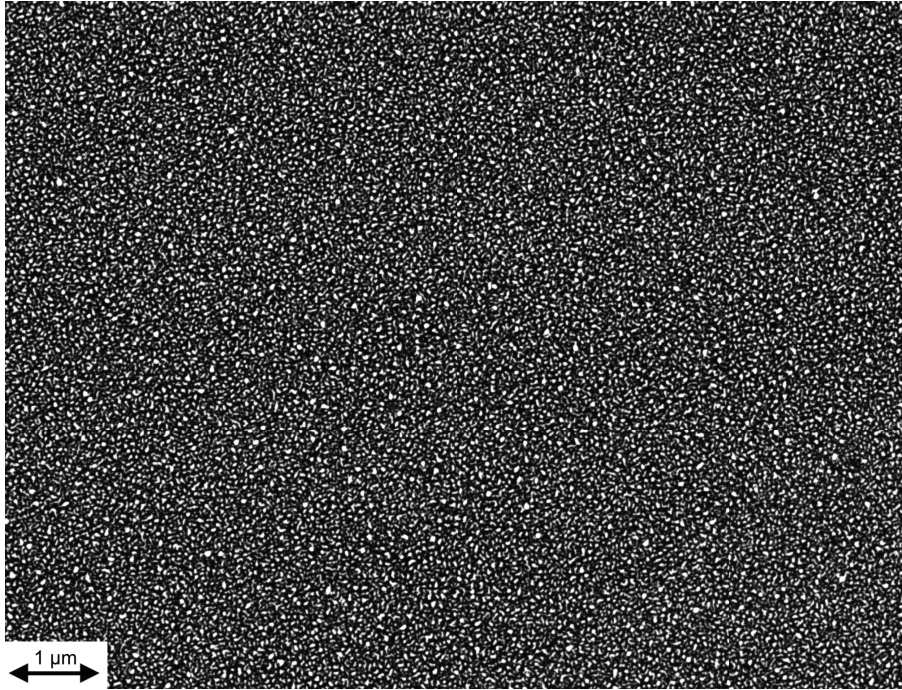


**Figure 3.6:** BSE image of gold speckles. This image equals one frame in Figure 3.7.

between each time the stage moves is essential. If not, small distortion due to the stage vibrations will make the stitching impossible as the distortions in the overlapping areas will be dissimilar. This will in turn strongly affect the DIC results. In order to measure the error from stitching and general distortions from the microscope, the recorded area is acquired twice at 0% strain. The images are then stitched together to obtain two mapped images of the recorded area at 0% strain. These images are then correlated using DIC to get an estimate of the error from the image collection. This systematical error is assumed to be the same for each loading step during the tensile test.

The gold speckle pattern is acquired by using BSE imaging mode in the SEM. A short working distance is selected to optimize the signal strength from the backscatter electrons. In addition, a short working distance is beneficial since the electron beam is scanning uninterrupted for up to several hours at the time. When having a short distance, the beam will travel a short distance between the gun and the specimen, and the specimen and the detector, which reduces noise. A summary of the settings used when acquiring the BSE images is given in Table 3.5. It is possible to acquire SE images of the speckled pattern, however, the quality in the BSE images is better. Also, the prolonged exposure to the electron beam will affect the SE images to a greater extent than in BSE images.

**Table 3.5:** SEM settings for BSE imaging of gold speckle pattern for DIC (see Figure 3.6).

Imaging mode	BSE
Working distance	4-5 mm
Acceleration voltage	8 kV
Aperture size	60 $\mu\text{m}$
Stage settle time	60 s

(1,1)		(1,2)		(1,3)		(1,4)		(1,5)		(1,6)		(1,7)
(2,1)		(2,2)		(2,3)		(2,4)		(2,5)		(2,6)		(2,7)
(3,1)		(3,2)		(3,3)		(3,4)		(3,5)		(3,6)		(3,7)
(4,1)		(4,2)		(4,3)		(4,4)		(4,5)		(4,6)		(4,7)
(5,1)		(5,2)		(5,3)		(5,4)		(5,5)		(5,6)		(5,7)
(6,1)		(6,2)		(6,3)		(6,4)		(6,5)		(6,6)		(6,7)
(7,1)		(7,2)		(7,3)		(7,4)		(7,5)		(7,6)		(7,7)

**Figure 3.7:** An illustration showing the image acquisition of a large area in an SEM with an overlapping area. Each frame is labelled with the row and column index.



## 3.4 Materials

### 3.4.1 NVE36 two-phase steel

NVE36 is a ferritic-pearlitic rolled steel plate. The combination of the two phases gives an alloy with superior strength and ductility compared to having a pure ferritic or pearlitic microstructure. Ferrite is  $\alpha$ -iron with a body-centered cubic crystal structure. At room temperature it dissolves close to no carbon. From the iron-carbon diagram (see Figure 2.8) it can be seen that ferrite takes 0.02 wt% of carbon in solid solution at 723°C. If the carbon amount exceeds this, pearlite is formed. Pearlite has a lamellar structure, where the lamellas are alternating between cementite and ferrite. Cementite is a hard and brittle phase, while the ferrite is a ductile phase. In Figure 3.8, a micrograph of NVE36 is shown. The darker grain here are ferrite, and the white grains are pearlite. When looking closely, the lamellar structure of pearlite can be seen in this image.

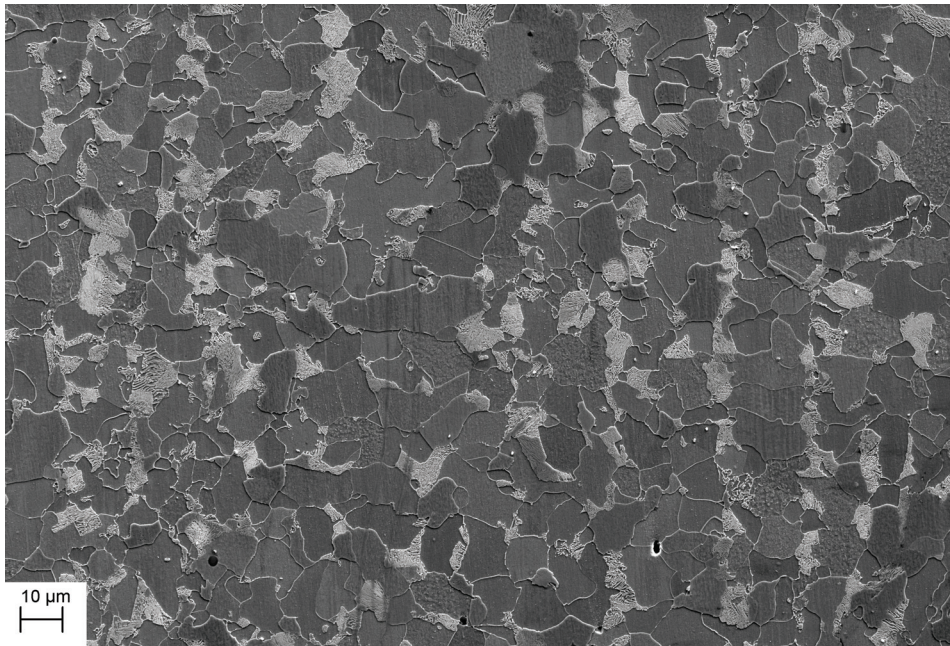


**Figure 3.8:** Secondary electron image of the undeformed microstructure. The darker areas are ferrite grains and the lighter areas are pearlite grains.

The steel used in this research contains 75% ferrite and 25% pearlite, with an average grain diameter of 15  $\mu\text{m}$ . In Table 3.6 the chemical composition is listed. All specimens used in this work were taken parallel to the rolling direction (RD) of the larger plate, with a thickness of 10 mm, illustrated in Figure 3.9. In Figure

3.9 RD, ND and TD illustrates the specimen reference frame and are the rolling direction, normal direction and transverse direction, respectively. The specimens were then prepared by mechanical grinding and polishing to 1  $\mu\text{m}$ , followed by either etching for 10 s in 2% Nital [121] or vibration polishing as described in Chapter 3.2. The difference between the two final polishing steps is that the etched surface provides good contrast between the phases and highlights the grain boundaries in SE imaging mode, while the vibration polisher provides a plane, deformation free surface suitable for EBSD. The etched surface can be used as "speckled" pattern for DIC without any additional treatments (see also Figure 3.8). Conversely, the surface from the vibration polisher can be used with a gold speckle pattern as described in Chapter 3.3

**Table 3.6:** Typical chemical composition of NVE36 (wt.%) [122].

Element	C	Si	Mn	P	S	Cr	Mo	Ni	Cu	Al	Nb	V	Ti
Content	0.18	0.5	0.9-1.6	0.035	0.035	0.2	0.08	0.4	0.35	0.02	0.03	0.05	0.01

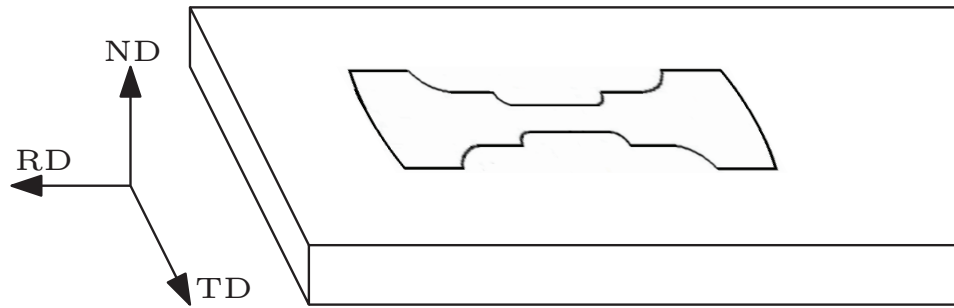


**Figure 3.9:** This figure shows how the specimen are taken from the NVE36 plate. The plate and the specimen are not in scale.

### 3.4.2 2507 super duplex stainless steel

Duplex stainless steels (DSS) consist of two phases, austenite ( $\gamma$ ) and ferrite ( $\alpha$ ). The two phases, in combination with the alloying elements, results in steel with superior mechanical properties and corrosion resistance compared to steels at similar cost. The oil and gas industry first developed DSS for use in the North Sea. Here, it is typically used in process pipe systems and fittings exposed to corrosive environments at elevated temperature (up to 150°C in a  $\text{H}_2\text{S}$  atmosphere) [123]. DSS typically contains 22% Cr, 5% Ni and 0.18% N to achieve the desired phase composition and corrosion properties. If better corrosion properties are required, super duplex stainless steel (SDSS) can be used instead. This alloy contains a higher amount of Cr, Ni, and N, and typical values are 25%, 7%, and 0.3%, respectively.

To achieve the desired phase composition the SDSS is annealed at 1050°C and left there until a 50-50 phase balance between ferrite and austenite is obtained. During cooling after the heat treatment, precipitation of intermetallic phases ( $\sigma$ ,  $\chi$ ,  $\pi$  and  $R$ ) may occur. These intermetallic phases have been found to considerably reduce the mechanical properties and corrosion resistance of the material [52–54, 93, 94, 124–130]. The most common of these phases is the  $\sigma$ -phase. Even small amounts (<0.5%) of  $\sigma$ -phase will significantly reduce the fracture toughness [52, 131]. This reduction, combined with the short time it takes for the phase to form and the deteriorating effect on corrosion properties, is what makes  $\sigma$ -phase a dangerous and strongly unwanted intermetallic phase.

The investigated material in this study was a 2507 SDSS, with the chemical composition listed in Table 3.7. This pipe was manufactured by welding a rolled plate along the length of the pipe. The microstructure of the steel investigated here contained more ferrite than austenite, respectively 56.3% and 43.7%. The grain size in the two phases is also different, with larger ferrite grains than austenite grains. These results have been summarized in Table 3.8. Also, the grains have different morphology in different directions. Figure 3.10(a) gives a phase map of the pipe material in three different directions. Here, LD, CD, and ND are abbreviations for longitudinal direction, circumferential direction, and normal directions, respectively. The meaning of these is illustrated in Figure 3.10(b). Specimens were spark eroded with a 2 mm thickness from a 10 mm thick pipe to the dimensions in Figure 3.2. All specimens were cut parallel to the length of the pipe wall, as illustrated in Figure 3.10(b). The observed plane of the specimen during an *in-situ* experiment has ND as the plane normal.

**Table 3.7:** Chemical composition of 2507 SDSS (wt.%).

Element	C	Si	Mn	P	S	Cr	Mo	Ni	Cu	W	N
Content	0.018	0.42	0.52	0.017	0.001	25.55	3.46	8.28	0.72	0.52	0.25

**Table 3.8:** Microstructure statistics summarized. The data was collected from EBSD scans.

Average	Ferrite	Austenite	Overall
Composition	56.3%	43.7%	100%
Grain size	9 $\mu\text{m}$	6.5 $\mu\text{m}$	7.9 $\mu\text{m}$

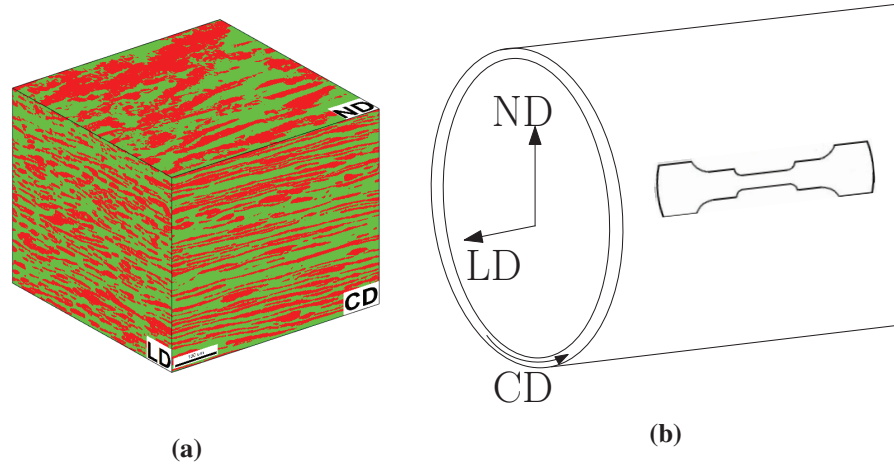


**Figure 3.10:** (a) An illustration of the microstructure with the phases illustrated. The dimensions of the cube are  $500\ \mu\text{m} \times 500\ \mu\text{m} \times 500\ \mu\text{m}$ , where green representing  $\alpha$  and red representing  $\gamma$ . In the bottom right corner of each side, the plane normal is given. LD, CD, ND are illustrated in (b). (b) This figure illustrates how the specimens were taken from the SDSS pipe wall and gives the definition of LD, CD and ND.

### 3.4.3 Dual-phase steel

DP steels are steels containing the two phases, ferrite ( $\alpha$ ) and martensite ( $\alpha'$ ). In these steels, there is a great difference in hardness, strength, and ductility between the two phases. Ferrite is much softer and more ductile compared with martensite. As a result, when combined, the material will have an increased strength compared to pure ferrite and increased ductility compared to pure martensite. By altering the ratio between the two phases, different combinations of strength and ductility can be achieved.

In this work, four different dual-phase (DP) steel plates were investigated. These are DP500, DP600, DP800, and DP980. Here, the number denotes the yield strength of the material. All specimens were spark eroded from a larger plate, as shown in Figure 3.9, to the dimensions shown in Figure 3.2(a). The thickness of the specimen was kept to the thickness of the plate. For DP500 this was 2 mm, and for the other three (DP600, DP800 and DP980) this was 1 mm. The chemical composition of the four steel plates is given in Table 3.9. In Figure 3.11 image quality (IQ) maps from EBSD scans of the four steel plates are shown to show the microstructure. These EBSD scans were acquired with a step size of  $0.1\ \mu\text{m}$  and have an area of  $80\ \mu\text{m} \times 80\ \mu\text{m}$ . These IQ maps were investigated in order to identify the phase composition of the steel. In an IQ map, a darker color indicates a poor correlation between the



scanned Kikuchi pattern and the database [65]. Conversely, a near perfect fit will appear white. Martensite has a BCT crystal structure, which is very similar to the ferritic BCC structure. As a result, the martensite grains will appear darker in the IQ map since it is indexed as poorly correlated ferrite. The BCC in the ferrite fits well with the EBSD indexing database and will appear white in the image. From this, it is possible to calculate the amount of each phase present in the material. In this work, a binary version of the IQ map is created, and the amount of martensite and size of martensite islands are calculated from the binary image. Both operations are performed using the Fiji distribution [118] of the OpenSource software ImageJ [120]. The results from this operation are listed in Table 3.10, alongside the average grain size of ferrite which is recorded using data from the EBSD scans.

**Table 3.9:** Chemical composition of DP steels.

Material	C	Mn	Si	Nb
DP500	0.079	0.7	0.3	
DP600	0.094	0.9	0.2	0.015
DP800	0.136	1.6	0.2	0.016
DP980	0.144	1.5	0.19	0.015

**Table 3.10:** Phase fraction of martensite in each DP steel and average size of ferrite grains and martensite islands recorded using EBSD.

Material	Fraction martensite	Average grain size ferrite	Average size martensite islands
DP500	0.14	8.4 $\mu\text{m}$	3.4 $\mu\text{m}$
DP600	0.18	3.5 $\mu\text{m}$	2.3 $\mu\text{m}$
DP800	0.28	3.3 $\mu\text{m}$	2.0 $\mu\text{m}$
DP980	0.54	2.7 $\mu\text{m}$	2.5 $\mu\text{m}$

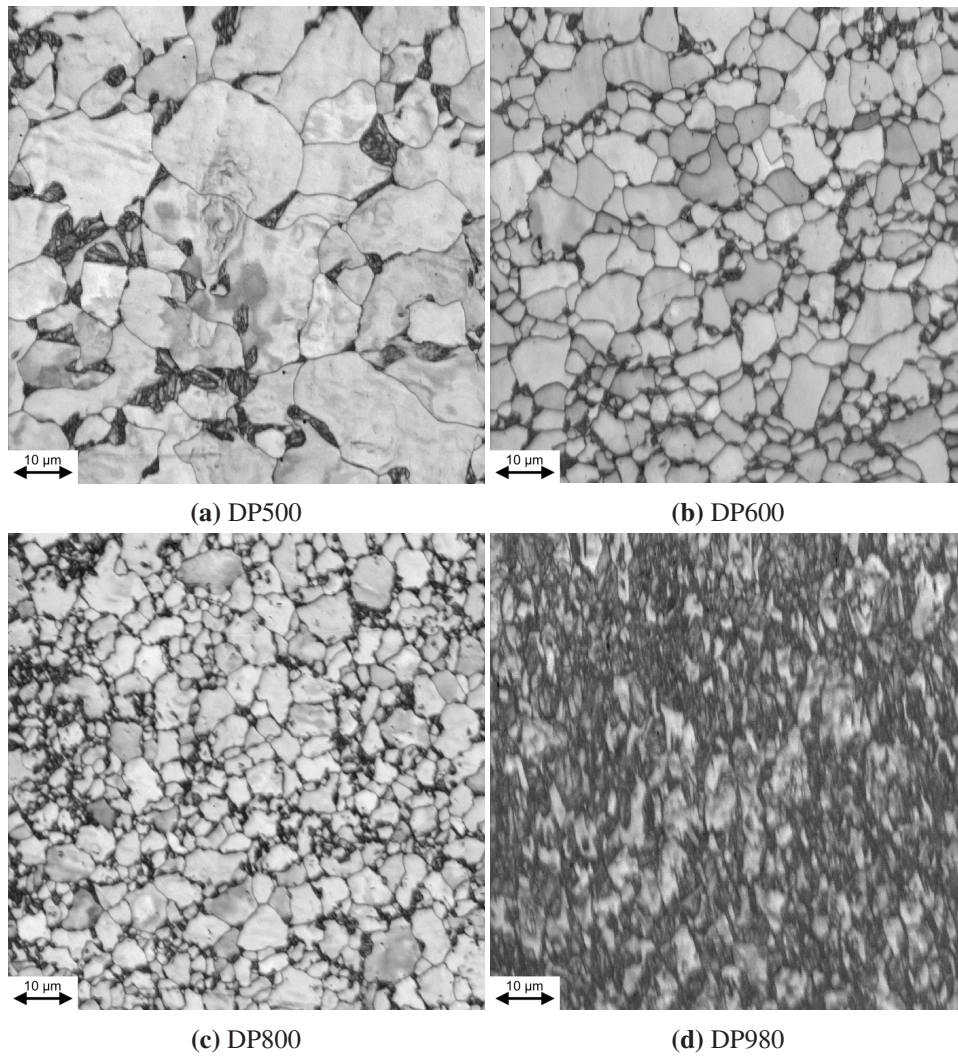


**Figure 3.11:** IQ maps of (a) DP500, (b) DP600, (c) DP800 and (d) DP980 microstructures. The white areas are ferrite grains and the darker areas are martensite islands. Each map was acquired with a step size of 0.1  $\mu\text{m}$ .



## **Chapter 4**

# **Effect of heat treatment on different steels**

The method for remodeling a thin continuous layer of gold into a speckled pattern is described in Chapter 3.3. This method requires an elevated temperature during the remodeling process. An investigation is conducted in order to investigate the effect of this heat treatment on the properties and microstructure of the steels studied. These materials are DP500, DP600, DP800, DP980, NVE36 and a 2507 superduplex stainless steel (SDSS). Each of them was characterized before and after the heat treatment process by using scanning electron (SEM) micrographs, electron backscatter diffraction (EBSD), hardness testing and tensile testing. The results demonstrate that the temperatures these steels are subjected to during gold remodeling will influence the tensile behavior of the dual-phase (DP) steels. Here, the yield strength increases and Lüders bands are introduced. This change is due to carbon redistribution during heat treatment. However, the rate of the hardening is close to identical for these steels. As a result, it is expected that the deformation behavior of these steels is the same as before heat treatment. For the NVE36 and SDSS, there are only small differences between the heat treated and as received curves. The variation here is within the natural variation of the material. These results are confirmed by performing several tensile tests of both heat-treated and as received material.

### **4.1 Material characterization**

In this work the materials studied are DP500, DP600, DP800, DP980, NVE36 and a 2507 SDSS. These are described in Chapter 3.4. The objective of this study is to investigate the effect of temperature during the gold remodeling on different

steels. There are two methods used for gold remodeling: First, the specimens are exposed to 300°C for 1 hour in a water vapor atmosphere. Second, a method where the specimens are exposed to 180°C for 96 hours in an argon/styrene atmosphere. These methods are described in further detail in Chapter 3.3. The heat treatment for the different specimens is summarized in Table 4.1. The SDSS is the only stainless material in this work and therefore the only specimen heat-treated according to the water vapor remodeling procedure.

**Table 4.1:** The different heat treatment times and temperatures for the different materials. These parameters are the same as during remodeling.

Material	Temperature	Time
DP500	180°C	96 hours
DP600	180°C	96 hours
DP800	180°C	96 hours
DP980	180°C	96 hours
NVE36	180°C	96 hours
SDSS	300°C	1 hour

All specimens were investigated before and after the heat treatment. Microhardness measurements, with seven different measurements, were taken from each phase. In order to fit the hardness imprint inside the grains, a small load was applied during acquisition. This load was 10 g, with a holding time of 15 s. The measurements were performed using a Leica VMHT MOT microhardness tester on polished specimens. All specimens were ground and polished to 1  $\mu\text{m}$  before the final step to reveal the microstructure. For DP steels this final step was vibration polishing using a VibroMet2 from Buehler for 12 hours using a suspension with pH 8 containing SiO<sub>2</sub> particles with the size 0.02  $\mu\text{m}$ . NVE36 was etched with 2% Nital for 10 s. Electropolishing was used as the final polishing step for SDSS. The settings for the electropolishing are summarized in Table 3.2. Finally, all specimens were cleaned in an ultrasonic bath for 5 minutes with acetone.

In addition to the hardness measurements, EBSD scans were acquired for each specimen to get the grain size and phase composition of the material. All steels were prepared for the EBSD acquisition in the same fashion as before the hardness measurements, except for NVE36. Here, the same method as for DP steels was used. However, for NVE36 it is too difficult to identify the pearlite in EBSD maps, but it is visible in secondary electron imaging mode on the etched surface. As a consequence, the grain size of ferrite and pearlite, and the phase composition of NVE36, are identified using microstructural secondary electron (SE) images instead of EBSD scans as for all the other materials. A total of three maps from both EBSD

and SE images was used for each specimen to identify the grain size. All maps had an area of  $80\text{ }\mu\text{m} \times 80\text{ }\mu\text{m}$  and included hundreds of grains each. The settings used during EBSD acquisition are presented in Chapter 3.2 and summarized in Table 3.1. In addition, tensile test curves were acquired before and after the heat treatment for all specimens. These tensile tests were performed using a MTS810 100kN conventional tensile test machine with digital image correlatin (DIC) as a virtual extensometer. All tensile tests were carried out using a constant strain rate of  $1.11 \times 10^{-3}\text{ s}^{-1}$ .

## 4.2 Results

The results from the hardness measurements and the microstructure statistics from the EBSD scans and SE images, before and after the heat treatment, are listed in Figure 4.1-4.3. These figures show the results from all measurements acquired in this work and compare the values before and after the heat treatment. It can be seen that there are only small differences between the measurements. Most measurements from after the heat treatment are within the standard deviation of the measurements from before the heat treatment.

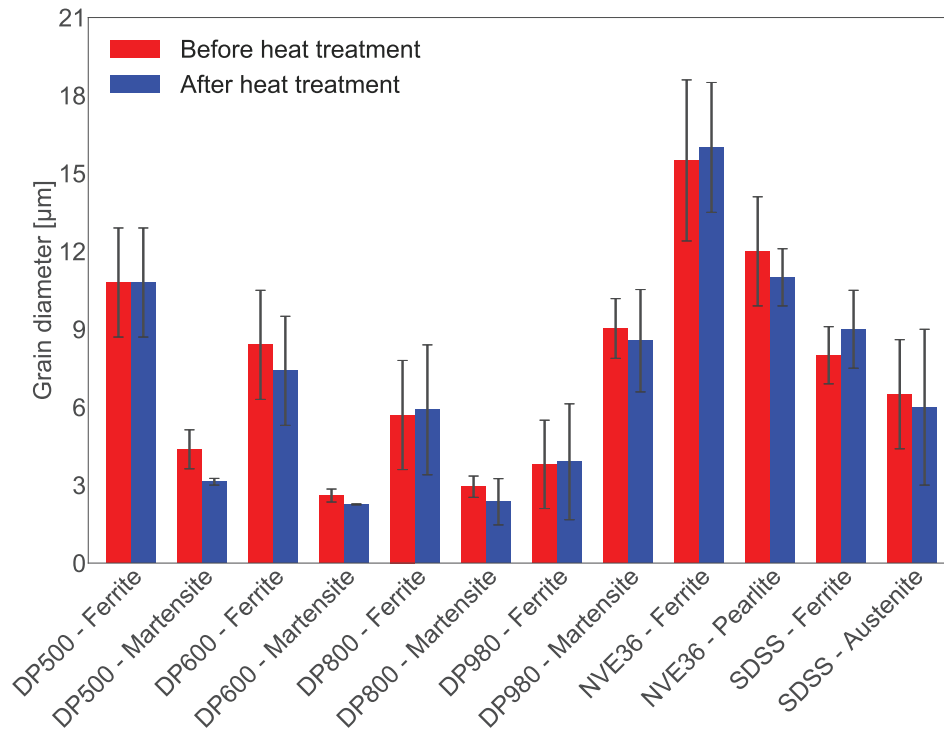


**Figure 4.1:** Grain size before and after heat treatment.

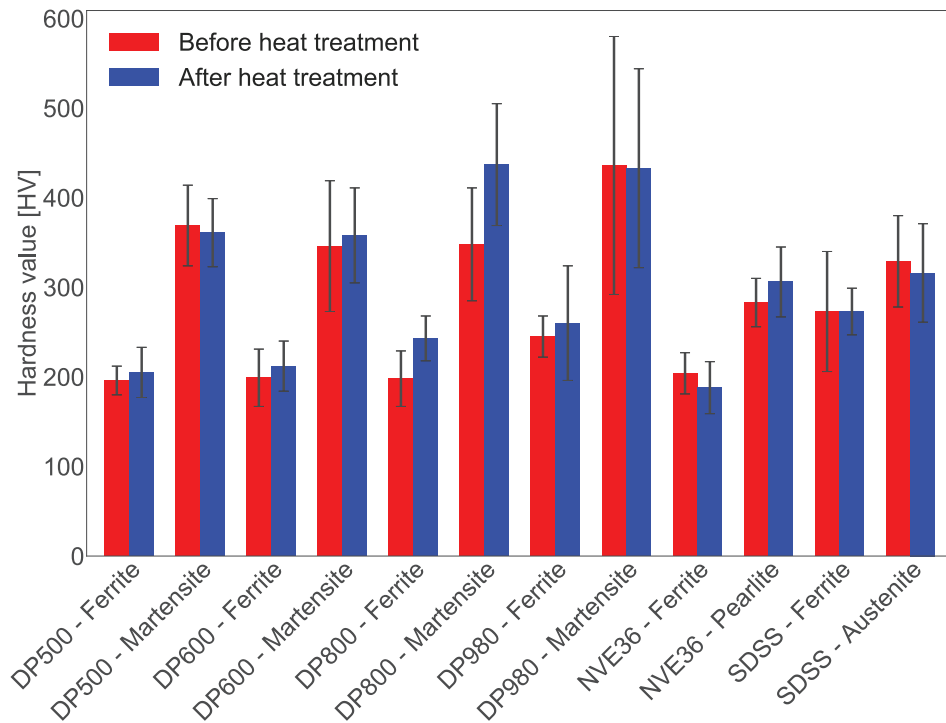


**Figure 4.2:** Hardness values before and after heat treatment.

In Figure 4.4 the engineering stress-strain curves for the different specimens, before and after the heat treatment, are shown. There is a clear difference in the curves for the DP steels. Here, the specimens exhibit a sharp yield point and a yield plateau with Lüders band propagation before the work hardening starts after heat treatment. One exception seen for DP980, where no sharp upper yield point is observed, and only the yield plateau and the Lüders bands propagation are observed. In addition, the yield strength is increased by 100 MPa - 150 MPa for each DP steel. However, the work hardening of DP steels is similar before and after the heat treatment. The tensile curves for NVE36 and SDSS are close to identical before and after heat treatment. Here, the small differences in the curves can be ascribed to the natural variation in the material.

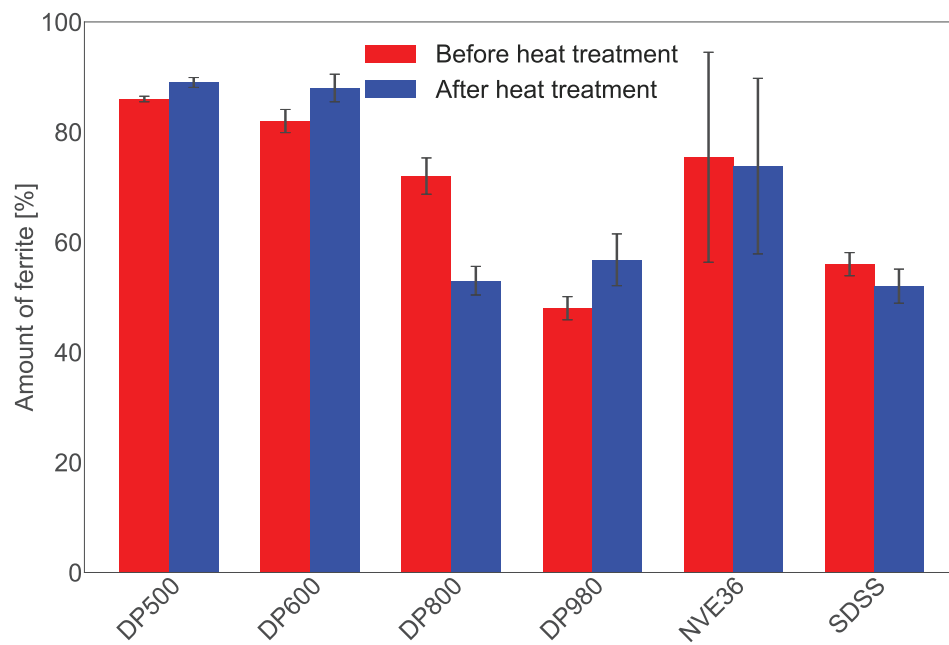


**Figure 4.3:** Phase composition before and after heat treatment.



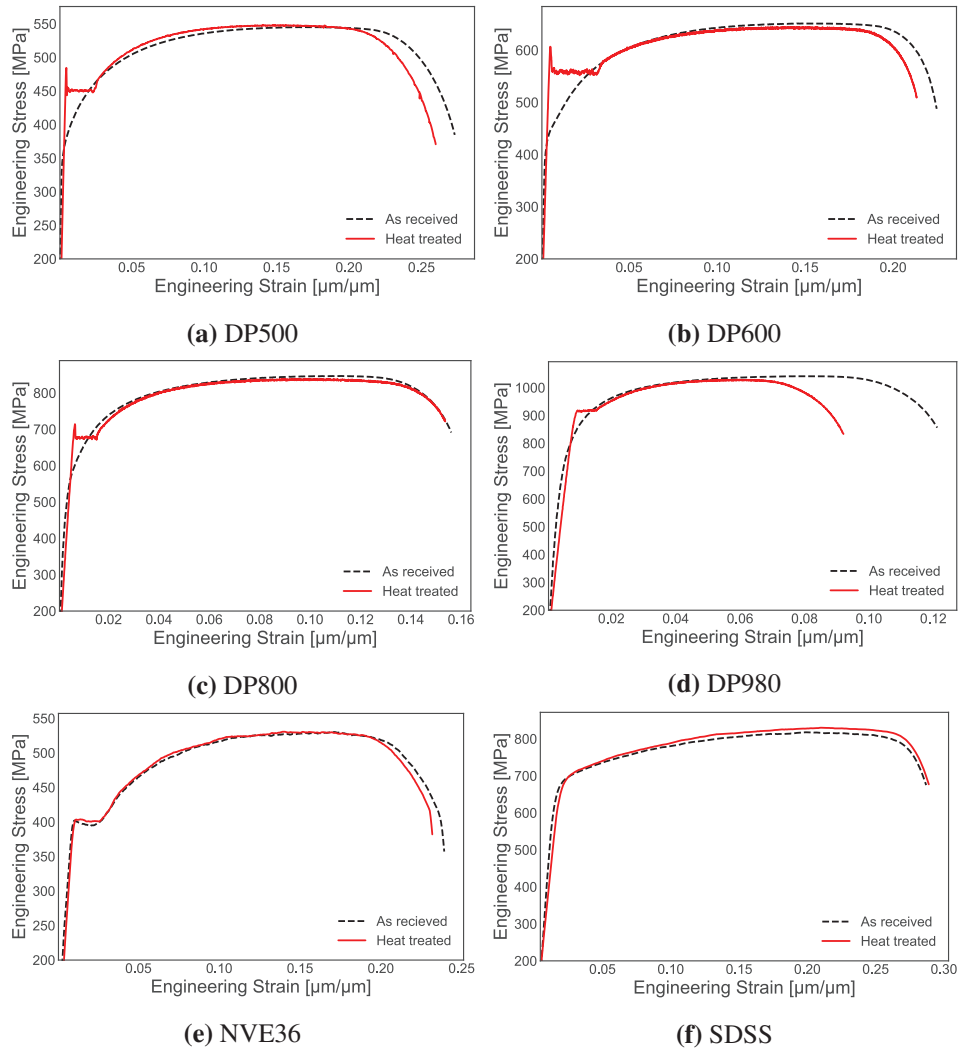


**Figure 4.4:** Tensile test curves for all specimens before and after heat treatment. The solid red lines are from after heat treatment, while the dashed black lines are without heat treatment. It can be seen that the DP500, DP600 and DP800 have a sharp upper yield point, a yield plateau and Lüders bands are introduced due to the heat treatment. In DP980, only a yield plateau and Lüders bands are introduced. For NVE36 and SDSS the tensile curves are nearly identical.

### 4.3 Discussion

In this work, six different steels have been heat-treated to replicate the conditions during the remodeling of a continuous layer of gold into a speckled pattern. This speckled pattern is used to correlate a DIC analysis from backscatter electron (BSE) images acquired during *in-situ* SEM tensile testing. When studying the microstructure and hardness measurements before and after heat treatment, it seems as no changes have taken place in any of the steels investigated. The before and after columns in Figure 4.1-4.3 are close to equal and within the standard deviation for all specimens. Also, from visual inspection of micrographs, it is not possible to distinguish which microstructure that has been heat-treated and which has not.

In addition to the microstructural investigations, tensile tests were performed on all steels before and after heat treatment. The NVE36 and SDSS specimens indicated no difference between the heat-treated tensile curve and the as-received tensile curve. However, this is not all that unexpected. The NVE36 microstructure is decided by the metastable Fe-C phase diagram (see Figure 2.8). As a result, NVE36 should withstand 180°C for an infinite amount of time without any changes to the microstructure. Also SDSS was kept at 300°C for one hour and remained stable. It is known that this temperature can affect the microstructure when kept for longer times [132]. In the work of Petterson et al. [132], a SDSS was heated to 300°C for up to 12,000 hours. During this time, Cr diffuse creating subtle fluctuations in the concentration within the ferrite phase due to spinodal decomposition. The amplitude of these Cr fluctuations increased with longer holding times. In addition, the ferrite hardness increased, and a reduction of fracture toughness in the heat-treated material was observed. These results are consistent with the time-temperature-transformation (TTT) diagram in Figure 2.19 and is termed 475°C embrittlement. However, in this work, the SDSS was heat-treated at 300°C for only one hour. As a result, hardness measurements from before and after the heat treatment (see Figure 4.2) are indistinguishable. The only difference is the size of the standard deviation. Further, the tensile curves from before and after heat treatment in Figure 4.4 are identical, with the same yield strength, ultimate tensile strength (UTS) and fracture strain.

Similarly to the NVE36 and SDSS, the microstructural investigations of DP steels seemed to indicate no major change in the material due to the heat treatment. The phase composition, hardness values and grain sizes all remained constant within the standard deviation. However, looking at the tensile curves in Figure 4.4, it is clear that some changes have taken place. After the heat treatment, a sharp upper yield point and a yield plateau with Lüders bands propagation have

been introduced. In addition, the yield strength increased significantly. These changes are due to static strain aging, also known as bake hardening [133]. Bake hardening typically occurs when automotive parts are painted and baked at elevated temperatures to cure the paint. During curing, the automotive part, in many cases a DP steel, experiences an increased yield strength and subsequent Lüders bands propagation. The fundamental mechanisms behind the bake hardening phenomena were studied by Waterschoot et al. [134]. After tempering for 5 hours at 170°C, clear signs of  $\eta$ -carbides precipitation were observed. Also, there were strong suggestions of relaxation of internal compressive stresses. These results were confirmed in an earlier study of Cheng et al. [135] which described the tempering process of martensite. In this work, we see the effect from the precipitated  $\eta$ -carbides and relaxation of stresses as increased yield strength and introduction of a yield plateau with Lüders bands propagation. Kozeschnik and Buchmayr [136] simulated the increase in yield stress that occurs when baking at 180°C, the same temperature as used for the gold remodeling. The increase started immediately, and the maximum yield strength was achieved in less than 100 minutes. Also, the influence of carbon was greater in ferrite compared to in martensite after bake hardening. This might help to explain the increased yield strength, since the carbon has diffused into the ferrite and precipitated as  $\eta$ -carbides. However, apart from the rearrangement of carbon, the microstructures are close to identical (as seen in Figure 4.1 - 4.3). As a result, during hardening (after Lüders bands propagation) the heat-treated curves follows the same trajectory, i.e., work-hardening, as the as-received material.

#### 4.4 Concluding remarks

The main motivation for this work was to see if the remodeling temperatures influenced the microstructure and mechanical properties of the investigated materials. Each specimen was heat-treated as during the gold remodeling, with the same temperature and holding time. All parameters listed in Figures 4.1-4.3 remain within the standard deviation of the measurements and seems unaffected by the heat treatment. However, for DP steels the tensile curves from before and after the heat treatment differ at low strains. Here, the yield strength increases and a Lüders plateau is introduced. In contrast, NVE36 and SDSS are behaving identically as before the heat treatment during a tensile test after the heat treatment. As a consequence, the conclusions from this work are the following:

- The temperature during gold remodeling does not affect the microstructure, properties, nor performance of NVE36 and SDSS.
- During the heat treatment of DP steels, a bake-hardening effect occurs, increasing the yield strength and introduces a sharp upper yield point and a yield plateau with Lüders bands propagation.
- The rate of hardening after the Lüders plateau is similar before and after being heat-treated for all DP steels.



## Chapter 5

# Verifying the *in-situ* DIC

To verify the digital image correlation (DIC) measurements during *in-situ* scanning electron microscope (SEM) tensile tests, grain rotations measured with DIC were compared with grain rotations measured using electron backscatter diffraction (EBSD) results. First, the undeformed specimen was scanned by EBSD. Second, an *in-situ* SEM tensile test was recorded and analyzed with DIC. The area recorded during the *in-situ* SEM tensile test was the same as the area recorded with EBSD. Finally, the deformed area was recorded with EBSD. Both DIC and EBSD are techniques that record the material at the surface. From DIC it is possible to extract the local rotation at each node, and in EBSD the rotation due to the deformation can be found by comparing the orientations before and after deformation. In the DIC data the deformation gradient ( $\mathbf{F}$ ) separates into one component of displacement ( $\mathbf{U}$ ) and one component of rotations ( $\mathbf{R}$ ) using polar decomposition, see Equation 5.1. Using Equation 5.2, it is possible to construct a map with the rotation data. The rotation data from DIC can be compared with grain rotations measured by EBSD. From the EBSD scans, the grain orientation before and after the deformation is known. By identifying the original grain orientation from before the deformation and comparing it to the grain orientation after deformation, the grain rotation due to the deformation can be extracted. Here, the rotation in a single point in the EBSD data is compared to the rotation of a node at the same location in the DIC map. EBSD is an established and verified experimental technique, and the rotations are compared to rotations measured by DIC to verify that the *in-situ* DIC measurements are true measurements of physical phenomena, and not artifacts. The results from this study show that the measurements from the two techniques are close to identical in 80% of the investigated grains. Also, in the grains where there is a difference, the EBSD data is poorly correlated due to the amount of deformation. Based on

the results from this study, it can be concluded that the *in-situ* SEM DIC technique captures material behavior and is a valid experimental technique when using SEM images.

## 5.1 Experimental

### 5.1.1 Specimen preparation and data acquisition

In this work, a 2507 super duplex stainless steel (SDSS) described in Chapter 3.4.2 was investigated using EBSD and DIC. All images and generated maps were taken from the same area inside the gauge length of the specimen. The specimen was spark eroded from a larger pipe with the geometries shown in Figure 3.2(a) to a thickness of 2 mm. First, the specimen was ground and polished until 1  $\mu\text{m}$ . The final polishing step was electropolishing. The settings for electropolishing are given in Table 3.2. Then two hardness indents were placed on the polished surface. These act as fiducial markers in order to ensure that the same area is recorded throughout the experiment with EBSD and DIC. Before creating the gold speckled pattern for DIC, an EBSD scan was performed of the undeformed specimen. Second, a gold layer was applied to the specimen and remodeled into a speckled pattern using the water vapor method, as described in Chapter 3.3. Third, an *in-situ* SEM tensile test was performed and the same area as recorded by the initial EBSD scan was measured. Finally, an EBSD scan of the deformed specimen was carried out.

The EBSD was recorded with a step size of 0.5  $\mu\text{m}$  using a ZEISS Ultra 55 Field Emission SEM. The microscope settings are described in Chapter 3.2. To record the deformation and microstructure evolution during the *in-situ* SEM tensile test, a ZEISS Supra 55 Field Emission SEM with a backscatter detector was used. A spindle-driven *in-situ* tensile test device was placed in the vacuum chamber, where it was mounted on top of the SEM stage after removal of the rotation unit. The device is shown in Figure 3.1, and described in Chapter 3.1. The image acquisition for DIC is described in Chapter 3.3. Each frame in the total image had the dimensions of 23  $\mu\text{m} \times 17 \mu\text{m}$  and contained 2,048 pixels  $\times$  1,536 pixels. The merged image consisted of 49 frames, acquired in a 7-by-7 grid with 20% overlap of each frame. As a result, the area recorded was 131  $\mu\text{m} \times 98 \mu\text{m}$  with a resolution of 11,671 pixels  $\times$  8,899 pixels. Before commencing the *in-situ* tensile test, two mapped images were acquired at 0% strain, and a third mapped image of the undeformed specimen was acquired after pulling the specimen 65  $\mu\text{m}$ , having a 50% overlapping area with the first image. These images were acquired in order to quantify unphysical strains recorded due to errors in the microscope (see Chapter 2.1.1) and the stitching process (see Chapter 3.3). During the *in-situ* SEM tensile test, a mapped image was acquired at 3%, 6%, 9%, 12%, and 15% (maximum force or ultimate tensile

strength (UTS)) global engineering strain. After the test, the image series were uploaded into the DIC software eCorr v.4.0 [11] for analysis. The mesh used in the DIC analysis was quadratic elements with size  $25 \text{ pixels} \times 25 \text{ pixels}$  resulting in a spatial resolution of  $0.279 \text{ } \mu\text{m}$  in the DIC measurements. After the final image at 15% was acquired, the specimen was unloaded and polished for 1 hour in a vibration polisher (VibroMet2 from Buehler). This to remove the gold speckles and prepare the surface for an EBSD scan of the deformed specimen. The vibration polisher is a gentle form of polishing, leading to the removal of the gold layer, but not erasing the fiducial markers, making it possible to locate the same area investigated earlier.

### 5.1.2 Extracting grain rotation

The final results from this study are the two EBSD scans of the same area at 0% and 15% strain, and the DIC data of the same area at 15% strain. From the EBSD maps, the grain rotation was extracted and compared with the rotational map provided by the DIC technique. The grain rotation measured with EBSD was extracted by comparing the original orientation in the undeformed map with the final orientation in the deformed map [137].

The results from the DIC analysis were represented by extracting the rotational matrix using the polar decomposition given in Equation 5.1. From this equation it is possible to separate the deformation gradient,  $\mathbf{F}$ , into one component of displacements,  $\mathbf{U}$ , and one component of rotations,  $\mathbf{R}$ . Here, the displacement and deformation gradient are calculated as presented in Chapter 2.2. As a result, the rotations can be extracted from Equation 5.2.

$$\mathbf{F} = \mathbf{R} \cdot \mathbf{U} \quad (5.1)$$

$$\mathbf{R} = \mathbf{F} \cdot \mathbf{U}^{-1} \quad (5.2)$$

Further reading on the theoretical background for the DIC approach used in this study is given in Chapter 2.2.

$\mathbf{R}$  is in this work illustrated as a field map superimposed on the deformed microstructure. The values represent the rotation of the nodes in the DIC mesh due to the deformation. This data can be compared with the change in orientation measured by EBSD. Here, two inverse pole figure (IPF) maps from before and after deformation give the rotational change. These are two independent techniques measuring the rotation of the grains on the surface. As a result, the measurements should give the same result using both techniques.



## 5.2 Results

In Figure 5.1 an IPF map from EBSD of the investigated area from (a) before and (b) after the tensile test is shown. The colors in these maps represent the grain orientations and are defined by the legend in (c). Here, red points have a  $[001]$  orientation, blue points have a  $[\bar{1}11]$  orientation, and green points have a  $[011]$  orientation, all aligned with the plane normal. The same grains are circled and numbered in both (a) and (b). In these grains, the misorientation due to the deformation was extracted for a specific point in the map and summarized in column EBSD in Table 5.1. Similarly, in Figure 5.2, the same grains are circled, and the rotation in the same point as in Figure 5.1 is extracted from the DIC data. The data is then reported in the column DIC in Table 5.1.

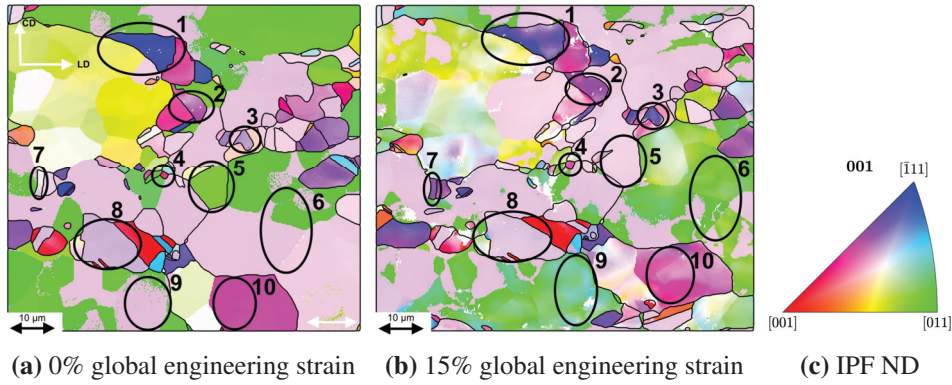


**Figure 5.1:** IPF maps of the recorded area (a) before and (b) after the *in-situ* SEM tensile test. The grains marked in the figures are used to compare the grain rotation measured with both DIC and EBSD. The IPF maps color coding is given in (c) with ND as normal. The tensile direction is horizontal, as marked in the bottom right of (a).

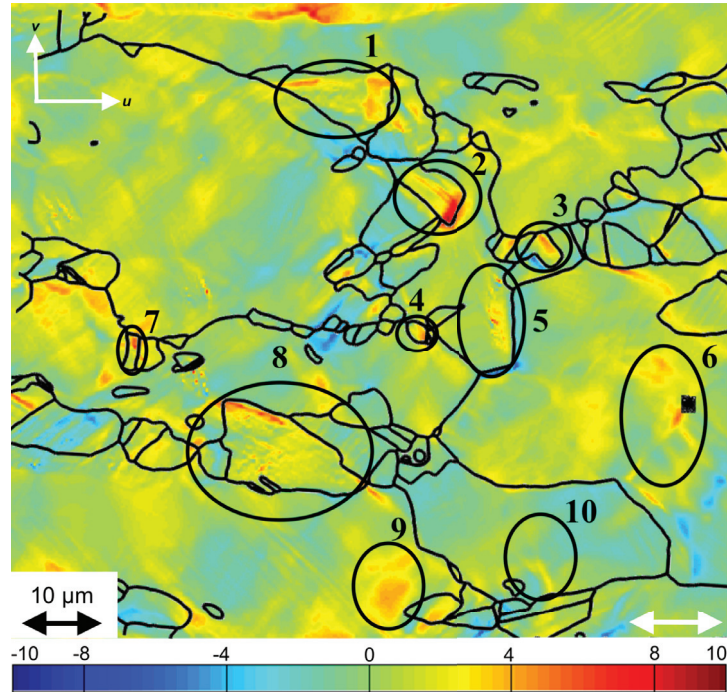


**Figure 5.2:** Rotation map from DIC showing rotations from  $-10^\circ$  to  $+10^\circ$ . The grain boundaries are taken from the EBSD scan and superimposed onto the DIC map. In the circle labelled 6 there is a black square. This is an uncorrelated area due to lack of gold speckles. The tensile direction is horizontal, as marked in the bottom right.

The IPF maps given in Figure 5.1 show the microstructure before and after the deformation. The change in colors from one map to the other reflects a change in orientation. This change is due to the rotation of the grain during deformation. Looking at the DIC map (see Figure 5.2), a small black square within the circle labeled 6 can be seen. This is an area where the DIC correlation failed. This was due to contamination on the surface before the gold remodeling, resulting in an area with no gold speckles.

Comparing the results in the DIC column and the EBSD column in Table 5.1, 8 out of 10 grains return the same rotation within  $1^\circ$ . In Grain 3 and Grain 9, the EBSD registered respectively a  $2^\circ$  and  $3^\circ$  larger rotation compared to the DIC measurements.

In addition to the EBSD measurements, two types of tests on an unstrained sample were also conducted. Here, no damage should be recorded with the DIC, and the strains measured should reflect the errors due to image acquisition and stitching

**Table 5.1:** The grain rotation after plastic deformation measured with DIC and EBSD.

Grain	DIC	EBSD
Grain 1	5°	6°
Grain 2	8°	8°
Grain 3	5°	7°
Grain 4	5°	4°
Grain 5	6°	5°
Grain 6	5°	5°
Grain 7	7°	6°
Grain 8	6°	6°
Grain 9	5°	8°
Grain 10	5°	4°

procedure (see Chapter 3.3). First, an area was mapped twice, while being undeformed, with the same acquisition settings as in the *in-situ* SEM tensile test. Due to the errors, a fictitious strain of about 1% was registered. Second, the specimen was pulled as a rigid body roughly 65  $\mu\text{m}$  before acquiring a third mapped image. 65  $\mu\text{m}$  gives a 50% overlap between the two recorded regions. This rigid body movement should not impose any strain in the specimen. As for the first test without any pulling, a fictitious strain of 1% was measured. From the same test, rotational maps were constructed. The resulting DIC map gave an unphysical rotation peak of 0.5°. Also, the EBSD recorded misorientations within the grains to be between 0.5°- 1°. These measurements from an undeformed specimen reflect the uncertainty in the results of this study.

### 5.3 Discussion

In this chapter, two independent techniques (DIC and EBSD) were utilized to measure the grain rotation due to plastic deformation. The objective of this study was to verify that the deformations measured with DIC during an *in-situ* SEM tensile test are real deformations and not artifacts from the SEM. The results of this study are summarized in Table 5.1. Here it can be seen that the EBSD results and DIC results compare well. Grain number 1, 2, 4-8, and 10, measure rotation within 1° between the two techniques. When considering a measured error of 0.5° in the DIC results and 0.5-1° uncertainty from the undeformed EBSD results, this can be said to be identical results. For grain 3, the EBSD measured 2° larger rotation than the DIC, which is relatively close when accounting for the error. However, in grain 9 the difference was 3°, which is too large of a difference to dismiss. Looking at the IPF map in Figure 5.1(b), a white area can be seen inside grain 9. The white

area signifies a poorly indexed or unindexed EBSD pattern. This might be due to the amount of deformation or contamination of the surface. As a result, the measurements from this grain is not as reliable as the others. Larger deformation in the specimen gives poorer EBSD result, which is reflected in the image quality (IQ) maps of EBSD. Figure 5.3 give the IQ maps of the (a) undeformed and (b) deformed specimen. The deformed map is more white compared to the undeformed map, and this means a more uncertain EBSD result. A qualitative observation is that the red areas in Figure 5.2 correspond well with the white areas in Figure 5.3(b). This is another indication of a correlation between the two measurement methods.

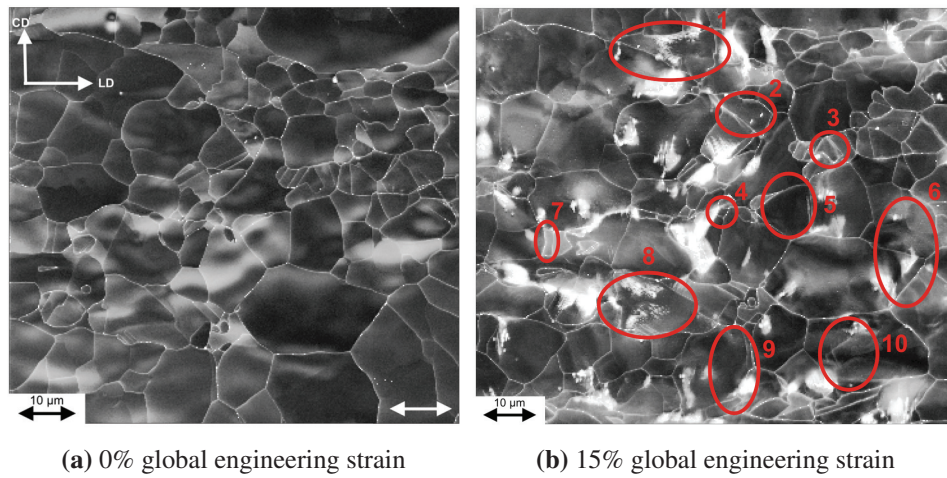


**Figure 5.3:** IQ maps of the recorded area (a) before and (b) after the *in-situ* SEM tensile test. The tensile direction is horizontal, as marked in the bottom right of (a). Dark areas indicates a well correlated Kikuchi pattern and white areas are poor or uncorrelated areas.

In addition to the EBSD results, a test measuring strains in an unstrained specimen was also conducted. This test recorded an unphysical strain of 1% when performing a DIC analysis on two mapped images of the same area. This error is due to the image acquisition in the SEM and the stitching procedure. The microscope used in this work has a mechanical stage, with an accuracy of 1 µm. As a result, some of the frames in the mapped image (see Figure 3.7) are not perfectly aligned, and as a result, the stitching process has been challenging. In addition, the image acquisition took 2 hours and 6 minutes to complete, which means that the last frame is acquired more than two hours later than the first. During this time the electron beam needs to remain stable, and there should be no external interference. When comparing the first and last frame of the recorded area, there are no visible differences in the quality of the pattern. From this, it can be concluded that the electron beam and the SEM has remained stable throughout the image

acquisition. Also, an area was recorded after a rigid body movement, where it had a 50% overlap with the previously recorded area. In this test, no new errors were measured. This rigid body movement test is similar to the validation test performed by Buljac et al. [34]. However, they registered an error of 0.3% in a DVC analysis, compared to 1% in this DIC analysis. One difference between these studies is the difference in image acquisition. Their images were X-ray diffraction patterns from a synchrotron, while an SEM is used here to acquire BSE images. A suggestion for further improvement would be to use an SEM with a piezoelectric stage. This would improve the accuracy when stitching the acquired images. Also, there is some research looking into removing artifacts from SEM images for DIC analysis [138]. Implementing these methods would improve the quality of DIC maps. However, this would be more useful in tests when investigating smaller strains in the elastic region of the material compared to the more significant strains during work-hardening investigated here.

## 5.4 Concluding remarks

In this chapter, two independent techniques (DIC and EBSD) were utilized in order to measure the grain rotation due to plastic deformation. In addition, a separate test investigating the measured strain on an unstrained specimen was conducted. The objective of this study was to verify that the deformations measured during an *in-situ* SEM tensile test with DIC are real displacements and not artifacts from the SEM. The two independent techniques, DIC and EBSD, measured the same grain rotation when accounting for uncertainties and errors. Based on the results from this study, it can be concluded that the *in-situ* SEM DIC technique captures material behavior and is a valid experimental technique also for quantitative studies when using SEM images.

## Chapter 6

# Comparing *in-situ* DIC results from an etched surface with a gold speckled surface

In the following chapter, NVE36, a ferrite-pearlite two-phase steel was investigated using *in-situ* scanning electron microscope (SEM) tensile testing combined with digital image correlation (DIC). Two different speckled patterns were used and compared. The first pattern was achieved by etching a polished surface in order to reveal the microstructural features. Second, a gold speckled pattern was obtained. Here, a continuous layer of gold was applied to a polished surface. This continuous layer was remodeled into gold nanoparticles by keeping the specimen at 180 °C for 96 hours with an argon/styrene mixture flowing across the specimen surface. The result is randomly distributed gold nanoparticles on the surface. These particles and the etched microstructure were then used by the DIC software to correlate an image series to obtain the local strain field of the material. The differences between the two techniques are numerous. Considering the etched surface, most microstructural features were grain boundaries and pearlite lamellas. As a consequence, large areas within grains did not provide sufficient contrast for DIC, thus restricting maximum resolution. However, the technique is fast and does not expose the material to any elevated temperatures. In contrast, the gold remodeling method provides a finely dispersed gold speckle pattern on the surface, giving excellent contrast across the recorded area. DIC with gold particles achieved a spatial resolution of 0.096  $\mu\text{m}$ , compared to 2.24  $\mu\text{m}$  in the DIC for the etched specimen. As a result, DIC with gold speckles can resolve slip lines. Conversely, DIC with etched microstructure resolves local strains on grain level. However, it is less cumbersome and faster to perform the test on the etched specimen.



## 6.1 Experimental

The material used in this study was NVE36. This is a two phase plate steel with a microstructure consisting of ferrite and pearlite, and it is described in more detail in Chapter 3.4.1. To record the microstructure evolution during the *in-situ* SEM tensile test, a Field Emission SEM Zeiss Supra 55 with a BSE detector applied was used when recording the gold speckled specimen. For the etched specimen a Field Emission SEM Zeiss Ultra 55 Limited Edition with an SE detector applied. A notched specimen geometry (see Figure 3.2(b)) was used for the *in-situ* SEM experiment presented in this study to make sure that the observed area was in the same region for both specimens. A spindle-driven *in-situ* tensile test device was placed in the vacuum chamber, where it was mounted on top of the SEM stage after removal of the rotation unit. The device is shown in Figure 3.1, and described in Chapter 3.1.

### 6.1.1 Etched surface

The specimens were ground and polished to 1  $\mu\text{m}$  before being etched for 10 s in 2% Nital. During the *in-situ* SEM tensile test on the etched surface, the same area was continuously recorded by an SE detector. This area is marked with the red square in Figure 6.1 and was located close to the most critical region of the specimen, i.e., in the region having the highest stress triaxiality. It should, however, be mentioned that it is challenging to select this area beforehand, and multiple tests may be required if fracture initiation is of interest. The recorded images had a resolution of 2048 pixels  $\times$  1385 pixels and the recorded area was 160  $\mu\text{m}$   $\times$  108  $\mu\text{m}$ , giving 0.078  $\mu\text{m}/\text{pixel}$ . This area was continuously recorded during straining. The frame rate of the line scan to acquire each image in the SEM was 6 s using an applied displacement rate of 0.2  $\mu\text{m}/\text{s}$ . This gave rise to some background noise and spatial distortion of the images. When conducting the experiment, a compromise among image resolution, exposure time and applied displacement rate had to be made to be able to perform the experiment in reasonable time and acquire enough images of sufficient quality for the DIC-analysis. After the test, the image series was uploaded into the in-house DIC software eCorr v.4.0 [11] for analysis. The mesh used in the DIC analysis was quadratic elements with size 30 pixels  $\times$  30 pixels or 2.24  $\mu\text{m}$   $\times$  2.24  $\mu\text{m}$ .

### 6.1.2 Gold speckled surface

To obtain the gold nanoparticle speckled pattern, the experimental set-up proposed by Orozco-Caballero et al. [10] was used. This method is described in detail in Chapter 3.3. First, the specimen has to be prepared for use in SEM, removing the deformation layer from the surface. Second, the polished surface is coated with gold, creating a thin continuous layer. Here, an Edwards S150B sputter coater

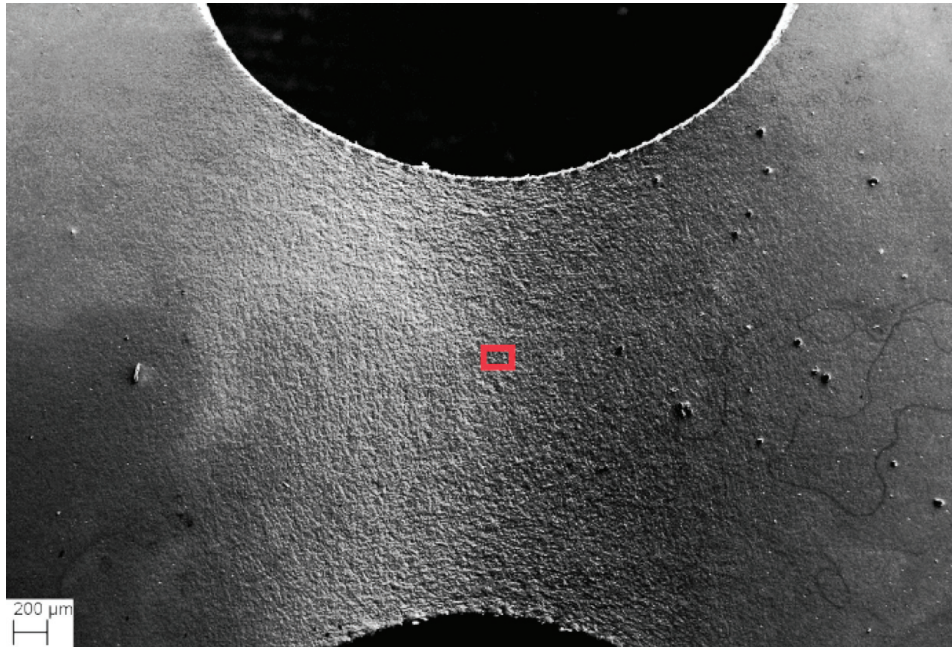


**Figure 6.1:** Area observed during the two *in-situ* SEM tensile tests. The red square has the dimensions  $160\ \mu\text{m} \times 120\ \mu\text{m}$  and is from the test on the etched specimen.

was used to coat the surface. The setting used to obtain this result is summarized in Table 3.3. Finally, to get this gold layer to remodel into particles, the gold-coated specimen is placed on a heat source with heated gas flowing across the surface. Here, a mixture of argon and styrene was used as the flow medium. A hot plate with the specimen placed on top was located inside a desiccator to create an atmosphere without oxygen. This was to prevent corrosion. In addition, by doing this, the argon/styrene fumes were contained. During the time the specimen was in the remodeling chamber, the gold layer transformed from a continuous layer to randomly distributed nanoparticles. The setup is illustrated in Figure 3.5.

When using a gold speckled pattern as the speckled pattern for the DIC, a continuous recording of the surface is not possible due to the long image acquisition time. Here, the specimen was strained, and then a BSE image was recorded while the tensile test was paused. The area recorded was closely aligned with the region recorded on the etched specimen (see Figure 6.1). The image acquisition is described in detail in Chapter 3.3. Here, each frame of the total image had a horizontal field of view of  $16.33\ \mu\text{m}$  and contained  $2048\ \text{pixels} \times 1536\ \text{pixels}$ . The total stitched image consisted of 81 frames, acquired in a 9-by-9 grid with 20% overlap of each frame. The final image had the dimensions  $119\ \mu\text{m} \times 90\ \mu\text{m}$  with 14,891 pixels



$\times 11,233$  pixels, yielding  $0.008 \mu\text{m}/\text{pixel}$ . Then, one mapped area was acquired at  $0 \mu\text{m}$  (undeformed),  $60 \mu\text{m}$  displacement (yield),  $240 \mu\text{m}$  displacement (during hardening) and  $610 \mu\text{m}$  displacement (maximum force). The images acquired after the maximum force could not be correlated with the DIC. This was due to the topography in the image, which yielded poor images with BSE imaging mode. After the test, the image series was uploaded into the in-house DIC software eCorr v.4.0 [11] for analysis. The mesh used in the DIC analysis were quadratic elements with size  $12 \text{ pixels} \times 12 \text{ pixels}$  or  $0.096 \mu\text{m} \times 0.096 \mu\text{m}$ .

## 6.2 Experimental results on etched specimen

Based on the measured elongation and force during the *in-situ* SEM tensile test on the etched specimen, the force–displacement curve shown in Figure 6.2 is plotted. As seen, the specimen exhibits a sharp yield point at a displacement of about  $60 \mu\text{m}$ , before the force drops abruptly. After this drop, the material starts to work harden and plastically deform. The force reaches a maximum of roughly  $3.6 \text{ kN}$  at a displacement of  $610 \mu\text{m}$ . The force then decreases continuously until fracture takes place after a displacement of  $1410 \mu\text{m}$ .

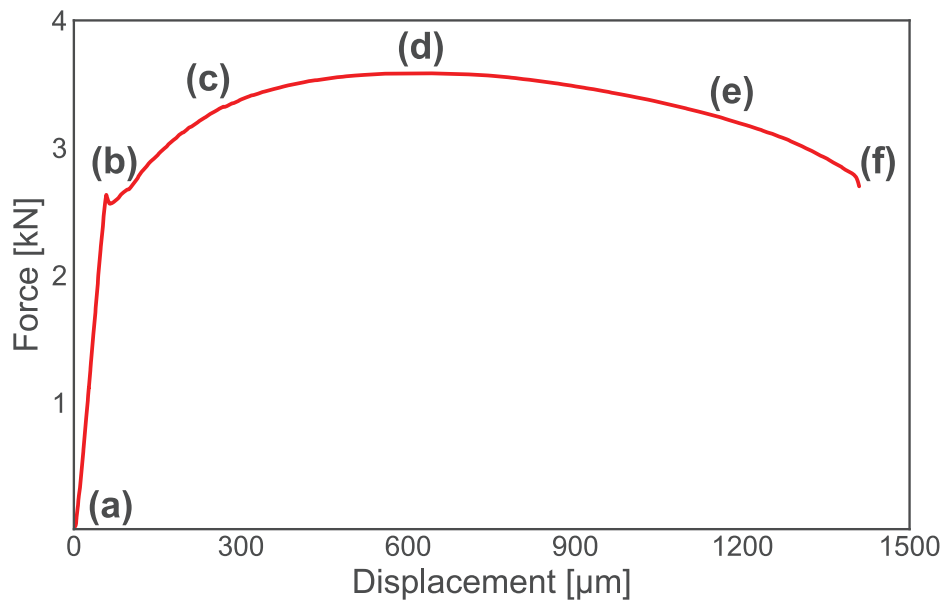


**Figure 6.2:** Measured force–displacement curve for the etched specimen during an *in-situ* SEM tensile test. The labels (a)–(f) are related to the micrographs in Figures 6.3 and 6.4.

Figure 6.3 shows the evolution of the microstructure during the tensile test, where Figure 6.3(a) reveals the undeformed microstructure. At the yield point (Fig-

ure 6.3(b)), there is very little difference from the undeformed microstructure, but in Figure 6.3(c) it is possible to see that some topography has started to evolve. Slip lines start to appear in Figure 6.3(d), i.e., at the maximum force. More and more slip lines and topography evolution can be seen in Figure 6.3(d)–6.3(f). During loading, the frames are also getting darker in some areas and whiter in others. This is an effect of the microscope. The reason for the frames getting darker is that the incoming electrons from the SEM contaminates the specimen surface, while the white areas are due to the topography contrast nature of SE imaging.

The strain field from the DIC measurements are shown in Figure 6.4. Here are the same micrographs as in Figure 6.3, but now with the strain field from the DIC measurements superimposed. When comparing Figures 6.3 and 6.4, it is seen that the straining takes place mostly within the soft ferrite, while the hard pearlite appears as less deformed islands within the microstructure. Another observation is that the maximum local strain, measured at element level close to fracture, is more than  $\varepsilon_{DIC} = 2.1$ . The corresponding average engineering strain across the recorded area was measured to be  $\bar{\varepsilon}_{DIC} = 0.86$ , using several virtual extensometers (vectors) in the DIC software with an initial length of 80  $\mu\text{m}$ . The deformation bands seen in Figure 6.4(c)–6.4(f) are oriented at an angle to the tensile direction, and the most heavily deformed bands seem to be oriented at about  $45^\circ$ . This is consistent with the results of, e.g., Ghadbeigi et al. [40]. Initially, the deformation takes place in the soft ferrite, as seen in Figure 6.4(b). Then, bands start to form in Figure 6.4(c) during the work-hardening stage. After the formation of these bands, nearly all subsequent deformation takes place inside the localized zones. Next to the heavily deformed bands, there is little deformation. Some places these bands cut through pearlite grains, but for the most part, the less deformed (blue) regions in the strain field are pearlite grains.

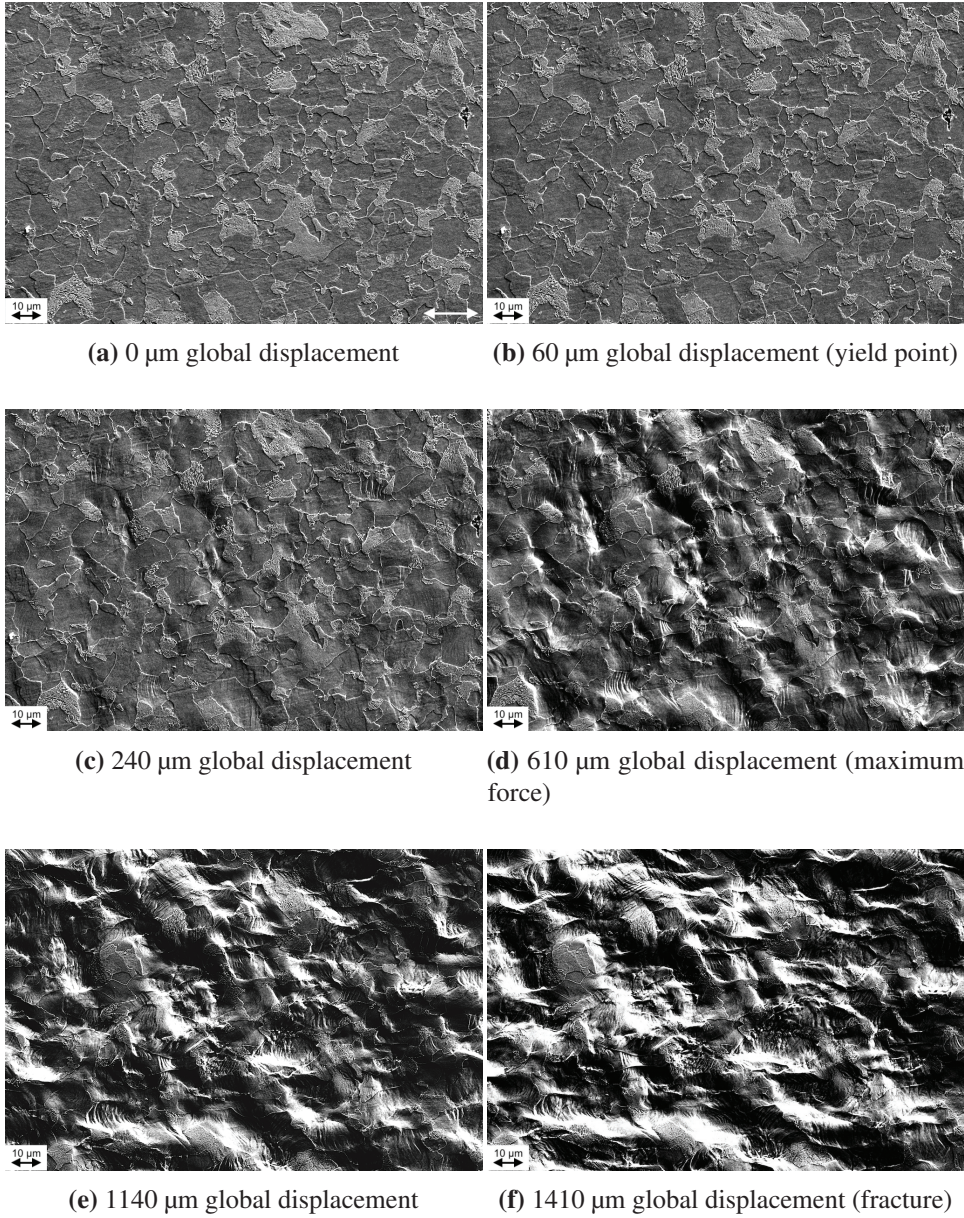


**Figure 6.3:** Micrographs at different displacements in the etched specimen. (a)–(f) The micrographs relate to the force–displacement curve in Figure 6.2. The pulling direction for the *in-situ* SEM tensile test is indicated in the bottom right in (a).



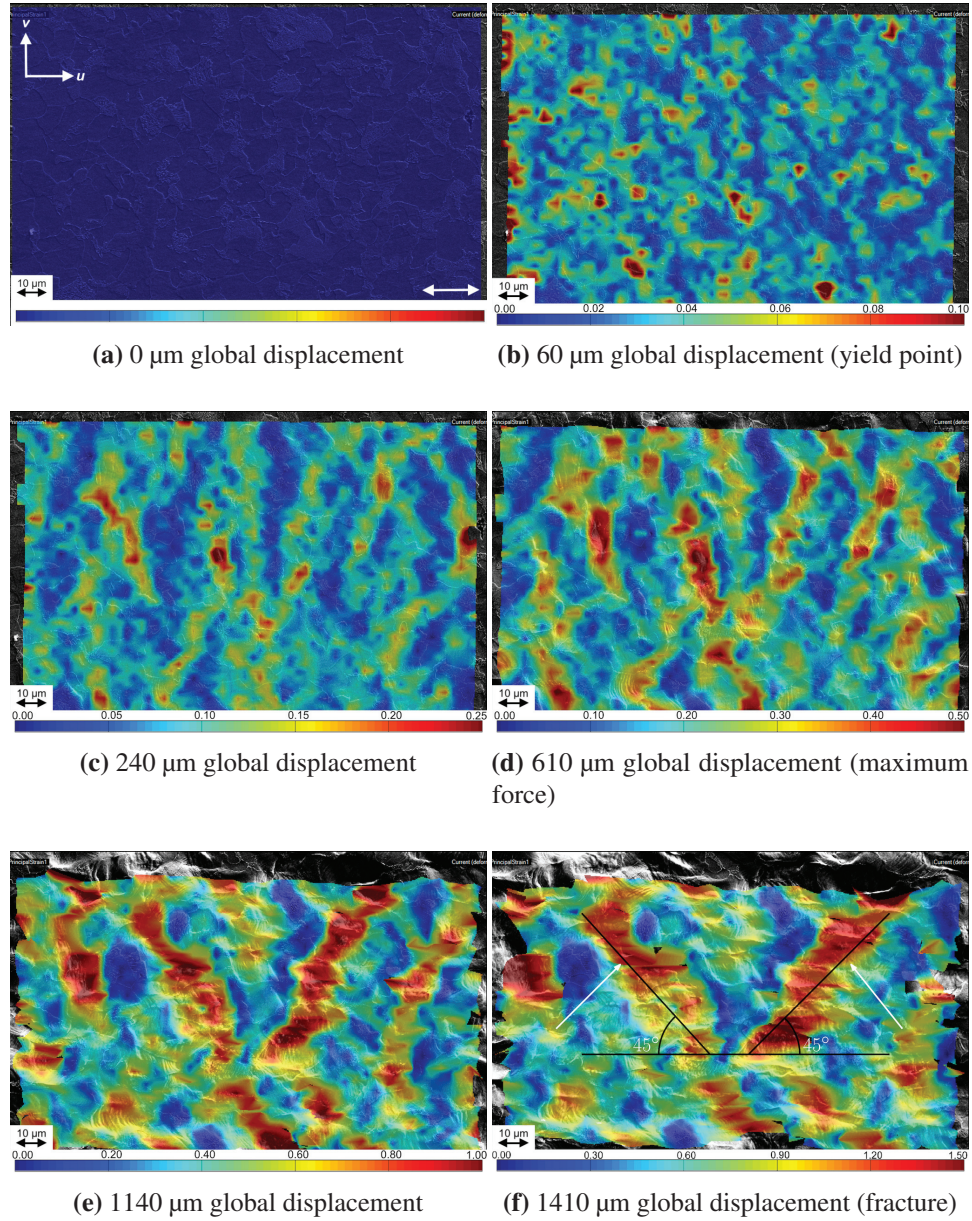


**Figure 6.4:** Micrographs with the measured strain field superimposed at different global displacements in the notched specimen. (a)–(f) The strain maps relate to the force–displacement curve in Figure 6.2. The white arrows in (f) indicate the deformation bands discussed in Figure 6.5. The pulling direction for the *in-situ* SEM tensile test is indicated in the bottom right in (a). The fringe colors give values of the major principle strain.

Figure 6.5 shows the evolution of local engineering strains in pearlite versus ferrite grains as compared to the average engineering strain over the recorded area. As observed on the etched microstructure in Figure 6.4, the harder pearlite deforms less than the softer ferrite. When  $\bar{\epsilon}_{DIC} = 0.86$  (i.e., the average engineering strain over the recorded area at fracture), the local engineering strain in the pearlite and ferrite grains were  $\bar{\epsilon}_{DIC} = 0.39$  and  $\bar{\epsilon}_{DIC} = 0.90$ , respectively. Both of these strain measures exhibit a rather linear relationship with the average engineering strain over the recorded area, but the spread is significant. In contrast, the heavily deformed bands seem to accommodate more and more of the deformation, especially after the ultimate tensile strength (UTS).

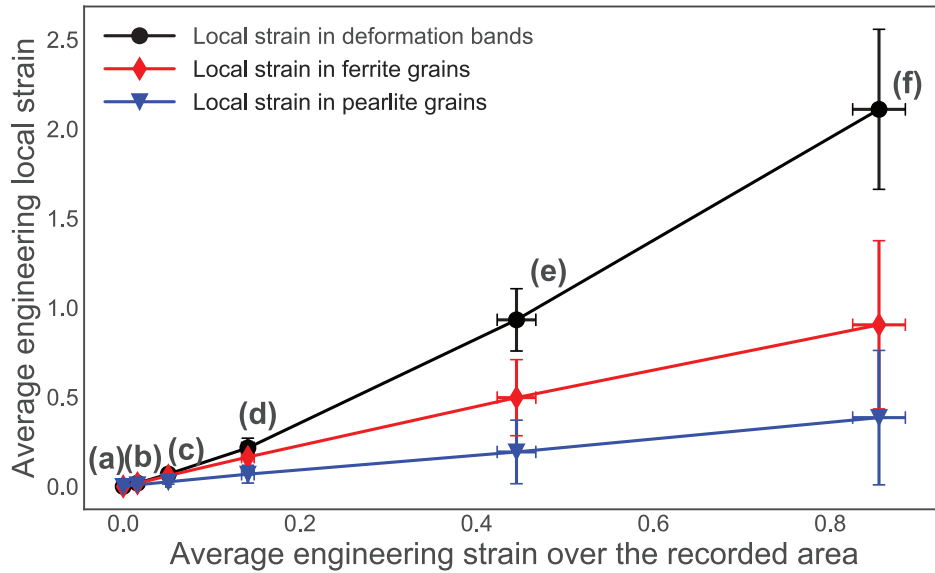


**Figure 6.5:** Local strain evolution in pearlite and ferrite grains and the localized deformation bands marked in Figure 6.4(f). The grains selected for the local strain measurements are indicated with blue squares and red diamonds in Figure 6.6(a) for pearlite and ferrite, respectively. The average engineering strain over the recorded area are measured using the vectors in Figure 6.6(b).

All values in Figure 6.5 were acquired using virtual extensometers in the DIC software. The grains selected for measuring local strain in ferrite and pearlite are marked in Figure 6.6(a), while the virtual extensometers for the average engineering strain across the recorded area are shown in Figure 6.6(b). In addition, the average value of the local engineering strain across the two deformation bands marked with white arrows in Figure 6.4(f) is extracted and plotted in Figure 6.5. This is done by placing ten virtual extensometers across the length of each band. From this, it

is seen that more and more local strain is accumulated in these bands and that the slope of this curve increases with increasing average engineering strain over the recorded area. It is also worth noting that the error bars in Figure 6.5 represent the standard deviation of the average strains measured and that the amount of variation in the measurements is seen as high.

In an attempt to validate the experimental results of the *in-situ* SEM measurements, two types of tests on an unstrained specimen were also conducted. First, a series of images without any pulling was recorded with the same acquisition settings as in the *in-situ* SEM tensile test, before being uploaded to the DIC software and analyzed. Due to the gray-scale pixel noise, a fictitious strain of about 1.5% was registered. This method is similar to the test performed by Buljac et al. [34]. However, they registered an error of 0.3% in a DVC analysis, compared to 1.5% in this DIC analysis. Second, a test with the same setup as in the *in-situ* SEM tensile test, where the specimen was only fixed at one end and then continuously pulled by the movable ramp (see Figure 3.1), was conducted. This rigid body movement should not impose any strain in the specimen. However, since the microscope loaded the images row-by-row, the last row of pixels was slightly shifted compared to the first row in the image due to the continuous recording. This resulted in a measured constant strain of roughly 3% by the DIC software. These strains are unphysical and should be accounted for. Note that the magnitude of the latter error is a function of exposure time and applied displacement rate during testing, which in this experiment were, respectively, 6 s and 0.2  $\mu\text{m/s}$ .

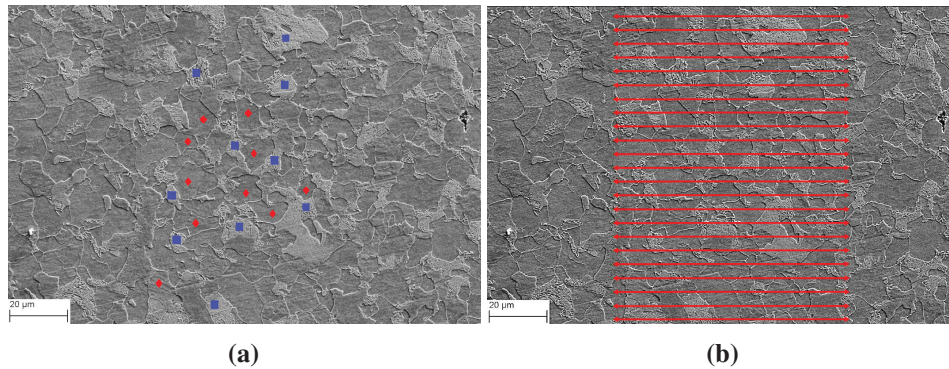


**Figure 6.6:** (a) Grains used for local strain measurements in Figure 6.5, where the blue squares are pearlite grains and the red diamonds are ferrite grains. (b) Vectors used as virtual extensometer for the average engineering strain over the recorded area, having an initial length of 80  $\mu\text{m}$ .

### 6.3 Experimental results on gold speckled specimen

Figure 6.7 shows the evolution of the microstructure during a tensile test using a gold speckled specimen, where Figure 6.7(a) reveals the undeformed microstructure. At the yield point (Figure 6.7(b)), there is very little difference from the undeformed microstructure, but in Figure 6.7(c) it is possible to see that some slip lines have started to appear. Some of these are seen in the white circles. In Figure 6.7(d), i.e., at the maximum force, many slip lines can be seen throughout the microstructure, and the microstructure looks quite deformed. During loading, the frames are also getting darker in a grid pattern. This is an effect of the microscope. The reason for the frames getting darker is that the incoming electrons from the SEM contaminates the specimen surface and it is in a grid pattern since there is an overlapping region being exposed more than the center of each frame. In addition, the middle frame is extra burned due to prolonged exposure between acquisitions.

The DIC results obtained by analyzing the micrographs in Figure 6.7 are shown in Figure 6.8. Large parts of the map are unstrained, while some areas are heavily influenced in narrow bands. Figure 6.9 gives the phase map and the same DIC map as in Figure 6.8(d), but with different scale bar to highlight the undeformed areas. The phase map was created by outlining the NVE36 grains manually from the mapped BSE image. The lamellar structure of NVE36 makes it easy to detect the pearlite and ferrite grains even with the gold coating. By comparing Figure 6.9(a) with Figure 6.9(b), it can be seen that the least strained parts of the microstructure are pearlite grains. In addition, the sharpest bands of strain in the strain field in Figure 6.8(d) are in areas near or on the interface between the two phases. These bands are initially formed at angles close to  $45^\circ$ . Another observation is that the maximum local strain, measured at element level at UTS, is more than  $\varepsilon_{DIC} = 1.4$ . The corresponding average engineering strain across the recorded area was measured to be  $\bar{\varepsilon}_{DIC} = 0.15$ , using several virtual extensometers (vectors) in the DIC software with an initial length of  $80\text{ }\mu\text{m}$ .



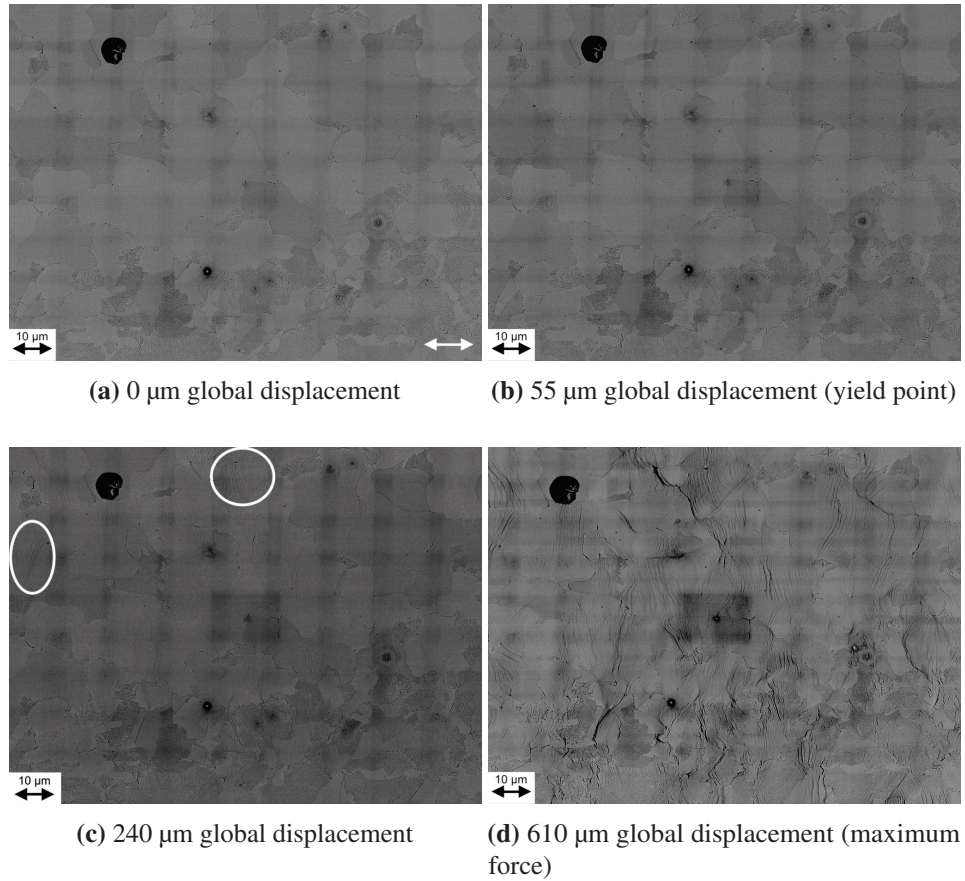


**Figure 6.7:** Stitched BSE images at different displacements in the notched specimen. (a)–(d) The micrographs relate to the force–displacement curve in Figure 6.2. The pulling direction for the *in-situ* SEM tensile test is indicated in the bottom right in (a).



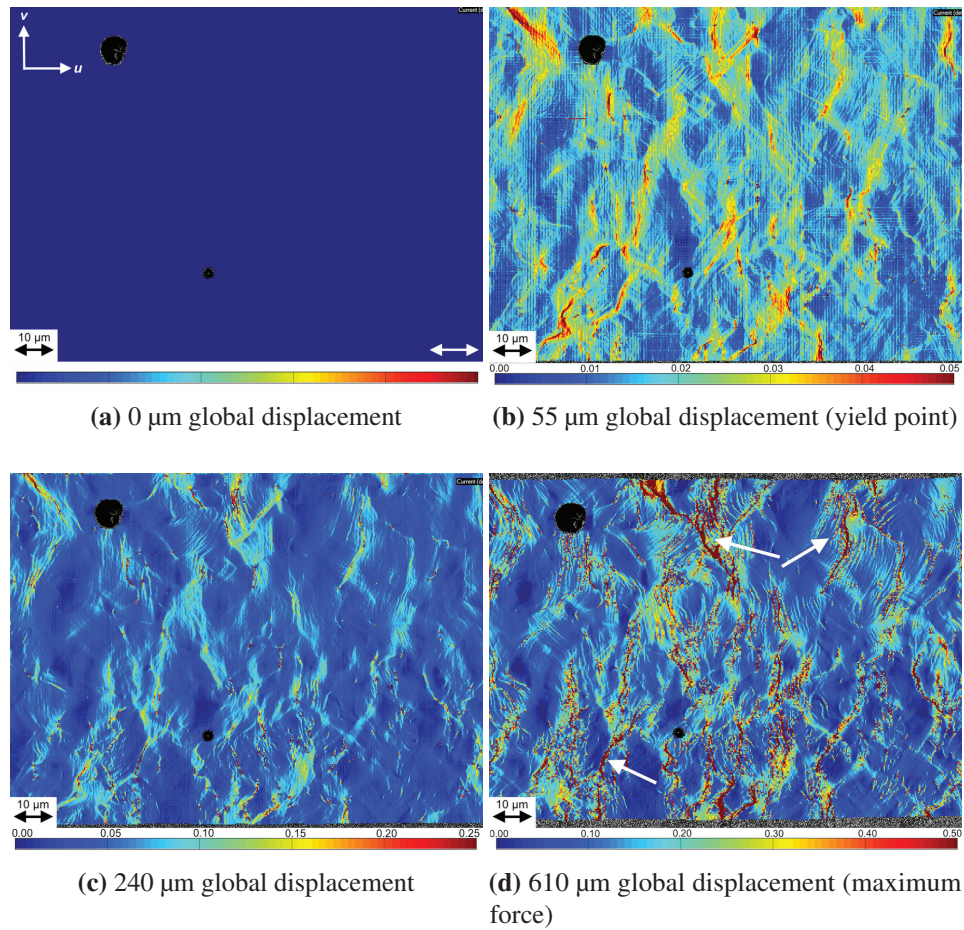


**Figure 6.8:** Measured strain field superimposed on the BSE images from Figure 6.7 at different global displacements in the notched specimen. (a)–(d) The strain maps relate to the force–displacement curve in Figure 6.2. The white arrows in (d) indicate the deformation bands discussed in Figure 6.10. The pulling direction for the *in-situ* SEM tensile test is indicated in the bottom right in (a). The fringe colors give values of the major principle strain.

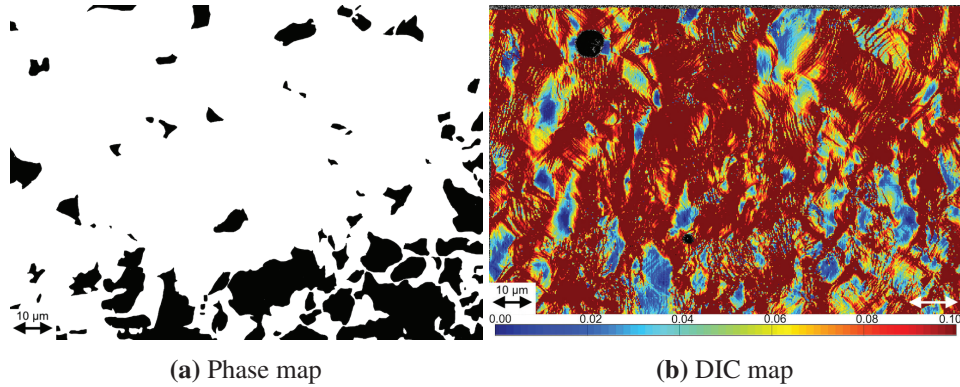


**Figure 6.9:** (a) A phase map of the same area as analyzed with DIC. The pearlitic phase is black and ferrite is white. (b) The same strain map as in Figure 6.8(d) with a lower max value for the color legend. The pulling direction for the *in-situ* SEM tensile test is indicated in the bottom right in (b).

Figure 6.10 shows the evolution of local engineering strains in pearlite versus ferrite grains as compared to the average engineering strain over the recorded area. As expected, the hard pearlite deforms much less than the soft ferrite. When  $\bar{\epsilon}_{DIC} = 0.15$  (i.e., the average engineering strain over the recorded area at UTS), the local engineering strain in the pearlite and ferrite grains were  $\bar{\epsilon}_{DIC} = 0.07$  and  $\bar{\epsilon}_{DIC} = 0.15$ , respectively. Both of these strain measures exhibit a rather linear relationship with the average engineering strain over the recorded area, but the spread is significant. All values in Figure 6.10 were acquired using virtual extensometers in the DIC software. The virtual extensometers for the local engineering strain across the different grains are shown in Figure 6.11(a), while the virtual extensometers for the average engineering strain across the recorded area are shown in Figure 6.11(b).

In addition, the average value of the local engineering strain across the three deformation bands marked with white arrows in Figure 6.8(d) is extracted and plotted in Figure 6.10. In each of the three bands, ten virtual extensometers were placed to measure the average strain across the band. It is shown that more and more local strain is accumulated in these bands and that the slope of this curve increases with increasing average engineering strain over the recorded area.

As for Figure 6.5, the error bars in Figure 6.10 represent the standard deviation of the average strains measured and that the amount of variation in the measurements is as seen higher at larger strains. In addition, the spread is greater in the bands compared to the grains. In contrast to Figure 6.5, Figure 6.10 is only plotted until UTS. The reason for this is that the gold specimen was only recorded to UTS. The damage and topography beyond this point made it impossible to correlate the DIC results.

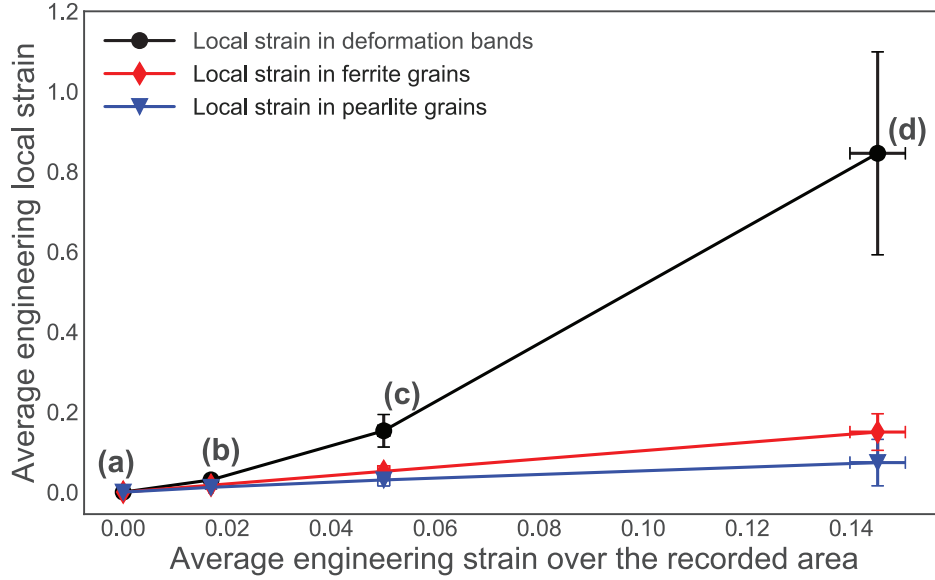


**Figure 6.10:** Local strain evolution in pearlite and ferrite grains and the localized deformation bands marked in Figure 6.8(d). The grains selected for the local strain measurements are indicated with blue squares and red diamonds in Figure 6.11(a) for pearlite and ferrite, respectively. The average engineering strain over the recorded area are measured using the vectors in Figure 6.11(b).

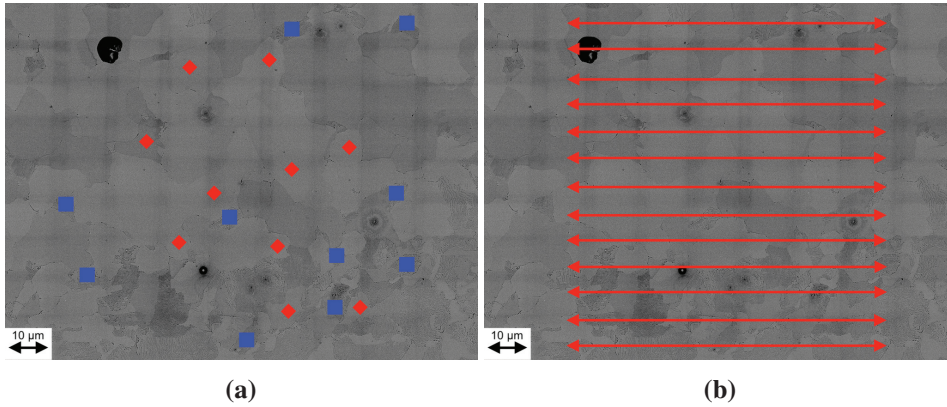


**Figure 6.11:** (a) Grains used for local strain measurements in Figure 6.10, where the blue squares are pearlite grains and the red diamonds are ferrite grains. (b) Vectors used as virtual extensometer for the average engineering strain over the recorded area, having an initial length of 80  $\mu\text{m}$ .

The systematic error was calculated by comparing two images from the same region before deformation. These images were then correlated using the DIC software. From this, a peak strain of 1.5% was observed. The error is introduced by the microscope when acquiring BSE images of the speckle pattern by mapping the region of interest (ROI) and stitching the individual frames together. Although there are some nodes in the correlated, undeformed map recording strains of more than 1%, 99.2% of the nodes record strains less than 0.1%.

Further, the gold speckled specimen was analyzed with a mesh size equal (in  $\mu\text{m}$ ) to the mesh size for the etched specimen. Here, both specimens have a mesh with quadratic element with the size  $2.24 \mu\text{m} \times 2.24 \mu\text{m}$ . This corresponds to  $280 \text{ pixels} \times 280 \text{ pixels}$  and  $30 \text{ pixels} \times 30 \text{ pixels}$  for the gold speckled specimen and etched specimen, respectively. The resulting strain fields are given in Figure 6.12, where Figure 6.12(a) gives the strain field for the etched specimen and Figure 6.12(b) for the gold specimen. Figure 6.12(a) is the same strain field as in Figure 6.4(c). It is worth noting that the area for these images is slightly different. The etched specimen has an area of  $141 \mu\text{m} \times 98 \mu\text{m}$  and the gold speckled specimen has an area of  $114 \mu\text{m} \times 85 \mu\text{m}$ . When comparing the strain maps in Figure 6.12, the patterns in both maps are similar. The bands in both have the same width and the strain levels are on the same scale. A difference between the two maps is that the strain map from the gold speckled specimen has smoother transitions between the deformed and undeformed areas.

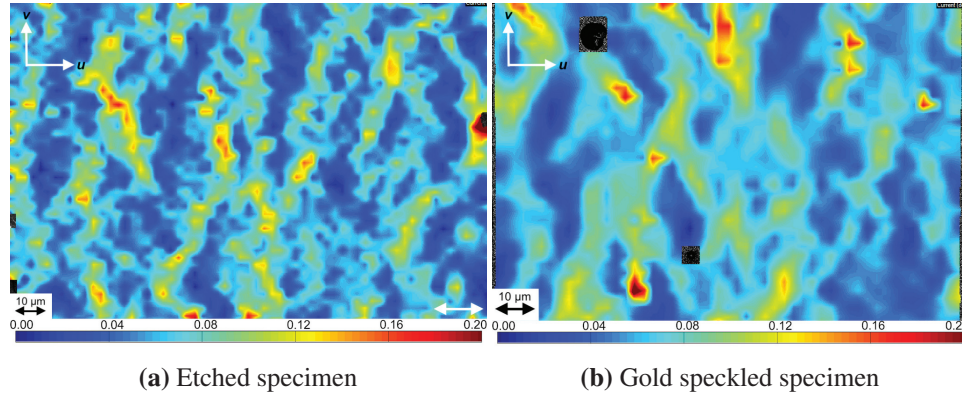


**Figure 6.12:** Comparing the two techniques when having the same mesh size (in  $\mu\text{m}$ ): (a) etched specimen and (b) gold speckled specimen. The pulling direction for the *in-situ* SEM tensile test is indicated in the bottom right in (a).



## 6.4 Discussion

This work demonstrated that it is possible to correlate a continuously recorded microstructure from an *in-situ* SEM tensile test by DIC using the gray-scale values provided by the micrographs imaged with the SE detector. From this, the strain field can be obtained and related to the evolution of the microstructure all the way to fracture. This technique was compared with a specimen covered with gold nanoparticles, which were used as the speckled pattern for DIC during an *in-situ* SEM tensile test. For the gold speckled specimen, images were acquired using the BSE detector and only at key locations on the tensile curve until UTS. In the present study, these techniques were demonstrated on the ferritic-pearlitic steel NVE36.

The resulting strain fields on the etched specimen obtained are similar to the results achieved by, e.g., Ghadbeigi et al. [40] and Tasan et al. [49], displaying localized deformation bands oriented at about  $45^\circ$  with respect to the loading direction (see Figure 6.4). These bands follow a path mostly within the soft ferrite grains, reaching local strain values up to 170% before fracture at a much lower global strain, clearly illustrating the heterogeneity in the deformation of the material. This is in line with the observed results by Banerjee et al. [45], who recorded strain values of 150% inside similar bands at a global strain less than 10%. As for the etched specimen, localized deformation bands were observed to form at  $45^\circ$  with respect to the loading direction (see Figure 6.8) in the gold speckled specimen. This indicates an association with the maximum shear stress locally within grains. Locally, within these bands, strain values of 110% were recorded at UTS, compared to 15% average engineering strain over the recorded area.

When performing the heat treatment to remodel the gold layer in order to obtain a gold speckled pattern, the specimen was kept at  $180^\circ\text{C}$  for 96 hours. To validate the effect of this heat treatment, new tensile tests and a microstructural investigation were conducted. This investigation is explained in further detail in Chapter 4. The grain size, phase composition, and hardness were all measured before and after heat treatment on three different specimens. The results from these investigations are summarized in Table 6.1, and it can be seen that all values for both specimens are within the standard deviation of each other. In Figure 6.13, engineering stress–strain curves from two tensile tests are presented. The curves indicate no difference between the heat-treated tensile curve and the as-received tensile curve. However, this result is not unexpected. The microstructure of NVE36 is decided by the metastable Fe-Fe<sub>3</sub>C phase diagram (see Figure 2.8). As a result, no changes took place in the microstructure during the heat-treating process to remodel the gold layer into the gold speckled pattern for this particular material. Other material can also be considered suitable for this method. These would typically be materials designed for

use at elevated temperatures, e.g., nickel alloys, duplex steels, austenitic steels, etc. However, this would not be the case for all materials. As an example, for aluminum alloys, the age hardening might take place at temperatures between 100 °C and 150 °C. If left at 180 °C for 96 hours, an overaged material would be the result [106]. In addition, in some cases, tempering of martensite occurs at temperatures of 200 °C [83]. In general, the remodeling method would benefit by reducing the remodeling temperature and remodeling time to increase versatility.

**Table 6.1:** Hardness, grain size and phase composition measured before and after heat treatment.

Variable	Ferrite	Pearlite	Ferrite	Pearlite
	Before		After	
Phase composition	75 ± 19% ferrite		74 ± 16% ferrite	
Hardness [HV]	204 ± 23	283 ± 27	188 ± 29	306 ± 39
Grain size [μm]	15.5 ± 3.1	12 ± 2.1	16 ± 2.5	11 ± 1.1

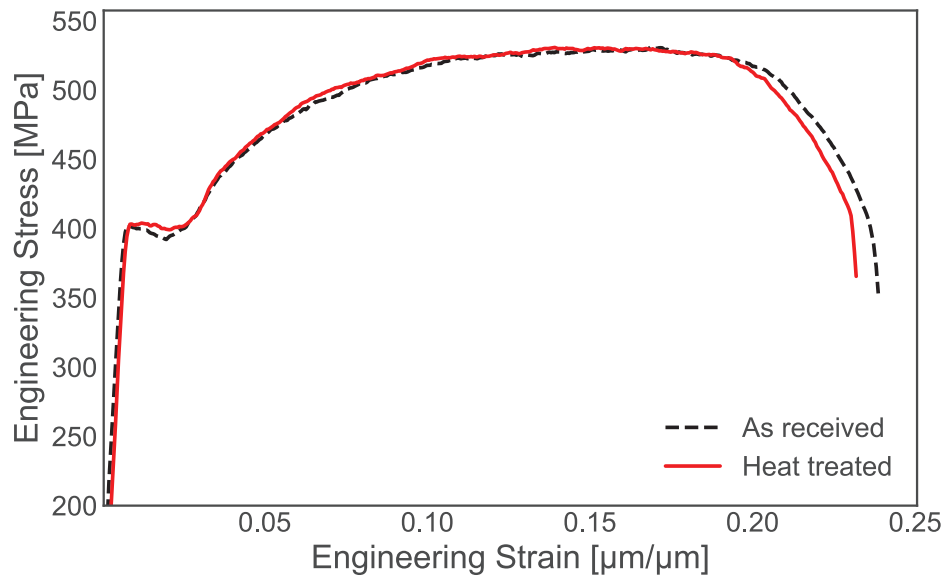


**Figure 6.13:** The tensile test curve of the heat treated and as received specimen.

During image acquisition, both the etched specimen and the gold speckled specimen were contaminated by the incoming electrons. In the etched specimen, this results in a gradually darker surface. To overcome this, the reference image in the DIC algorithm was updated several times. The result is an accumulation of errors, as

discussed in Tang et al. [69]. For the gold specimen, the contamination resulted in a grid pattern due to the overlapping area during the image acquisition. When studying the overlapping area, it was seen that the intensity of gold speckles are faded. However, from the strain field no apparent changes were observed. The amount of contamination is related to the amount of electrons impacting the surface (i.e., accelerating voltage and aperture size) and absorbed current by the microscope. By reducing the accelerating voltage and aperture size and increasing conductivity between specimen and *in-situ* tensile stage, and *in-situ* tensile stage and microscope stage, the contamination would be reduced.

When studying the strain fields in Figure 6.4 and the plots in Figure 6.5, the local strain evolution can be investigated at grain level. The localized deformation initiates in the soft ferrite grains, as seen in Figure 6.4(b). Then, distinct bands of localized strain are formed, which mostly consists of ferrite grains, but occasionally propagate through hard pearlite grains. When the deformation continues to increase, the intensity of the localized strain inside the bands leads to more inhomogeneous plastic flow and unloading of the material outside the bands. In addition, the formation of slip lines was observed, and some of the ferrite grains experienced significant plastic deformation, also activating secondary slip systems. Conversely, some pearlite grains are hardly strained at all having an average engineering strain  $\bar{\epsilon}_{DIC}$  less than 10% at fracture. Figure 6.4 also confirms that most of the undeformed regions consist of pearlite grains. A few of these grains (situated in the localized strain bands) experienced some slip activity, but no secondary slip systems were observed in this phase. Figure 6.3 shows the large deformation experienced by the microstructure. From these surface observations, few damage sites were detected, and no void growth could be seen. However, as shown by Maire et al. [139] on dual-phase steel revealing the initiation and growth of damage observed by X-ray microtomography, the void volume fraction is much higher in the center of the specimen where the stress triaxiality is maximum compared to the surface. Such void growth is also well-known from ductile damage mechanics (see, e.g., [140]). This may also explain why the specimen fractured abruptly, with seemingly few damage sites, since a macrocrack might have propagated from below the surface, leading to the final fracture.

In the *in-situ* SEM tensile test with the etched specimen, it was hard to get any meaningful results from the strain maps during the initial stage of the test, i.e., at low strains in the elastic region. This is related to the level of noise in the recorded micrographs. To be able to record a continuous *in-situ* tensile test in the SEM, the exposure time for each micrograph has to be low. Conversely, if the time spent to acquire each micrograph is long compared to the applied displacement rate, the recorded area will move during the imaging. As a result, the final line in the

line-scan moved  $1.2\ \mu\text{m}$  in the pulling direction compared to the first line. This can, at least to a certain degree, be compensated for with a lower applied displacement rate in the test. In the current experimental set-up, the applied displacement rate was  $0.2\ \mu\text{m/s}$ , and the frame rate was 6 s. Thus, the ratio between the applied displacement rate and the frame rate has to be sufficiently low, leaving enough time to acquire good quality micrographs, but high enough to avoid unwanted effects from the low applied displacement rate. In the *in-situ* SEM tensile test on the gold-coated specimen, this issue was resolved by increasing the acquisition time. Here, a snapshot of the current state of the material is seen with slip lines and shear bands forming. Conversely, for the gold speckled specimen, high-quality images were acquired at the desired strain level. The resulting DIC maps achieve an excellent spatial resolution, but the image acquisition time is long. As a result, a strain map was not obtained throughout the tensile test, but at a few selected locations on the tensile curve. In addition, the images acquired for the gold speckled specimen were acquired by mapping the surface frame by frame and then stitching all frames into the ROI. To obtain the best results possible, a very precise stage is required. Ideally, this should be a piezoelectric stage as they have superior precision when the stage moves between each frame acquired. The mechanical stage used here has a precision of  $1\ \mu\text{m}$ . However, new piezoelectric stages are 500–1000 times more precise [141].

Figure 6.14 compares the local strain evolution of techniques used on the specimens tested here. It can be seen that the behavior of the grains and local average strain for both techniques captures the same behavior for the pearlite and ferrite grains. However, in the deformation bands, there is a clear difference. The maximum principal strain at UTS was found to be 325% higher in the gold speckled specimen than in the etched specimen. Haltom et al. [142] reported similar differences based on microscopic and macroscopic strain measurements in an aluminum alloy. From the *in-situ* SEM strain maps, it is readily observed where and in which type of grain strain localization takes place, and at what time this occurs during the deformation process. It is also straightforward to relate these measurements to the applied force or stress magnitude. Moreover, the technique can be further developed by investigating other materials, such as quasi-brittle alloys at various temperatures where fracture is essential.



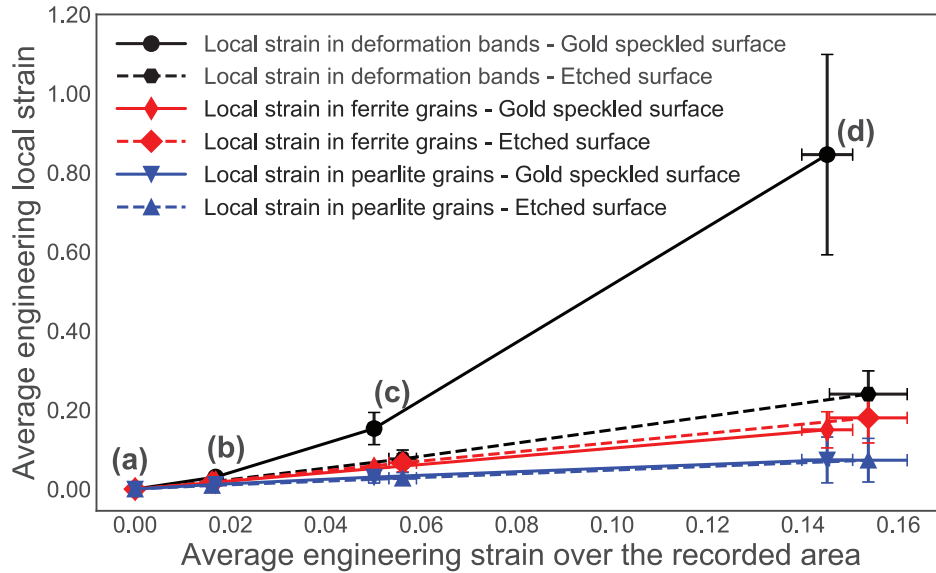


**Figure 6.14:** The local strain evolution in Figures 6.5 and 6.10 plotted together until UTS.

## 6.5 Concluding remarks

In this study, the differences between two specimen preparation methods for DIC on images acquired in an SEM have been demonstrated on the two-phased ferritic-pearlitic steel NVE36. The gold speckled specimen has a significantly higher spatial resolution, and, as a consequence, more local deformation is captured. In addition, if local information is required at the early stages of deformation, the gold speckled specimen is the preferred method. Conversely, the images from the etched specimen surface contain more noise, and in the first stages of deformation less local information is captured. As a consequence of the lack of contrast for the DIC analysis, the etched specimen is not able to resolve strains within grains. However, the advantages of using an etched surface are that no heating of the specimen and fewer steps are required to obtain the strain field. In addition, continuous recordings of the strain field are particularly important when studying localization and fracture, which may occur abruptly. As a conclusion, the method with gold speckles is only required when a fine spatial resolution is necessary to obtain results at only certain stages of the tensile curve.

The gold speckled specimen gives more detail and higher accuracy compared to the etched specimen. Local strain bands are found to be more narrow and more heavily deformed using this approach. However, with the gold speckled specimen, only a few snapshots throughout the tensile test are acquired, and after UTS the

topography on the surface makes the image acquisition more challenging. This is a consequence of acquiring BSE images. For the etched specimen, images are captured continuously through the test. When performing a DIC analysis on the gold speckled specimen with a mesh size (in  $\mu\text{m}$ ) equal to the etched specimen, the results are close to identical. The differences between the two techniques are specimen preparation, image acquisition, acquisition time, DIC quality, DIC resolution, and the number of strain fields available throughout the stress–strain curve. The technique to be chosen will mainly depend on the material, and the spatial resolution required.



## Chapter 7

# A numerical study of NVE36

In this Chapter, tensile tests recorded with digital image correlation (DIC) were first conducted on both *in-situ* specimen geometries in Figure 3.2 using high-resolution digital cameras (5120 pixels  $\times$  3840 pixels). These tests were carried out in air, in contrast to in a vacuum chamber as in the scanning electron microscope (SEM) tensile tests. A specimen with a smooth geometry was also tested to identify the material constants used in subsequent numerical simulations. Then a specimen with a notched geometry was tested. The resulting strain fields from both the smooth and notched specimen was compared with numerical finite element (FE) simulations. The simulated strain fields compare reasonably well with the measured strain fields using DIC in tensile tests outside the SEM. However, local variations and heterogeneous deformation were not captured. The force-displacement curves for both smooth and notched specimens are also found to be in good agreement between the tests and simulations until necking. After necking there is a steeper drop in force in the simulated curve compared to the experimental curve.

### 7.1 Tensile tests recorded with a macro lens

#### 7.1.1 Experimental setup

Tensile tests were carried out in air using the *in-situ* tensile test device to get the macroscopic strain fields. The tensile tests were recorded using high-resolution digital cameras (5120 pixels  $\times$  3840 pixels). As a result, the spatial resolution of the DIC mesh was 47  $\mu\text{m}$ , compared to 2.24  $\mu\text{m}$  and 0.096  $\mu\text{m}$  obtained in the microscopic strain fields in Chapter 6. One distinct difference between the *in-situ* SEM tensile tests and the tensile tests conducted in air, is that the *in-situ* SEM tensile test was carried out with an applied displacement rate of 0.2  $\mu\text{m/s}$ , while the

test conducted in air was performed using an applied displacement rate of 1  $\mu\text{m/s}$ . Even so, the resulting force-displacement curves were nearly identical, which was expected because both loading rates may be considered quasi-static.

First, the smooth specimen shown in Figure 3.2(a) was tested. This test was mainly done to get data for the identification of material constants required for the subsequent numerical simulations. Second, the notched specimen given in Figure 3.2(b) was tested. Finally, the strain fields of the notched specimen are compared to numerical FE simulations of a notched specimen based on the material constants obtained from the smooth specimen.

### 7.1.2 Experimental results

The force-displacement curve (and the corresponding engineering stress-strain curve) from the smooth specimen test carried out in air is shown in Figure 7.1. The engineering stress  $s$  and the engineering strain  $e$  were obtained from the measured force  $F$  and elongation  $\Delta L$  as

$$s = F/A_0, \quad e = \Delta L/L_0 \quad (7.1)$$

where  $A_0$  is the initial cross-section area and  $L_0$  is the initial length of the specimen's gauge area. For further details, see Chapter 2.4. At yielding, the material starts exhibiting Lüders bands that propagate throughout the gauge area of the specimen, causing a distinct yield plateau with a constant yield stress of  $s_0 = 333$  MPa. After passing of the Lüders bands, which were captured by the DIC software, the stress continues to increase due to work hardening caused by plastic deformation. Diffuse necking occurred at an ultimate engineering stress  $s_u = 467$  MPa and engineering strain  $e_u = 0.21$ , while fracture occurred at a global engineering strain of  $e_f = 0.41$  (see Figure 7.1). The engineering strain measured using a virtual extensometer in the DIC code with an initial length of 5500  $\mu\text{m}$  gave an average fracture strain of  $e_{DIC} = 0.55$ , while the highest major principal strain recorded locally was  $\varepsilon_{DIC} = 1.5$  (measured at element level). NVE36 typically has an engineering strain at fracture in the order of 20-25% [122], but here it is reported to be 41%. This difference is due to the short gauge length and size effects [13].

Figure 7.2 shows the evolution of the strain field in the smooth specimen from the onset of diffuse necking until fracture. In Figure 7.2, it is possible to spot bands with high strains relative to the rest of the specimen. These bands tend to orient themselves  $45^\circ$  to the pulling direction of the specimen. A similar tendency is also seen at the microstructural level in Figure 6.4 and Figure 6.8. This second instability in the uniaxial tensile test of specimens having a rectangular cross-section is termed localized necking and is well known from the literature (see, e.g., [13, 40]).

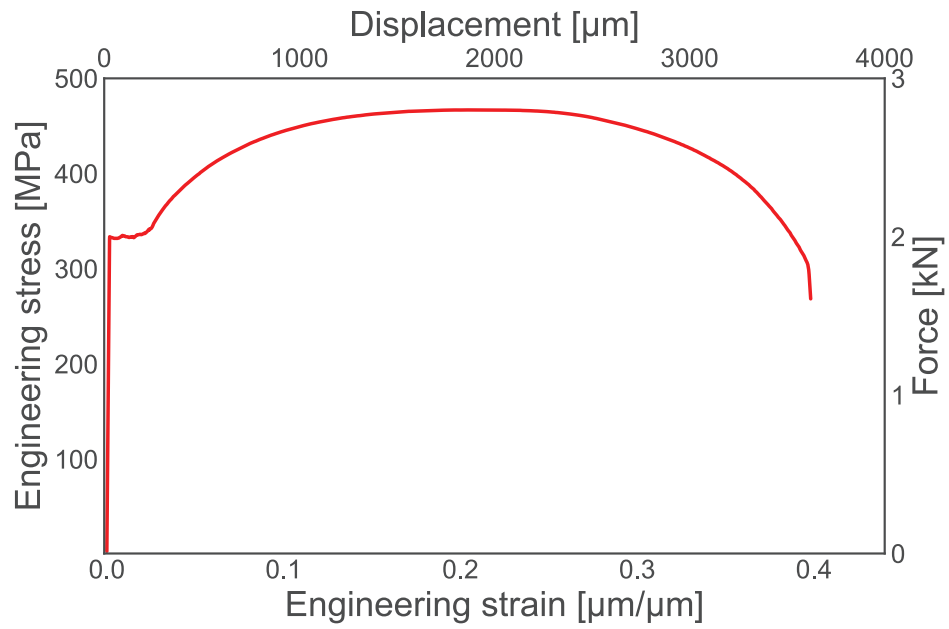


**Figure 7.1:** Measured engineering stress-strain curve for the smooth specimen, recorded by the *in-situ* SEM device during tensile testing in air.

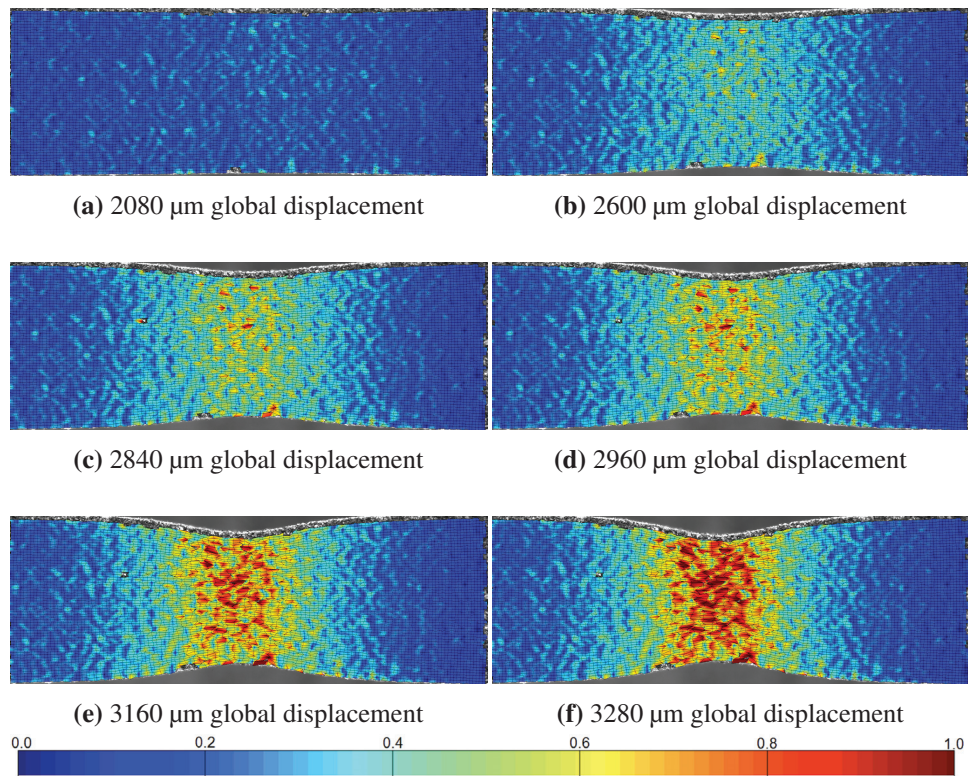


**Figure 7.2:** Measured strain field in smooth specimen tested in air from diffuse necking until fracture. In all frames, the pulling direction is from right to left. The fringe colors give values of the major principle strain.

The measured force-displacement curve for the notched specimen recorded at macro-level was equivalent to the corresponding curve from the *in-situ* SEM tensile test shown in Figure 6.2. At the yield point, labeled **(b)** in Figure 6.2, Lüders bands were captured by the DIC software, and these are displayed in Figure 7.3. Note that due to the extreme resolution of the digital camera applied in this test, local variations in the strain fields are captured. The Lüders bands started to propagate from the center of the specimen, against the pulling direction, before they changed direction and started to propagate in the opposite direction. After the Lüders bands have propagated, work-hardening took place, and the deformation localized in the center of the notch, as seen from the measured strain fields in Figure 7.4.

For this experimental setup, fracture occurred at a measured local peak strain of  $\varepsilon_{DIC} = 1.25$  at the element level, while the average engineering strain across the recorded area was  $e_{DIC} = 0.28$ . The latter was obtained using a virtual extensometer in the DIC code with an initial length of 3000  $\mu\text{m}$ . These values are as seen significantly lower than those of  $\varepsilon_{DIC} = 1.6$  and  $e_{DIC} = 0.92$  obtained at micro-level in the *in-situ* SEM tensile test on the etched specimen. However, it is important to realize that the average engineering strains were obtained using different initial lengths of the virtual extensometer in the DIC code (80  $\mu\text{m}$  versus 3000  $\mu\text{m}$ ), so a direct comparison of the engineering strains is not possible.



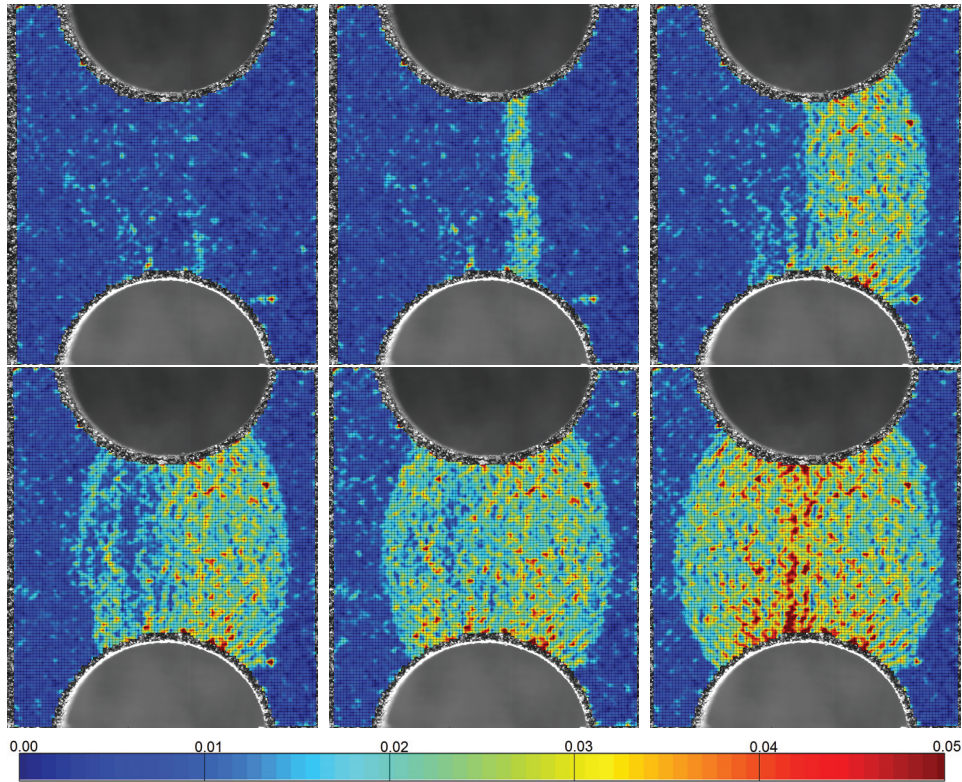


**Figure 7.3:** Propagation of Lüders bands during the tensile test in air for the notched sample. In all frames, the pulling direction is from right to left. The fringe colors give values of the major principle strain in the range  $0 \leq \varepsilon_{DIC} \leq 0.05$

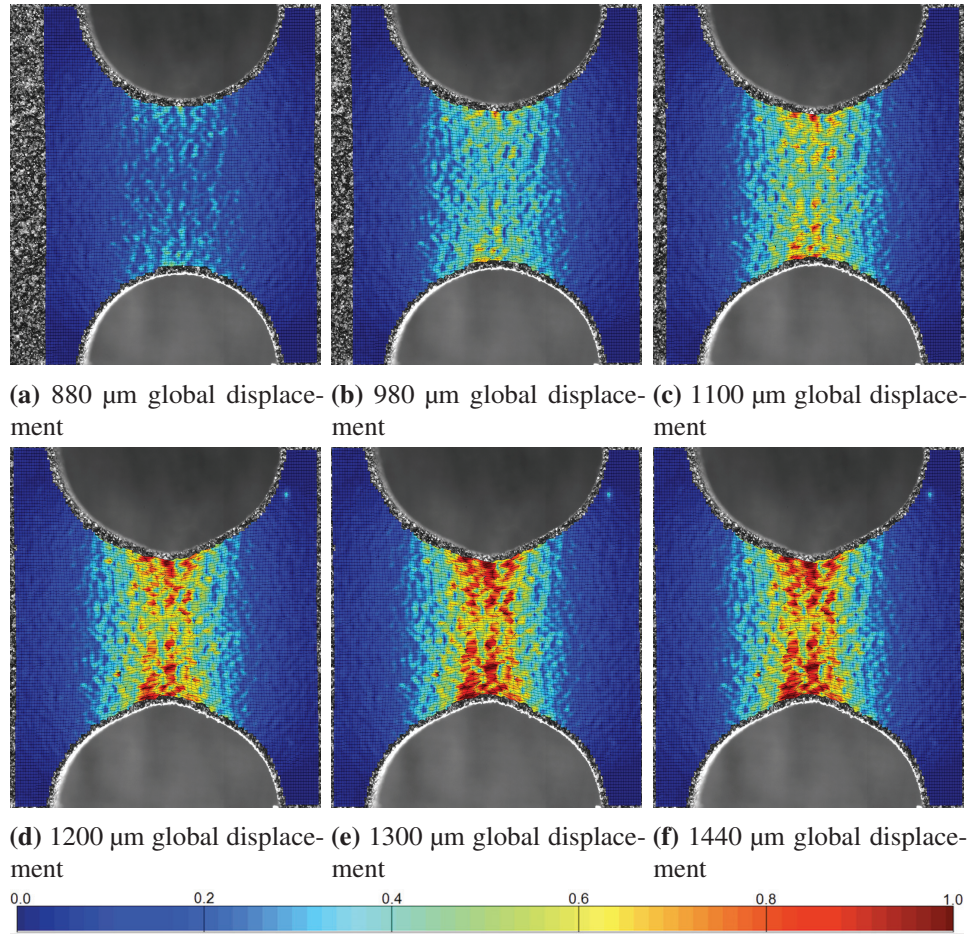


**Figure 7.4:** Measured strain field in notched specimen tested in air until fracture. In all frames, the pulling direction is from right to left. The fringe colors give values of the major principle strain in the range  $0 \leq \varepsilon_{DIC} \leq 1.0$

## 7.2 Numerical simulations

### 7.2.1 Constitutive relation

The material was modeled with an elastic-thermoviscoplastic constitutive relation that incorporated linear elasticity, the von Mises yield criterion, the associated flow rule, Voce non-linear isotropic hardening, strain-rate hardening, and thermal softening due to adiabatic heating. This equation is explained in greater detail in Chapter 2.5.1. The equivalent stress  $\sigma_{eq}$  is defined as [103]

$$\sigma_{eq} = \begin{cases} \sigma_0 & \text{for } p \leq p_0 \\ \left[ \sigma_0 + \sum_{i=1}^2 Q_i \left( 1 - \exp \left( -\frac{\theta_i}{Q_i} (p - p_0) \right) \right) \right] (1 + \dot{p}^*)^C (1 - T^{*m}) & \text{for } p > p_0 \end{cases} \quad (7.2)$$

where  $\sigma_0$  is the yield stress,  $Q_i$  and  $\theta_i$  ( $i = 1, 2$ ) are the Voce hardening constants,  $p$  is the equivalent plastic strain,  $p_0$  is the value of  $p$  at the end of the yield plateau,  $\dot{p}^* = \dot{p}/\dot{p}_0$  where  $\dot{p}$  is the equivalent plastic strain rate and  $\dot{p}_0$  is a reference strain rate,  $C$  is the strain-rate sensitivity constant,  $T^* = (T - T_r) / (T_m - T_r)$  is the homologous temperature where  $T$  is the ambient temperature,  $T_r$  is the room temperature and  $T_m$  is the melting temperature of the material, respectively, and  $m$  is an exponent defining the thermal softening. Based on plastic dissipation the temperature increment under adiabatic conditions can be estimated as

$$\Delta T = \int_0^p \beta \frac{\sigma_{eq} dp}{\rho c_\varepsilon} \quad (7.3)$$

where  $\rho$  is the density,  $c_\varepsilon$  the specific heat of the material and  $\beta$  is the Taylor-Quinney coefficient (often taken as  $\beta = 0.9$  in numerical simulations of adiabatic processes). In this study, isothermal conditions are assumed and  $\beta = 0$  in all simulations. Furthermore, fracture is not considered in the following simulations, so a ductile failure criterion is not applied.

### 7.2.2 Identification of material constants

To identify the material parameters for the constitutive relation given in Equation 7.2, the experimental results from the smooth specimen tensile test conducted in air and shown in Figure 7.2 were applied. Assuming small elastic strains compared to the plastic strains, in addition to plastic incompressibility, the true (Cauchy) stress and the true (logarithmic) strain can be calculated based on the obtained engineering values until diffuse necking (i.e.,  $e_u = 0.21$ ) as [13]

$$\sigma_t = s(1 + e), \quad \varepsilon_t = \ln(1 + e) \quad (7.4)$$

where the true plastic strain is found as  $\varepsilon_t^p = \varepsilon_t - \sigma_t/E$ , and  $E$  is Young's modulus. Since  $\sigma_t = \sigma_{eq}$  and  $\varepsilon_t^p = p$  until diffuse necking in a uniaxial tension test, the material parameters  $(\sigma_0, Q_i, \theta_i, p_0)$  in Equation 7.2 were fitted to the true stress-strain data in order to obtain a best possible fit using the method of least squares. A comparison of the measured true stress-plastic strain curve until necking to the fitted curve using the material parameters listed in Table 7.1 is shown in Figure 7.5. The remaining constants  $(E, v, \rho, \dot{p}_0, C, m)$  in Equation 7.2, also given in Table 7.1, were taken from the literature [143, 144]. The agreement between measured and fitted data is as expected excellent.

**Table 7.1:** Material parameters used in the simulations of the material test.

$E$ [GPa]	$v$ [-]	$\rho$ [kg/m <sup>3</sup> ]	$\sigma_0$ [MPa]	$Q_1$ [MPa]	$\theta_1$ [MPa]	$Q_2$ [MPa]	$\theta_2$ [MPa]	$p_0$ [-]	$\dot{p}_0$ [1/s]	$C$ [-]	$\beta$ [-]	$m$ [-]
210	0.3	7850	381.9	35.4	1729	269.4	2211	0.02	$5 \times 10^{-4}$	0.001	0	1

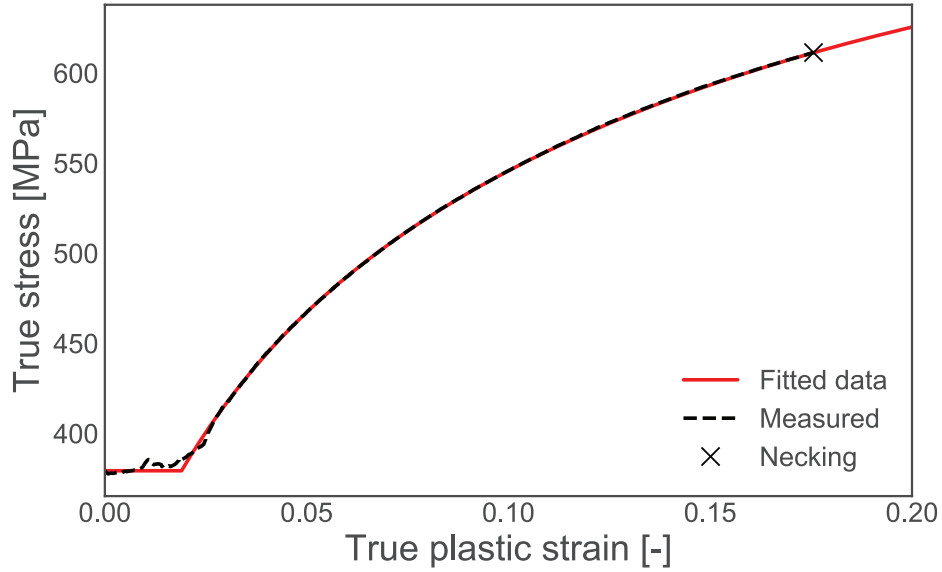


**Figure 7.5:** Measured versus fitted true stress–plastic strain curves.

### 7.2.3 Numerical model

Numerical simulations of the smooth and notched tensile tests presented in Chapter 7.1.2 were performed using the explicit solver of the non-linear FE code LS-DYNA [145]. Mass scaling was applied to scale the stable time step, and it was checked that the kinetic energy remained negligible compared with the internal energy of the samples during the deformation process. A fixed mesh of 8-node 3D solid elements with one-point integration and stiffness-based hourglass control was used in both models, while contact was established using an automatic node-to-surface algorithm in LS-DYNA. The material was modeled using the constitutive relation in Equation 7.2 with the parameters listed in Table 7.1, while the fixtures were modeled as rigid. Since the constitutive relation is not available in standard LS-DYNA, it was implemented as a user-defined subroutine (UMAT) using a semi-implicit return-map algorithm with a sub-stepping scheme to ensure stability and accuracy of the computations. The loading was defined by prescribing a constant velocity at one end of the specimen (giving an initial strain rate similar to the one in the tests), while the other end was fixed. To reduce elastic oscillations due to an instantaneous loading, the velocity was imposed on the specimen using a cosine function with a rise time of approximately 10% of the termination time. After that, the velocity was kept constant until the termination time was reached.

Figure 7.6 shows the geometry and the mesh of the smooth and notched specimens, respectively. The smooth specimen has an element size in the gauge area of  $75\text{ }\mu\text{m} \times 75\text{ }\mu\text{m} \times 200\text{ }\mu\text{m}$  in the x, y and z-direction, respectively, where x is the pulling direction and z the thickness direction. For the notched specimen, the elements have slightly different geometry and size. The smallest elements at the edge of the notch have an element size of  $59\text{ }\mu\text{m} \times 75\text{ }\mu\text{m} \times 200\text{ }\mu\text{m}$  in the x, y and z-direction, respectively, while the largest elements in the center of the notch have dimensions  $75\text{ }\mu\text{m} \times 75\text{ }\mu\text{m} \times 200\text{ }\mu\text{m}$ . This resulted in roughly 150 000 elements in both FE models. As seen, the element size used in the numerical simulations is comparable to the element size used in the DIC analysis for the tensile tests carried out in air, i.e., outside the SEM.



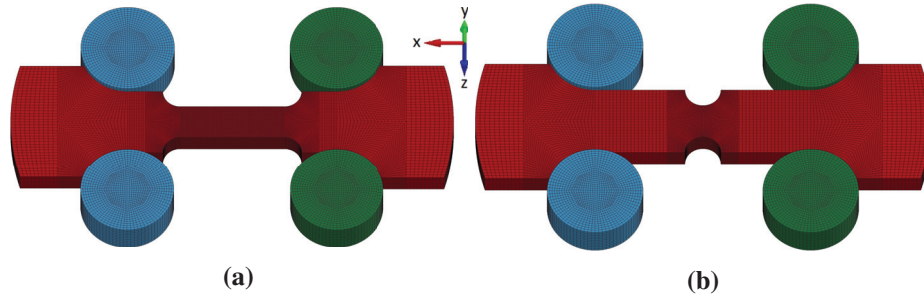


**Figure 7.6:** Numerical models of the (a) smooth and (b) notched specimen geometries. These specimen have the same dimensions as the smooth and notched geometry used in the physical tests and defined in Figure 3.2.

#### 7.2.4 Numerical results

The evolution of the strain field within the gauge area in terms of the maximum principal strain from the simulation of the smooth specimen can be seen in Figure 7.7, and it compares qualitatively well with the experimental result conducted in air given in Figure 7.2. In Figure 7.8(a), the simulated force-displacement curve is plotted and compared with the experimental data. Due to some flexibility in the *in-situ* tensile test device used in the experiments, the measured curves in Figure 7.8 have been adjusted to have the same initial stiffness as the simulated curve. As seen from these curves, the response is similar both in terms of shape, yield stress, and ultimate tensile strength (UTS). After necking the two curves differ somewhat, where the simulated curve has a faster drop in force compared to the measured curve. However, no effort has been made in this study to fit the material model after diffuse necking. Also the maximum principal strain value from the experiment and simulation compare well, with  $\varepsilon_{DIC} = 1.5$  in the experiment and  $\varepsilon_{SIM} = 1.45$  in the simulation at a displacement of 3500  $\mu\text{m}$ . In the experiment, the material is seen to be heterogeneous with some local variations in properties and measured strains (see Figure 7.2). In the simulation, on the other hand, a homogeneous material is assumed and this results in a more uniform strain field. This can be seen by comparing Figure 7.2 and Figure 7.7.

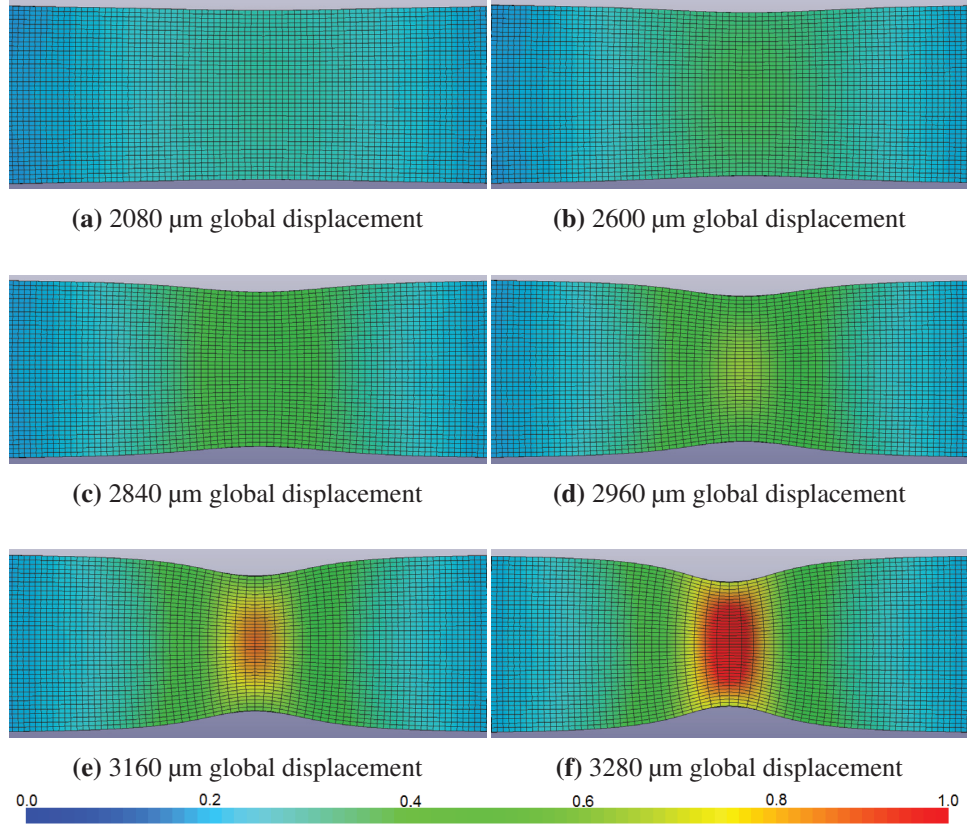


**Figure 7.7:** Simulated strain field in the smooth specimen plotted as fringes of the maximum principle strain. In all frames, the pulling direction is from right to left.

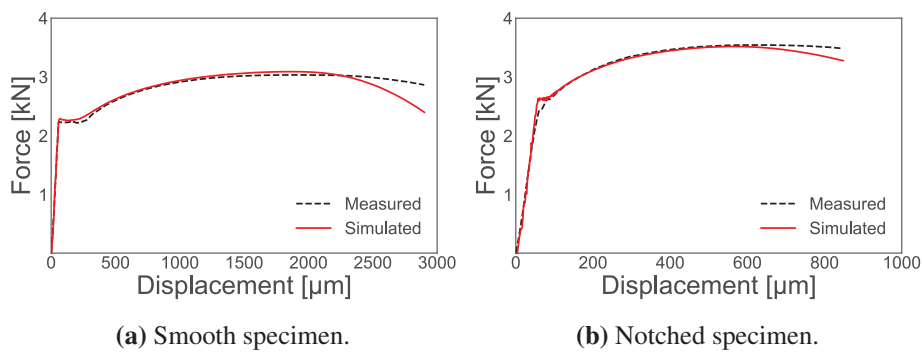


**Figure 7.8:** Measured versus simulated force-displacement curves for the (a) smooth specimen geometry and the (b) notched specimen geometry.

Also for the notched specimen, the simulated and experimentally obtained strain fields from the tension test conducted in air are in reasonable agreement, as can be seen by comparing Figure 7.4 and Figure 7.9. The force-displacement curves from both the experiment and simulation are displayed in Figure 7.8(b). The two curves compare qualitatively and quantitatively well until the maximum force is reached. However, there is a slight difference during yielding. The simulated curve still retains a yield plateau, while this is not observed in the experimental test on the notched specimen. Similarly, as for the smooth specimen, the simulated curve has a somewhat faster drop in force compared to the measured curve. Again, the maximum principal strain values compare relatively well at a displacement of 1500  $\mu\text{m}$ , with  $\varepsilon_{DIC} = 1.25$  for the experiment and  $\varepsilon_{SIM} = 1.32$  in the simulation.

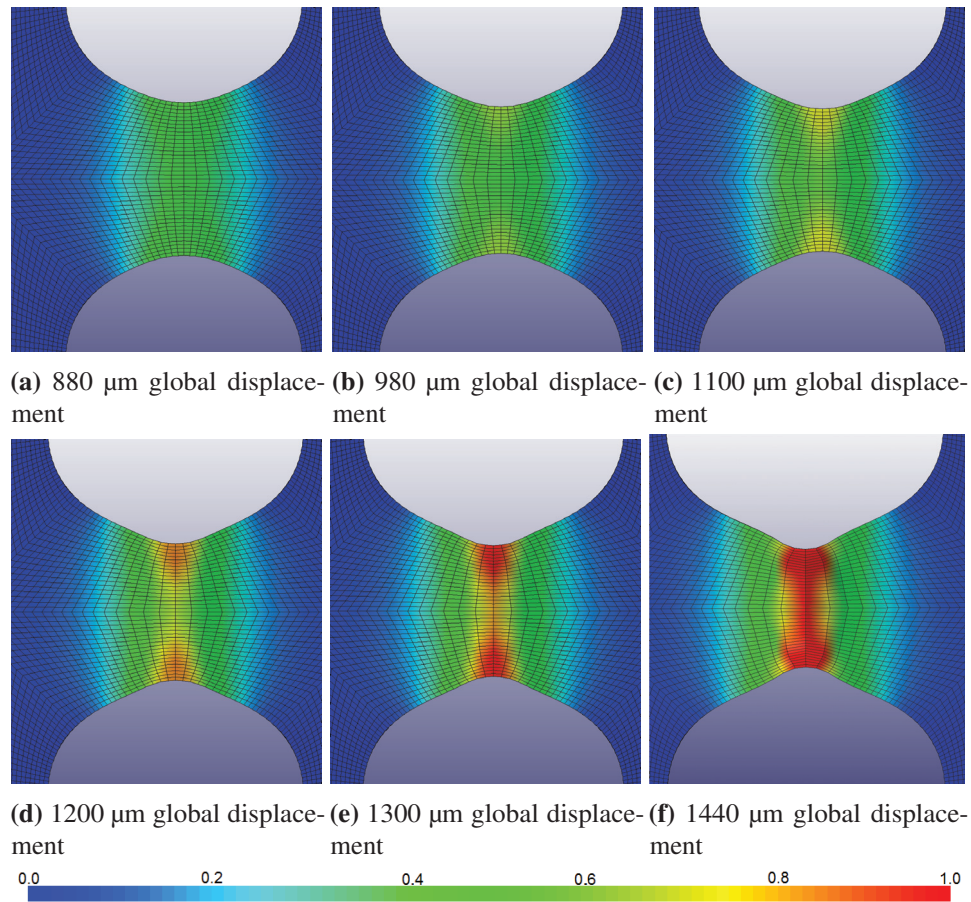


**Figure 7.9:** Simulated strain field in the notched specimen plotted as fringes of the maximum principle strain. In all frames, the pulling direction is from right to left.



### 7.3 Discussion

The simulated strain fields compare reasonably well with the measured strain fields using DIC in tensile tests outside the SEM. The DIC elements used in the latter are slightly finer ( $47\text{ }\mu\text{m}$ ), and able to capture local variations as seen in Figure 7.2 and Figure 7.4, than the element size of  $75\text{ }\mu\text{m}$  used in the FE simulation. Still, when comparing the local principal strain values for the tests and simulations, they are in good agreement. The peak values are respectively  $\varepsilon_{DIC} = 1.50$  and  $\varepsilon_{SIM} = 1.45$  for the smooth specimen, while for the notched specimen the corresponding values are  $\varepsilon_{DIC} = 1.25$  and  $\varepsilon_{SIM} = 1.32$ . The force-displacement curves for both smooth and notched specimens are also found to be in good agreement between the tests and simulations until necking, as seen in Figure 7.8. After reaching the peak load the simulations show a steeper drop in force compared to the experimental curves, but no effort has been made in this study to fit the material model used in the numerical simulations after this point.

The local average strain (measured across the recorded area using virtual extensometers of  $80\text{ }\mu\text{m}$  in the DIC code) for the *in-situ* SEM tensile test on a notched specimen was found to be  $e_{DIC} = 0.92$  at fracture. For the test conducted in air, i.e., outside the SEM on the same specimen geometry, the local average strain was recorded to be  $e_{DIC} = 0.28$ , now using an virtual extensometer of  $3000\text{ }\mu\text{m}$ . The maximum principal strain observed in the two strain fields (measured at element level) was found to be  $\varepsilon_{DIC} = 1.6$  and  $\varepsilon_{DIC} = 1.25$  for the *in-situ* SEM tensile test and the test in air, respectively. As seen, from the *in-situ* SEM tensile test the maximum principal strain at fracture is found to be 25% higher than the one measured at macroscopic level. Similar differences were reported by Haltom et al. [142] based on microscopic and macroscopic strain measurements in an aluminum alloy.

### 7.4 Concluding remarks

In addition to the experimental work, numerical simulations of the same tensile tests were performed. The numerical results were in good agreement with the experimental observations, both in terms of force-displacement curves and strain fields. However, the local variations and heterogeneous deformation in the material were, as expected, not captured in these simulations since the numerical model chosen assumes a homogeneous material behavior. This is not the case when studying the experimental results from the DIC measurements. To capture such local variations, a more exhaustive numerical model that takes the heterogeneity of the material into account is required. One such numerical model is the crystal plasticity model [146, 147].

## Chapter 8

# Investigating dual-phase steels using *in-situ* SEM tensile tests and micromechanical-based finite element simulations

In the following chapter, four different dual-phase (DP) steels were investigated using electron backscatter diffraction (EBSD) and *in-situ* scanning electron microscope (SEM) tensile testing combined with digital image correlation (DIC). The four different DP steels are DP500, DP600, DP800 and DP980, earlier presented in Chapter 3.4.3. From the EBSD results the microstructures were characterized and the grain size of ferrite, the size of the martensite islands, and the amount of martensite present for each steel are reported. Localization of damage in the microstructure was studied for each of the DP steel using DIC strain maps and micrographs from the *in-situ* SEM tensile tests. In DP500, DP600 and DP800 the most severe damage takes place within larger ferrite grains. The deformation mechanisms in the DP500 and the DP600 specimens are dominated by slip activity. However, the DP800 steel differs from the other steels by having large cracks on the specimen surface. Here, cracks accommodate most of the damage during the tensile test. Due to the amount of martensite in DP980, the martensitic phase is an interconnected network where there are fewer large ferrite grains. As a consequence, most of the damage is observed to take place on the interface between martensite and ferrite.

In addition to the experimental characterization and DIC study of the DP steels, the microstructure of DP800 was analyzed in a FE model. Here, the same microstructure as studied with DIC during the *in-situ* SEM tensile test was translated into a finite element (FE) model. The FE analysis was performed by Dr. Afaf Saai at Sintef Materials and Nanotechnology. A separate DIC analysis was performed to have the same mesh size in both the DIC mesh and the FE mesh (measured in  $\mu\text{m}$ ) and to extract the displacements from the DIC boundary nodes and use them as boundary conditions in the FE analysis. From the FE analysis, a strain map on the same microstructure as in the DIC strain map was generated. The strain map from the FE analysis was not able to capture the cracks observed in the experiments. The largest strains recorded in the FE simulations were localized on the interface between martensite and ferrite. However, it should be noted that this study is preliminary and work in progress. The reason for including it here is to illustrate a method to link the high-resolution DIC results to FE simulations on a real microstructure.

## 8.1 Experimental

In this study four different DP steels are investigated, namely DP500, DP600, DP800 and DP980. These materials are described in more detail in Chapter 3.4.3. To record the microstructure evolution during the *in-situ* SEM tensile test, a ZEISS Supra 55 Field Emission SEM with a backscatter electron (BSE) detector was used. A spindle-driven *in-situ* tensile test device was placed in the vacuum chamber, where it was mounted on top of the SEM stage after removal of the rotation unit. This device is shown in Figure 3.1 and described in Chapter 3.1. The image acquisition for the BSE images acquired for DIC analyses is described in detail in Chapter 3.3. For all specimens, each frame of the total image was acquired with a resolution of 2048 pixels  $\times$  1536 pixels. The size of the speckles determined the size of the recorded area for each specimen, but for all specimens the recorded area was close to 65  $\mu\text{m}$   $\times$  50  $\mu\text{m}$ . Two images were acquired at 0% strain in order to quantify the error due to the microscope (see chapter 2.1.1). Then three images were acquired at key locations on the tensile test curve: at the yield point, during hardening and at the maximum force, i.e., the ultimate tensile strength (UTS). After the test, the image series was analyzed by the DIC software eCorr v.4.0 [11]. The mesh size used in the DIC analysis was given by quadratic elements with size 25 pixels  $\times$  25 pixels for all specimens. As a result, a spatial resolution of 140 nm, 120 nm, 107 nm, and 140 nm were achieved for the DP500, DP600, DP800 and DP980 specimen, respectively.

To characterize the steels and to provide information from the area investigated with DIC, EBSD scans were acquired as described in Chapter 3.2. The SEM used for the EBSD acquisition was a Zeiss Ultra 55 Field Emission SEM using a NORDIF UF-1100 EBSD detector. In order to prepare the specimens for EBSD and gold remodeling, they were ground and polished to 1  $\mu\text{m}$  before being polished for 16 hours using a vibration polisher with a 0.2  $\mu\text{m}$   $\text{SiO}_2$  pH 8 solution. Buhler is the manufacturer of both the vibration polisher and the solution. This preparation method produces a flat, deformation free, surface. Before applying the gold, EBSD was performed on the same region as the region later recorded for DIC. In addition, two hardness indents were placed near the center of the gauge length. These act as fiducial markers in order to ensure that the area recorded with EBSD before gold remodeling is the same area for all loading steps recorded with BSE. After the EBSD acquisition, the surface was coated with a continuous layer of gold using an Edwards S150B sputter coater. The final step before performing the *in-situ* SEM tensile test is to remodel the continuous gold layer into gold nanoparticles. This is done by placing the specimen on a hot plate at 180°C for 96 hours inside a sealed remodeling chamber. During the remodeling process, an argon/styrene mixture is flowing across the surface of the polished and gold coated specimen. The result is finely dispersed gold nanoparticles across the specimen surface. This method is explained in further detail in Chapter 3.3.

In addition to the EBSD acquired of the area analyzed with DIC, a total of 3 EBSD scans of each DP steel were acquired to characterize the microstructure of each DP steel. Each EBSD scan had a recorded area of 80  $\mu\text{m} \times 80 \mu\text{m}$ . The resulting EBSD data were used to find the phase composition, the ferritic grain size, and the size of the martensite islands for the different DP steels. The phase composition was found by creating a binary version of the image quality (IQ) map from the EBSD results. From these binary images, the amount of martensite and the size of the martensite islands were calculated. The mean free path of ferrite ( $L_\alpha$ ) is calculated using Equation 8.1 and the linear size of martensite ( $L_{\alpha'}$ ) is calculated using Equation 8.2 [148]. In these equations,  $\alpha$  denotes ferrite,  $\alpha'$  denotes martensite,  $V_{\alpha'}$  is the volume fraction of martensite, and  $P_L$  is the number of interceptions (per unit length) between virtually drawn lines on the binary image and a ferrite-martensite interface. Here, a total of 160 lines are drawn, 80 lines vertically and 80 lines horizontally for each binary phase map. This was done on three phase maps for each DP steel. Each instance when the line intersects with a phase boundary was then counted and divided by the length of the drawn line (80  $\mu\text{m}$ ) to obtain  $P_L$ . The physical meaning of the free path of ferrite and the linear size of martensite is illustrated in Figure 8.1. All these operations were performed using the Fiji distribution [118] of the OpenSource software ImageJ [120]. Also, the grain area of martensite was calculated using ImageJ. From this area, the grain diameter of

martensite is calculated by assuming each grain being a circle. The same method is used for calculating the grain size of ferrite. However, here the EBSD data from the ferrite grains are used to get the grain areas instead of the binary map.

$$L_{\alpha} = 2 \frac{1 - V_{\alpha'}}{P_L} \quad (8.1)$$

$$L_{\alpha'} = 2 \frac{V_{\alpha'}}{P_L} \quad (8.2)$$

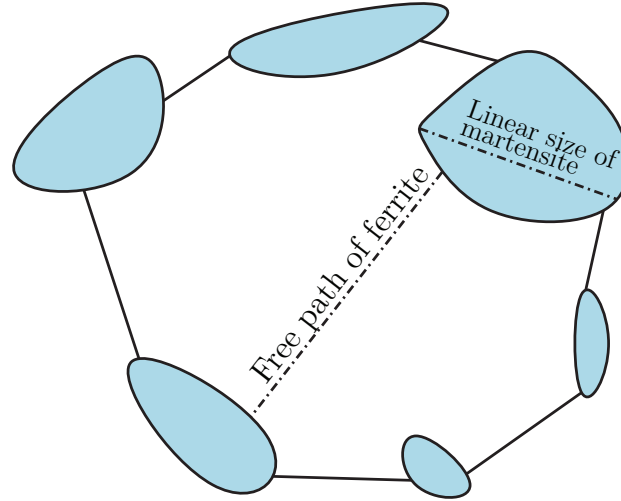


**Figure 8.1:** The definition of the free path of ferrite and linear size of martensite shown on a representation of the DP microstructure. The black lines represent grain boundaries, the white area inside the black lines is the ferrite grain, and the smaller light blue areas on the ferrite grain boundary are martensite island. This figure is inspired by Lai et al. [108].

## 8.2 Experimental Results

### 8.2.1 Microstructure characterization

The engineering stress–strain curves for all DP specimens are given in Figure 8.2. These curves were obtained by performing tensile tests using an MTS810 100 kN conventional test machine with DIC as virtual extensometer. Correlations between tensile data and fraction martensite are visualized in Figure 8.3. Here, a strong linear relationship between fraction martensite and UTS, yield strength and elongation at UTS is observed with all coefficient of determination values,  $R^2$ ,  $> 0.96$ . If excluding larger amounts of martensite, in this case  $> 50\%$ , all  $R^2$  values would be

$> 0.998$ . However, for the relationship between the UTS and elongation at UTS, the linear correlation also holds for the DP980 specimen. Here,  $R^2 = 0.9996$ . For each specimen, four tensile tests were conducted and as seen from the error bars in Figure 8.3 there is little spread in the tensile data.

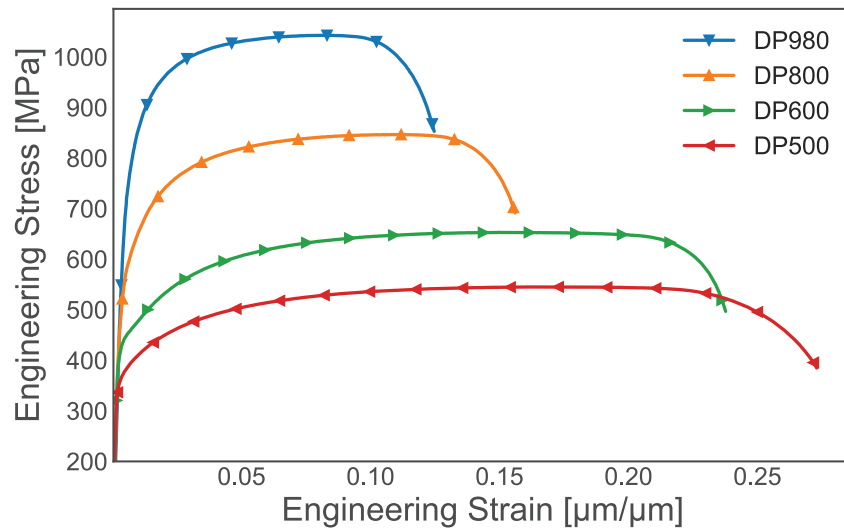


**Figure 8.2:** Engineering stress–strain curve from tensile tests of different DP steels. These curves are acquired from tensile tests using a MTS810 100 kN conventional tensile test machine with DIC as virtual extensometer.

The results from the EBSD characterization are summarized in Figure 8.4. The average grain size of ferrite is declining with increasing amounts of martensite. A similar trend is seen for the free path of ferrite. It decreases with an increasing amount of martensite except for the DP980 specimen. Here, the free path of ferrite again increases. The same is observed for the average martensite grain size and the linear size of martensite. For the linear size of martensite, there is a substantial increase in the DP980 steel. The reason for this increase is due to a lower  $P_L$  since there are fewer ferrite-martensite boundaries since more of the martensite is interconnected. Another observation is that the ferrite grains in DP500 are more than twice as large as the martensite grains. Also, in DP600, DP800 and DP980, the grain size of ferrite is larger than the martensite grain size but, not by the same amount as in DP500.

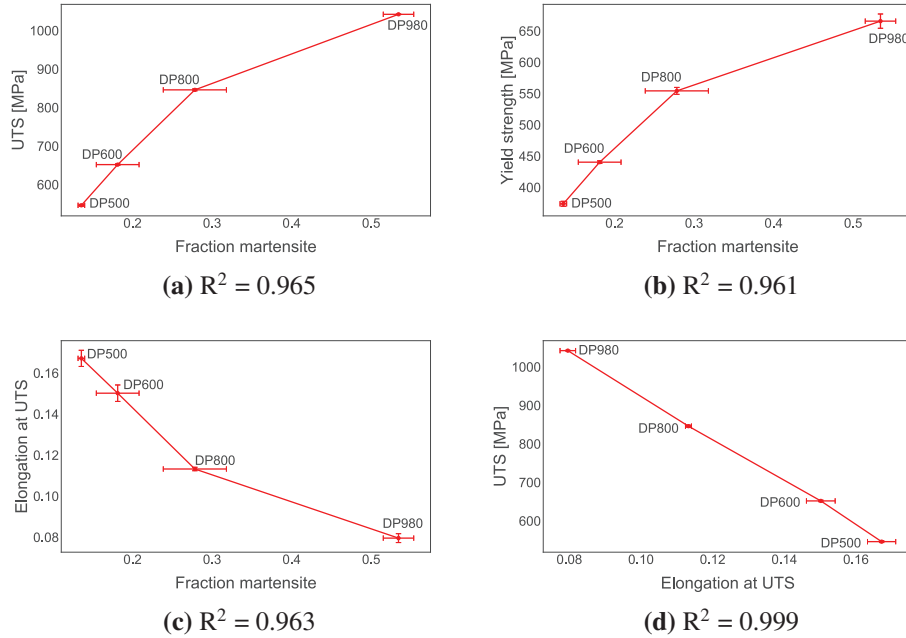


**Figure 8.3:** Correlation between the tensile data and the fraction of martensite.

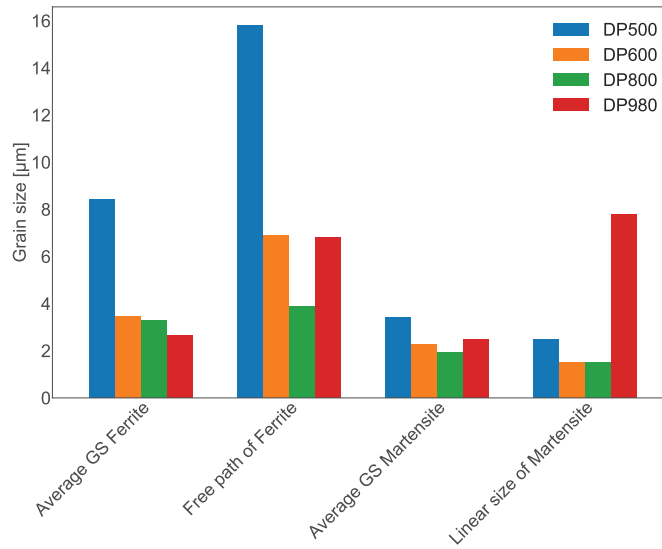
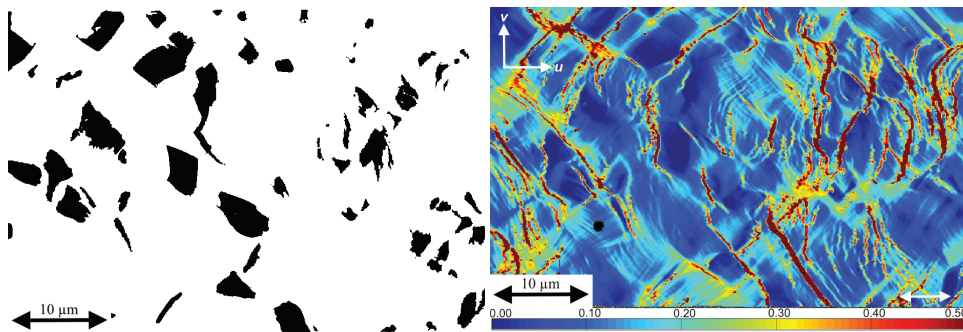


**Figure 8.4:** Comparison of the different properties of the different DP steels. In the figure, the grain size is abbreviated GS on the x-axis. Free path of ferrite and linear size of martensite are calculated using Equations 8.1 and 8.2, respectively. The grain size is the grain diameter, calculated from measured grain area, assuming the grain being a circle.

### 8.2.2 DIC investigation of DP steel acquired during an *in-situ* SEM tensile test

In Figure 8.5, the phase map and the corresponding strain map obtained from the *in-situ* SEM tensile test and EBSD scan of the DP500 steel are shown. The strain map was acquired at 16.9% global engineering strain, which is at UTS. When comparing the strain map with the phase map, it can be seen that the black martensite islands correspond well with the undeformed zones (dark blue areas) in the strain map. In addition, the more highly deformed bands seem to occur mostly within ferrite and at the interface between ferrite and martensite.

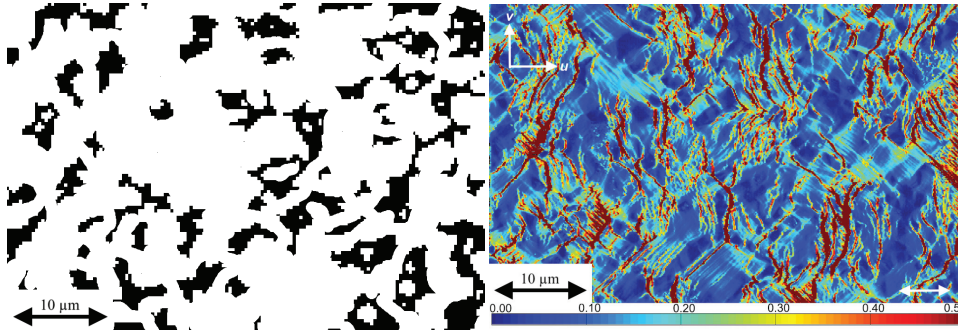


(a) Phase map of recorded area with 13.5% martensite. (b) DIC map taken at UTS, 16.9% global strain.

**Figure 8.5:** DP500 (a) The phase map of the same area as observed with DIC. The white area is ferrite and the black islands are martensite. (b) DIC map showing major principle strain. The DIC map has a spatial resolution of 140 nm and the pulling direction for the *in-situ* SEM tensile test is indicated in the bottom right in (b).

Looking at the phase map and DIC map of DP600 in Figure 8.6, a more heavily deformed microstructure is seen. Compared to DP500, DP600 has an increased amount of martensite in the microstructure. However, it still retains much of the same ductility as the DP500 steel. DP600 has 60% more martensite compared to DP500, but still deforms until 15% global engineering strain at UTS. DP500 deforms until 16.9% global engineering strain at UTS. Similarly to the DP500 steel, the ferrite in DP600 accommodates most of the damage.





(a) Phase map of recorded area with 21.5% martensite (b) DIC map taken at UTS, 15% global strain.

**Figure 8.6:** DP600 (a) The phase map of the same area as observed with DIC. The white area is ferrite and the black island is martensite. (b) DIC map showing major principle strain. The DIC map has a spatial resolution of 120 nm and the pulling direction for the *in-situ* SEM tensile test is indicated in the bottom right in (b).

In contrast to DP500 and DP600, where the deformation mainly takes place in multiple slip lines throughout the ferrite grains, DP800 seems to accommodate much of the deformation by cracks. All of these cracks are oriented vertically in the strain field in Figure 8.7(b), which is perpendicular to the tensile direction. The corresponding phase map of this DIC map is shown in Figure 8.7(a). In the bottom center in Figure 8.7(b), a white square is highlighted. A close up of this area is shown in Figure 8.8. Here, numerous cracks are seen in just a small area. The widest part of the largest crack is measured to be 0.3  $\mu\text{m}$  with a length of 3.8  $\mu\text{m}$ .

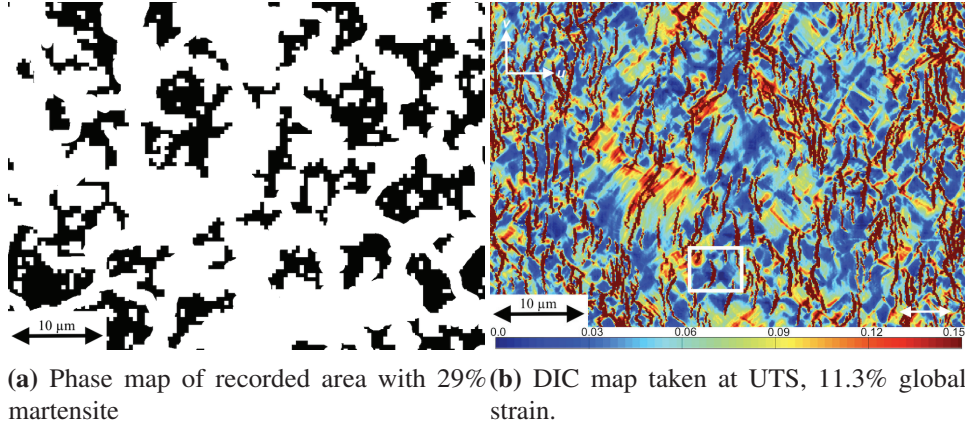


**Figure 8.7:** DP800 (a) The phase map of the same area as observed with DIC. The white area is ferrite and the black island is martensite. (b) DIC map showing major principle strain. The DIC map has a spatial resolution of 107 nm and the pulling direction for the *in-situ* SEM tensile test is indicated in the bottom right in (b). Figure 8.8 shows the area inside the white square in the bottom center of (b).

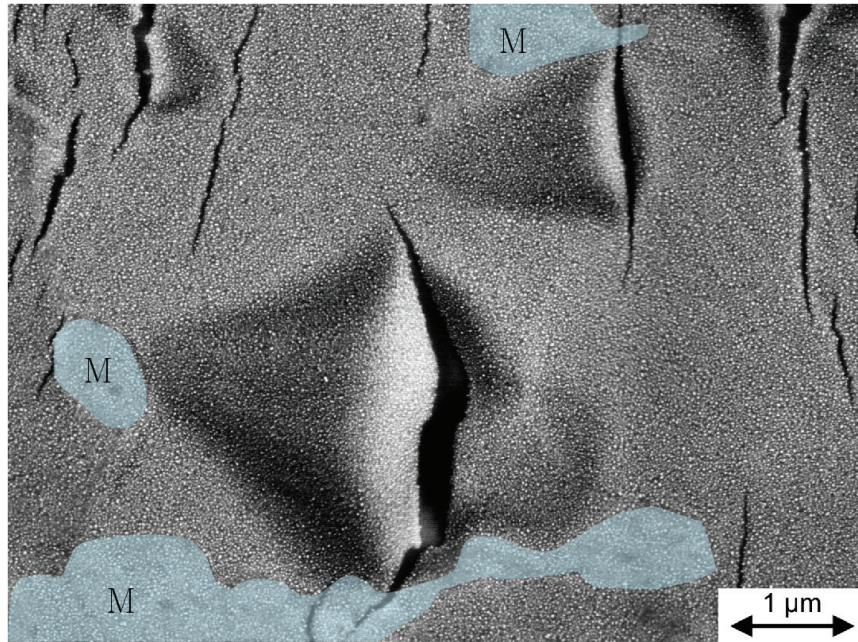
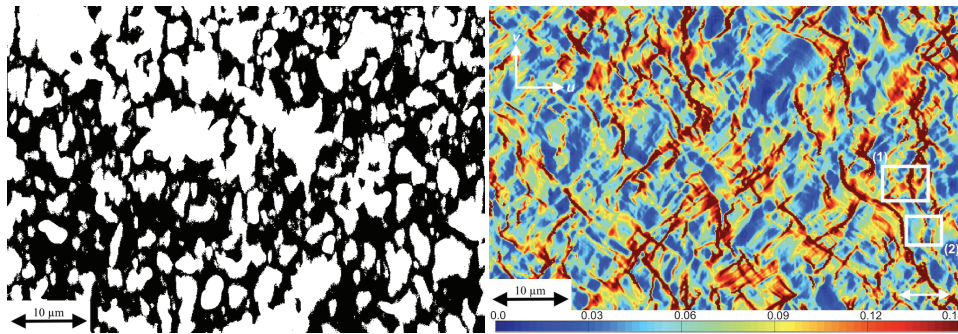


**Figure 8.8:** This figure shows the cracks within the white square in Figure 8.7 and has an area of  $7.6 \mu\text{m} \times 5.6 \mu\text{m}$ . These cracks appear throughout the surface of the DP800 steel. The maximum strain recorded by DIC at element level in these cracks was  $\varepsilon_{DIC} = 0.9$ .

In the DP980 steel there more than 50% martensite in the recorded area and UTS occurs after 7.9% of global engineering strain. The phase map and strain map of DP980 are shown in Figure 8.9(a) and Figure 8.9(b), respectively. In the resulting strain map, the most localized strain bands are on the interface between ferrite and martensite. The martensite is mostly interconnected, and there are fewer large ferrite grains for the deformation to occur in. Unlike for the other three DP steels, the martensite is visibly deformed in DP980, and the deformation bands propagate through the martensitic phase. A close up of the white squares in Figure 8.9(b) is shown in Figure 8.10. The blue area labeled **M** marks the martensite islands. In Figure 8.10(a), the white square labeled (1) in Figure 8.9(b) is shown, and here the crack propagates through the martensitic phase. However, most of the shear bands observed in this microstructure are deflected by the martensitic islands, as seen in Figure 8.10(b) (shown in the white square labeled (2) in Figure 8.9(b)).



(a) Phase map of recorded area with more than 50% martensite. (b) DIC map taken at UTS, 7.9% global strain.

**Figure 8.9:** DP980 (a) The phase map of the same area as observed with DIC. The white area is ferrite and the black island is martensite. (b) DIC map showing major principle strain. The DIC map has a spatial resolution of 140 nm and the pulling direction for the *in-situ* SEM tensile test is indicated in the bottom right in (b). The area in the two white squares in (b) are shown in Figure 8.10.

Using the DIC data for all DP specimens, local strains have been extracted, and this data is summarized in Table 8.1. The global strain in the second column is the engineering strain from the tensile test at UTS. For the local average strains and local grain strains in the third column and fifth column in Table 8.1, data were acquired from the DIC strain maps at UTS. Here, ten virtual extensometers with an initial length of 60 μm were placed horizontally using the DIC software to measure the local average strain for each DP steel. This is illustrated in Figure 8.11 for the DP800 steel. A similar approach was used to obtain local grain strain values. Here, a virtual extensometer was placed horizontally on ten different ferrite grains



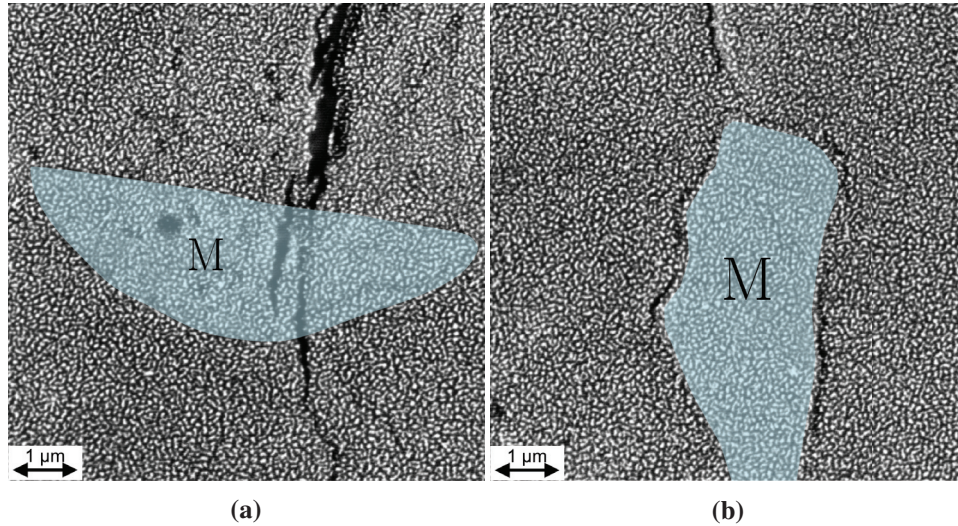


**Figure 8.10:** In both (a) and (b) the martensite is under the blue area labeled M. (a) This figure shows damaged martensite, with a crack propagating through the martensite island. This area is a closer look of the white square marked (1) in Figure 8.9(b). (b) This figure shows the damage being deflected by the martensite. The shear band is split into two bands around the martensitic phase. This area is the same as the white square marked (2) in Figure 8.9(b).

and ten different martensite grains, from grain boundary to grain boundary, in all DP steels. These virtual extensometers recorded the local grain strains in the ferrite and the martensite listed in Table 8.1. In DP500, DP600 and DP800 the martensite deformed very little, about 2% for all specimens. However, for DP980, the martensite was strained more than twice this amount, with an average strain of 4.7%. In general, the local grain strain in ferrite and the local average strain are roughly equal. However, it is worth noting that the ferrite in DP800 deforms less than in DP980. This is probably due to the large cracks in DP800. Most of the damage is absorbed by the cracks, leaving the rest of the grain relatively undeformed. For the other steels, larger areas of the grains are deformed.

**Table 8.1:** Local engineering strains in martensite and ferrite for the different DP steels. All data are acquired at UTS. The data in the global strain column are obtained from the tensile curves in Figure 8.2. The measurements in the local average strain column and the local grain strain column are engineering strains obtained from the DIC data using vectors as virtual extensometers.

Steel	Global strain	Local average strain	Phase	Local grain strain
DP500	16.9 %	18.4 % $\pm$ 0.9 %	Ferrite	18.2 % $\pm$ 6.8 %
			Martensite	2.2 % $\pm$ 1.6 %
DP600	15 %	15.5 % $\pm$ 1 %	Ferrite	15.8 % $\pm$ 4.4 %
			Martensite	2 % $\pm$ 2.3 %
DP800	11.3 %	8.8 % $\pm$ 0.9 %	Ferrite	8.8 % $\pm$ 3.4 %
			Martensite	1.9 % $\pm$ 0.9 %
DP980	7.9 %	8 % $\pm$ 0.3 %	Ferrite	9.9 % $\pm$ 4.7 %
			Martensite	4.7 % $\pm$ 1.8 %

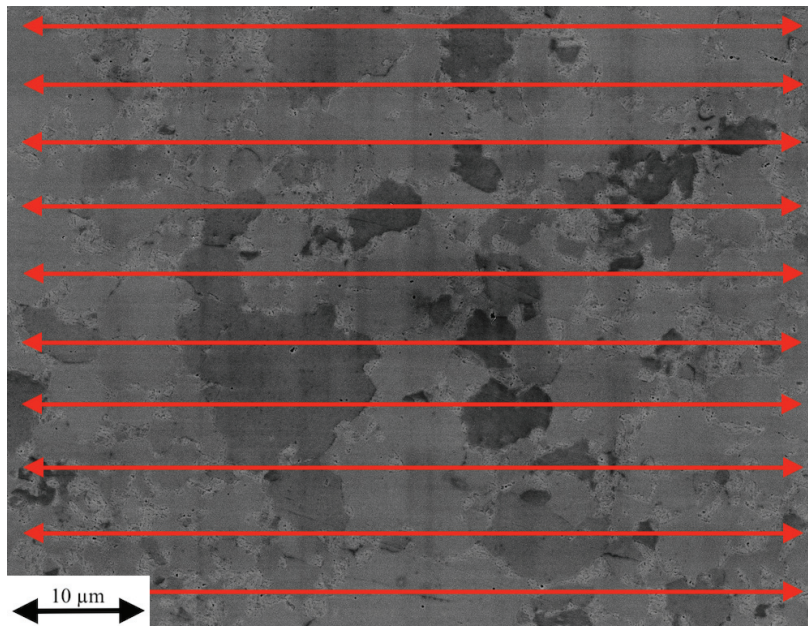


**Figure 8.11:** Vectors used as virtual extensometer for the average engineering strain over the recorded area, all having an initial length of 60  $\mu\text{m}$ . This method was used on all DP steels to get the local average strain in Table 8.1.

### 8.3 Finite element model

A new DIC analysis was conducted on a cropped region of the DIC analysis presented in Figure 8.7 in order to match the mesh size and phase map with the FE model exactly. A representative volume element (RVE) of DP800 was generated by translating the binary map as seen in Figure 8.12(a) into an FE model and extending it in the thickness direction. A script was created to read the phase map and detect the phase boundaries between ferrite and martensite. This script then generated a geometrical part with two sections, i.e., one section for martensite and one section for ferrite. Both parts were then meshed with 8-node hexahedral elements where the element size on the boundary was equal to the mesh size from the DIC analysis. The total area was  $32.314 \mu\text{m} \times 32.314 \mu\text{m}$ . In Figure 8.12(b), the generated RVE is presented. The mesh size used was  $0.214 \mu\text{m} \times 0.214 \mu\text{m}$  for all nodes in the DIC analysis and the boundary nodes in the FE analysis. In addition, the RVE thickness was  $0.214 \mu\text{m}$ . The interactions between the phases were accounted for by assuming displacement continuity of the finite elements at the interface between the phases. The measured displacement was extracted from the nodes on the boundary lines from the DIC results. The boundary lines are marked with the red border in Figure 8.12(a), i.e., for the nodes at  $x = 0$ ,  $x = l$ ,  $y = 0$  and  $y = h$ . The displacements were then applied to the corresponding node in the FE analysis. In addition, it should be mentioned that the same displacement as used as boundary conditions on the 2D-area was applied on the nodes through the thickness, i.e., for  $z \neq 0$ .

A Taylor-type equation computed the responses of the martensite phase and the ferrite phase. A description of this model is found in Chapter 2.5.2. In this work, the same equations as in the work of Ramazani et al. [111] were utilized. The equivalent stress is given by

$$\sigma_{eq}(\varepsilon) = \sigma_0 + \Delta\sigma + \alpha M_T \mu \sqrt{b} \sqrt{\frac{1 - \exp(-M_T k_r \varepsilon_{eq})}{k_r L}} \quad (8.3)$$

where  $\sigma_0$  describes the strengthening contribution from elements in solid solution following (in MPa)

$$\begin{aligned} \sigma_0 = & 77 + 750 (\% \text{ P}) + 60 (\% \text{ Si}) + 80 (\% \text{ Cu}) + 45 (\% \text{ Ni}) \\ & + 60 (\% \text{ Cr}) + 80 (\% \text{ Mn}) + 11 (\% \text{ Mo}) + 5000 (\% \text{ N}_{\text{solid solution}}) \end{aligned} \quad (8.4)$$

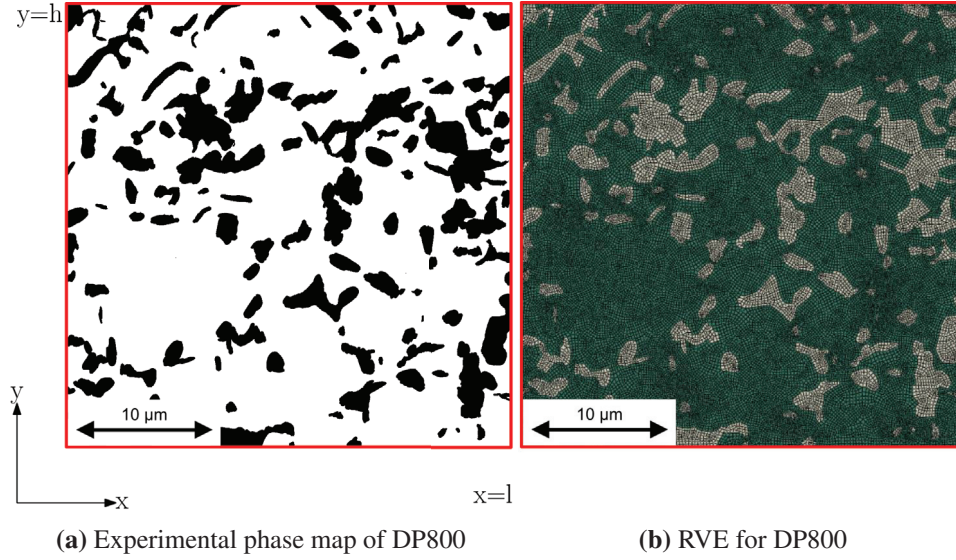


**Figure 8.12:** (a) The experimentally obtained phase map of DP800. This is a cropped region of Figure 8.7(a). The black area is martensite and the white area is ferrite. (b) Representative volume element for DP800. The white islands are martensite and the green matrix is ferrite. Both areas have the dimension  $32.314 \mu\text{m} \times 32.314 \mu\text{m}$ . The measured displacements from the nodes at the red boundary in (a) are used as boundary condition in the FE analysis.

Further,  $\Delta\sigma$  is the strengthening contribution from carbon in solid solution given as (in MPa)

$$\Delta\sigma = 5000 \times (\% C_{\text{solid solution}})^{\alpha} \quad \text{for ferrite} \quad (8.5a)$$

$$\Delta\sigma = 3065 \times (\% C_{\text{solid solution}})^{\alpha'} - 161 \quad \text{for martensite} \quad (8.5b)$$

The final term in Equation 8.3 describes the strain hardening of the material where  $M_T$  is the Taylor constant,  $k_r$  is the recovery rate, and  $L$  is the dislocation mean free path.  $\alpha$ ,  $\mu$ ,  $b$  and  $M_T$  are material constants. These are available in the literature for DP steels [112]:  $\alpha = 0.33$ ,  $\mu = 80000 \text{ MPa}$ ,  $b = 2.5 \cdot 10^{-10} \text{ m}$  and  $M_T = 3$ .  $k_r$  and  $L$  are microstructural characteristics, identified by inverse modeling of the martensite. In ferrite, these are based on the grain size. The dislocation mean free path is assumed equal to the average grain size,  $L = d_{\alpha}$ , and the recovery rate is given by  $k_r = 10^{-5}/d_{\alpha}$ . The RVE presented in Figure 8.12(b) and the calibrated material models for the martensite and ferrite phases were used in implicit finite element simulations [149] of the tension tests.



In Figure 8.13 the strain map from the FE analysis and strain map from the DIC analysis are shown. From the strain map in Figure 8.13(a) it is seen that the strain gradient, localization and localization bands highly depend on the distance between the martensite. The strain is localized on the interface and in the area where the distance between the martensite islands is small, the last comment applies also on maximum stress and stress localization (not shown here). The cracks observed from the *in-situ* SEM tensile test are not captured by the FE simulation.

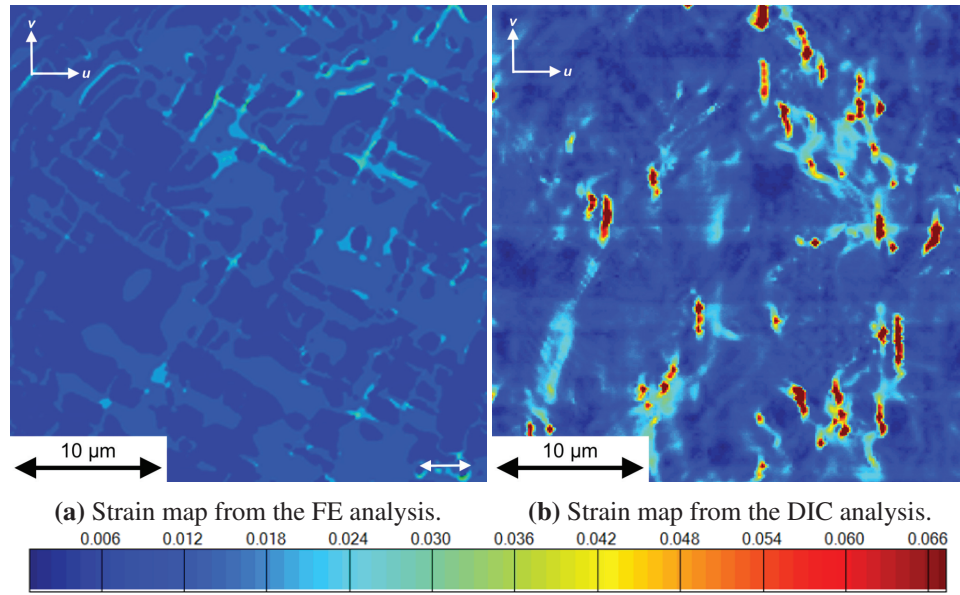


**Figure 8.13:** DP800 (a) The strain map from the FE analysis. (b) The strain map from the DIC analysis. Both maps are showing Lagrange max principal strain and are displayed after roughly 5 % global engineering strain. The pulling direction for both tests are indicated in the bottom right in (a).

## 8.4 Discussion

This chapter has investigated four different DP steels using EBSD and *in-situ* SEM tensile testing combined with DIC. On each specimen, a gold speckled pattern was created. In order to create this pattern, the specimens were coated with a continuous layer of gold and then kept in an argon/styrene atmosphere at 180°C for 96 hours. This process is described in detail in Chapter 3.3. A consequence of this heat treatment is a bake hardening process and the introduction of Lüders bands. However, as discussed in Chapter 4, the hardening behavior of the steels remained the same. In this work, the concern is the deformation process after yielding.

EBSD was used to characterize the different DP-steels. A total of three EBSD



scans with an area of  $80\text{ }\mu\text{m} \times 80\text{ }\mu\text{m}$  was conducted. From this, the average grain size of ferrite, the size of the martensite islands and the fraction martensite were measured and calculated. In addition, four conventional tensile tests were carried out. In Figure 8.3 the fraction of martensite is plotted against tensile properties from the tensile test curves. It shows that increasing amounts of martensite give higher yield strength and UTS and a reduction of elongation at UTS. These seem to exhibit an exact linear relationship for lower amounts of martensite. The correlation is not as linear when having larger amounts of martensite, i.e., for DP980. These observations correspond well with the observations of Bergström et al. [113]. The relationship between UTS and elongation at necking is plotted in Figure 8.3(d). Here, the exact linear relationship is also observed for DP980. It is also worth noting the small variations of each tensile test. Here, four tensile tests were carried out for each specimen, and the resulting curves are very close to identical. The short vertical error bars in Figure 8.3 reflect this.

The results from this study are a detailed microstructural investigation and local strain maps with a resolution able to resolve slip bands within grains. In the DIC investigation, all steels were deformed until UTS. As a consequence, the global strains for all steels will be different. The DP500 and DP600 steels appear to deform similarly. Both these steels contain more than 75% ferrite with all deformation taking place in the ferrite and no instance of damage is observed to take place within the martensite. However, some damage is observed on the interface between ferrite and martensite in both DP500 and DP600. In DP800 large cracks are observed. These cracks sometimes propagate into the martensite, as seen in Figure 8.8. All cracks are perpendicular to the tensile direction, and this is a typical behavior observed in earlier works (see e.g. [3]). The large cracks in DP800 propagate to some extent into the martensite. However, the martensite seems to retard the crack propagation. Outside these cracks little damage is observed. While many grains are affected by multiple slip and shear bands in the DP500 and DP600 steels, most of the deformation is accommodated by these cracks in DP800. In DP980 the cracks observed for DP800 are not present. However, shear bands are propagating through the microstructure. These also propagate through the martensite, as illustrated in Figure 8.10(a). This is hard to avoid due to the large amount of martensite present. In the DP980 steel there is roughly 50% martensite, and this is present as a nearly continuous network. This can be observed in Figure 8.9(a).

In Table 8.1 the local strain of ferrite and martensite at UTS for the different DP steels are listed. These local measurements are extracted using a virtual extensometer in the DIC software. For all specimens, except DP800, the local average strain is larger than the global strain measured from the tensile data. This is expected since when measuring engineering strain with a shorter extensometer, a larger strain

is recorded. However, this is not the case for the DP800. Here, the local average strain is 2.5% lower compared to the global strain. This is believed to be due to the deformation mechanisms in DP800. From the *in-situ* SEM tensile test, cracks were observed at the surface. These cracks accommodated all the damage and little slip activity was observed. As a consequence, most of the damage is absorbed by a crack, and due to the local relaxation, the rest of the grain is relatively undeformed. In contrast, for the other steels larger areas of the grains are deformed. Further, in DP500, DP600 and DP800, the strain in martensite is measured to be roughly 2%. When investigating the strain maps, it is clear that the damage mostly occurs in ferrite grains and occasionally on the interface between ferrite and martensite for DP500 and DP600. For DP980, the damage mostly occurs on the interface between ferrite and martensite. Also, some damage observed is inside the martensite with shear bands cutting through martensite islands. As a result, the local grain strain for martensite is measured to be 4.7%. This is more than twice the other DP-steels.

When the martensite deforms in DP500, DP600 and DP800, it is an elastic deformation for the most part. Conversely, in DP980 the amount of martensite is roughly 50% and at this point, the martensite starts to accumulate some damage and plastically deform to a greater extent. An indication of this is observed in Figure 8.3. Here, the tensile properties have a linear relationship with the amount of martensite in the structure for DP500, DP600 and DP800. For DP980, this linear relationship does not hold, and the curves flatten. During the deformation of DP980 the most severe damage takes place on the interface between ferrite and martensite. At this interface, there is a pile-up of dislocations and this area hardens [150, 151]. This also occurs to a certain extent in the other DP-steels. However, due to the amount of martensite and the smaller ferrite grain size in DP980, the number of ferrite–martensite grain boundaries is greater here compared to the other steels. A consequence of the increased stress concentrations on the phase boundaries is an increased deformation of the martensite. This increase is reflected in the DIC measurements listed in Table 8.1.

In addition to the experimental results, an FE analysis was performed on the DP800 steel. Here, an RVE was generated from the experimentally acquired phase map shown in Figure 8.12(a). This is similar to what has been done earlier [152–154]. The boundary condition used during the simulation was the measured displacement of the boundary nodes in the DIC map. This is similar to having the FE model as a sub-model [155, 156] of the DIC analysis. Normally the boundary conditions for the sub-model would have been determined from results in a macro-model and applied in the sub-modeling analysis. To the author's best knowledge, this is the first instance of using the node displacements experimentally acquired from DIC maps on the microstructural level as boundary conditions during an FE simulation.

The results from the FE simulations showed that the strain gradient, localization and localization bands highly depend on the distance between the martensite islands. The strain is localized on the interface and in the area where the distance between martensite island is small, the last comment applies also on maximum stress and stress localization. These results are more similar to the behavior of DP500 and DP600. The cracks observed in the *in-situ* SEM tensile test were not observed in the FE results. As a result, the maximum strains in the FE strain map are lower than those obtained by DIC. This might be explained by the fact that the RVE is only a thin layer on the surface and assuming a free surface below. However, the material below the surface applies additional constraints on the surface deformation. A suggestion for future work is to generate a statistical RVE representative of the bulk material and connected it to the surface RVE. In addition, some of the boundary nodes in the DIC map contain significant error and are not representing the correct displacement. In this work, nothing has been done to correct for this. However, it was not the case for many nodes. Another consideration is that in the RVE at the ferrite–martensite interface there has to be a node. The node locations are not accounted for when creating the DIC mesh. As a consequence, the boundary nodes in the RVE does not exactly match the position in the DIC map. In order to counter this issue, the mesh size can be reduced and if possible, when performing the DIC analysis, avoid martensite on the boundary. However, the purpose of this study was to demonstrate a possible route to link DIC results from an *in-situ* SEM tensile test with numerical simulations.

## 8.5 Concluding remarks

- The specimens from each of the four DP steels tested had only very small variations in the tensile data. Even so, the microstructure measurements did vary some.
- The size of the martensite islands decreases for increasing amounts of martensite until it becomes an interconnected network. After becoming an interconnected network, the linear size of martensite and the free path of ferrite increase with larger amounts of martensite. This occurs when having 50% or more martensite in the microstructure.
- The deformation behavior of DP500 and DP600 is very similar. Here, most of the deformation takes place in the ferrite grains and some at the interface between ferrite and martensite. No martensite damage is observed in these DP steels.

- In DP800, large cracks are observed throughout the surface. These cracks are within the ferrite grains but sometimes cut into the martensite. Fewer shear bands are observed compared to the other DP steels, as these cracks accommodate most of the damage.
- The mechanisms deforming the DP980 microstructure are more similar to the DP500 and DP600 compared to DP800. However, in DP980 the shear bands are also observed to propagate through the martensite, and most of the damage occurs on the interface between ferrite and martensite. This is not observed in DP500 and DP600.
- The martensite in DP500, DP600 and DP800 record a similar average deformation, i.e., 2%, at the UTS. For DP980, more damage is taking place in the martensite, and it deforms on average 4.7% at UTS.
- A method to link the experimental DIC maps acquired during an *in-situ* SEM tensile test with FE analysis is proposed. Here, the boundary condition from DIC was successfully implemented for the FE simulation on the same microstructure as the microstructure observed experimentally.



## Chapter 9

# Low-temperature study of super duplex stainless steel containing $\sigma$ -phase

In the following chapter, an *in-situ* scanning electron microscope (SEM) study was conducted on a super duplex stainless steel (SDSS) containing 0%, 5% and 10%  $\sigma$ -phase. The material was heat treated at 850°C for 12 min and 15 min, respectively, to achieve the different amounts of  $\sigma$ -phase. The specimens were investigated at room temperature and at -40°C. The microstructure evolution during the deformation process was recorded using electron backscatter diffraction (EBSD) at different strain levels. Both  $\sigma$ -phase and  $\chi$ -phase were observed along the grain boundaries in the microstructure in all heat treated specimens. Cracks started to form after 3-4% strain and were always oriented perpendicular to the tensile direction. After the cracks formed, they were initially arrested by the matrix. At later stages of the deformation process, cracks in larger  $\sigma$ -phase constituents started to coalesce. When the tensile test was conducted at -40°C, the ductility increased for the specimen without  $\sigma$ -phase, but with  $\sigma$ -phase present, the ductility was slightly reduced. With larger amounts of  $\sigma$ -phase present, however, an increase in tensile strength was also observed. With  $\chi$ -phase present along the grain boundaries, a reduction of tensile strength was observed. This reduction seems to be related to  $\chi$ -phase precipitating at the grain boundaries, creating imperfections, but not contributing towards the increase in strength. Compared to the effect of  $\sigma$ -phase, the low temperature is not as influential on the materials performance.

## 9.1 Experimental

In the present study, *in-situ* SEM tensile tests have been conducted on an SDSS with 0%, 5% and 10%  $\sigma$ -phase present in the microstructure. The tensile tests were carried out at both room temperature and sub-zero temperature ( $-40^{\circ}\text{C}$ ). The microstructure was monitored with secondary electron imaging and EBSD. Images were acquired at different loading steps. From these results it is possible to observe the microstructure evolution and study the effects  $\chi$ -phase and  $\sigma$ -phase have on the microstructure during the deformation process. In order to monitor the microstructure evolution, a spindle-driven *in-situ* tensile device was placed in the vacuum chamber in the SEM. This equipment and how the specimen was cooled is described in Chapter 3.1. When performing the sub-zero experiments a cold finger was attached to the specimen as shown in Figure 3.3. A thermocouple was placed between the screw-head and specimen to record the temperature. The temperature was measured to be in the interval  $-35^{\circ}\text{C}$  and  $-45^{\circ}\text{C}$  for all specimens. However, the fluctuations in temperature are assumed to be due to the variable thermal resistance between the thermocouple and specimen. During loading, the specimen would move, and the thermocouple could change its position to no longer be placed between the screw-head and specimen. The temperature is assumed constant and reported as  $-40^{\circ}\text{C}$  in this paper.

The material was heat treated to achieve different amounts of  $\sigma$ -phase in the structure. Specimens were placed in a pre-heated oven at  $850^{\circ}\text{C}$  for 12 min, 15 min, 20 min, and 25 min. Cooling was performed by quenching in a water bath at room temperature. The heat treatment and the resulting amount of  $\sigma$ -phase achieved are summarized in Table 9.1. Phase maps from EBSD scans were used to quantify amounts of  $\sigma$ -phase present. These will not be exact measurements since they were only taken from the surface. The results from Elstad [56] was used to determine the heat treatment procedures used in this work. However,  $\sigma$ -phase precipitation was not constant with the same heat treatment being performed. Resulting in significant variation in  $\sigma$ -phase content during the heat treatment. All specimens in this work are heat treated as described in Table 9.1, but only specimens with amounts roughly in the region indicated in the third column were used for the *in-situ* tests. However, the deviation was less than 1% for the 5% specimen, measured by EBSD. For the specimens with larger amounts of  $\sigma$ -phase present, the deviation was 1-2%.

During this experiment, the microstructure was monitored using secondary electron imaging and EBSD. Images were acquired at different loading steps. At each step, the same area ( $350\text{ }\mu\text{m} \times 350\text{ }\mu\text{m}$ ) was recorded with EBSD, using a step size of  $1\text{ }\mu\text{m}$ . From these results, it is possible to observe the microstructure evolution and study the effects of  $\sigma$ -phase and  $\chi$ -phase on the microstructure during the



**Table 9.1:** Heat treatment and resulting amount of  $\sigma$ -phase in the specimens tested.

Temperature [°C]	Time [min]	Amount $\sigma$ -Phase [%]
-	-	0
850	12	5
850	15	10
850	20	15
850	25	20

deformation process. The EBSD acquisition settings are described in Chapter 3.2. Z-contrast imaging mode was used in order to distinguish  $\sigma$ -phase from  $\chi$ -phase during the experiments.

## 9.2 Results

### 9.2.1 Tensile testing

The tensile test curves for the specimens tested in this work are shown in Figure 9.1. As seen from these curves, the specimens with more than 10%  $\sigma$ -phase present exhibit a purely brittle behavior at room temperature and do not deform plastically before fracture. For that reason, these specimens are not suitable for *in-situ* and low-temperature investigations. Hence, only specimens containing roughly 5% and 10%  $\sigma$ -phase are further investigated. The specimens containing 0%  $\sigma$ -phase is included as a reference.

The stress-strain curves in Figure 9.1 show that small amounts of  $\sigma$ -phase greatly affect the tensile properties of the material. Another observation is the short time at the critical temperature it takes before the material is completely brittle (cf. Table 9.1). Specimens containing 15% and 20%  $\sigma$ -phase only deforms elastically before fracture. A general remark is that the yield strength increases at low temperature and the strain at fracture decrease with an increasing amount of intermetallic phases. Conversely, for the material not heat treated there is an increase in fracture strain. Also, the drops in the curves are from when the tensile test is paused for EBSD acquisition. A curious observation from the tensile test curve is that the tests containing 5%  $\sigma$ -phase have a lower yield strength and ultimate tensile strength (UTS). Figure 9.2 the microstructure of one of these specimens can be seen. Along the grain boundaries, the  $\chi$ -phase has precipitated as a thin continuous layer of approximately 200 nm thickness. This image was acquired during the test at room temperature, after 4% strain. In the center of the image is a  $\sigma$ -phase island, with two cracks marked with white circles. The  $\chi$ -phase also contains numerous small cracks, seen in the black circles in Figure 9.2, which seem to contribute towards a

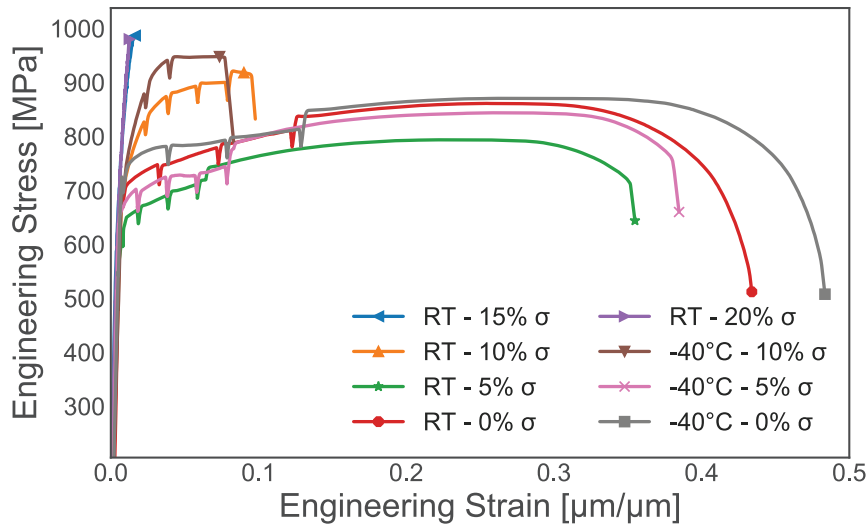


**Figure 9.1:** Tensile test curves obtained during the *in-situ* tensile tests. The drops in the curves are when the test is paused for acquiring EBSD data.

reduction in strength. When the amount of  $\sigma$ -phase increases, it also adds towards increased tensile strength.

In Figure 9.3 the fracture surfaces of the specimens tested at room temperature with 0%, 5% and 10%  $\sigma$ -phase are presented. To the left is an overview of the total surface area and to the right is a close up image showing the fracture surface at a higher magnification. The reference sample exhibits classic ductile fracture features; with a large reduction of area and the typical cup and cone dimpled structure at the surface. This is also expected when compared to the tensile test curve (Figure 9.1). In the specimen with 5%  $\sigma$ -phase present, Figure 9.3(b), some reduction in area is observed. However, not as great as in the test with 0%  $\sigma$ -phase present. Also, here the fracture surface appears to be mixed between a ductile dimpled structure and a brittle faceted structure. Conversely, the specimen containing 10%  $\sigma$ -phase, Figure 9.3(c), has all the characteristics of a brittle fracture. There is little to no reduction in area and completely faceted fracture surface, despite having a 10% fracture strain.

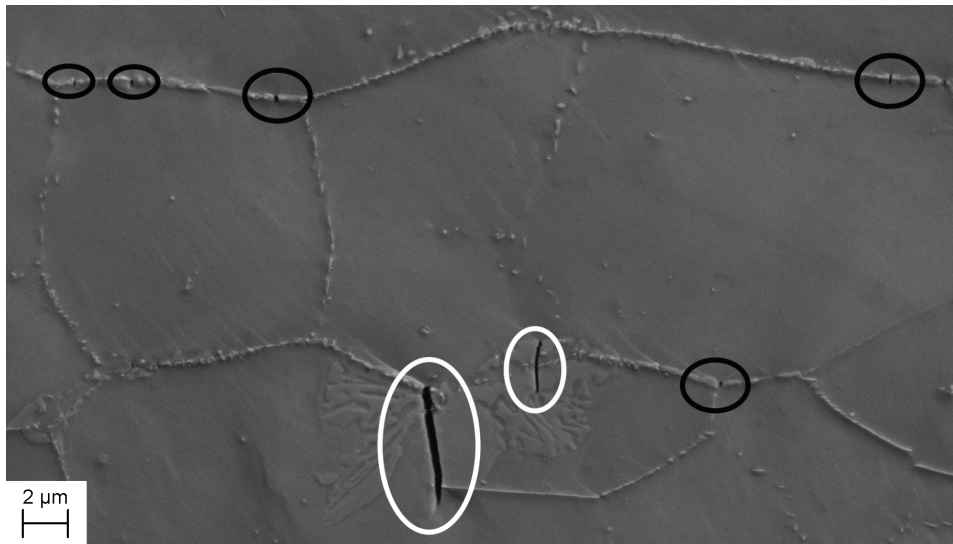


**Figure 9.2:** A close-up micrograph from the specimen containing 5%  $\sigma$ -phase, after 4% strain, tested at room temperature. Along the grain boundaries the  $\chi$ -phase can be found, and in the center, a larger island of  $\sigma$ -Phase is seen. The white circles show cracks in the  $\sigma$ -phase and the black circles show the cracks in the  $\chi$ -phase.

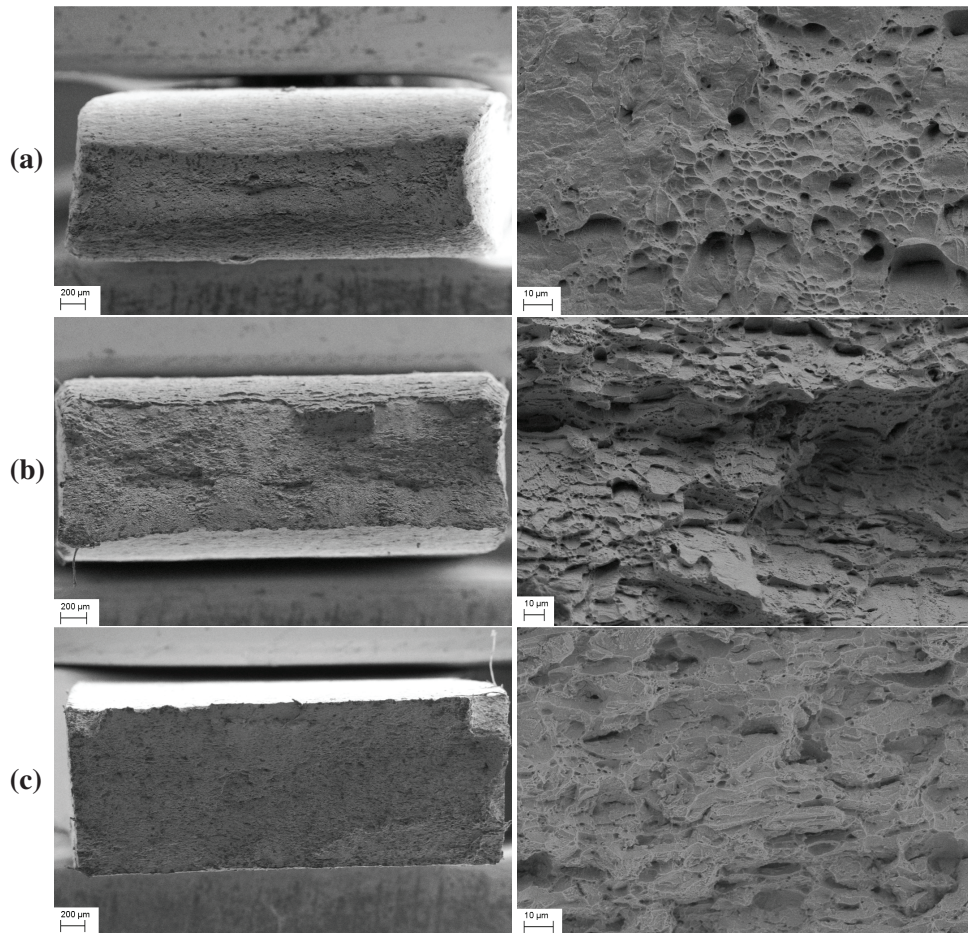


**Figure 9.3:** Fracture surfaces for the tensile test specimens with (a) 0%, (b) 5% and (c) 10%  $\sigma$ -phase, tested at room temperature. To the left is the total fracture area and to the right is a close up of the fracture surface.

### 9.2.2 Microstructure evolution

During the tensile tests, specimens containing different amounts of  $\sigma$ -phase were recorded using secondary electron imaging and EBSD to observe the microstructure throughout the deformation process. EBSD scans were obtained in the same area at approximately 0%, 2% and 6% strain of all tested specimens. Each of the tensile test curves in Figure 9.1 showed a drop when the test was paused for the acquisition of EBSD scans and secondary electron imaging. An observation is that the specimen with 0%  $\sigma$ -phase, tested at  $-40^{\circ}\text{C}$ , has a greater fracture strain than the specimen tested at room temperature.

In all specimens containing  $\sigma$ -phase, cracks were observed throughout the microstructure. These were observed to form after 3-4% strain in all the specimens, initiating in the  $\sigma$ -phase. Typical size of the cracks is seen in Figure 9.4. In Figure 9.5 two micrographs acquired at 6% and 10% strain show several micro-sized cracks in the  $\sigma$ -phase. During further straining, these cracks widen and appears to propagate deeper into the specimen. The ferrite and austenite grain boundaries act as a barrier for the cracks to propagate further. However, the larger constituents of  $\sigma$ -phase in the matrix contains large cracks, which eventually will propagate through the matrix. This is seen in the center of both frames in Figure 9.5. The microcracks in Figure 9.5(a) grow and in Figure 9.5(b) (black circle) they have coalesced, forming one large crack. A close up of this crack is shown in Figure 9.6. This is a phase map superimposed on to an image quality (IQ) map from EBSD, acquired with a step size of 50 nm. From this map, it can be seen that the crack propagates along grain boundaries when it is moving through the matrix. When the cracks start to coalesce, the material is close to fracturing, as the volume fraction of cracks is increasing fast. The micrograph in Figure 9.5(b) was acquired after 10% strain. The specimen fractured after being strained less than 1% further. It is possible to see how the cracks in the white circles widen from Figure 9.5(a) to 9.5(b). Presumably, they are propagating through the thickness of the material.



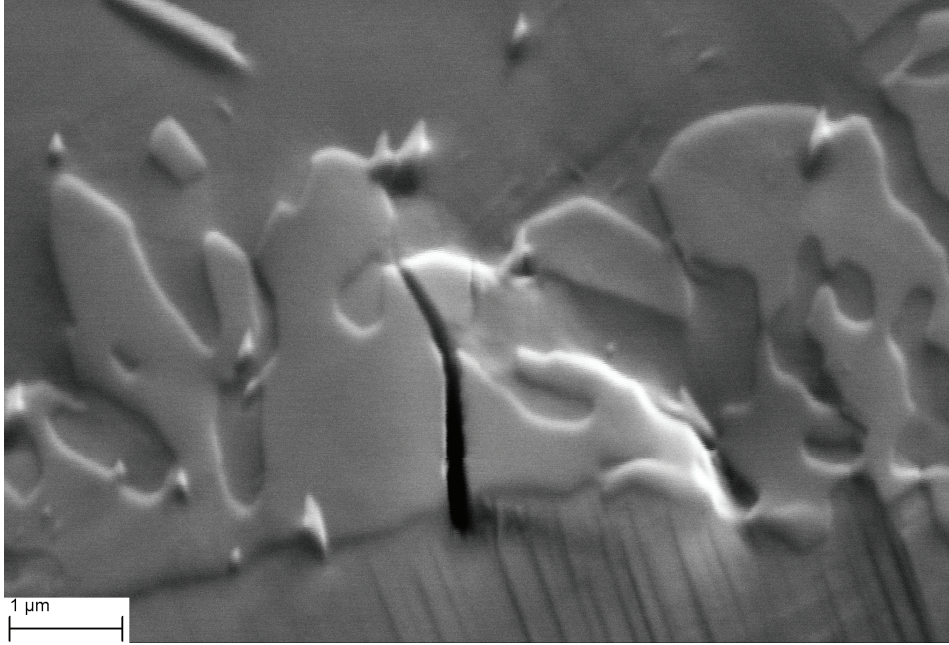


**Figure 9.4:** Micro-crack formed in the  $\sigma$ -phase during the initial stages of deformation. This frame is acquired after 6% strain, during the low temperature test with 5%  $\sigma$ -phase.

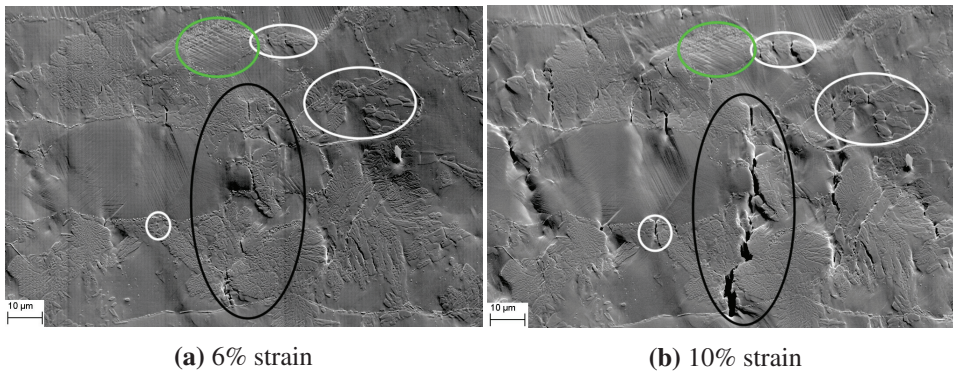


**Figure 9.5:** Micrographs of cracks formed in the  $\sigma$ -phase, taken from the test carried out at room temperature with 10%  $\sigma$ -phase present. Some cracks are restricted by the matrix while some propagate and coalesce. In the green circle, a heavily deformed austenite grain with cross-slip is seen. The white circles show microcracks restrained by the matrix and the large crack in the black circle was formed when many smaller cracks coalesce. A close up of this crack is shown in Figure 9.6.

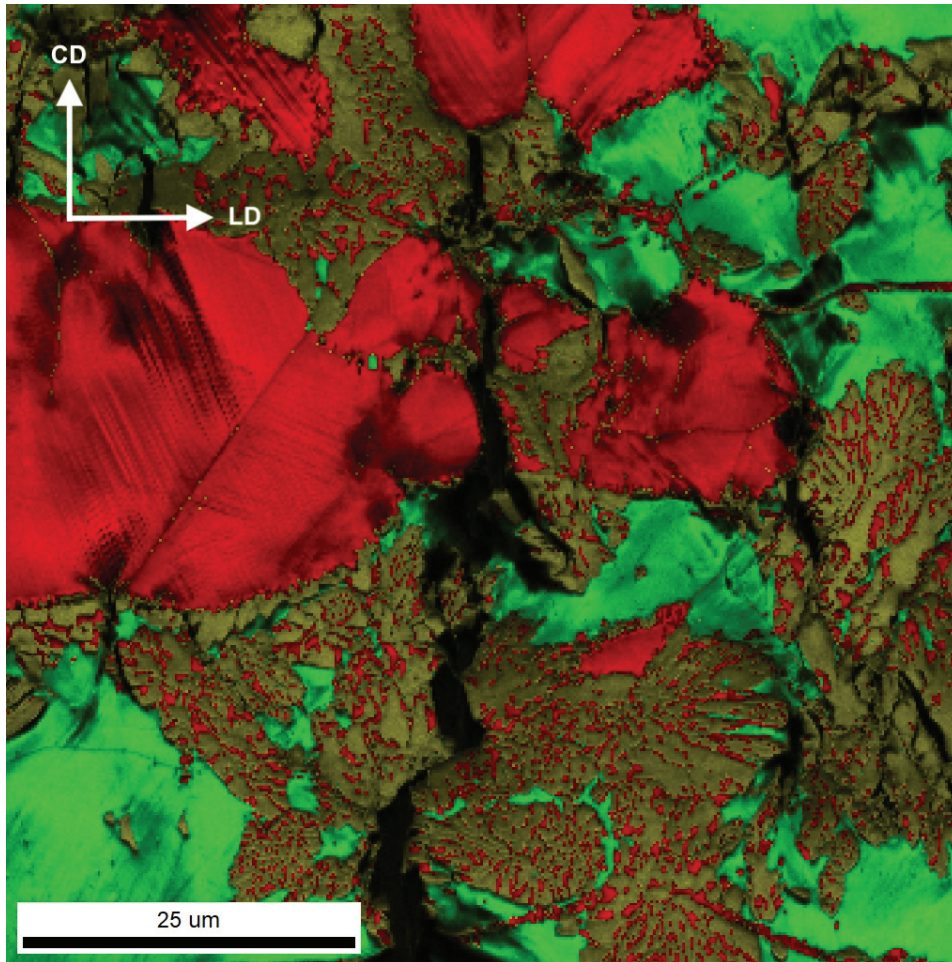


**Figure 9.6:** A close up of the crack shown in the black circle in Figure 9.5(b). This is a phase map with an IQ map overlay, acquired by EBSD. The red is austenite, green is ferrite and mustard yellow is  $\sigma$ -phase. The EBSD scan of this area was acquired with a step size 50 nm.



In Figure 9.7 the grain orientation spread (GOS) in the different tests are shown. All curves are obtained after 6% global strain. The GOS gives a quantitative description of the crystallographic orientation gradients in individual grains [157, 158]. It is found by calculating the average orientation deviation of all points in a grain from the average grain orientation. A higher spread would indicate that those grains are accommodating a larger deformation compared to a lower spread. However, as seen from the graphs, there is, in general, a low spread, with peaks for all tests around 1-2°. One notable deviation is the curves from the experiment at -40°C with 0%  $\sigma$ -phase present in Figure 9.7(b). These grains seem to accommodate more deformation, with a larger GOS distribution compared to other curves in Figure 9.7. Another observation is that the ferrite and austenite phases have nearly identical curves in the low-temperature test in Figure 9.7(b), while the phases are behaving differently at room temperature (Figure 9.7(a)). During the room temperature tests, all curves for ferrite grains have a taller peak compared to austenite grains. Also, the specimen with 5%  $\sigma$  has a higher GOS peak-value compared to the specimen containing 10%  $\sigma$ -phase when tested at -40°C. At room temperature, the austenite for both tests is fairly similar, while the ferrite is accommodating more deformation in the specimen with 5%  $\sigma$ -phase.

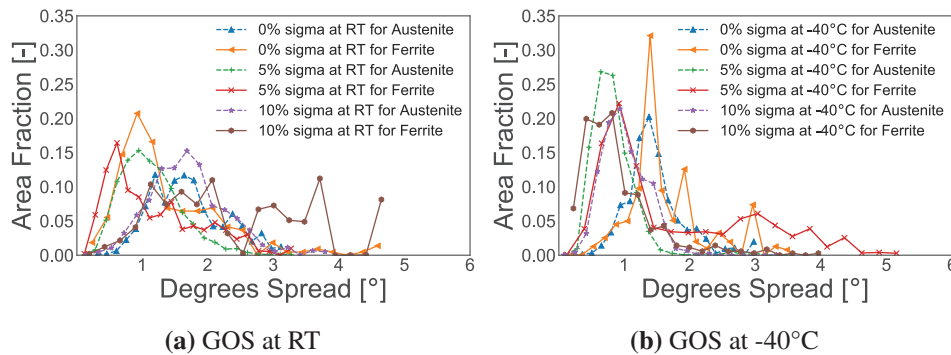


**Figure 9.7:** The grain orientation spread curves for the different specimens. (a) are the specimens tested at room temperature and (b) are the specimens tested at -40°C. All curves were taken after 6% strain. The solid lines are ferrite and the dashed lines are austenite.

### 9.3 Discussion

During this work, different specimens of super duplex stainless steel, containing varying amounts of  $\sigma$ -phase have been investigated, during an *in-situ* SEM tensile test. Each specimen was taken from a pipe segment and heat treated to get different amounts of  $\sigma$ -phase present. In general, it took roughly 10 min for the intermetallic phases to start forming at 850°C. During the next 10 min approximately 15% of  $\sigma$ -phase had precipitated, and the material had changed to an utterly brittle behavior,

as seen in Figure 9.1. It proved hard to meet our targets of 5% and 10%  $\sigma$ -phase, sometimes achieving 0% after 13 min and other times 15% after 15 min at 850°C. However, when the  $\sigma$ -phase starts to precipitate, it forms fast. Since duplex steels are being heat treated, typically at 1050°C, to achieve its final microstructure and often goes through other heat treatment, e.g. welding, a thorough control of the cooling rate is crucial. Also, no ductile-to-brittle transition was observed in this work. This was also the case in the work of Børvik et al. [52] and Kim et al. [98]. In these works duplex stainless steels (DSS) and SDSS, respectively, were tested at -50°C and no transition was observed. This means if the material has a ductile-to-brittle transition temperature, it is lower than -50°C.

As seen from Figure 9.1, small additions of  $\sigma$ -phase significantly reduces the ductility. This phenomenon is also well documented by others in previous studies [52, 53, 124, 125, 127]. However, in this study, the microstructure has been closely monitored during the tensile test to elucidate how it is accommodating the  $\sigma$ -phase in relation to deformation. The GOS in grains from the austenite and ferrite (shown in Figure 9.7) suggests that the presence of  $\sigma$ -phase and low temperature (-40°C) is influencing the deformation behavior of the matrix. A consequence of the presence of  $\sigma$ -phase is a lower fraction of ferrite. This altered phase balance, in combination with much harder particles containing numerous cracks, explains this difference in behavior between specimens with and without  $\sigma$ -phase present. However, the primary concern is the brittle nature of  $\sigma$ -phase. Cracks were observed in the  $\sigma$ -phase at 3-4% strain in all specimens, and all cracks were oriented perpendicular to the tensile direction. During the initial stages, the surrounding matrix restricts the growth of the crack. As the material is strained further, the cracks continue to widen. Eventually, the cracks start to propagate and coalesce. In specimens with higher amounts of  $\sigma$ -phase, the propagation occurs earlier, following the shorter distance to the nearest  $\sigma$ -phase inclusion. Also, the  $\sigma$ -phase particles are larger and the cracks, therefore, grow to a larger size.

The influence of temperature seems to make the  $\sigma$ -phase somewhat more brittle, resulting in a higher UTS and lower ductility. Austenite and ferrite grains seem to behave similarly during the low-temperature tests with  $\sigma$ -phase present when studying Figure 9.7(b). However, during the test at room temperature, the ferrite accommodates more deformation compared to the austenite. This is seen from the curves in Figure 9.7(a). The reason for the ferrite being more active is believed to be due to the fact that ferrite has 48 active slip systems at room temperature. Conversely, austenite has 12 slip systems and they are not dependent on temperature. With more slip systems available, there are more ways for the dislocations to propagate. In addition, the specimens without any  $\sigma$ -phase present have a larger GOS compared to the specimens containing  $\sigma$ -phase. This indicates that the presence of  $\sigma$ -phase in the

structure is retarding the deformation of ferrite and austenite. This is also observed through visual inspection of micrographs. There are more slip lines present, at equal strain level, in specimens without  $\sigma$ -phase present.

An observation of a specimen with 0%  $\sigma$ -phase, tested at  $-40^{\circ}\text{C}$ , has a greater fracture strain than the specimen tested at room temperature. It could be expected that the ferrite would have a brittle behavior at this temperature. A reason for this behavior might be due to the fact that SDSS is a highly alloyed material, containing elements improving the low-temperature performance of ferrite. In addition, the presence of austenite will improve low-temperature performance. It has been reported in several studies that austenitic steels have increased ductility at  $-50^{\circ}\text{C}$  in static uniaxial tensile tests [159–161].

Looking at the tensile test curve in Figure 9.1 for the tests with 5%  $\sigma$ -phase a lower tensile strength compared to the curve without any  $\sigma$ -phase present is observed. Conversely, a greater amount of  $\sigma$ -phase gives a contribution towards increased strength. An explanation for this can be the relative amount of  $\chi$ -phase present. As seen from the black circles in Figure 9.2, the  $\chi$ -phase precipitates along grain boundaries and is very brittle containing many cracks. These cracks result in the observed reduction of tensile strength. However, the size of the cracks in  $\chi$ -phase are subcritical and does not contribute towards a large reduction in ductility. The specimen containing 5%  $\sigma$ -phase is still a very ductile material, with a fracture strain of 35%–38%. This is in contrast to previously reported literature. As mentioned in the Introduction, it has been reported that specimens with only 0.5%  $\sigma$ -phase have significantly reduced fracture toughness. However, as discussed in Børvik et al. [52] and Børvik et al. [53], DSS are more sensitive towards  $\sigma$ -phase with respect to fracture toughness than to tensile ductility. In this work, all specimens were tested strain rate of  $1.11 \times 10^{-4} \text{ s}^{-1}$ . Also, the tensile tests were paused at certain intervals to acquire images and EBSD scans. In Børvik et al. [52], an increase in flow stress of about 30% was found for DSS when the strain rate was increased from  $5 \times 10^{-4} \text{ s}^{-1}$  to  $50 \text{ s}^{-1}$  based on tensile tests.

No strain-induced martensite was observed in any of the specimens investigated in this work. This indicates a very stable austenitic phase. However, this is not unexpected, since the  $\sigma$ -phase is formed at the expense of ferrite, not austenite. The alloying elements added to stabilize the austenitic phase are still present in the matrix. In the work by Kim et al. [98] there was also no martensite observed.

## 9.4 Concluding remarks

- The cracks in  $\chi$ -phase contributes towards a lower flow stress, but were not of critical size concerning a large reduction in tensile ductility. The specimens with small amounts of  $\chi$ -phase and  $\sigma$ -phase still retained a ductility of 35%.
- Visible cracks start to form after 3-4% strain, regardless of  $\sigma$ -phase content and they all form perpendicular to the tensile direction.
- During the initial stages of deformation, the cracks are constrained by the ferrite-austenite matrix. However, during the later stages, these cracks start to propagate through the material and coalesce. This occurs moments before fracture.
- The ferrite accommodates more deformation than austenite at room temperature tests, however, during low-temperature tests, both phases have a more equal behavior during deformation.
- At low temperature, with  $\sigma$ -present, the material had slightly higher flow stress and lower ductility. However, the amount of  $\sigma$ -phase present is the most important aspect when it comes to duplex steels. It alters the phase balance of ferrite and austenite and deteriorates the mechanical properties.



## Chapter 10

# Summary, conclusions and recommendations

### 10.1 Summary

In this thesis, one of the main objectives has been to develop an experimental technique for *in-situ* scanning electron microscope (SEM) tensile testing combined with digital image correlation (DIC) at the Department of Materials Science and Engineering (IMA), Norwegian University of Technology and Science (NTNU). The setup is based on the gold remodeling technique first presented by Di Gioacchino and Quinta da Fonseca [9] and Orozco-Caballero et al. [10], and tailored to the resources available at IMA. The goal was to create a speckled pattern on different two-phase steel specimens with sufficient contrast when imaging at large magnifications in an SEM. A representative area of the tested specimen containing this pattern was then recorded throughout an *in-situ* SEM tensile test. The in-house DIC software eCorr [11] was then used to analyze the resulting image series. The result is a strain map with a spatial resolution capable of resolving strains at a sub-grain level.

When creating a gold speckled pattern, three main steps are required. First, the specimen is polished to provide a smooth, flat and deformation free surface. Second, a continuous layer of gold with a thickness of 30  $\mu\text{m}$  - 80  $\mu\text{m}$  is coated on the polished specimen. Third, the specimen is placed on a hot plate with a gas flowing across the surface. The final result is a specimen covered with a random speckled pattern of gold nanoparticles. This pattern provides excellent contrast for the DIC analyses when imaging in backscatter electron (BSE) mode in an SEM. However, a challenge with this technique is the remodeling temperature and its possible

influence on different metals. The lowest temperature used in this work was 180°C, with a remodeling time of 96 hours (four days). The effect of the remodeling process on the steels used in this thesis was investigated in Chapter 4. From this study, both super duplex stainless steel (SDSS) and NVE36 were proven to withstand their respective remodeling procedures. In contrast, for dual-phase (DP) steels a bake hardening effect took place. As a result, DP steels experienced an increased yield strength and an introduction of a sharp yield point and Lüders band propagation. However, the DP steels exhibited the same rate of work-hardening after the initial differences at the yield point in the heat-treated specimen as in the as-received specimen.

In order to verify the DIC measurements, an independent technique, electron backscatter diffraction (EBSD), was used to measure grain rotations during deformation. This information is also available from the DIC results. This study is described in Chapter 5 and is performed on an SDSS specimen during the experiment. Here, EBSD scans were conducted before and after the *in-situ* SEM tensile test on the same area as investigated with DIC. Then ten different grains were selected, and the grain rotation of these was extracted from both DIC and EBSD before they were compared. 8 out of 10 grains measured returned the same rotation within 1°. In addition to the comparison between measured grain rotation in EBSD and DIC, other results also proved the validity of the DIC results from *in-situ* SEM tensile tests. By comparing the strain field with a phase map in a two-phased microstructure, as for NVE36 in Figure 6.9, it can be seen that the undeformed areas correspond well with the harder pearlitic phase. A final test was to perform a DIC analysis on image series of an undeformed specimen as described in the final paragraph in Chapter 5.3. Here, an unphysical strain of 1% was recorded. This error was most likely due to the image acquisition in the SEM and the stitching procedure. As a consequence of all these investigations, the DIC technique can be said to provide real strain measurements with insignificant errors in future tests.

After having established the gold remodeling method, the DIC results from the gold speckles were compared with DIC results obtained by using microstructural features of an etched surface in Chapter 6. The differences between the two techniques are numerous. Considering the etched surface, most microstructural features were grain boundaries and pearlite lamellas. As a consequence, large areas within grains did not provide sufficient contrast for DIC, thus restricting the maximum resolution. However, the technique is fast and does not expose the material to any elevated temperatures. In contrast, the gold remodeling method provides a finely dispersed gold speckle pattern on the surface, giving excellent contrast across the recorded area. The gold particles were achieved with the method described above and in Chapter 3.3. DIC with gold particles achieved a spatial resolution of 0.096



$\mu\text{m}$ , compared to  $2.24\ \mu\text{m}$  for the etched specimen. As a result, DIC with gold speckles can resolve slip lines within ferrite grains. Conversely, DIC with etched microstructure resolves local strains on grain level. However, it is less cumbersome and faster to perform the test on the etched specimen.

The NVE36 steel investigated in Chapter 6 was also investigated using numerical finite element (FE) simulations in Chapter 7. Macro DIC measurements recorded with a high-resolution digital camera were compared to results from FE simulations. The smooth specimen geometry in Figure 3.2(a) was first investigated to calibrate the material constants used in the numerical model. Then the results from the notched specimen geometry in Figure 3.2(b) were investigated using both DIC and FE simulations. The numerical results were in good agreement with the experimental observations, both in terms of force-displacement curves and strain fields. However, the local variations and the heterogeneous deformation in the material were, as expected, not captured in these simulations since the numerical model chosen assumes a homogeneous material behavior. This is not the case when studying the experimental results from the DIC measurements. To capture such local variations, a more exhaustive numerical model that takes the heterogeneity of the material into account is required.

In Chapter 8, DP steels were investigated using EBSD and *in-situ* SEM tensile testing combined with DIC. The different DP steels were DP500, DP600, DP800 and DP980. The EBSD results were used to characterize the microstructure and grain size of ferrite, size of the martensite islands, and amount of martensite present for each steel. From the DIC result, a localization of damage in the microstructure was studied in each of the DP steels. In DP500, DP600 and DP800 the most severe damage takes place within larger ferrite grains. DP800 differs from the other steels by having large cracks on the specimen surface. These cracks accommodate most of the damage during the tensile test. This is in contrast to the other steels where the most severe damage occurs in shear bands. In DP980 the amount of martensite constitutes an interconnected network. Here there are fewer larger ferrite grains, and most of the damage takes place on the interface between martensite and ferrite. In addition, DP800 was investigated using micromechanically-based FE simulations.

In addition to the experiments in Chapter 8, a FE analysis of DP800 was performed. Here, an RVE was generated from an experimentally acquired phase map. This is similar to what has been done earlier [152–154]. The boundary condition used during the simulation was the displacement of the boundary nodes in the DIC map. This is similar to using a sub-model [155, 156], where the boundary conditions are determined from a macro-model result and applied in sub-modeling analysis. In contrast, here the displacement from DIC boundary nodes are used as boundary conditions instead of a macro-model. To the author's knowledge, this is the first

instance of using the node displacements experimentally acquired from DIC maps on the microstructural level as boundary conditions during an FE simulation. In Figure 8.13 the two strain maps are compared. Here, the strain is localized on the interface between the ferrite and the martensite. However, the FE simulations are not able to capture the surface cracks observed in the *in-situ* SEM tensile test.

In addition to the work done on combining DIC with SEM, other *in-situ* SEM tensile test experiments were conducted on an SDSS containing  $\sigma$ -phase, combined with *in-situ* cooling. In Chapter 9, SDSS were tested with different amounts of  $\sigma$ -phase present at both room temperature and - 40°C. These *in-situ* SEM tensile tests showed that cooling had limited effect on the microstructure after intermetallic phases as  $\sigma$ -phase and  $\chi$ -phase had precipitated. However, the presence of these intermetallic phases strongly influenced the properties of the material and led to a degradation of the mechanical performance. The damage was initiated inside these phases. Initially, small cracks are constrained by the surrounding ferrite-austenite matrix. However, during the later stages, these cracks start to propagate before they coalesce through the material. This occurs immediately before fracture. Also, the ferrite was found to accommodate more deformation than austenite during the *in-situ* SEM tensile test conducted at room temperature. Conversely, during low-temperature tests, both phases have similar behavior during deformation.

## 10.2 Concluding remarks

In order to acquire images for DIC in SEM, a mapping software is needed to record a large field of view. This software acquires a given number of frames in a grid pattern, which can be stitched together later (see Figure 3.7). The area of each frame is determined by the gold particles, and in turn, this determines the number of images acquired for a given area. For high-resolution DIC, the horizontal field of view of each frame was in the range of 10  $\mu\text{m}$  for all acquisitions in this work. To obtain the best results possible, a very precise stage is required. Ideally, this should be a piezoelectric stage as they have superior precision when the stage moves between each frame acquired. The stage precision in the microscope used here is 1  $\mu\text{m}$ , and with a horizontal field of view of 10  $\mu\text{m}$ , an offset of 1  $\mu\text{m}$  is equal to an error of 10%. An error of this magnitude can lead to issues when stitching the images, resulting in errors and difficulties in correlating the DIC analysis. However, new piezoelectric stages are 500-1000 times more precise [141] and as a consequence, would improve the stitching process a great deal.

Throughout this work, the gold remodeling process has been somewhat unpredictable. This is believed to be due to the gold sputter coater used. Today, an Edwards S150B sputter coater is used, which is an older unit, where the control of the process parameters is not ideal. As a result, the quality and thickness of the gold

layer differ between each use. This will, in turn, affect the final pattern. Ideally, a more modern instrument, with better control over the processing parameters, should be used. However, initial investigations have shown that gold layers produced with modern coaters are more difficult to remodel. A theory for this is that modern gold sputter coaters produce a denser, more stable gold layer. As described in Chapter 2.2.3, the gold remodeling process relies on nucleation at voids within the gold layer. As a result, the continuous gold layers produced by the modern instruments are not remodeling into a speckled pattern using similar process parameters as here. A solution for this could be to increase the temperature. However, increasing the temperature is an undesirable measure since it may affect the microstructure and the mechanical behavior of the investigated material.

The speckled gold surface provides excellent contrast for DIC when imaging in BSE imaging mode in the SEM. The resulting strain fields can resolve individual slip lines inside grains. However, the application of a gold speckled pattern and the subsequent image acquisition process are time-consuming and require precise SEM equipment. In addition, the specimen is subjected to a heating process. Another method for creating contrast for the DIC in SEM images is to etch the microstructure. This is a faster method, where more images can be acquired throughout the deformation process. Also, no heating of the specimen is necessary. However, the contrast within grains is poor, and there have to be microstructural features providing some contrast for the DIC analysis. As a consequence, if heating of the specimen is not possible and strain information on a sub-grain level is not required, the etching method is a possible option. The technique chosen will mainly depend on the material, the specimen preparation methods available for this material, and the spatial resolution required.

The DP steels were characterized using EBSD and *in-situ* SEM tensile testing combined with DIC. The EBSD results revealed that the linear size of martensite decreased for increasing amounts of martensite until the martensite became a continuous network, then the linear size of martensite increased (see Figure 8.4). During the *in-situ* SEM tensile test the microstructure was monitored for all steels. In DP500, DP600 and DP800 the ferrite accommodated all of the damage. DP800 contained large cracks within the ferrite, accommodating most of the damage. These cracks were also observed to cut through martensite islands. Slip activity was the primary deformation mechanism in DP500, DP600 and DP980. Most of the damage in DP980 took place at the interface between ferrite and martensite.

The simulations performed on the DP800 steel demonstrates a possibility to link the DIC results obtained during an *in-situ* SEM tensile test with FE simulations. Here, the boundary conditions were successfully applied from the DIC results to the FE model. The results from these simulations have some differences between

the DIC strain map and FE strain map. However, it is important to note that this is a work in progress. The reason for including these preliminary results in this thesis is to highlight future possibility to link high-resolution DIC results acquired during an *in-situ* SEM tensile test with FE simulations on a real microstructure.

Low-temperature tests on duplex steels with and without intermetallic phases revealed that ferrite accommodates more of the deformation at room temperature compared to austenite. At lower temperatures ferrite and austenite both equally accommodate deformation. At lower temperatures, with the presence of intermetallic phases, the flow stress is slightly higher, and the ductility is slightly lower. Cracks start appearing after 3-4% strain and form perpendicular to the tensile direction. During the initial stages, these are arrested by the ferrite–austenite matrix. However, at later stages, shortly before fracture, the cracks start propagating through the material and coalesce. In general, SDSS performs well at lower temperatures, even with the presence of some intermetallic phases.

This work has shown that *in-situ* SEM tensile tests combined with high-resolution DIC provides valuable results for micromechanical investigations. Further, the results produced are verified through an independent technique. In addition, the DIC results can be incorporated into a modeling framework and used to verify the simulation results. This enables a further understanding of the material behavior.

### 10.3 Recommendations for further work

- Improve reliability and control of the gold remodeling process. The most unpredictable process today is the gold coating. A consistently smooth surface finish is produced using vibration polishing.
- Enable production of a wide range of speckled sizes tailored to the desired spatial resolution in the resulting DIC analysis.
- A future possibility is to acquire SEM images with different tilting angles and create 3D-DIC maps of deformed microstructures. From these results, it would be possible to investigate topological effects arising in the microstructure during plastic deformation. Also, by using 3D-DIC, the topography of the material can be measured, reducing the need for experimental equipment.
- Lower the remodeling temperature to expand the possible materials being investigated. The lowest remodeling temperature achieved here was 180°C and then the remodeling took 96 hours. One possibility is to incorporate the gold remodeling in the heat treatment of the material. As an example, the aging of aluminum occurs on these time scales and temperatures.

- Use the *in-situ* SEM-DIC technique on other materials and more complex specimen geometries (e.g. tensile test specimens with a pre-machined hole or shear specimens).
- Perform *in-situ* SEM-DIC experiments using different deformation modes (e.g. bending, compression or torsion)
- Further work on integrating the *in-situ* SEM-DIC results with numerical simulations. In addition to results from *in-situ* SEM-DIC, EBSD results can also be included in a future model which accounts for grain orientations.



# Bibliography

- [1] E. Fagerholt, “Field measurements in mechanical testing using close-range photogrammetry and digital image analysis”, PhD thesis, Norwegian University of Science and Technology, 2012. [Online]. Available: [http://folk.ntnu.no/egilf/Thesis\\_Egil\\_Fagerholt.pdf](http://folk.ntnu.no/egilf/Thesis_Egil_Fagerholt.pdf) (visited on 06/20/2019).
- [2] C. O. Paulsen, E. Fagerholt, T. Børvik, and I. Westermann, “Comparing In Situ DIC Results from an Etched Surface with a Gold Speckled Surface”, *Metals*, vol. 9, no. 8, p. 820, 2019. DOI: 10.3390/met9080820.
- [3] C. O. Paulsen, R. Broks, M. Karlsen, J. Hjelen, and I. Westermann, “Microstructure Evolution in Super Duplex Stainless Steels Containing  $\sigma$ -Phase Investigated at Low-Temperature Using In Situ SEM/EBSD Tensile Testing”, *Metals*, vol. 8, no. 7, p. 478, 2018. DOI: 10.3390/met8070478.
- [4] C. O. Paulsen, E. Fagerholt, T. Børvik, and I. Westermann, “Use of digital image correlation on local deformations in pearlitic steel during in situ tensile testing in SEM”, Trondheim, Norway: SCANDEM2016, 2016.
- [5] —, “Deformation and damaging mechanisms of a ferritic-pearlitic dual phase steel by in situ SEM tensile test”, Rhodes, Greece: 17<sup>th</sup> International Conference on Experimental Mechanics, 2016.
- [6] —, “Deformation and damage mechanisms in a high strength dual-phase steel investigated by in situ scanning electron microscope tensile testing and digital image correlation”, Brussels, Belgium: 17<sup>th</sup> European Mechanics of Materials Conference, 2016.
- [7] C. O. Paulsen, T. Børvik, and I. Westermann, “Deposition of gold for use of DIC on images acquired during an in situ SEM tensile test”, Houston, TX,



- USA: International Conference and Exhibition on Materials & Engineering, 2019.
- [8] M. Kristoffersen, M. Costas, T. Koenis, V. Brøtan, C. O. Paulsen, and T. Børvik, “On the ballistic perforation resistance of additively manufactured AlSi10Mg aluminium plates”, *Submitted for possible journal publication*, 2019.
- [9] F. Di Gioacchino and J. Quinta da Fonseca, “Plastic Strain Mapping with Sub-micron Resolution Using Digital Image Correlation”, *Experimental Mechanics*, vol. 53, no. 5, pp. 743–754, 2013. DOI: 10.1007/s11340-012-9685-2.
- [10] A. Orozco-Caballero, D. Lunt, J. D. Robson, and J. Quinta da Fonseca, “How magnesium accommodates local deformation incompatibility: A high-resolution digital image correlation study”, *Acta Materialia*, vol. 133, pp. 367–379, 2017. DOI: 10.1016/j.actamat.2017.05.040.
- [11] E. Fagerholt, *Ecorr user manual*. [Online]. Available: <http://folk.ntnu.no/egilf/ecorr/doc/> (visited on 06/18/2019).
- [12] H. Bhadeshia and S. R. Honeycombe, “Thermomechanical Treatment of Steels”, in *Steels: Microstructure and Properties*, Elsevier, 2017, pp. 271–301. DOI: 10.1016/B978-0-08-100270-4.00010-X.
- [13] G. E. Dieter and D. J. Bacon, *Mechanical metallurgy*. McGraw-hill New York, 1988, vol. 3, ISBN: 0071004068.
- [14] Centre for Advanced Structural Analysis, *Research Methodology and Scope*. [Online]. Available: <https://www.ntnu.edu/casa/research-casa> (visited on 02/20/2019).
- [15] A. L. Gurson, “Continuum Theory of Ductile Rupture by Void Nucleation and Growth: Part I - Yield Criteria and Flow Rules for Porous Ductile Media”, *Journal of Engineering Materials and Technology*, vol. 99, no. 1, pp. 2–15, 1977. DOI: 10.1115/1.3443401.
- [16] V. Tvergaard, “Influence of voids on shear band instabilities under plane strain conditions”, *International Journal of Fracture*, vol. 17, no. 4, pp. 389–407, 1981. DOI: 10.1007/BF00036191.
- [17] —, “On localization in ductile materials containing spherical voids”, *International Journal of Fracture*, vol. 18, no. 4, pp. 237–252, 1982. DOI: 10.1007/BF00015686.
- [18] W. H. Peters and W. F. Ranson, “Digital Imaging Techniques In Experimental Stress Analysis”, *Optical Engineering*, vol. 21, no. 3, pp. 427–432, 1982, ISSN: 0091-3286. DOI: 10.1117/12.7972925.

- 
- [19] M. A. Sutton, W. J. Wolters, W. H. Peters, W. F. Ranson, and S. R. McNeill, "Determination of displacements using an improved digital correlation method", *Image and Vision Computing*, vol. 1, no. 3, pp. 133–139, 1983. DOI: 10.1016/0262-8856(83)90064-1.
- [20] M. A. Sutton, C. Mingqi, W. H. Peters, Y. J. Chao, and S. R. McNeill, "Application of an optimized digital correlation method to planar deformation analysis", *Image and Vision Computing*, vol. 4, no. 3, pp. 143–150, 1986. DOI: 10.1016/0262-8856(86)90057-0.
- [21] M. A. Sutton, J. L. Turner, H. A. Bruck, and T. A. Chae, "Full-field representation of discretely sampled surface deformation for displacement and strain analysis", *Experimental Mechanics*, vol. 31, no. 2, pp. 168–177, 1991. DOI: 10.1007/BF02327571.
- [22] H. A. Bruck, S. R. McNeill, M. A. Sutton, and W. H. Peters, "Digital image correlation using Newton-Raphson method of partial differential correction", *Experimental Mechanics*, vol. 29, no. 3, pp. 261–267, 1989. DOI: 10.1007/BF02321405.
- [23] G. Besnard, F. Hild, and S. Roux, "'Finite-element' displacement fields analysis from digital images: Application to Portevin-Le Châtelier bands", *Experimental Mechanics*, vol. 46, no. 6, pp. 789–803, 2006. DOI: 10.1007/s11340-006-9824-8.
- [24] J. Réthoré, S. Roux, and F. Hild, "From pictures to extended finite elements: extended digital image correlation (X-DIC)", *Comptes Rendus - Mécanique*, vol. 335, no. 3, pp. 131–137, 2007. DOI: 10.1016/j.crme.2007.02.003.
- [25] J. Réthoré, F. Hild, and S. Roux, "Extended digital image correlation with crack shape optimization", *International Journal for Numerical Methods in Engineering*, vol. 73, no. 2, pp. 248–272, 2008. DOI: 10.1002/nme.2070.
- [26] gom, *ARAMIS Professional*. [Online]. Available: <https://www.gom.com/3d-software/gom-system-software/aramis-professional.html> (visited on 02/13/2019).
- [27] Image Systems, *DIC*. [Online]. Available: <http://www.imagesystems.se/tema/dic/> (visited on 02/13/2019).
- [28] Dantec Dynamics, *DIC - Digital Image Correlation*. [Online]. Available: <https://www.dantecdynamics.com/digital-image-correlation> (visited on 02/13/2019).
- [29] LaVision, *2D-/3D Stereo Digital Image Correlation*. [Online]. Available: <https://www.lavision.de/en/products/strainmaster/2d-stereo-dic/index.php> (visited on 02/13/2019).

- [30] G. Gruben, E. Fagerholt, O. S. Hopperstad, and T. Børvik, “Fracture characteristics of a cold-rolled dual-phase steel”, *European Journal of Mechanics - A/Solids*, vol. 30, no. 3, pp. 204–218, 2011. DOI: 10.1016/j.euromechsol.2011.01.004.
- [31] T. Nishiwaki, M. Murata, and Y. Yoshida, “Evaluation of neck shape of notched round-bar specimens during tensile test”, *Procedia Manufacturing*, vol. 15, pp. 1762–1768, 2018. DOI: 10.1016/j.promfg.2018.07.248.
- [32] V. Aune, E. Fagerholt, M. Langseth, and T. Børvik, “A shock tube facility to generate blast loading on structures”, *International Journal of Protective Structures*, vol. 7, no. 3, pp. 340–366, 2016. DOI: 10.1177/2041419616666236.
- [33] A. Buljac, T. Taillandier-Thomas, T. F. Morgeneyer, L. Helfen, S. Roux, and F. Hild, “Slant strained band development during flat to slant crack transition in AA 2198 T8 sheet: in situ 3D measurements”, *International Journal of Fracture*, vol. 200, no. 1, pp. 49–62, 2016. DOI: 10.1007/s10704-015-0052-z.
- [34] A. Buljac, F. Hild, L. Helfen, and T. F. Morgeneyer, “On deformation and damage micromechanisms in strong work hardening 2198 T3 aluminium alloy”, *Acta Materialia*, vol. 149, pp. 29–45, 2018. DOI: 10.1016/j.actamat.2018.01.026.
- [35] H. Schreier, J. J. Orteu, and M. A. Sutton, *Image correlation for shape, motion and deformation measurements: Basic concepts, theory and applications*. Springer, 2009, ISBN: 9780387787473. DOI: 10.1007/978-0-387-78747-3.
- [36] L. Allais, M. Bornert, T. Bretheau, and D. Caldemaison, “Experimental characterization of the local strain field in a heterogeneous elastoplastic material”, *Acta Metallurgica Et Materialia*, vol. 42, no. 11, pp. 3865–3880, 1994.
- [37] F. Lagattu, F. Bridier, P. Villechaise, and J. Brillaud, “In-plane strain measurements on a microscopic scale by coupling digital image correlation and an in situ SEM technique”, *Materials Characterization*, vol. 56, no. 1, pp. 10–18, 2006. DOI: 10.1016/j.matchar.2005.08.004.
- [38] Y. Ososkov, D. S. Wilkinson, M. Jain, and T. Simpson, “In-situ measurement of local strain partitioning in a commercial dual-phase steel”, *International Journal of Materials Research*, vol. 98, no. 8, pp. 664–673, 2007. DOI: 10.3139/146.101526.

- 
- [39] J. Kang, Y. Ososkov, J. D. Embury, and D. S. Wilkinson, “Digital image correlation studies for microscopic strain distribution and damage in dual phase steels”, *Scripta Materialia*, vol. 56, no. 11, pp. 999–1002, 2007. DOI: 10.1016/j.scriptamat.2007.01.031.
- [40] H. Ghadbeigi, C. Pinna, S. Celotto, and J. R. Yates, “Local plastic strain evolution in a high strength dual-phase steel”, *Materials Science and Engineering A*, vol. 527, no. 18-19, pp. 5026–5032, 2010. DOI: 10.1016/j.msea.2010.04.052.
- [41] M. Kapp, T. Hebesberger, and O. Kolednik, “A micro-level strain analysis of a high-strength dual-phase steel”, *International Journal of Materials Research*, vol. 102, no. 6, pp. 687–691, 2011. DOI: 10.3139/146.110522.
- [42] H. Ghadbeigi, C. Pinna, and S. Celotto, “Quantitative Strain Analysis of the Large Deformation at the Scale of Microstructure: Comparison between Digital Image Correlation and Microgrid Techniques”, *Experimental Mechanics*, vol. 52, no. 9, pp. 1483–1492, 2012. DOI: 10.1007/s11340-012-9612-6.
- [43] E. Lindfeldt, M. Ekh, K. Cvetskovski, and M. Schilke, “Using DIC to Identify Microscale Strain Fields from In-situ SEM Images of a Pearlitic Steel”, *Experimental Mechanics*, vol. 54, no. 9, pp. 1503–1513, 2014. DOI: 10.1007/s11340-014-9937-4.
- [44] F. Latourte, T. Salez, A. Guery, N. Rupin, and M. Mahé, “Deformation studies from in situ SEM experiments of a reactor pressure vessel steel at room and low temperatures”, *Journal of Nuclear Materials*, vol. 454, no. 1, pp. 373–380, 2014. DOI: 10.1016/j.jnucmat.2014.07.079.
- [45] S. Banerjee, T. Dasgupta, S. Mukherjee, M. Shome, P. C. Chakraborti, and S. K. Saha, “Digital image correlation for grain scale strain measurement in interstitial free high strength steel”, *Materials Science and Technology*, vol. 32, no. 4, pp. 328–337, 2016. DOI: 10/cfh8.
- [46] N. Ishikawa, K. Yasuda, H. Sueyoshi, S. Endo, H. Ikeda, T. Morikawa, and K. Higashida, “Microscopic deformation and strain hardening analysis of ferrite-bainite dual-phase steels using micro-grid method”, *Acta Materialia*, vol. 97, pp. 257–268, 2015. DOI: 10.1016/j.actamat.2015.06.037.
- [47] D. Yan, C. C. Tasan, and D. Raabe, “High resolution in situ mapping of microstrain and microstructure evolution reveals damage resistance criteria in dual phase steels”, *Acta Materialia*, vol. 96, pp. 399–409, 2015. DOI: 10.1016/j.actamat.2015.05.038.

- [48] J. P. M. Hoefnagels, C. C. Tasan, F. Maresca, F. J. Peters, and V. G. Kouznetsova, “Retardation of plastic instability via damage-enabled microstrain delocalization”, *Journal of Materials Science*, vol. 50, no. 21, pp. 6882–6897, 2015. DOI: 10.1007/s10853-015-9164-0.
- [49] C. C. Tasan, J. P. M. Hoefnagels, and M. G. D. Geers, “Microstructural banding effects clarified through micrographic digital image correlation”, *Scripta Materialia*, vol. 62, no. 11, pp. 835–838, 2010. DOI: 10.1016/j.scriptamat.2010.02.014.
- [50] D. A. Porter, K. E. Easterling, and G. D. W. Smith, “Dynamic studies of the tensile deformation and fracture of pearlite”, *Acta Metallurgica*, vol. 26, no. 9, pp. 1405–1422, 1978. DOI: 10.1016/0001-6160(78)90156-6.
- [51] H. Sidhom, H. Yahyaoui, C. Braham, and G. Gonzalez, “Analysis of the Deformation and Damage Mechanisms of Pearlitic Steel by EBSD and in-situ SEM Tensile Tests”, *Journal of Materials Engineering and Performance*, vol. 24, no. 7, pp. 2586–2596, 2015. DOI: 10.1007/s11665-015-1537-7.
- [52] T. Børvik, H. Lange, L. A. Marken, M. Langseth, O. S. Hopperstad, M. Aursand, and G. Rørvik, “Pipe fittings in duplex stainless steel with deviation in quality caused by sigma phase precipitation”, *Materials Science and Engineering A*, vol. 527, no. 26, pp. 6945–6955, 2010. DOI: 10.1016/j.msea.2010.06.087.
- [53] T. Børvik, L. A. Marken, M. Langseth, G. Rørvik, and O. S. Hopperstad, “Influence of sigma-phase precipitation on the impact behaviour of duplex stainless steel pipe fittings”, *Ships and Offshore Structures*, vol. 11, no. January 2015, pp. 1–13, 2014. DOI: 10.1080/17445302.2014.954303.
- [54] N. Lopez, M. Cid, and M. Puiggali, “Influence of  $\sigma$ -phase on mechanical properties and corrosion resistance of duplex stainless steels”, *Corrosion Science*, vol. 41, no. 8, pp. 1615–1631, 1999. DOI: 10.1016/S0010-938X(99)00009-8.
- [55] Z. Stradomski and D. Dyja, “Sigma phase precipitation in duplex phase stainless steels”, in *4th Youth Symposium on Experimental Solid Mechanics*, 2009, pp. 17–18. [Online]. Available: <http://www.yseesm.ing.unibo.it/Abstract/57Dyja.pdf> (visited on 05/25/2018).
- [56] K. R. Elstad, “In Situ Tensile Testing During Continuous EBSD Mapping of Super Duplex Stainless Steel Containing Sigma Phase”, Master Thesis, NTNU, 2016. [Online]. Available: <http://hdl.handle.net/11250/2418016> (visited on 05/25/2018).

- 
- [57] Y. Wang, Y. H. Yao, Z. P. Wang, Y. H. Jin, X. L. Zhang, and J. N. Liu, “Thermal ageing on the deformation and fracture mechanisms of a duplex stainless steel by quasi in-situ tensile test under OM and SEM”, *Materials Science and Engineering: A*, vol. 666, pp. 184–190, 2016. DOI: 10.1016/j.msea.2016.04.051.
- [58] F. Danoix, P. Auger, and D. Blavette, “Hardening of Aged Duplex Stainless Steels by Spinodal Decomposition”, *Microscopy and Microanalysis*, vol. 10, no. 3, pp. 349–354, 2004. DOI: 10.1017/S1431927604040516.
- [59] J. I. Goldstein, C. E. Lyman, D. E. Newbury, E. Lifshin, M. P. Echlin, L. Sawyer, D. C. Joy, and J. R. Micheal, *Scanning Electron Microscopy and X-ray Microanalysis*, 8. Springer, 2003, vol. 34, p. 690. DOI: 10.1007/978-1-4615-0215-9.
- [60] J. Hjelen, *Scanning elektron-mikroskopi*. Metallurgisk Institutt, NTH, 1989. [Online]. Available: [https://urn.nb.no/URN:NBN:no-nb\\_digibok\\_2013070305116](https://urn.nb.no/URN:NBN:no-nb_digibok_2013070305116) (visited on 05/25/2018).
- [61] Claudionico, *Interaction Volume*, 2013. [Online]. Available: [https://commons.wikimedia.org/wiki/File:Electron\\_Interaction\\_with\\_Matter.svg](https://commons.wikimedia.org/wiki/File:Electron_Interaction_with_Matter.svg) (visited on 08/31/2018).
- [62] Creative Commons, *Attribution-ShareAlike 4.0 International (CC BY-SA 4.0)*, 2013. [Online]. Available: <https://creativecommons.org/licenses/by-sa/4.0/> (visited on 07/29/2018).
- [63] T. E. Everhart and R. F. M. Thornley, “Wide-band detector for micro-microampere low-energy electron currents”, *Journal of Scientific Instruments*, vol. 37, no. 7, pp. 246–248, 1960. DOI: 10.1088/0950-7671/37/7/307.
- [64] E. de Chambost, *Everhart-Thornley Detector*. [Online]. Available: [https://commons.wikimedia.org/wiki/File:Everhart-Thornley\\_detector.JPG](https://commons.wikimedia.org/wiki/File:Everhart-Thornley_detector.JPG) (visited on 07/29/2018).
- [65] A. J. Schwartz, M. Kumar, B. L. Adams, and D. P. Field, *Electron backscatter diffraction in materials science*. Springer, 2009, vol. 2, pp. 1–403, ISBN: 9780387881355. DOI: 10.1007/978-0-387-88136-2.
- [66] BenBritton, *EBSP*. [Online]. Available: [https://commons.wikimedia.org/wiki/File:EBSD\\_Si.png](https://commons.wikimedia.org/wiki/File:EBSD_Si.png) (visited on 07/29/2018).
- [67] Creative Commons, *Attribution-ShareAlike 3.0 Unported (CC BY-SA 3.0)*, 2011. [Online]. Available: <http://creativecommons.org/licenses/by-sa/3.0/> (visited on 07/29/2018).

- [68] D. Stojakovic, “Electron backscatter diffraction in materials characterization”, *Processing and Application of Ceramics*, vol. 6, no. 1, pp. 1–13, 2012. DOI: 10.2298/PAC1201001S.
- [69] Z. Tang, J. Liang, Z. Xiao, and C. Guo, “Large deformation measurement scheme for 3D digital image correlation method”, *Optics and Lasers in Engineering*, vol. 50, no. 2, pp. 122–130, 2012. DOI: 10.1016/j.optlaseng.2011.09.018.
- [70] G. A. Holzapfel, *Nonlinear Solid Mechanics: A Continuum Approach for Engineering*. John Wiley & Sons, 2000, p. 470, ISBN: 9780471823193. DOI: 10.1023/A:1020843529530.
- [71] J. Quinta da Fonseca and L. Ko, “The kinematics of deformation and the development of substructure in the particle deformation zone”, in *IOP Conference Series: Materials Science and Engineering*, vol. 89, 2015, p. 012012. DOI: 10.1088/1757-899X/89/1/012012.
- [72] E. Polatidis, W.-N. Hsu, M. Šmíd, and H. Van Swygenhoven, “A High Resolution Digital Image Correlation Study under Multiaxial Loading”, *Experimental Mechanics*, 2018. DOI: 10.1007/s11340-018-00443-6.
- [73] D. Lunt, A. Orozco-Caballero, R. Thomas, P. Honniball, P. Frankel, M. Preuss, and J. Quinta da Fonseca, “Enabling high resolution strain mapping in zirconium alloys”, *Materials Characterization*, vol. 139, pp. 355–363, 2018. DOI: 10.1016/j.matchar.2018.03.014.
- [74] J. Kang, D. S. Wilkinson, J. D. Embury, and M. Jain, “Microscopic Strain Mapping Using Scanning Electron Microscopy Topography Image Correlation at Large Strain”, *The Journal of Strain Analysis for Engineering Design*, vol. 40, no. 6, pp. 559–570, 2005. DOI: 10.1243/030932405X16151.
- [75] A. E. B. Presland, G. L. Price, and D. L. Trimm, “Kinetics of hillock and island formation during annealing of thin silver films”, *Progress in Surface Science*, vol. 3, pp. 63–96, 1972. DOI: 10.1016/0079-6816(72)90006-8.
- [76] Y. Luo, J. Ruff, R. Ray, Y. Gu, H. J. Ploehn, and W. A. Scrivens, “Vapor-Assisted Remodeling of Thin Gold Films”, *Chemistry of Materials*, vol. 17, no. 20, pp. 5014–5023, 2005. DOI: 10.1021/cm051127w.
- [77] K. Sieradzki, K. Bailey, and T. L. Alford, “Agglomeration and percolation conductivity”, *Applied Physics Letters*, vol. 79, no. 21, pp. 3401–3403, 2001. DOI: 10.1063/1.1419043.
- [78] E. Jiran and C. V. Thompson, “Capillary instabilities in thin films”, vol. 19, no. 11, pp. 1153–1160, 1990. DOI: 10.1007/BF02673327.



- [79] S. K. Sharma and J. Spitz, “Agglomeration in chemically deposited silver films”, *Thin Solid Films*, vol. 66, no. 3, pp. L51 –L53, 1980. DOI: 10.1016/0040-6090(80)90398-3.
- [80] —, “Hillock formation, hole growth and agglomeration in thin silver films”, *Thin Solid Films*, vol. 65, no. 3, pp. 339–350, 1980. DOI: 10.1016/0040-6090(80)90244-8.
- [81] M. S. Rahman Khan, “Hillock and island formation during annealing of gold films”, *Bulletin of Materials Science*, vol. 9, no. 1, pp. 55–60, 1987. DOI: 10.1007/BF02744393.
- [82] W. A. Scrivens, Y. Luo, M. A. Sutton, S. A. Collette, M. L. Myrick, P. Miney, P. E. Colavita, A. P. Reynolds, and X. Li, “Development of Patterns for Digital Image Correlation Measurements at Reduced Length Scales”, *Experimental Mechanics*, vol. 47, no. 1, pp. 63–77, 2007. DOI: 10.1007/s11340-006-5869-y.
- [83] W. Callister and D. Rethwisch, *Materials science and engineering: an introduction*. John Wiley & Sons, 2007. DOI: 10.1016/0025-5416(87)90343-0.
- [84] Stannered, *BCC*. [Online]. Available: <https://commons.wikimedia.org/wiki/File:Cubic-body-centered.svg> (visited on 07/29/2018).
- [85] —, *FCC*. [Online]. Available: <https://commons.wikimedia.org/wiki/File:Cubic-face-centered.svg> (visited on 07/29/2018).
- [86] H. Bhadeshia and S. R. Honeycombe, “Formation of Martensite”, in *Steels: Microstructure and Properties*, Butterworth-Heinemann, 2017, pp. 135–177, ISBN: 9780750680844. DOI: 10.1016/B978-0-08-100270-4.00005-6.
- [87] Stannered, *BCT*. [Online]. Available: <https://commons.wikimedia.org/wiki/File:Tetragonal-body-centered.svg> (visited on 07/29/2018).
- [88] B. Verlinden, J. Driver, I. Samajdar, and R. D. Doherty, “Chapter 15 Thermo-mechanical processing of steel”, in *Pergamon Materials Series*, vol. 11, Pergamon, 2007, pp. 405–448, ISBN: 9780080444970. DOI: 10.1016/S1470-1804(07)80019-8.
- [89] Y. Granbom, “Structure and mechanical properties of dual phase steels - An experimental and theoretical analysis”, PhD thesis, KTH, 2010, ISBN: 9789174157406. [Online]. Available: <https://www.diva-portal.org/smash/get/diva2:353680/FULLTEXT10.pdf> (visited on 07/30/2019).

- [90] H. Bhadeshia and S. R. Honeycombe, “The Effects of Alloying Elements on Iron-Carbon Alloys”, in *Steels*, Butterworth-Heinemann, 2006, pp. 71–93, ISBN: 9780080462929. DOI: 10.1016/B978-075068084-4/50006-6.
- [91] International Molybdenum Association, *Practical Guidelines for the Fabrication of Duplex Stainless Steels*, 2014. [Online]. Available: [https://www.imoa.info/download\\_files/stainless-steel/Duplex\\_Stainless\\_Steel\\_3rd\\_Edition.pdf](https://www.imoa.info/download_files/stainless-steel/Duplex_Stainless_Steel_3rd_Edition.pdf) (visited on 09/19/2018).
- [92] D. M. Escriba, E. Materna-Morris, R. L. Plaut, and A. F. Padilha, “Chi-phase precipitation in a duplex stainless steel”, *Materials Characterization*, vol. 60, no. 11, pp. 1214–1219, 2009. DOI: 10.1016/j.matchar.2009.04.013.
- [93] M. Pohl, O. Storz, and T. Glogowski, “Effect of intermetallic precipitations on the properties of duplex stainless steel”, *Materials Characterization*, vol. 58, no. 1, pp. 65–71, 2007. DOI: 10.1016/j.matchar.2006.03.015.
- [94] Y. H. Lee, K. T. Kim, Y. D. Lee, and K. Y. Kim, “Effects of W substitution on  $\varsigma$  and  $\chi$  phase precipitation and toughness in duplex stainless steels”, *Materials Science and Technology*, vol. 14, no. 8, pp. 757–764, 1998. DOI: 10.1179/mst.1998.14.8.757.
- [95] A. F. Padilha and P. R. Rios, “Decomposition of Austenite in Austenitic Stainless Steels”, *ISIJ International*, vol. 42, no. 4, pp. 325–327, 2002. DOI: 10.2355/isijinternational.42.325.
- [96] R. W. Cahn, P. Haasen, and E. J. Kramer, “Volume 1: Structure of Solids”, in *Materials Science and Technology: A Comprehensive Treatment*, Wiley-VCH, 2005, ISBN: 3527313958.
- [97] —, “Volume 7: Constitution and Properties of Steel”, in *Materials Science and Technology: A Comprehensive Treatment*, Wiley-VCH, 2005, ISBN: 3527313958.
- [98] S.-K. Kim, K.-Y. Kang, M.-S. Kim, and J.-M. Lee, “Low-Temperature Mechanical Behavior of Super Duplex Stainless Steel with Sigma Precipitation”, *Metals*, vol. 5, no. 3, pp. 1732–1745, 2015. DOI: 10/ctkh.
- [99] A. P. Mouritz, “Fracture toughness properties of aerospace materials”, in *Introduction to Aerospace Materials*, Woodhead Publishing, 2012, pp. 454–468, ISBN: 9781855739468. DOI: 10.1533/9780857095152.454.
- [100] H. Bhadeshia and S. R. Honeycombe, “The Embrittlement and Fracture of Steels”, in *Steels: Microstructure and Properties*, Elsevier, 2017, pp. 303–341, ISBN: 9780081002704. DOI: 10.1016/B978-0-08-100270-4.00011-1.

- 
- [101] American Society for Testing and Materials, *ASTM E23 - 16b: Standard Test Methods for Notched Bar Impact Testing of Metallic Materials*. 2016. DOI: 10.1520/E0023-16B.
- [102] M. J. Perez-Martin, J. K. Holmen, S. Thomesen, O. S. Hopperstad, and T. Børvik, “Dynamic Behaviour of a High-Strength Structural Steel at Low Temperatures”, *Journal of Dynamic Behavior of Materials*, 2019. DOI: 10.1007/s40870-019-00206-x.
- [103] E. L. Grimsmo, A. H. Clausen, A. Aalberg, and M. Langseth, “A numerical study of beam-to-column joints subjected to impact”, *Engineering Structures*, vol. 120, pp. 103–115, 2016. DOI: 10.1016/j.engstruct.2016.04.031.
- [104] A. Saai, O. S. Hopperstad, Y. Granbom, and O. G. Lademo, “Influence of Volume Fraction and Distribution of Martensite Phase on the Strain Localization in Dual Phase Steels”, *Procedia Materials Science*, vol. 3, pp. 900–905, 2014. DOI: 10.1016/j.mspro.2014.06.146.
- [105] J. Christopher, B. K. Choudhary, E. Isaac Samuel, V. S. Srinivasan, and M. D. Mathew, “Tensile flow and work hardening behaviour of 9Cr-1Mo ferritic steel in the frame work of Voce relationship”, *Materials Science and Engineering A*, vol. 528, no. 21, pp. 6589–6595, 2011. DOI: 10.1016/j.msea.2011.05.026.
- [106] I. Westermann, O. S. Hopperstad, K. Marthinsen, and B. Holmedal, “Ageing and work-hardening behaviour of a commercial AA7108 aluminium alloy”, *Materials Science and Engineering A*, vol. 524, no. 1-2, pp. 151–157, 2009. DOI: 10.1016/j.msea.2009.06.036.
- [107] A. P. Pierman, O. Bouaziz, T. Pardoen, P. J. Jacques, and L. Brassart, “The influence of microstructure and composition on the plastic behaviour of dual-phase steels”, *Acta Materialia*, vol. 73, pp. 298–311, 2014. DOI: 10.1016/j.actamat.2014.04.015.
- [108] Q. Lai, L. Brassart, O. Bouaziz, M. Gouné, M. Verdier, G. Parry, A. Perlade, Y. Bréchet, and T. Pardoen, “Influence of martensite volume fraction and hardness on the plastic behavior of dual-phase steels: Experiments and micromechanical modeling”, *International Journal of Plasticity*, vol. 80, pp. 187–203, 2016. DOI: 10.1016/j.ijplas.2015.09.006.
- [109] U. F. Kocks and H. Mecking, “Physics and phenomenology of strain hardening: The FCC case”, *Progress in Materials Science*, vol. 48, no. 3, pp. 171–273, 2003. DOI: 10.1016/S0079-6425(02)00003-8.

- [110] G. I. Taylor, “The Mechanism of Plastic Deformation of Crystals. Part I. Theoretical”, *Proceedings of the Royal Society A: Mathematical, Physical and Engineering Sciences*, vol. 145, no. 855, pp. 362–387, 1934. DOI: 10.1098/rspa.1934.0106.
- [111] A. Ramazani, K. Mukherjee, A. Schwedt, P. Goravanchi, U. Prahl, and W. Bleck, “Quantification of the effect of transformation-induced geometrically necessary dislocations on the flow-curve modelling of dual-phase steels”, *International Journal of Plasticity*, vol. 43, pp. 128–152, 2013. DOI: 10.1016/j.ijplas.2012.11.003.
- [112] R.-M. Rodriguez and I. Gutiérrez, “Unified Formulation to Predict the Tensile Curves of Steels with Different Microstructures”, in *Materials Science Forum*, ser. Materials Science Forum, vol. 426-432, Trans Tech Publications, 2003, pp. 4525–4530. DOI: 10.4028/www.scientific.net/MSF.426-432.4525.
- [113] Y. Bergström, Y. Granbom, and D. Sterkenburg, “A Dislocation-Based Theory for the Deformation Hardening Behavior of DP Steels: Impact of Martensite Content and Ferrite Grain Size”, *Journal of Metallurgy*, vol. 2010, pp. 1–16, 2010. DOI: 10.1155/2010/647198.
- [114] M. Karlsen, J. Hjelen, Ø. Grong, G. Rørvik, R. Chiron, U. Schubert, and E. Nilsen, “SEM/EBSD based in situ studies of deformation induced phase transformations in supermartensitic stainless steels”, *Materials Science and Technology*, vol. 24, no. 1, pp. 64–72, 2008. DOI: 10/fn25rt.
- [115] M. Karlsen, Ø. Grong, M. Sjøfferud, J. Hjelen, G. Rørvik, and R. Chiron, “Scanning electron microscopy/electron backscatter diffraction - Based observations of martensite variant selection and slip plane activity in supermartensitic stainless steels during plastic deformation at elevated, ambient, and subzero temperatures”, *Metallurgical and Materials Transactions A: Physical Metallurgy and Materials Science*, vol. 40, no. 2, pp. 310–320, 2009. DOI: 10.1007/s11661-008-9729-5.
- [116] D. Lunt, T. Busolo, X. Xu, J. Quinta da Fonseca, and M. Preuss, “Effect of nanoscale  $\alpha_2$  precipitation on strain localisation in a two-phase Ti-alloy”, *Acta Materialia*, vol. 129, pp. 72–82, 2017. DOI: 10.1016/j.actamat.2017.02.068.
- [117] D. Lunt, X. Xu, T. Busolo, J. Quinta da Fonseca, and M. Preuss, “Quantification of strain localisation in a bimodal two-phase titanium alloy”, *Scripta Materialia*, vol. 145, pp. 45–49, 2018. DOI: 10.1016/j.scriptamat.2017.10.012.

- [118] J. Schindelin, I. Arganda-Carreras, E. Frise, V. Kaynig, M. Longair, T. Pietzsch, S. Preibisch, C. Rueden, S. Saalfeld, B. Schmid, J.-Y. Tinevez, D. J. White, V. Hartenstein, K. Eliceiri, P. Tomancak, and A. Cardona, “Fiji: an open-source platform for biological-image analysis”, *Nat. Methods*, vol. 9, no. 7, pp. 676–682, 2012. DOI: 10.1038/nmeth.2019.
- [119] S. Preibisch, S. Saalfeld, and P. Tomancak, “Globally optimal stitching of tiled 3D microscopic image acquisitions”, *Bioinformatics*, vol. 25, no. 11, pp. 1463–1465, 2009. DOI: 10.1093/bioinformatics/btp184.
- [120] C. A. Schneider, W. S. Rasband, and K. W. Eliceiri, “NIH Image to ImageJ: 25 years of image analysis”, *Nature Methods*, vol. 9, no. 7, pp. 671–675, 2012. DOI: 10.1038/nmeth.2089.
- [121] D. Zipperian, *Metallographic Handbook*. PACE Technologies, 2011, vol. 1, ISBN: 9788578110796.
- [122] DNV, *Newbuildings Materials and Welding - Metallic Materials*, 2011. [Online]. Available: <https://rules.dnvgl.com/docs/pdf/DNV/ruleship/2011-01/ts202.pdf> (visited on 03/28/2019).
- [123] Norsok Standard, “Materials selection”, *M-001, Rev*, vol. 4, 1994. [Online]. Available: <http://www.standard.no/pagefiles/1174/m-dp-001r1.pdf> (visited on 05/25/2018).
- [124] M. J. Huh, S. B. Kim, K. W. Paik, and Y. G. Kim, “Effect of Mo substitution by W on impact property of heat affected zone in duplex stainless steels”, *Scripta Materialia*, vol. 36, no. 7, pp. 775–781, 1997. DOI: 10.1016/S1359-6462(96)00377-6.
- [125] T. H. Chen and J. R. Yang, “Effects of solution treatment and continuous cooling on  $\sigma$ -phase precipitation in a 2205 duplex stainless steel”, *Materials Science and Engineering A*, vol. 311, no. 1-2, pp. 28–41, 2001. DOI: 10.1016/S0921-5093(01)00911-X.
- [126] T. H. Chen, K. L. Weng, and J. R. Yang, “The effect of high-temperature exposure on the microstructural stability and toughness property in a 2205 duplex stainless steel”, *Materials Science and Engineering A*, vol. 338, no. 1-2, pp. 259–270, 2002. DOI: 10.1016/S0921-5093(02)00093-X.
- [127] I. Zucato, M. C. Moreira, I. F. Machado, and S. M. Giampietri, “Microstructural Characterization and the Effect of Phase Transformations on Toughness of the UNS S31803 Duplex Stainless Steel Aged Treated at 850°C”, *Materials Research*, vol. 5, no. 3, pp. 385–389, 2002. DOI: 10.1590/S1516-14392002000300026.

- [128] Z. Cvijović and G. Radenković, “Microstructure and pitting corrosion resistance of annealed duplex stainless steel”, *Corrosion Science*, vol. 48, no. 12, pp. 3887–3906, 2006. DOI: 10.1016/j.corsci.2006.04.003.
- [129] J. Michalska and M. Sozańska, “Qualitative and quantitative analysis of  $\sigma$  and  $\chi$  phases in 2205 duplex stainless steel”, *Materials Characterization*, vol. 56, no. 4-5 Special Issue, pp. 355–362, 2006. DOI: 10.1016/j.matchar.2005.11.003.
- [130] C. M. Souza, H. F. G. Abreu, S. S. M. Tavares, and J. M. A. Rebello, “The  $\sigma$  phase formation in annealed UNS S31803 duplex stainless steel: Texture aspects”, *Materials Characterization*, vol. 59, no. 9, pp. 1301–1306, 2008. DOI: 10.1016/j.matchar.2007.11.005.
- [131] I. Calliari, M. Zanesco, and E. Ramous, “Influence of isothermal aging on secondary phases precipitation and toughness of a duplex stainless steel SAF 2205”, *Journal of Materials Science*, vol. 41, no. 22, pp. 7643–7649, 2006. DOI: 10.1007/s10853-006-0857-2.
- [132] N. Pettersson, S. Wessman, M. Thuvander, P. Hedström, J. Odqvist, R. F. Pettersson, and S. Hertzman, “Nanostructure evolution and mechanical property changes during aging of a super duplex stainless steel at 300°C”, *Materials Science and Engineering: A*, vol. 647, pp. 241–248, 2015. DOI: 10.1016/J.MSEA.2015.09.009.
- [133] E. Pereloma and I. Timokhina, “Bake hardening of automotive steels”, *Automotive Steels*, pp. 259–288, 2017. DOI: 10.1016/B978-0-08-100638-2.00009-2.
- [134] T. Waterschoot, K. Verbeken, and B. C. De Cooman, “Tempering Kinetics of the Martensitic Phase in DP Steel”, *ISIJ International*, vol. 46, no. 1, pp. 138–146, 2006. DOI: 10.2355/isijinternational.46.138.
- [135] L. Cheng, C. M. Brakman, B. M. Korevaar, and E. J. Mittemeijer, “The tempering of iron- carbon martensite; dilatometric and calorimetric analysis”, *Metallurgical Transactions A*, vol. 19, no. 10, pp. 2415–2426, 1988. DOI: 10.1007/BF02645469.
- [136] E. Kozeschnik and B. Buchmayr, “A contribution to the increase in yield strength during the bake hardening process”, *Steel Research*, vol. 68, no. 5, pp. 224–230, 1997. DOI: 10.1002/srin.199701783.
- [137] G. Zhu, W. Mao, and Y. Yu, “Calculation of misorientation distribution between recrystallized grains and deformed matrix”, *Scripta Materialia*, vol. 42, no. 1, pp. 37–41, 1999. DOI: 10.1016/S1359-6462(99)00306-1.

- [138] S. Maraghechi, J. P. M. Hoefnagels, R. H. J. Peerlings, and M. G. D. Geers, “Correction of scan line shift artifacts in scanning electron microscopy: An extended digital image correlation framework”, *Ultramicroscopy*, vol. 187, pp. 144–163, 2018. DOI: 10.1016/j.ultramicro.2018.01.002.
- [139] E. Maire, O. Bouaziz, M. Di Michiel, and C. Verdu, “Initiation and growth of damage in a dual-phase steel observed by X-ray microtomography”, *Acta Materialia*, vol. 56, no. 18, pp. 4954–4964, 2008. DOI: 10.1016/j.actamat.2008.06.015.
- [140] T. L. Anderson, *Solutions Manual: Fracture Mechanics: Fundamentals and Applications*. CRC press, 1995, p. 640, ISBN: 0849316561. DOI: 10.1016/j.jmps.2010.02.008.
- [141] kleindiek nanotechniek, *LT12830 Substage*. [Online]. Available: <https://www.kleindiek.com/fileadmin/public/brochures/lt12830.pdf> (visited on 03/29/2019).
- [142] S. S. Haltom, S. Kyriakides, and K. Ravi-Chandar, “Ductile failure under combined shear and tension”, *International Journal of Solids and Structures*, vol. 50, no. 10, pp. 1507–1522, 2013. DOI: 10.1016/j.ijsolstr.2012.12.009.
- [143] T. Børvik, S. Dey, and A. H. Clausen, “Perforation resistance of five different high-strength steel plates subjected to small-arms projectiles”, *International Journal of Impact Engineering*, vol. 36, no. 7, pp. 948–964, 2009. DOI: 10.1016/j.ijimpeng.2008.12.003.
- [144] J. Kristian, J. Ketil, O. Sture, and T. Børvik, “Ballistic impact of layered and case-hardened steel plates”, *International Journal of Impact Engineering*, vol. 110, pp. 4–14, 2017. DOI: 10.1016/j.ijimpeng.2017.02.001.
- [145] J. O. Hallquist, “Theory manual”, *Livermore software Technology corporation*, vol. 3, no. March, pp. 25–31, 2006.
- [146] B. H. Frodal, L. E. B. Dæhli, T. Børvik, and O. S. Hopperstad, “Modelling and simulation of ductile failure in textured aluminium alloys subjected to compression-tension loading”, *International Journal of Plasticity*, vol. 118, pp. 36–69, 2019. DOI: 10.1016/j.ijplas.2019.01.008.
- [147] A. Saai, Z. Wang, M. Pezzotta, J. Friis, A. P. Ratvik, and P. E. Vullum, “Multi-scale Modelling of Titanium Diboride Degradation Using Crystal Elasticity Model and Density Functional Theory”, in *Light Metals 2018*, Springer, 2018, pp. 1329–1336. DOI: 10.1007/978-3-319-72284-9\_174.



- [148] H. E. Exner, “Chapter 10 - Qualitative and Quantitative Surface Microscopy”, in *Physical Metallurgy*, Fourth edition, North-Holland, 1996, pp. 943–1032, ISBN: 9780444898753. DOI: 10.1016/B978-044489875-3/50015-6.
- [149] ABAQUS, “Version 6.12”, *Dassault Systèmes Simulia Corp*, 2012.
- [150] H. Ghassemi-Armaki, R. Maaß, S. P. Bhat, S. Sriram, J. R. Greer, and K. S. Kumar, “Deformation response of ferrite and martensite in a dual-phase steel”, *Acta Materialia*, vol. 62, pp. 197–211, 2014. DOI: 10.1016/j.actamat.2013.10.001.
- [151] J. Kadkhodapour, S. Schmauder, D. Raabe, S. Ziaei-Rad, U. Weber, and M. Calcagnotto, “Experimental and numerical study on geometrically necessary dislocations and non-homogeneous mechanical properties of the ferrite phase in dual phase steels”, *Acta Materialia*, vol. 59, no. 11, pp. 4387–4394, 2011. DOI: 10.1016/j.actamat.2011.03.062.
- [152] C. C. Tasan, M. Diehl, D. Yan, C. Zambaldi, P. Shanthraj, F. Roters, and D. Raabe, “Integrated experimental–simulation analysis of stress and strain partitioning in multiphase alloys”, *Acta Materialia*, vol. 81, pp. 386–400, 2014. DOI: 10.1016/J.ACTAMAT.2014.07.071.
- [153] C. C. Tasan, J. P. M. Hoefnagels, M. Diehl, D. Yan, F. Roters, and D. Raabe, “Strain localization and damage in dual phase steels investigated by coupled in-situ deformation experiments and crystal plasticity simulations”, *International Journal of Plasticity*, vol. 63, pp. 198–210, 2014. DOI: 10.1016/j.ijplas.2014.06.004.
- [154] S. K. Paul, “Real microstructure based micromechanical model to simulate microstructural level deformation behavior and failure initiation in DP 590 steel”, *Materials and Design*, vol. 44, pp. 397–406, 2013. DOI: 10.1016/j.matdes.2012.08.023.
- [155] C.-L. Lin, S.-F. Huang, H.-C. Tsai, and W.-J. Chang, “Finite element sub-modeling analyses of damage to enamel at the incisor enamel/adhesive interface upon de-bonding for different orthodontic bracket bases”, *Journal of Biomechanics*, vol. 44, no. 1, pp. 134–142, 2011. DOI: 10.1016/j.jbiomech.2010.08.038.
- [156] E. Narvydas and N. Puodziuniene, “Applications of sub-modeling in structural mechanics”, Kaunas, Lithuania: Proceedings of 19th International Conference. Mechanika. 2014, 2014.
- [157] D. Jorge-Badiola, A. Iza-Mendia, and I. Gutiérrez, “Study by EBSD of the development of the substructure in a hot deformed 304 stainless steel”, *Materials Science and Engineering A*, vol. 394, no. 1-2, pp. 445–454, 2005. DOI: 10.1016/j.msea.2004.11.049.

- [158] S. Mitsche, P. Poelt, and C. Sommitsch, “Recrystallization behaviour of the nickel-based alloy 80 a during hot forming”, *Journal of Microscopy*, vol. 227, no. 3, pp. 267–274, 2007. DOI: 10.1111/j.1365-2818.2007.01810.x.
- [159] T. S. Byun, N. Hashimoto, and K. Farrell, “Temperature dependence of strain hardening and plastic instability behaviors in austenitic stainless steels”, *Acta Materialia*, vol. 52, no. 13, pp. 3889–3899, 2004. DOI: 10.1016/j.actamat.2004.05.003.
- [160] K. J. Lee, M. S. Chun, M. H. Kim, and J. M. Lee, “A new constitutive model of austenitic stainless steel for cryogenic applications”, *Computational Materials Science*, vol. 46, no. 4, pp. 1152–1162, 2009. DOI: 10.1016/j.commatsci.2009.06.003.
- [161] W. S. Park, S. W. Yoo, M. H. Kim, and J. M. Lee, “Strain-rate effects on the mechanical behavior of the AISI 300 series of austenitic stainless steel under cryogenic environments”, *Materials and Design*, vol. 31, no. 8, pp. 3630–3640, 2010. DOI: 10.1016/j.matdes.2010.02.041.



# Appendix A

Christian Oen Paulsen, Egil Fagerholt, Tore Børvik, Ida Westermann

**Comparing in situ DIC results from an etched surface with a gold speckled surface**

Metals 9 (2019) 820.





## Article

# Comparing In Situ DIC Results from an Etched Surface with a Gold Speckled Surface

Christian Oen Paulsen <sup>1,2,\*</sup>, Egil Fagerholt <sup>2,3,†</sup>, Tore Børvik <sup>2,3,†</sup> and Ida Westermann <sup>1,2,†</sup>

<sup>1</sup> Department of Materials Science and Engineering, Norwegian University of Science and Technology (NTNU), NO-7491 Trondheim, Norway

<sup>2</sup> Centre for Advanced Structural Analysis (CASA), NTNU, NO-7491 Trondheim, Norway

<sup>3</sup> Structural Impact Laboratory (SIMLab), Department of Structural Engineering, NTNU, NO-7491 Trondheim, Norway

\* Correspondence: christian.o.paulsen@ntnu.no; Tel.: +47-73-59-49-21

† These authors contributed equally to this work.

Received: 22 June 2019; Accepted: 22 July 2019; Published: 25 July 2019



**Abstract:** A ferrite-pearlite two-phase steel was investigated using in situ scanning electron microscope (SEM) tensile testing combined with digital image correlation (DIC). Two different speckled patterns were used and compared. The first pattern was achieved by etching a polished surface in order to reveal the microstructural features. Second, a gold speckled pattern was obtained. Here, a continuous layer of gold was applied to a polished surface. This continuous layer was remodeled into gold nanoparticles by keeping the specimen at 180 °C for 96 h with an Ar/Styrene mixture flowing across the specimen surface. The result is randomly distributed gold nanoparticles on the surface. These particles and the etched microstructure were then used by the DIC software to correlate an image series to obtain the local strain field of the material. The differences between the two techniques are numerous. Considering the etched surface, most microstructural features were grain boundaries and pearlite lamellas. As a consequence, large areas within grains did not provide sufficient contrast for DIC, thus restricting maximum resolution. However, the technique is fast and does not expose the material to any elevated temperatures. In contrast, the gold remodeling method provides a finely dispersed gold speckle pattern on the surface, giving excellent contrast across the recorded area. DIC with gold particles achieved a spatial resolution of 0.096 µm, compared to 2.24 µm in the DIC for the etched specimen. As a result, DIC with gold speckles can resolve slip lines. Conversely, DIC with etched microstructure resolves local strains on grain level. However, it is less cumbersome and faster to perform the test on the etched specimen.

**Keywords:** digital image correlation; in situ testing; scanning electron microscopy; strain localization

## 1. Introduction

The industry commonly uses steels with a ferritic-pearlitic microstructure. In such steels, the properties of the soft ferrite are combined with the harder pearlite to achieve a good combination of strength and ductility [1]. Knowing the heterogeneous strain field at the grain scale is an important tool in order to understand the relationship between the microstructure and the elastoplastic response. Elastic deformations are reversible, meaning that the material returns to its original shape when the applied loads are released. On the other hand, plastic deformations are permanent, introducing non-reversible changes and damage to the material. During plastic deformation, typically micro-void formation or micro-cracking is the dominating damaging mechanism leading to fracture [2]. Thus, a thorough understanding of these processes is important in the design of steel structures.

Some studies have looked into the deformation process of pearlite. For instance, an early work using the in situ scanning electron microscope (SEM) technique was performed by Porter et al. [3].

They were able to study the effect of coarse versus fine pearlite and show how the deformation process of the two phases differed. Building on their work, Sidhom et al. [4] combined in situ SEM with electron backscatter diffraction (EBSD) to correlate the observations with the different orientations of the grains. The conclusion from this investigation was that coarse pearlite has a more brittle behavior than fine pearlite during tensile deformation. As a result, the damage caused by the plastic deformation was found to be somewhat delayed by incorporating a fine pearlitic structure.

Peters and Ranson [5] published one of the earliest papers on the use of digital image correlation (DIC) in mechanical testing and later others further developed the technique [6–13]. Recently, the DIC technique has caught interest for images acquired with an SEM [14–16]. All that is required for DIC is an image series of the desired region containing a speckled pattern with sufficient contrast and the pixel-to-mm ratio. Using an SEM, it is possible to record high-resolution images with high magnification. These images can be correlated using DIC to get strain fields which can resolve the slip bands within grains (see, e.g., [16–20]). A challenge is to have a speckled pattern suitable for DIC analysis. Several different approaches are taken, depending on the desired resolution. Allais et al. [21] developed a technique using a micro-grid to measure the local strains in a dual phase (DP) steel. This micro-grid consisted of several hundred gold dots. These were deposited on the surface using a microelectrolithographic technique. The technique is briefly described here and is based on Appendix A in Allais et al. [21]. First, the surface is covered with a thin layer of an electro-sensitive resin. To polymerize the resin, it was cured for 30 min at 140 °C. The desired pattern was drawn using the SEM electron beam. This irradiation lowered the molecular weight of the resin, making it easily soluble. After the dotted pattern was created, the resin inside the dots was dissolved using a solvent, before a gold layer was applied to the specimen surface. Finally, the remaining resin was then dissolved using a different solvent, leaving only the dotted gold micro-grid pattern on the surface. The displacement of the gold dots during an in situ SEM tensile test was used to calculate the strain field in the microstructure. The resulting spatial resolution was 0.5–1 µm. Several other techniques have been utilized over the years to study the local straining of a microstructure, including, but not limited to: etching, surface deposition and creation of micro-grids using electron beam lithography [16,22–25].

One technique not mentioned above is to use secondary electron images of the microstructure. These images can then be correlated to find local strain values and distributions. The technique relies on using the variation of gray-scale values in the recorded micrographs without any adaptations (such as adding a micro-grid or a speckled pattern). The features in the microstructure (grain boundaries, particles, different phases, etc.) are used as reference points for the subsequent DIC analysis. Using the microstructure of the specimen to correlate images was first shown by Kang et al. [26] and later by others [15,27–32]. Ghadbeigi et al. [27] compared results from DIC using the microstructure as a reference to the micro-grid method. The results were quantitatively similar for the two techniques, demonstrating the reliability of using the microstructure directly for the DIC analysis. Banerjee et al. [30] correlated SEM topography images based on micrographs to investigate the local strain variations in a grain of high strength steel. The applied global strain in that study was 8.3%, but locally, inside a grain, strain values as high as 150% were observed. Other grains were found to have a local average strain value of 1.9%. In the study by Kang et al. [26], a micrograph was acquired for every 3–5% of macroscopic strain and then loaded into a DIC software and correlated to obtain the microscopic strain field.

Recent advances in in situ SEM DIC is the ability to get higher spatial resolution. For instance, Orozco-Caballero et al. [18] achieved a spatial resolution of 44 nm in their strain fields. This fine resolution is accomplished by using a refined method developed by Gioacchino and da Fonseca [16]. Orozco-Caballero et al. [18] applied a gold speckled pattern on a magnesium alloy. This pattern provides great contrast between the specimen surface and the gold particles in an SEM BSE image, providing excellent conditions for DIC analysis. The resulting strain field in a magnesium alloy is capable of resolving slip bands within grains, thereby quantifying the strain ratio between these bands, the grain boundaries, and the overall average strain.



The main objective of the current study was to demonstrate the difference between two techniques for in situ SEM tensile testing. In these techniques, two different specimen preparation methods were used, in combination with two different SEM imaging modes. For both methods, the same steel was used, i.e., an NVE36 ferritic-pearlitic rolled plate steel. The first method presented uses an etched specimen surface. Here, the grain boundaries and the lamellar structure of pearlite provides contrast for the DIC using an secondary electron (SE) imaging mode when recording the microstructure. However, inside the ferrite grains, there is little contrast for the DIC. The second method uses a gold speckled pattern applied to correlate the images in the DIC. This method provides excellent contrast for DIC when recording in backscatter electron (BSE) imaging mode. Compared to etching the specimen surface to obtain contrast for SEM imaging, applying a gold speckled pattern takes much longer time and exposes the specimen for an elevated temperature. However, the spatial resolution in the DIC is much higher.

## 2. Material

The specimens used in this study were taken from a commercial ferritic-pearlitic rolled steel plate, named NVE36, with chemical composition as listed in Table 1. This steel contains 75% ferrite and 25% pearlite, with an average grain diameter of 15  $\mu\text{m}$ . Figure 1 illustrates the microstructure of the material, where the darker grains are ferrite, and the lighter grains are pearlite. Micro-hardness measurements of the ferrite and pearlite gave average hardness values of 204 HV and 283 HV, respectively. The hardness measurements were performed with 10 g of force and a holding time of 15 s. The combination of the two phases gives an alloy with superior strength and ductility compared to having a pure ferritic or pearlitic microstructure. To make sure that the observed area is in the necked region and close to the fracture initiation point, a notched specimen geometry was chosen. All specimens used in this work were taken parallel to the rolling direction of the larger plate, with a thickness of 10 mm, illustrated in Figure 2a. Then, the specimens were spark eroded to a 2 mm thickness to the dimensions shown in Figure 2b. To reveal the microstructure in SE imaging mode, the specimens were prepared by mechanical grinding and polishing to 1  $\mu\text{m}$ , followed by etching for 10 s in 2% Nital. In addition, the specimens were prepared for EBSD analysis and subsequent application of a gold speckled pattern (see Section 4.3). These specimens were also prepared by mechanical grinding and polishing to 1  $\mu\text{m}$ , before vibration polishing using a VibroMet2 from Buehler (Lake Bluff, IL, USA) for 16 h. In the vibration polisher, there is a suspension with pH 8 containing  $\text{SiO}_2$  particles with the size 0.02  $\mu\text{m}$ . Finally, all specimens were rinsed in an ultrasonic bath with acetone for 5 min to obtain a clean surface finish.

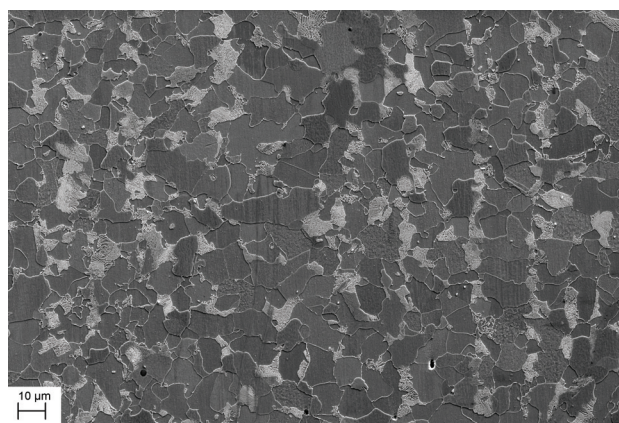
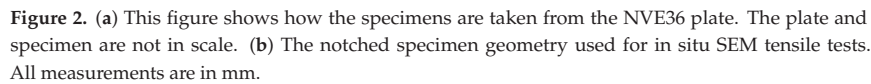


**Figure 1.** Secondary electron image of the undeformed microstructure. The darker areas are ferrite grains and the lighter areas are pearlite grains.

Element	C	Si	Mn	P	S	Cr	Mo	Ni	Cu	Al	Nb	V	Ti
Content	0.18	0.5	0.9–1.6	0.035	0.035	0.2	0.08	0.4	0.35	0.02	0.03	0.05	0.01



Digital Image Correlation (DIC) has become a well-established tool for full-field displacement and strain measurements during mechanical testing. Various formulations of DIC exist in the literature, where the principle of optical flow forms the basis for the technique. The traditional formulation of DIC (see, e.g., Sutton et al. [6]) is the subset-based formulation, where subsets are optimized individually. In contrast, the finite-element (FE) formulation of DIC proposed by Besnard et al. [10] is a global approach where the parameters describing the displacement field are solved in a single global procedure. FE-DIC uses a mesh of two-dimensional elements to describe the displacement field, and the degrees-of-freedom (DOF) of the elements are optimized for each image in the series. Various types of elements have been investigated in the literature (see, e.g., Réthoré et al. [12]) and the technique is in principle independent of the choice of the element type. However, Q4 elements (elements with four nodes and eight DOFs) are the most used. The reader is referred to Fagerholt [34] for the mathematical details of the FE-DIC approach applied in this study.

From the principle of optical flow, DIC assumes all images in a series to be a transformed version of the reference image, where the displacement field gives the transformation. Thus, effects such as gray-scale pixel noise (or signal-to-noise ratio), light variations, propagating cracks, etc., cause increasing residuals in the DIC optimization process and pose challenges to the algorithm. The pixel noise must be considered in the design and setup of the experiment, in terms of choice of camera, lighting conditions, room temperature, etc. In the analysis stage, it is possible to increase the element size to overcome a high noise level, with the downside of losing resolution in the displacement field measurements. Temporal changes in the ambient lighting conditions during the test may be optimized by a normalization of the pixel gray values. Here, an elementwise normalization based on both mean and variance of the gray-scale values is applied, i.e., using a zero-mean normalized sum of squared differences (ZNSSD) criterion [14]. Updating of reference images in the DIC algorithm acts as a reset of gray-scale value residuals and can be used when the appearance of the specimen surface has deviated significantly from the reference image. Reference updates may be challenging and should, in general,

be reduced to a minimum because errors in the displacement field are accumulated, as also discussed by Tang et al. [35].

When studying the etched specimen, reference updates were crucial to be able to analyze the specimen until fracture and to overcome the deviations in specimen surface appearance, as seen in the SE micrographs. Further, a robust DIC algorithm needs functionality to overcome large jumps in displacements between succeeding images in a series. As the series of micrographs recorded in the SEM needed continuous manual re-positioning of the specimen, such jumps were present for all micrographs. To overcome this, a multi-scale coarse-search procedure motivated by Hild et al. [36] was applied. Calibration of the SEM recordings (drift and spatial distortion) [14] were also considered. However, due to the relatively low magnification and short exposure time in these tests, these effects were assumed small. The error caused by spatial distortion was, however, quantified in a simple test with a rigid moving specimen (see the last paragraph in Section 5).

Most strains in this study are referred to as average engineering strains. These strains are calculated using virtual extensometers in the DIC software, defined as a vector between two material points in the DIC mesh. The average engineering strain ( $\bar{\epsilon}_{DIC}$ ) is then calculated as

$$\bar{\epsilon}_{DIC} = \sum_{i=1}^N e_{DIC_i}, \quad e_{DIC_i} = \frac{\Delta L}{L_0} \quad (1)$$

where  $L_0$  is the initial length of the virtual extensometer (vector), and  $\Delta L$  is the change in length of the virtual extensometer (vector).

Local strain at the nodes is calculated as principal logarithmic strains at element level (see, e.g., [37]). Here,  $\mathbf{X} = (X, Y)$  refers to the image coordinates in the reference configuration and bold variables denotes vectors. First, the deformation gradient  $\mathbf{F} = \mathbf{F}(\mathbf{X}, t) = \mathbf{1} + \partial \mathbf{u} / \partial \mathbf{X}$  is found from the measured two-dimensional displacement field  $\mathbf{u} = \mathbf{u}(\mathbf{X}, t)$  for a particular location  $\mathbf{X}$  and time  $t$ . The right Cauchy–Green tensor is then calculated as

$$\mathbf{C} = \mathbf{F}^T \mathbf{F} \quad (2)$$

The principal stretches  $\mu_i, i = 1, 2$  are found by solving the eigenvalue problem for the right Cauchy–Green tensor

$$(\mu_i^2 \mathbf{1} - \mathbf{C}) \mathbf{n}_i = \mathbf{0} \quad (3)$$

where the vectors  $\mathbf{n}_i$  gives the direction of the principal stretches  $\mu_i$ . The in-plane logarithmic principal strains  $\epsilon_i = \epsilon_i(\mathbf{X}, t)$  are finally found as

$$\epsilon_i = \ln(\mu_i), i = 1, 2 \quad (4)$$

The index  $i$  is arranged so that  $\epsilon_1 > \epsilon_2$ . In this work, the major logarithmic principal strain  $\epsilon_i$  was used for visualization of the strain fields as well as to access the local maximum strain within a DIC element (and named  $\epsilon_{DIC}$ ). These measured strains were eventually compared to the corresponding maximum principal strains.

## 4. Experimental

### 4.1. Tensile Testing Using In Situ SEM Stage

The experimental work was based on in situ tensile testing in SEM. The in situ device used is shown in Figure 3. This is a spindle-driven device, with the outer dimensions 155 mm × 95 mm × 45 mm. The device is placed inside the vacuum chamber, where it is mounted on top of the SEM stage after removal of the rotation unit. It consists of a rigid frame with two gripping cross-heads, where one is movable, and the other one is fixed. An electrical direct current motor drives the movable cross-head. During testing, the displacement and load transducers record the elongation and applied

force, respectively. Additional modules for the device can be mounted to provide other deformation modes, such as compression and bending. For further reading and previous use of the in situ SEM device, the reader is referred to [38–40]. During an in situ SEM tensile test, a selected area was recorded with a series of images of the microstructure. These images were recorded using either SE imaging or BSE imaging. An image series was loaded into the DIC software and correlated to obtain a local strain field of the recorded area.

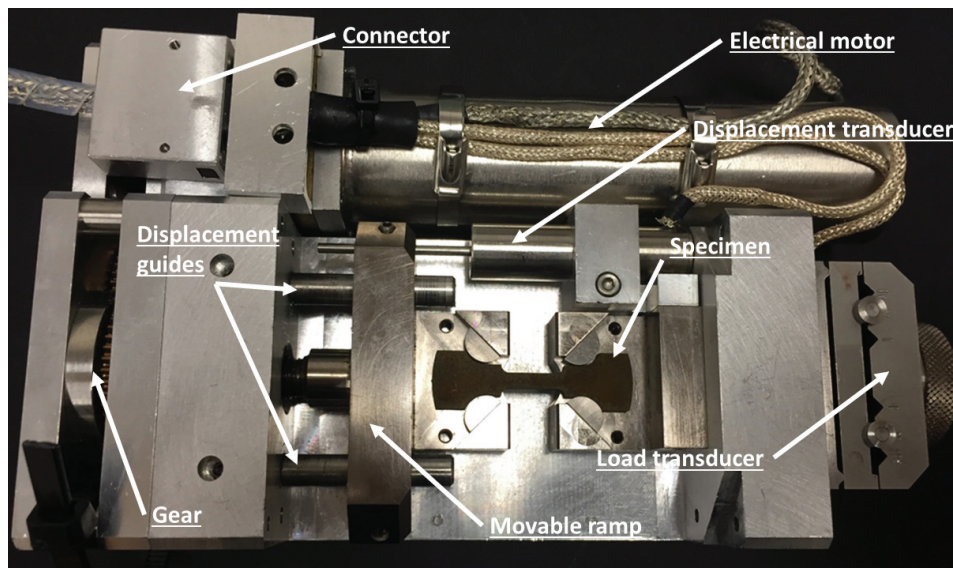
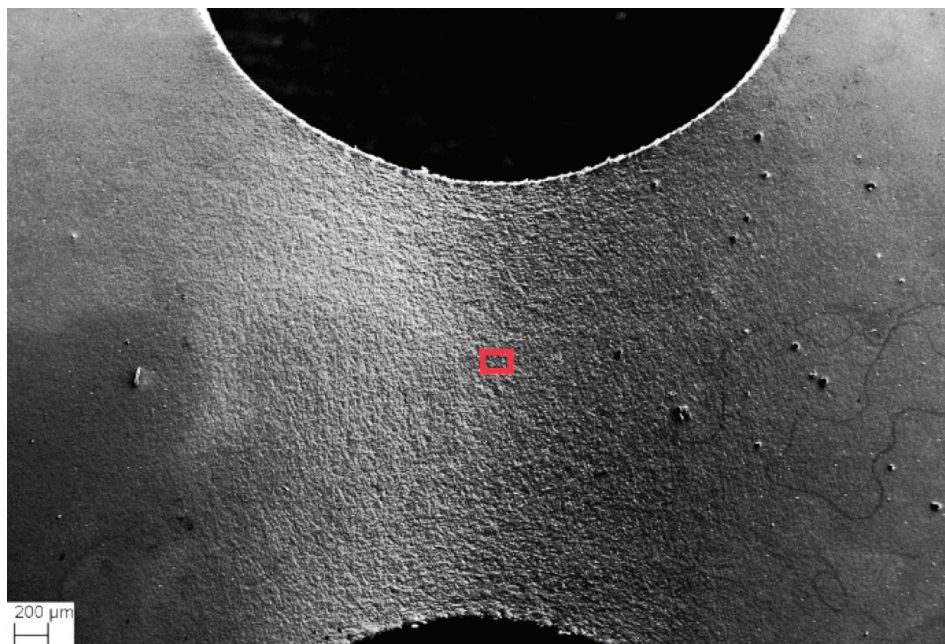


Figure 3. Image showing the in situ SEM tensile test device.

#### 4.2. Etched Surface

The specimens were ground and polished to 1  $\mu\text{m}$  before being etched for 10 s in 2% Nital. The microscope used for the etched specimen was a Field Emission SEM Zeiss Ultra 55 Limited Edition. During the in situ SEM tensile test on the etched surface, the same area was continuously recorded by an SE detector. This area is marked with the red square in Figure 4 and was located close to the most critical region of the specimen, i.e., in the region having the highest stress triaxiality. It should, however, be mentioned that it is challenging to select this area beforehand, and multiple tests may be required if fracture initiation is of interest. The recorded images had a resolution of 2048 pixels  $\times$  1385 pixels and the recorded area was 160  $\mu\text{m}$   $\times$  108  $\mu\text{m}$ , giving 0.078  $\mu\text{m}/\text{pixel}$ . This area was continuously recorded during straining. The frame rate of the line scan to acquire each image in the SEM was 6 s using an applied displacement rate of 0.2  $\mu\text{m}/\text{s}$ . This gave rise to some background noise and spatial distortion of the images. When conducting the experiment, a compromise among image resolution, exposure time and applied displacement rate had to be made to be able to perform the experiment in reasonable time and acquire enough images of sufficient quality for the DIC-analysis. After the test, the image series was uploaded into the DIC software eCorr v.4.0 [41] (described in Section 3) for analysis. The mesh used in the DIC analysis was quadratic elements with size 30 pixels  $\times$  30 pixels or 2.24  $\mu\text{m}$   $\times$  2.24  $\mu\text{m}$ .





**Figure 4.** Area observed during the two in situ SEM tensile tests. The red square has the dimensions  $160\ \mu\text{m} \times 120\ \mu\text{m}$  and is from the test on the etched specimen.

#### 4.3. Gold Speckled Surface

To obtain the gold nanoparticle speckled pattern, the experimental set-up proposed by Orozco-Caballero et al. [18] was used. First, the specimen has to be prepared for use in SEM, removing the deformation layer from the surface. Second, the polished surface is coated with gold, creating a thin continuous layer. Here, an Edwards S150B sputter coater was used to coat the surface. The setting used to obtain this result is summarized in Table 2. Finally, to get this gold layer to remodel into particles, the gold-coated specimen is placed on a heat source with heated gas flowing across the surface. Here, a mixture of argon and styrene was used as the flow medium. A hot plate with the specimen placed on top was located inside a desiccator to create an atmosphere without oxygen. This was to prevent corrosion. In addition, by doing this, the argon/styrene fumes were contained. During the time the specimen was in the remodeling chamber, the gold layer transformed from a continuous layer to randomly distributed nanoparticles. The setup is illustrated in Figure 5.

**Table 2.** Settings used when coating the specimen with gold.

Parameter	Setting
Current [mA]	40
Voltage [kV]	0.5
Time [min]	3–4
Pressure [mbar]	7.8

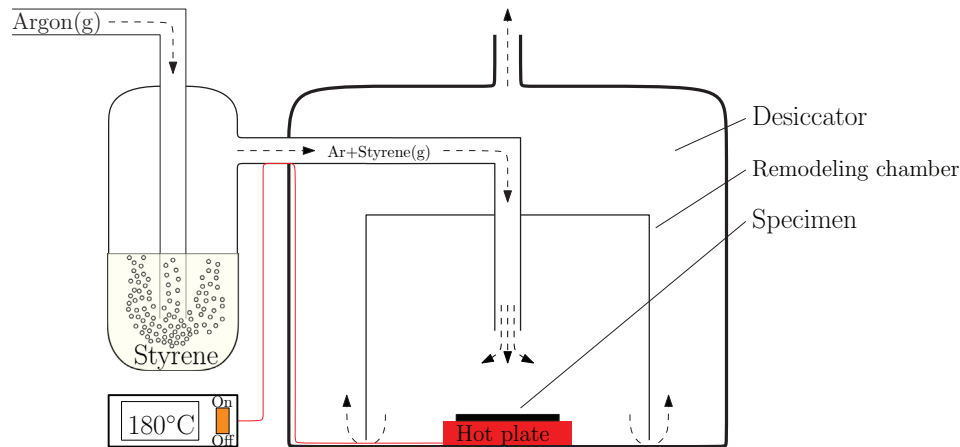


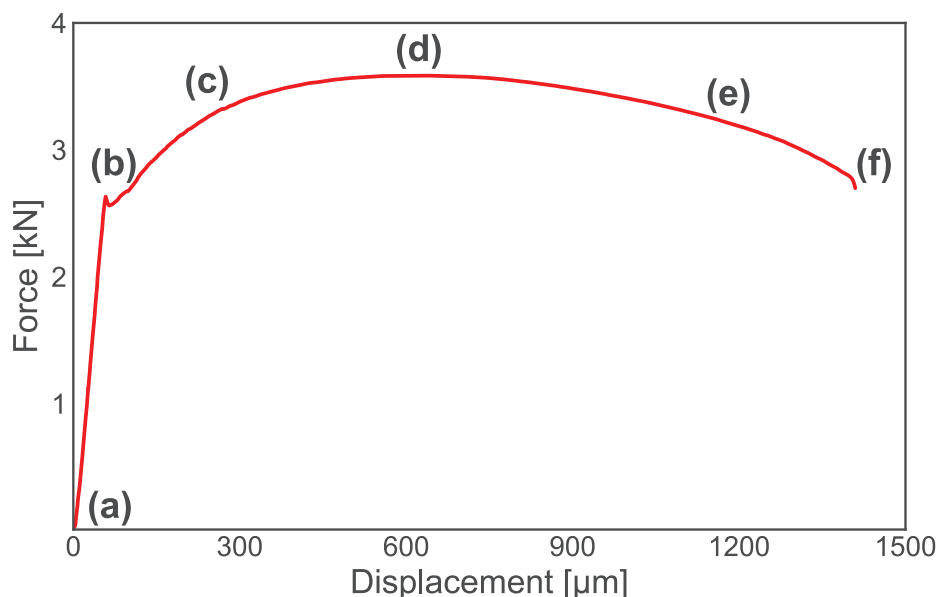
**Figure 5.** Experimental setup for gold remodeling in an argon/styrene atmosphere. Argon gas flows into a gas washing bottle filled with styrene. From here, a mixture of argon and styrene is guided into a remodeling chamber placed inside a desiccator. Inside the remodeling chamber, the specimen is placed on top of a hot plate. The control box sets the temperature of the hot plate on the outside of the desiccator.

When using a gold speckled pattern as the speckled pattern for the DIC, a continuous recording of the surface is not possible due to the long image acquisition time. Here, the specimen was strained, and then a BSE image was recorded while the tensile test was paused. The microscope used was a Field Emission SEM Zeiss Supra 55 (Jena, Germany). The area recorded was closely aligned with the region recorded on the etched specimen (see Figure 4). The field of view in the acquired BSE image is dependent on the speckle size. To ensure a good quality speckle pattern for DIC, each speckle should be covered by a minimum of 3–6 pixels in the image [14]. Depending on the size of the speckles, the horizontal field of view is typically 10–15  $\mu\text{m}$ . However, these images are not a representative area for most materials. To overcome this, an area was mapped by acquiring images in a grid pattern and merged. By doing this, a larger area of the microstructure could be imaged. Here, the limiting factors were acquisition time, electron beam stability, and final image file size. Here, each frame of the total image had a horizontal field of view of 16.33  $\mu\text{m}$  and contained 2048 pixels  $\times$  1536 pixels. The total stitched image consisted of 81 frames, acquired in a 9-by-9 grid with 20% overlap of each frame. The final image had the dimensions 119  $\mu\text{m}$   $\times$  90  $\mu\text{m}$  with 14,891 pixels  $\times$  11,233 pixels, yielding 0.008  $\mu\text{m}$ /pixel. Then, one mapped area was acquired at 0  $\mu\text{m}$  (undeformed), 60  $\mu\text{m}$  displacement (yield), 240  $\mu\text{m}$  displacement (during hardening) and 610  $\mu\text{m}$  displacement (maximum force). The images acquired after the maximum force could not be correlated with the DIC. This was due to the topography in the image, which yielded poor images with BSE imaging mode. After the test, the image series was uploaded into the DIC software eCorr v.4.0 [41] for analysis. The mesh used in the DIC analysis were quadratic elements with size 12 pixels  $\times$  12 pixels or 0.096  $\mu\text{m}$   $\times$  0.096  $\mu\text{m}$ .

After the acquisition, a set of images from each loading step were obtained, which needed to be stitched together into one single image before DIC analysis. This stitching process was performed using a plugin to the open source software ImageJ [42–44]. To measure the error from the stitching and general distortions from the microscope, the recorded area was acquired twice at 0% strain. The images were then stitched together to obtain two mapped images of the recorded area at 0% strain. These images were then correlated using DIC to get an estimate of the error from the image collection. The systematical error was assumed to be the same for each loading step during the tensile test.

### 5. Experimental Results on Etched Specimen

Based on the measured elongation and force during the in situ SEM tensile test on the etched specimen, the force–displacement curve shown in Figure 6 is plotted. As seen, the specimen exhibits a sharp yield point at a displacement of about 60  $\mu\text{m}$ , before the force drops abruptly. After this drop, the material starts to work harden and plastically deform. The force reaches a maximum of roughly 3.6 kN at a displacement of 610  $\mu\text{m}$ . The force then decreases continuously until fracture takes place after a displacement of 1410  $\mu\text{m}$ .



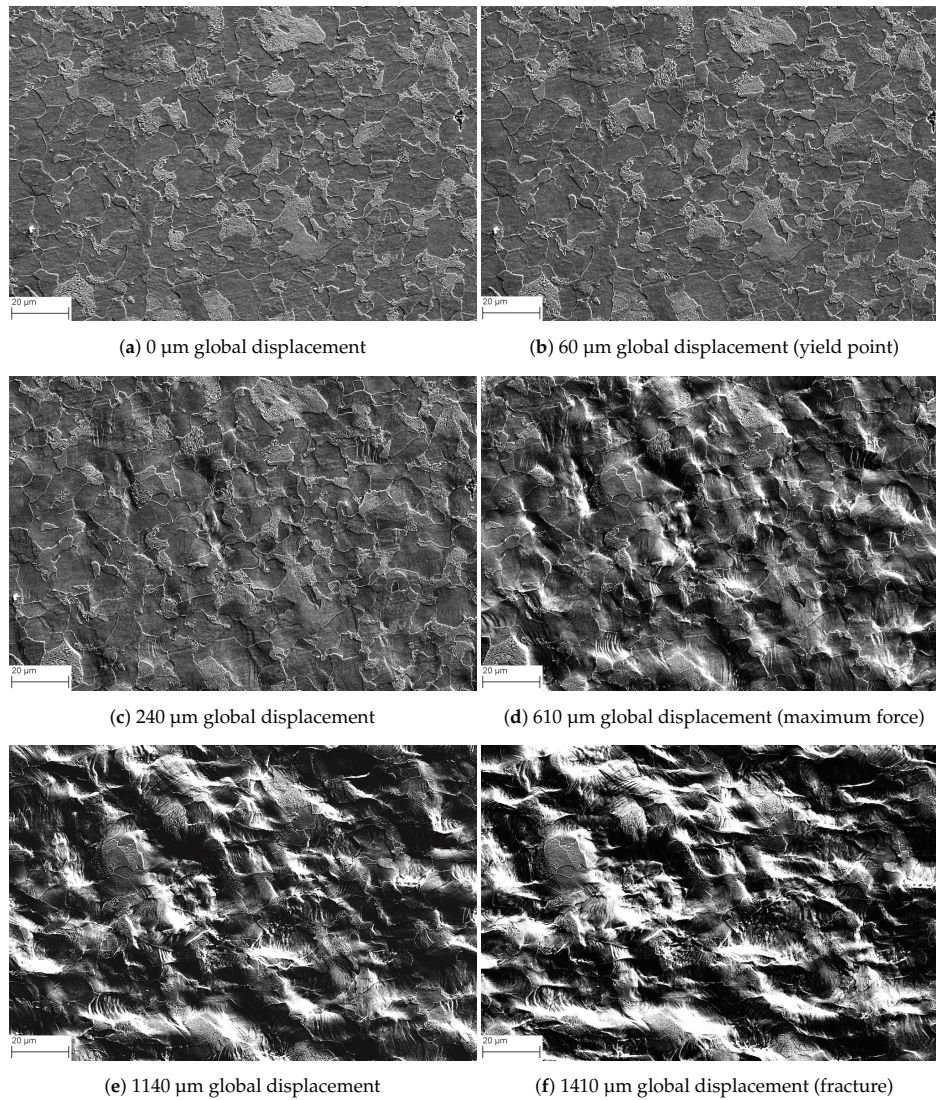
**Figure 6.** Measured force–displacement curve for the etched specimen during an in situ SEM tensile test. The labels (a–f) are related to the micrographs in Figures 7 and 8.

Figure 7 shows the evolution of the microstructure during the tensile test, where Figure 7a reveals the undeformed microstructure. At the yield point (Figure 7b), there is very little difference from the undeformed microstructure, but in Figure 7c it is possible to see that some topography has started to evolve. Slip lines start to appear in Figure 7d, i.e., at the maximum force. More and more slip lines and topography evolution can be seen in Figure 7d–f. During loading, the frames are also getting darker in some areas and whiter in others. This is an effect of the microscope. The reason for the frames getting darker is that the incoming electrons from the SEM contaminates the specimen surface, while the white areas are due to the topography contrast nature of SE imaging.

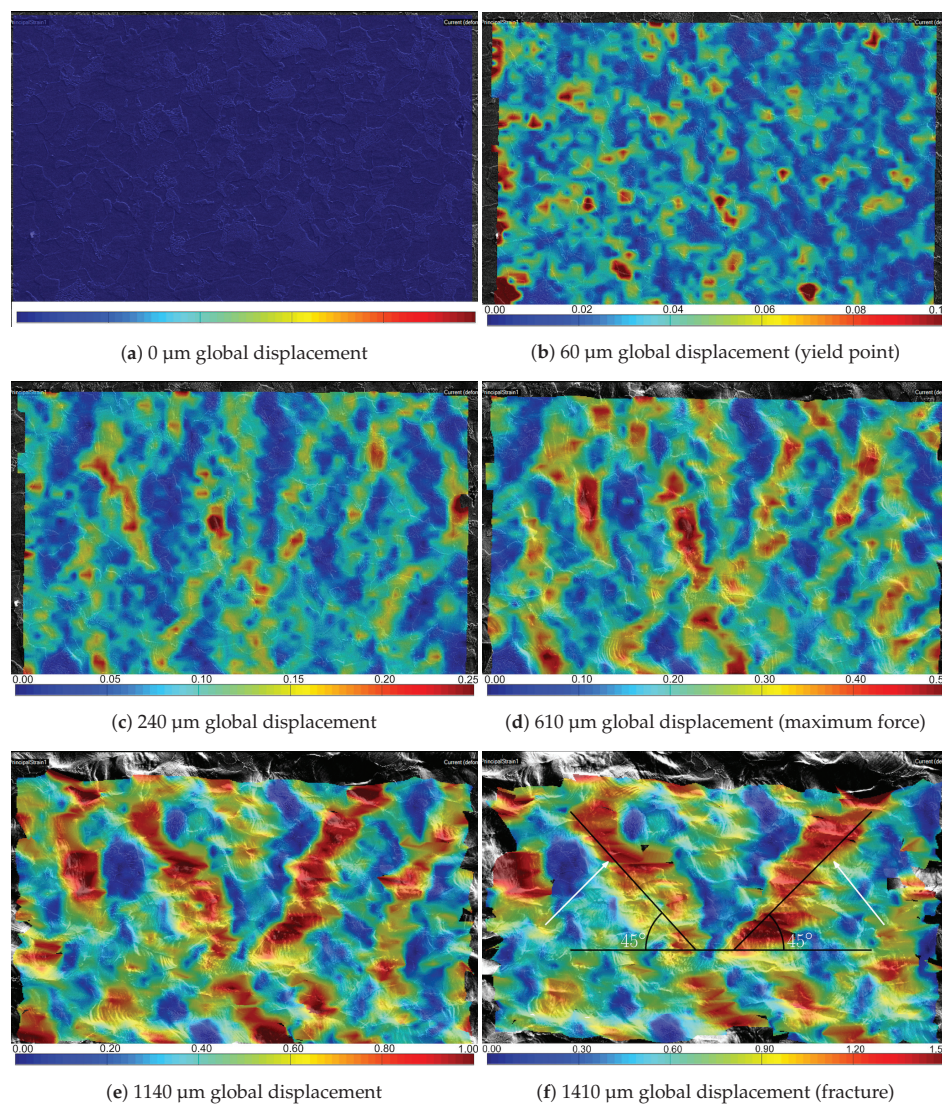
The strain field from the DIC measurements are shown in Figure 8. Here are the same micrographs as in Figure 7, but now with the strain field from the DIC measurements superimposed. When comparing Figures 7 and 8, it is seen that the straining takes place mostly within the soft ferrite, while the hard pearlite appears as less deformed islands within the microstructure. Another observation is that the maximum local strain, measured at element level close to fracture, is more than  $\epsilon_{DIC} = 2.1$ . The corresponding average engineering strain across the recorded area was measured to be  $\bar{\epsilon}_{DIC} = 0.86$ , using several virtual extensometers (vectors) in the DIC software with an initial length of 80  $\mu\text{m}$ . The deformation bands seen in Figure 8c–f are oriented at an angle to the tensile direction, and the most heavily deformed bands seem to be oriented at about 45°. This is consistent with the results of, e.g., Ghadbeigi et al. [28]. Initially, the deformation takes place in the soft ferrite, as seen in



Figure 8b. Then, bands start to form in Figure 8c during the work-hardening stage. After the formation of these bands, nearly all subsequent deformation takes place inside the localized zones. Next to the heavily deformed bands, there is little deformation. Some places these bands cut through pearlite grains, but for the most part, the less deformed (blue) regions in the strain field are pearlite grains.



**Figure 7.** Micrographs at different displacements in the etched specimen. (a–f) The micrographs relate to the force–displacement curve in Figure 6. In all frames, the pulling direction in the in situ SEM tensile test is from right to left. Each frame has the same dimensions, 160  $\mu\text{m} \times 108 \mu\text{m}$ .



**Figure 8.** Micrographs with the measured strain field superimposed at different global displacements in the notched specimen. (a–f) The strain maps relate to the force–displacement curve in Figure 6. The white arrows in (f) indicate the deformation bands discussed in Figure 9. In all frames, the pulling direction in the in situ SEM tensile test is from right to left. Each frame has the same dimension,  $160\ \mu\text{m} \times 108\ \mu\text{m}$ . The fringe colors give values of the major principle strain.

Figure 9 shows the evolution of local engineering strains in pearlite versus ferrite grains as compared to the average engineering strain over the recorded area. As observed on the etched microstructure in Figure 8, the harder pearlite deforms less than the softer ferrite. When  $\bar{\epsilon}_{DIC} = 0.86$  (i.e., the average engineering strain over the recorded area at fracture), the local engineering strain in the pearlite and ferrite grains were  $\bar{\epsilon}_{DIC} = 0.39$  and  $\bar{\epsilon}_{DIC} = 0.90$ , respectively. Both of these strain measures exhibit a rather linear relationship with the average engineering strain over the recorded



area, but the spread is significant. In contrast, the heavily deformed bands seem to accommodate more and more of the deformation, especially after the ultimate tensile strength (UTS).

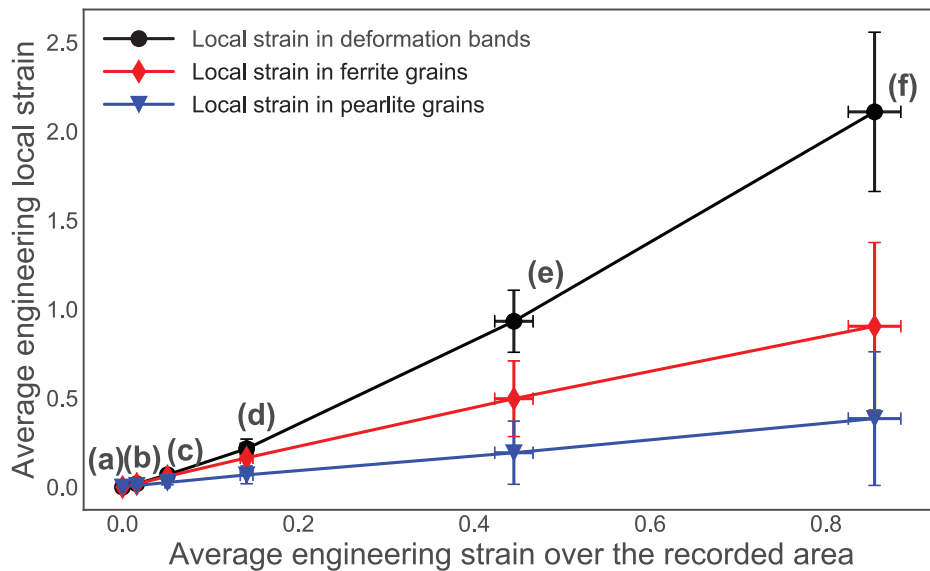


**Figure 9.** Local strain evolution in pearlite and ferrite grains and the localized deformation bands marked in Figure 8f. The grains selected for the local strain measurements are indicated with blue squares and red diamonds in Figure 10a for pearlite and ferrite, respectively. The average engineering strain over the recorded area are measured using the vectors in Figure 10b.

All values in Figure 9 were acquired using virtual extensometers in the DIC software. The grains selected for measuring local strain in ferrite and pearlite are marked in Figure 10a, while the virtual extensometers for the average engineering strain across the recorded area are shown in Figure 10b. In addition, the average value of the local engineering strain across the two deformation bands marked with white arrows in Figure 8f is extracted and plotted in Figure 9. This is done by placing ten virtual extensometers across the length of each band. From this, it is seen that more and more local strain is accumulated in these bands and that the slope of this curve increases with increasing average engineering strain over the recorded area. It is also worth noting that the error bars in Figure 9 represent the standard deviation of the average strains measured and that the amount of variation in the measurements is seen as high.

In an attempt to validate the experimental results of the in situ SEM measurements, two types of tests on an unstrained specimen were also conducted. First, a series of images without any pulling was recorded with the same acquisition settings as in the in situ SEM tensile test, before being uploaded to the DIC software and analyzed. Due to the gray-scale pixel noise, a fictitious strain of about 1.5% was registered. This method is similar to the test performed by Buljac et al. [45]. However, they registered an error of 0.3% in a DVC analysis, compared to 1.5% in this DIC analysis. Second, a test with the same setup as in the in situ SEM tensile test, where the specimen was only fixed at one end and then continuously pulled by the movable ramp (see Figure 3), was conducted. This rigid body movement should not impose any strain in the specimen. However, since the microscope loaded the images row-by-row, the last row of pixels was slightly shifted compared to the first row in the image due to the continuous recording. This resulted in a measured constant strain of roughly 3% by the DIC software. These strains are unphysical and should be accounted for. Note that the magnitude of the

latter error is a function of exposure time and applied displacement rate during testing, which in this experiment were, respectively, 6 s and 0.2  $\mu\text{m/s}$ .

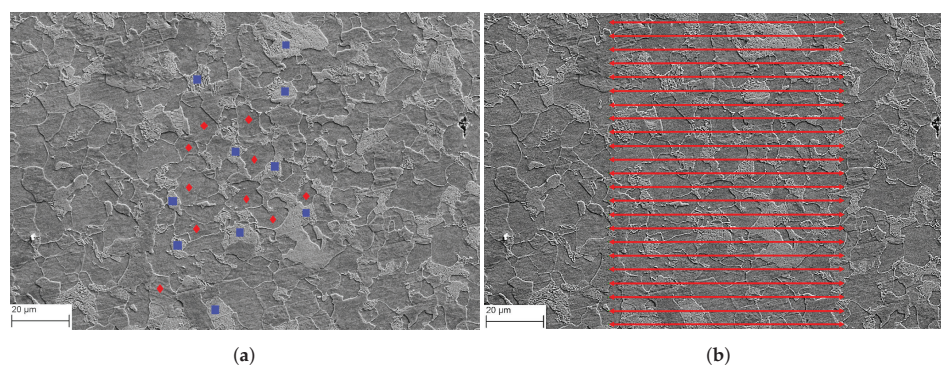
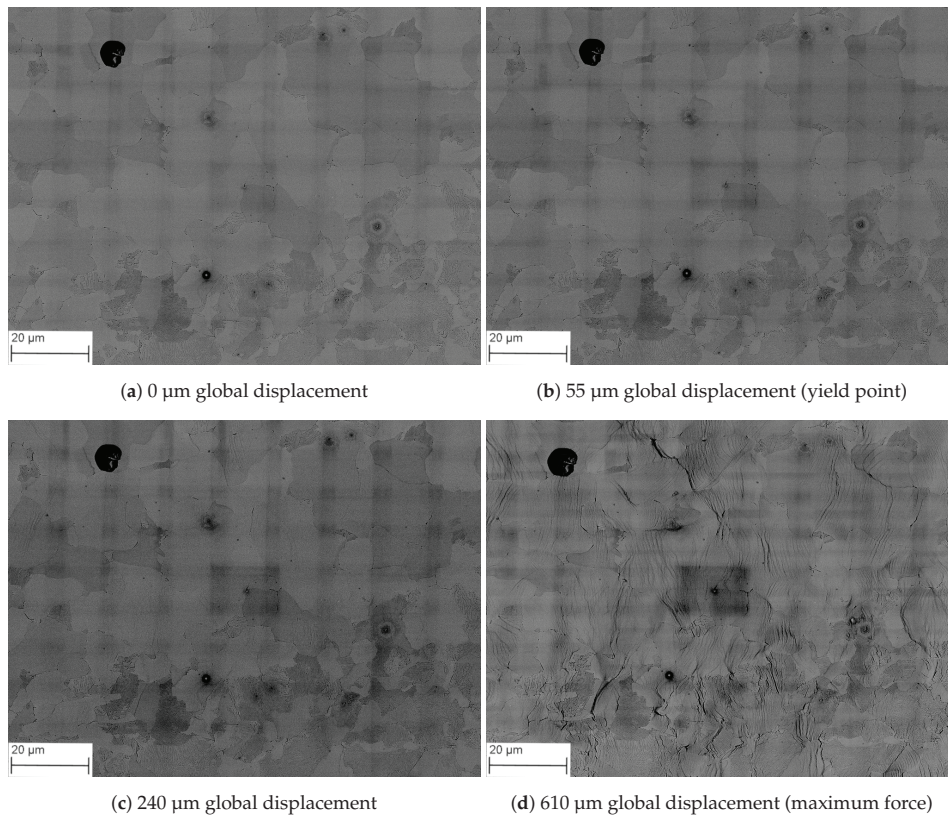


**Figure 10.** (a) Grains used for local strain measurements in Figure 9, where the blue squares are pearlite grains and the red diamonds are ferrite grains. (b) Vectors used as virtual extensometer for the average engineering strain over the recorded area, having an initial length of 80  $\mu\text{m}$ .

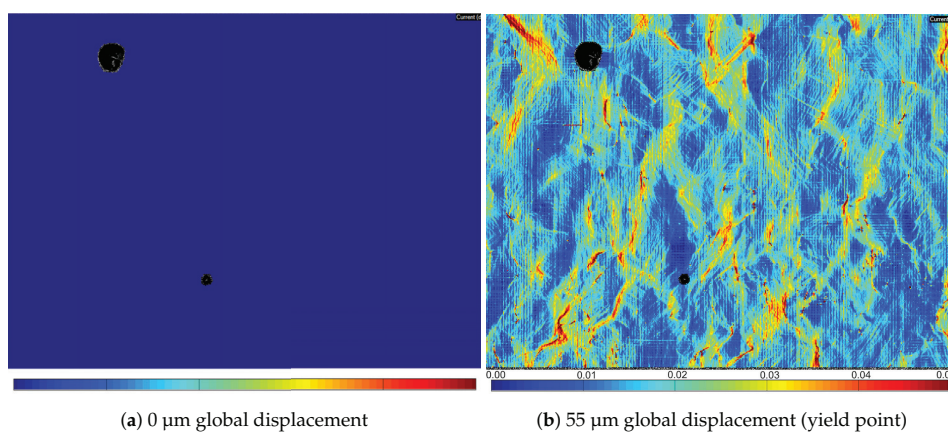
## 6. Experimental Results for Gold Speckled Specimen

Figure 11 shows the evolution of the microstructure during a tensile test using a gold speckled specimen, where Figure 11a reveals the undeformed microstructure. At the yield point (Figure 11b), there is very little difference from the undeformed microstructure, but in Figure 11c it is possible to see that some slip lines have started to appear. In Figure 11d, i.e., at the maximum force, many slip lines can be seen throughout the microstructure, and the microstructure looks quite deformed. During loading, the frames are also getting darker in a grid pattern. This is an effect of the microscope. The reason for the frames getting darker is that the incoming electrons from the SEM contaminates the specimen surface and it is in a grid pattern since there is an overlapping region being exposed more than the center of each frame. In addition, the middle frame is extra burned due to prolonged exposure between acquisitions.

The DIC results obtained by analyzing the micrographs in Figure 11 are shown in Figure 12. Large parts of the map are unstrained, while some areas are heavily influenced in narrow bands. Figure 13 gives the phase map and the same DIC map as in Figure 12d, but with different scale bar to highlight the undeformed areas. The phase map was created by outlining the NVE36 grains manually from the mapped BSE image. The lamellar structure of NVE36 makes it easy to detect the pearlite and ferrite grains even with the gold coating. By comparing Figure 13a,b, it can be seen that the least strained parts of the microstructure are pearlite grains. In addition, the sharpest bands of strain in the strain field in Figure 12d are in areas near or on the interphase between the two phases. These bands are initially formed at angles close to 45°. Another observation is that the maximum local strain, measured at element level at UTS, is more than  $\epsilon_{DIC} = 1.4$ . The corresponding average engineering strain across the recorded area was measured to be  $\bar{\epsilon}_{DIC} = 0.15$ , using several virtual extensometers (vectors) in the DIC software with an initial length of 80  $\mu\text{m}$ .

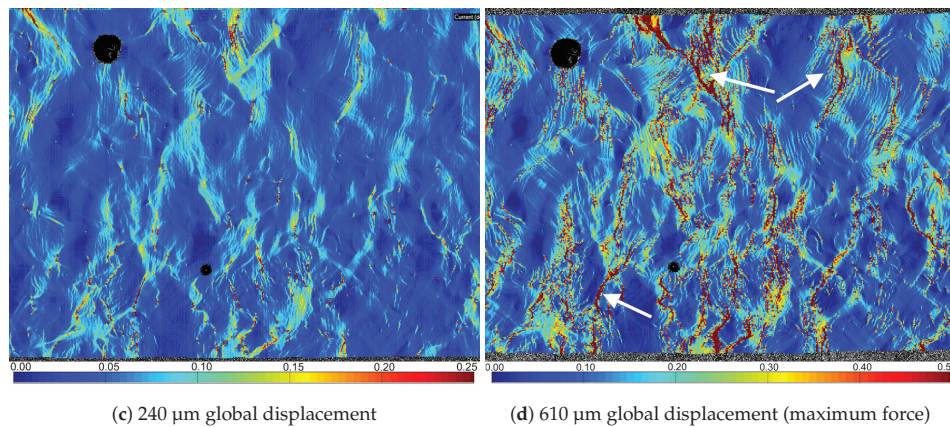


**Figure 11.** Stitched BSE images at different displacements in the notched specimen. (a–d) The micrographs relate to the force–displacement curve in Figure 6. In all frames, the pulling direction in the in situ SEM tensile test is from right to left. Each frame has the same dimensions, 119  $\mu\text{m} \times 90 \mu\text{m}$ .

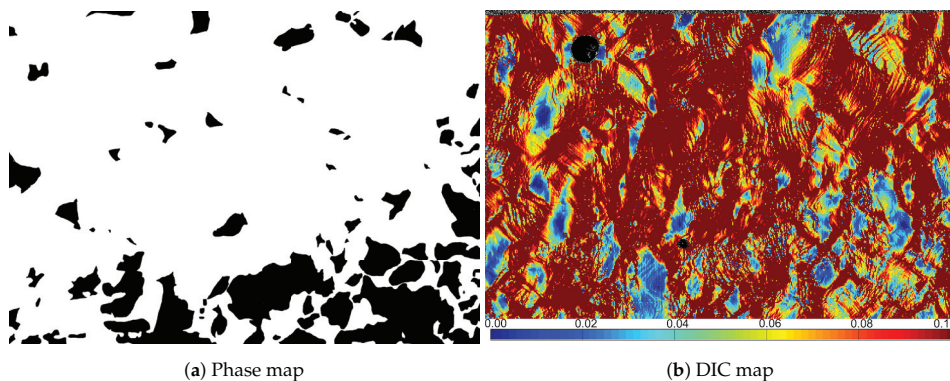


**Figure 12.** Cont.





**Figure 12.** Measured strain field superimposed on the BSE images from Figure 11 at different global displacements in the notched specimen. (a–d) The strain maps relate to the force–displacement curve in Figure 6. The white arrows in (d) indicate the deformation bands discussed in Figure 14. In all frames, the pulling direction in the in situ SEM tensile test is from right to left. Each frame has the same dimensions,  $119\ \mu\text{m} \times 90\ \mu\text{m}$ . The fringe colors give values of the major principle strain.



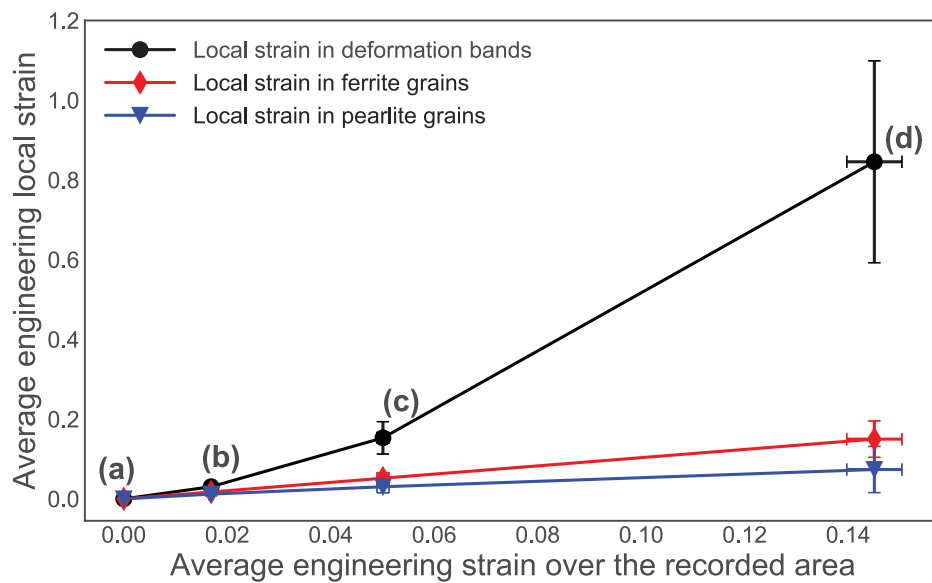
**Figure 13.** (a) A phase map of the same area as analyzed with DIC. The pearlitic phase is black and ferrite is white. (b) The same strain map as in Figure 12d with a lower max value for the color legend.

Figure 14 shows the evolution of local engineering strains in pearlite versus ferrite grains as compared to the average engineering strain over the recorded area. As expected, the hard pearlite deforms much less than the soft ferrite. When  $\bar{\epsilon}_{DIC} = 0.15$  (i.e., the average engineering strain over the recorded area at UTS), the local engineering strain in the pearlite and ferrite grains were  $\bar{\epsilon}_{DIC} = 0.07$  and  $\bar{\epsilon}_{DIC} = 0.15$ , respectively. Both of these strain measures exhibit a rather linear relationship with the average engineering strain over the recorded area, but the spread is significant. All values in Figure 14 were acquired using virtual extensometers in the DIC software. The virtual extensometers for the local engineering strain across the different grains are shown in Figure 15a, while the virtual extensometers for the average engineering strain across the recorded area are shown in Figure 15b.

In addition, the average value of the local engineering strain across the three deformation bands marked with white arrows in Figure 12d is extracted and plotted in Figure 14. In each of the three bands, ten virtual extensometers were placed to measure the average strain across the band. It is

shown that more and more local strain is accumulated in these bands and that the slope of this curve increases with increasing average engineering strain over the recorded area.

As for Figure 9, the error bars in Figure 14 represent the standard deviation of the average strains measured and that the amount of variation in the measurements is as seen higher at larger strains. In addition, the spread is greater in the bands compared to the grains. In contrast to Figure 9, Figure 14 is only plotted until UTS. The reason for this is that the gold specimen was only recorded to UTS. The damage and topography beyond this point made it impossible to correlate the DIC results.



**Figure 14.** Local strain evolution in pearlite and ferrite grains and the localized deformation bands marked in Figure 12d. The grains selected for the local strain measurements are indicated with blue squares and red diamonds in Figure 15a for pearlite and ferrite, respectively. The average engineering strain over the recorded area are measured using the vectors in Figure 15b.

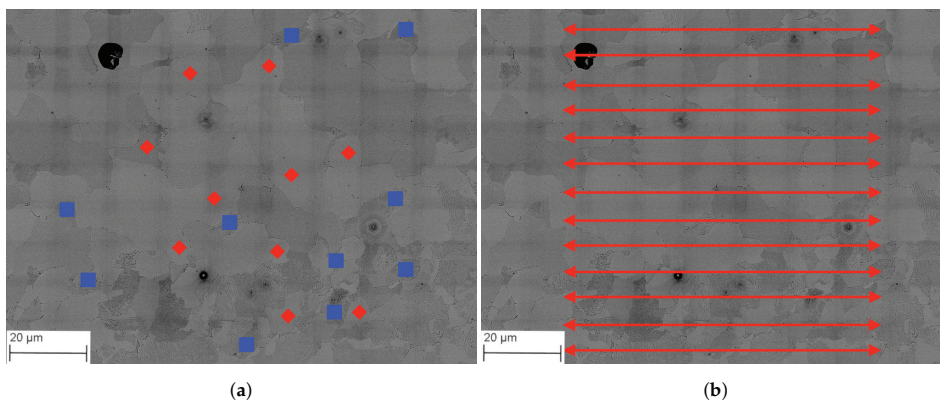


**Figure 15.** (a) Grains used for local strain measurements in Figure 14, where the blue squares are pearlite grains and the red diamonds are ferrite grains. (b) Vectors used as virtual extensometer for the average engineering strain over the recorded area, having an initial length of 80  $\mu\text{m}$ .



The systematic error was calculated by comparing two images from the same region before deformation. These images were then correlated using the DIC software. From this, a peak strain of 1.5% was observed. The error is introduced by the microscope when acquiring BSE images of the speckle pattern by mapping the region of interest (ROI) and stitching the individual frames together. Although there are some nodes in the correlated, undeformed map recording strains of more than 1%, 99.2% of the nodes record strains less than 0.1%.

Further, the gold speckled specimen was analyzed with a mesh size equal (in  $\mu\text{m}$ ) to the mesh size for the etched specimen. Here, both specimens have a mesh with quadratic element with the size  $2.24 \mu\text{m} \times 2.24 \mu\text{m}$ . This corresponds to  $280 \text{ pixels} \times 280 \text{ pixels}$  and  $30 \text{ pixels} \times 30 \text{ pixels}$  for the gold speckled specimen and etched specimen, respectively. The resulting strain fields are given in Figure 16, where Figure 16a gives the strain field for the etched specimen and Figure 16b for the gold speckled specimen. Figure 16a is the same strain field as in Figure 8c. It is worth noting that the area for these images is slightly different. The etched specimen has an area of  $141 \mu\text{m} \times 98 \mu\text{m}$  and the gold speckled specimen has an area of  $114 \mu\text{m} \times 85 \mu\text{m}$ . When comparing the strain maps in Figure 16, the patterns in both maps are similar. The bands in both have the same width and the strain levels are on the same scale. A difference between the two maps is that the strain map from the gold speckled specimen has smoother transitions between the deformed and undeformed areas.

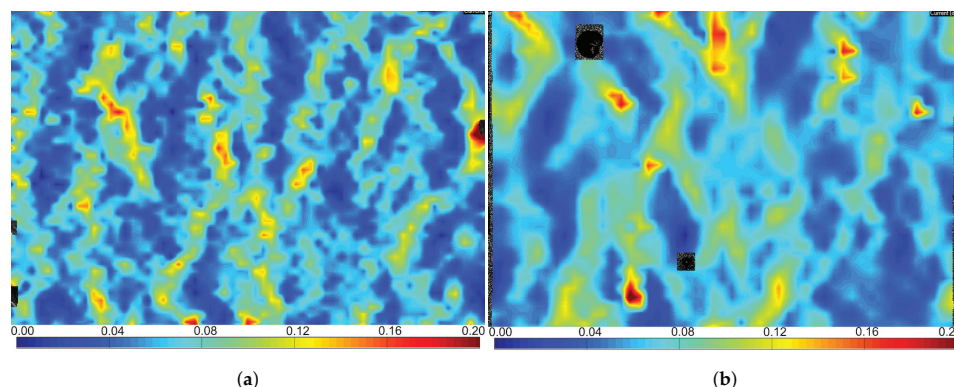


**Figure 16.** Comparing the two techniques when having the same mesh size (in  $\mu\text{m}$ ): (a) etched specimen with an area of  $141 \mu\text{m} \times 98 \mu\text{m}$ ; and (b) gold speckled specimen with an area of  $114 \mu\text{m} \times 85 \mu\text{m}$ .

## 7. Discussion

This work demonstrated that it is possible to correlate a continuously recorded microstructure from an in situ SEM tensile test by DIC using the gray-scale values provided by the micrographs imaged with the SE detector. From this, the strain field can be obtained and related to the evolution of the microstructure all the way to fracture. This technique was compared with a specimen covered with gold nanoparticles, which were used as the speckled pattern for DIC during an in situ SEM tensile test. For the gold speckled specimen, images were acquired using the BSE detector and only at key locations on the tensile curve until UTS. In the present study, these techniques were demonstrated on the ferritic-pearlitic steel NVE36.

The resulting strain fields on the etched specimen obtained are similar to the results achieved by, e.g., Ghadbeigi et al. [28] and Tasan et al. [31], displaying localized deformation bands oriented at about  $45^\circ$  with respect to the loading direction (see Figure 8). These bands follow a path mostly within the soft ferrite grains, reaching local strain values up to 170% before fracture at a much lower global strain, clearly illustrating the heterogeneity in the deformation of the material. This is in line with the observed results by Banerjee et al. [30], who recorded strain values of 150% inside similar bands at a global strain less than 10%. As for the etched specimen, localized deformation bands were

observed to form at  $45^\circ$  with respect to the loading direction (see Figure 12) in the gold speckled specimen. This indicates an association with the maximum shear stress locally within grains. Locally, within these bands, strain values of 110% were recorded at UTS, compared to 15% average engineering strain over the recorded area.

When performing the heat treatment to remodel the gold layer in order to obtain a gold speckled pattern, the specimen was kept at  $180^\circ\text{C}$  for 96 h. To validate the effect of this heat treatment, new tensile tests and a microstructural investigation were conducted. The grain size, phase composition, and hardness were all measured before and after heat treatment on three different specimens. The results from these investigations are summarized in Table 3, and it can be seen that all values for both specimens are within the standard deviation of each other. In Figure 17, engineering stress–strain curves from two tensile tests are presented. The curves indicate no difference between the heat-treated tensile curve and the as-received tensile curve. However, this result is not unexpected. The microstructure of NVE36 is decided by the metastable Fe-Fe<sub>3</sub>C phase diagram (see Figure 9.24 in [46]). As a result, no changes took place in the microstructure during the heat-treating process to remodel the gold layer into the gold speckled pattern for this particular material. Other material can also be considered suitable for this method. These would typically be materials designed for use at elevated temperatures, e.g., nickel alloys, duplex steels, austenitic steels, etc. However, this would not be the case for all materials. As an example, for aluminum alloys, the age hardening might take place at temperatures between  $100^\circ\text{C}$  and  $150^\circ\text{C}$ . If left at  $180^\circ\text{C}$  for 96 h, an overaged material would be the result [47]. In addition, in some cases, tempering of martensite occurs at temperatures of  $200^\circ\text{C}$  [46]. In general, the remodeling method would benefit by reducing the remodeling temperature and remodeling time to increase versatility.

**Table 3.** Hardness, grain size and phase composition measured before and after heat treatment.

Variable	Ferrite	Pearlite	Ferrite	Pearlite
	Before		After	
Phase composition	$75 \pm 19\%$ ferrite		$74 \pm 16\%$ ferrite	
Hardness [HV]	$204 \pm 23$	$283 \pm 27$	$188 \pm 29$	$306 \pm 39$
Grain size [ $\mu\text{m}$ ]	$15.5 \pm 3.1$	$12 \pm 2.1$	$16 \pm 2.5$	$11 \pm 1.1$

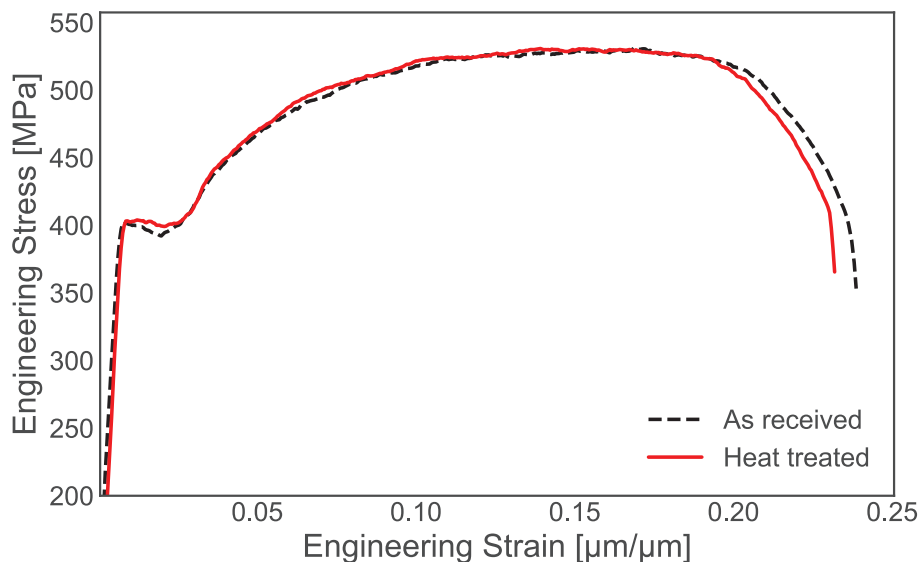


**Figure 17.** The tensile test curve of the heat treated and as received specimen.

During image acquisition, both the etched specimen and the gold speckled specimen were contaminated by the incoming electrons. In the etched specimen, this results in a gradually darker surface. To overcome this, the reference image in the DIC algorithm was updated several times. The result is an accumulation of errors, as discussed in Tang et al. [35]. For the gold specimen, the contamination resulted in a grid pattern due to the overlapping area during the image acquisition. When studying the overlapping area, it was seen that the intensity of gold speckles are faded. However, from the strain field no apparent changes were observed. The amount of contamination is related to the amount of electrons impacting the surface (i.e., accelerating voltage and aperture size) and absorbed current by the microscope. By reducing the accelerating voltage and aperture size and increasing conductivity between specimen and in situ tensile stage, and in situ tensile stage and microscope stage, the contamination would be reduced.

When studying the strain fields in Figure 8 and the plots in Figure 9, the local strain evolution can be investigated at grain level. The localized deformation initiates in the soft ferrite grains, as seen in Figure 8b. Then, distinct bands of localized strain are formed, which mostly consists of ferrite grains, but occasionally propagate through hard pearlite grains. When the deformation continues to increase, the intensity of the localized strain inside the bands leads to more inhomogeneous plastic flow and unloading of the material outside the bands. In addition, the formation of slip lines was observed, and some of the ferrite grains experienced significant plastic deformation, also activating secondary slip systems. Conversely, some pearlite grains are hardly strained at all having an average engineering strain  $\bar{\epsilon}_{DIC}$  less than 10% at fracture. Figure 8 also confirms that most of the undeformed regions consist of pearlite grains. A few of these grains (situated in the localized strain bands) experienced some slip activity, but no secondary slip systems were observed in this phase. Figure 7 shows the large deformation experienced by the microstructure. From these surface observations, few damage sites were detected, and no void growth could be seen. However, as shown by Maire et al. [48] on dual-phase steel revealing the initiation and growth of damage observed by X-ray microtomography, the void volume fraction is much higher in the center of the specimen where the stress triaxiality is maximum compared to the surface. Such void growth is also well-known from ductile damage mechanics (see, e.g., [49]). This may also explain why the specimen fractured abruptly, with seemingly few damage sites, since a macrocrack might have propagated from below the surface, leading to the final fracture.

In the in situ SEM tensile test with the etched specimen, it was hard to get any meaningful results from the strain maps during the initial stage of the test, i.e., at low strains in the elastic region. This is related to the level of noise in the recorded micrographs. To be able to record a continuous in situ tensile test in the SEM, the exposure time for each micrograph has to be low. Conversely, if the time spent to acquire each micrograph is long compared to the applied displacement rate, the recorded area will move during the imaging. As a result, the final line in the line-scan moved 1.2  $\mu\text{m}$  in the pulling direction compared to the first line. This can, at least to a certain degree, be compensated for with a lower applied displacement rate in the test. In the current experimental set-up, the applied displacement rate was 0.2  $\mu\text{m/s}$ , and the frame rate was 6 s. Thus, the ratio between the applied displacement rate and the frame rate has to be sufficiently low, leaving enough time to acquire good quality micrographs, but high enough to avoid unwanted effects from the low applied displacement rate. In the in situ SEM tensile test on the gold-coated specimen, this issue was resolved by increasing the acquisition time. Here, a snapshot of the current state of the material is seen with slip lines and shear bands forming. Conversely, for the gold speckled specimen, high-quality images were acquired at the desired strain level. The resulting DIC maps achieve an excellent spatial resolution, but the image acquisition time is long. As a result, a strain map was not obtained throughout the tensile test, but at a few selected locations on the tensile curve. In addition, the images acquired for the gold speckled specimen were acquired by mapping the surface frame by frame and then stitching all frames into the ROI. To obtain the best results possible, a very precise stage is required. Ideally, this should be a piezoelectric stage as they have superior precision when the stage moves between each frame

acquired. The mechanical stage used here has a precision of 1  $\mu\text{m}$ . However, new piezoelectric stages are 500–1000 times more precise [50].

Figure 18 compares the local strain evolution of techniques used on the specimens tested here. It can be seen that the behavior of the grains and local average strain for both techniques captures the same behavior for the pearlite and ferrite grains. However, in the deformation bands, there is a clear difference. The maximum principal strain at UTS was found to be 325% higher in the gold speckled specimen than in the etched specimen. Haltom et al. [51] reported similar differences based on microscopic and macroscopic strain measurements in an aluminum alloy. From the in situ SEM strain maps, it is readily observed where and in which type of grain strain localization takes place, and at what time this occurs during the deformation process. It is also straightforward to relate these measurements to the applied force or stress magnitude. Moreover, the technique can be further developed by investigating other materials, such as quasi-brittle alloys at various temperatures where fracture is essential.

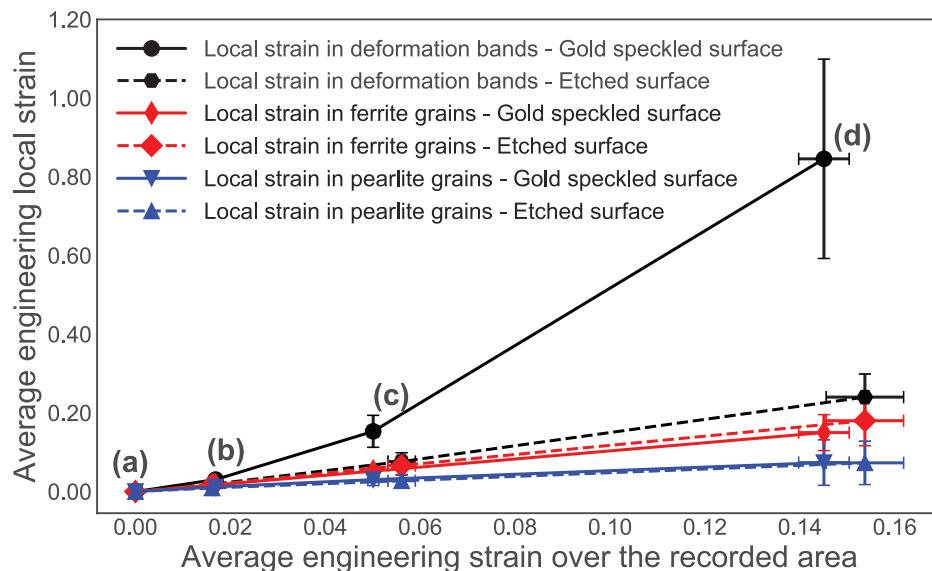


Figure 18. The local strain evolution in Figures 9 and 14 plotted together until UTS.

## 8. Concluding Remarks

In this study, the differences between two specimen preparation methods for DIC on images acquired in an SEM have been demonstrated on the two-phased ferritic-pearlitic steel NVE36. The gold speckled specimen has a significantly higher spatial resolution, and, as a consequence, more local deformation is captured. In addition, if local information is required at the early stages of deformation, the gold speckled specimen is the preferred method. Conversely, the images from the etched specimen surface contain more noise, and in the first stages of deformation less local information is captured. As a consequence of the lack of contrast for the DIC analysis, the etched specimen is not able to resolve strains within grains. However, the advantages of using an etched surface are that no heating of the specimen and fewer steps are required to obtain the strain field. In addition, continuous recordings of the strain field are particularly important when studying localization and fracture, which may occur abruptly. As a conclusion, the method with gold speckles is only required when a fine spatial resolution is necessary to obtain results at only certain stages of the tensile curve.

The gold speckled specimen gives more detail and higher accuracy compared to the etched specimen. Local strain bands are found to be more narrow and more heavily deformed using this approach. However, with the gold speckled specimen, only a few snapshots throughout the tensile test are acquired, and after UTS the topography on the surface makes the image acquisition more challenging. This is a consequence of acquiring BSE images. For the etched specimen, images are captured continuously through the test. When performing a DIC analysis on the gold speckled specimen with a mesh size (in  $\mu\text{m}$ ) equal to the etched specimen, the results are close to identical. The differences between the two techniques are specimen preparation, image acquisition, acquisition time, DIC quality, DIC resolution, and the number of strain fields available throughout the stress–strain curve. The technique to be chosen will mainly depend on the material, and the spatial resolution required.

**Author Contributions:** C.O.P. is the first author and analyzed the data, wrote most of the paper, and performed the experiments. E.F. contributed to the DIC parts of the paper. He helped to perform the DIC analysis, writing the section on DIC and is the DIC expert. I.W. and T.B. conceived, designed, and supervised the experiments. In addition, they contributed to the interpretation of data and editing the paper.

**Funding:** The authors gratefully appreciate the financial support from NTNU and the Research Council of Norway through CASA, Project No. 237885.

**Conflicts of Interest:** The authors declare no conflict of interest.

## Abbreviations

The following abbreviations are used in this manuscript:

BSE	Backscatter Electron
CASA	Centre for Advanced Structural Analysis
DIC	Digital Image Correlation
DOF	Degrees of Freedom
EBSD	Electron Backscatter Diffraction
FE	Finite Element
NTNU	Norwegian University of Science and Technology
ROI	Region of Interest
SE	Secondary Electron
SEM	Scanning Electron Microscope
SIMLab	Structural Impact Laboratory
UTS	Ultimate Tensile Strength
ZNSSD	Zero-Mean Normalized Sum of Squared Differences

## References

1. Bhadeshia, H.; Honeycombe, R. Thermomechanical Treatment of Steels. In *Steels: Microstructure and Properties*; Elsevier: Oxford, UK, 2017; pp. 271–301. [\[CrossRef\]](#)
2. Dieter, G.E.; Bacon, D.J. *Mechanical Metallurgy*; McGraw-Hill: New York, NY, USA, 1988; Volume 3.
3. Porter, D.A.; Easterling, K.E.; Smith, G.D.W. Dynamic studies of the tensile deformation and fracture of pearlite. *Acta Metall.* **1978**, *26*, 1405–1422. [\[CrossRef\]](#)
4. Sidhom, H.; Yahyaoui, H.; Braham, C.; Gonzalez, G. Analysis of the Deformation and Damage Mechanisms of Pearlitic Steel by EBSD and in-situ SEM Tensile Tests. *J. Mater. Eng. Perform.* **2015**, *24*, 2586–2596. [\[CrossRef\]](#)
5. Peters, W.H.; Ranson, W.F. Digital Imaging Techniques In Experimental Stress Analysis. *Opt. Eng.* **1982**, *21*, 427–432. [\[CrossRef\]](#)
6. Sutton, M.A.; Wolters, W.J.; Peters, W.H.; Ranson, W.F.; McNeill, S.R. Determination of displacements using an improved digital correlation method. *Image Vis. Comput.* **1983**, *1*, 133–139. [\[CrossRef\]](#)
7. Sutton, M.A.; Mingqi, C.; Peters, W.H.; Chao, Y.J.; McNeill, S.R. Application of an optimized digital correlation method to planar deformation analysis. *Image Vis. Comput.* **1986**, *4*, 143–150. [\[CrossRef\]](#)

8. Sutton, M.A.; Turner, J.L.; Bruck, H.A.; Chae, T.A. Full-field representation of discretely sampled surface deformation for displacement and strain analysis. *Exp. Mech.* **1991**, *31*, 168–177. [\[CrossRef\]](#)
9. Bruck, H.A.; McNeill, S.R.; Sutton, M.A.; Peters, W.H. Digital image correlation using Newton-Raphson method of partial differential correction. *Exp. Mech.* **1989**, *29*, 261–267. [\[CrossRef\]](#)
10. Besnard, G.; Hild, F.; Roux, S. “Finite-element” displacement fields analysis from digital images: Application to Portevin-Le Châtelier bands. *Exp. Mech.* **2006**, *46*, 789–803. [\[CrossRef\]](#)
11. Réthoré, J.; Roux, S.; Hild, F. From pictures to extended finite elements: extended digital image correlation (X-DIC). *C. R.-Mec.* **2007**, *335*, 131–137. [\[CrossRef\]](#)
12. Réthoré, J.; Hild, F.; Roux, S. Extended digital image correlation with crack shape optimization. *Int. J. Numer. Methods Eng.* **2008**, *73*, 248–272. [\[CrossRef\]](#)
13. Fagerholt, E.; Børvik, T.; Hopperstad, O. Measuring discontinuous displacement fields in cracked specimens using digital image correlation with mesh adaptation and crack-path optimization. *Opt. Lasers Eng.* **2013**, *51*, 299–310. [\[CrossRef\]](#)
14. Schreier, H.; Orteu, J.J.; Sutton, M.A. *Image Correlation for Shape, Motion and Deformation Measurements: Basic Concepts, Theory and Applications*; Springer: London, UK, 2009. [\[CrossRef\]](#)
15. Kang, J.; Ososkov, Y.; Embury, J.D.; Wilkinson, D.S. Digital image correlation studies for microscopic strain distribution and damage in dual phase steels. *Scr. Mater.* **2007**, *56*, 999–1002. [\[CrossRef\]](#)
16. Di Gioacchino, F.; Quinta da Fonseca, J. Plastic Strain Mapping with Sub-micron Resolution Using Digital Image Correlation. *Exp. Mech.* **2013**, *53*, 743–754. [\[CrossRef\]](#)
17. Quinta da Fonseca, J.; Ko, L. The kinematics of deformation and the development of substructure in the particle deformation zone. In *IOP Conference Series: Materials Science and Engineering*; IOP Publishing: Bristol, UK, 2015; Volume 89, p. 012012. [\[CrossRef\]](#)
18. Orozco-Caballero, A.; Lunt, D.; Robson, J.D.; Quinta da Fonseca, J. How magnesium accommodates local deformation incompatibility: A high-resolution digital image correlation study. *Acta Mater.* **2017**, *133*, 367–379. [\[CrossRef\]](#)
19. Polatidis, E.; Hsu, W.N.; Šmíd, M.; Van Swygenhoven, H. A High Resolution Digital Image Correlation Study under Multiaxial Loading. *Exp. Mech.* **2018**, *59*, 309–317. [\[CrossRef\]](#)
20. Lunt, D.; Orozco-Caballero, A.; Thomas, R.; Honniball, P.; Frankel, P.; Preuss, M.; Quinta da Fonseca, J. Enabling high resolution strain mapping in zirconium alloys. *Mater. Charact.* **2018**, *139*, 355–363. [\[CrossRef\]](#)
21. Allais, L.; Bornert, M.; Bretheau, T.; Caldemaison, D. Experimental characterization of the local strain field in a heterogeneous elastoplastic material. *Acta Metall. Mater.* **1994**, *42*, 3865–3880. [\[CrossRef\]](#)
22. Ishikawa, N.; Yasuda, K.; Sueyoshi, H.; Endo, S.; Ikeda, H.; Morikawa, T.; Higashida, K. Microscopic deformation and strain hardening analysis of ferrite-bainite dual-phase steels using micro-grid method. *Acta Mater.* **2015**, *97*, 257–268. [\[CrossRef\]](#)
23. Latourte, F.; Salez, T.; Guery, A.; Rupin, N.; Mahé, M. Deformation studies from in situ SEM experiments of a reactor pressure vessel steel at room and low temperatures. *J. Nucl. Mater.* **2014**, *454*, 373–380. [\[CrossRef\]](#)
24. Lagattu, F.; Bridier, F.; Villechaise, P.; Brillaud, J. In-plane strain measurements on a microscopic scale by coupling digital image correlation and an in situ SEM technique. *Mater. Charact.* **2006**, *56*, 10–18. [\[CrossRef\]](#)
25. Ososkov, Y.; Wilkinson, D.S.; Jain, M.; Simpson, T. In-situ measurement of local strain partitioning in a commercial dual-phase steel. *Int. J. Mater. Res.* **2007**, *98*, 664–673. [\[CrossRef\]](#)
26. Kang, J.; Wilkinson, D.S.; Embury, J.D.; Jain, M. Microscopic Strain Mapping Using Scanning Electron Microscopy Topography Image Correlation at Large Strain. *J. Strain Anal. Eng. Des.* **2005**, *40*, 559–570. [\[CrossRef\]](#)
27. Ghadbeigi, H.; Pinna, C.; Celotto, S. Quantitative Strain Analysis of the Large Deformation at the Scale of Microstructure: Comparison between Digital Image Correlation and Microgrid Techniques. *Exp. Mech.* **2012**, *52*, 1483–1492. [\[CrossRef\]](#)
28. Ghadbeigi, H.; Pinna, C.; Celotto, S.; Yates, J.R. Local plastic strain evolution in a high strength dual-phase steel. *Mater. Sci. Eng. A* **2010**, *527*, 5026–5032. [\[CrossRef\]](#)
29. Kapp, M.; Hebesberger, T.; Kolednik, O. A micro-level strain analysis of a high-strength dual-phase steel. *Int. J. Mater. Res.* **2011**, *102*, 687–691. [\[CrossRef\]](#)
30. Banerjee, S.; Dasgupta, T.; Mukherjee, S.; Shome, M.; Chakraborti, P.C.; Saha, S.K. Digital image correlation for grain scale strain measurement in interstitial free high strength steel. *Mater. Sci. Technol.* **2016**, *32*, 328–337. [\[CrossRef\]](#)



31. Tasan, C.C.; Hoefnagels, J.P.M.; Geers, M.G.D. Microstructural banding effects clarified through micrographic digital image correlation. *Scr. Mater.* **2010**, *62*, 835–838. [CrossRef]
32. Lindfeldt, E.; Ekh, M.; Cvetskovski, K.; Schilke, M. Using DIC to Identify Microscale Strain Fields from In-situ SEM Images of a Pearlitic Steel. *Exp. Mech.* **2014**, *54*, 1503–1513. [CrossRef]
33. DNV. Newbuildings Materials and Welding-Metallic Materials. Available online: <https://rules.dnvgl.com/docs/pdf/DNV/ruleship/2011-01/ts202.pdf> (accessed on 20 June 2019).
34. Fagerholt, E. Field Measurements in Mechanical Testing Using Close-Range Photogrammetry and Digital Image Analysis. Ph.D. Thesis, Norwegian University of Science and Technology, Trondheim, Norway, 2012. Available online: [http://folk.ntnu.no/egilf/Thesis\\_Egil\\_Fagerholt.pdf](http://folk.ntnu.no/egilf/Thesis_Egil_Fagerholt.pdf) (accessed on 20 June 2019).
35. Tang, Z.; Liang, J.; Xiao, Z.; Guo, C. Large deformation measurement scheme for 3D digital image correlation method. *Opt. Lasers Eng.* **2012**, *50*, 122–130. [CrossRef]
36. Hild, F.; Raka, B.; Baudequin, M.; Roux, S.; Cantelaube, F. Multiscale displacement field measurements of compressed mineral-wool samples by digital image correlation. *Appl. Opt.* **2002**, *41*, 6815–6828. [CrossRef]
37. Holzapfel, G.A. *Nonlinear Solid Mechanics: A Continuum Approach for Engineering*; John Wiley and Sons Ltd.: Hoboken, NJ, USA, 2000.
38. Karlsen, M.; Hjelen, J.; Grong, Ø.; Rørvik, G.; Chiron, R.; Schubert, U.; Nilsen, E. SEM/EBSD based in situ studies of deformation induced phase transformations in supermartensitic stainless steels. *Mater. Sci. Technol.* **2008**, *24*, 64–72. [CrossRef]
39. Karlsen, M.; Grong, Ø.; Søfferud, M.; Hjelen, J.; Rørvik, G.; Chiron, R. Scanning electron microscopy/electron backscatter diffraction—Based observations of martensite variant selection and slip plane activity in supermartensitic stainless steels during plastic deformation at elevated, ambient, and subzero temperatures. *Metall. Mater. Trans. A: Phys. Metall. Mater. Sci.* **2009**, *40*, 310–320. [CrossRef]
40. Paulsen, C.; Broks, R.; Karlsen, M.; Hjelen, J.; Westermann, I. Microstructure Evolution in Super Duplex Stainless Steels Containing  $\sigma$ -Phase Investigated at Low-Temperature Using In Situ SEM/EBSD Tensile Testing. *Metals* **2018**, *8*, 478. [CrossRef]
41. Fagerholt, E. Ecorr User Manual. Available online: <http://folk.ntnu.no/egilf/ecorr/doc/> (accessed on 20 June 2019).
42. Schindelin, J.; Arganda-Carreras, I.; Frise, E.; Kaynig, V.; Longair, M.; Pietzsch, T.; Preibisch, S.; Rueden, C.; Saalfeld, S.; Schmid, B.; et al. Fiji: An open-source platform for biological-image analysis. *Nat. Methods* **2012**, *9*, 676–682. [CrossRef] [PubMed]
43. Preibisch, S.; Saalfeld, S.; Tomancak, P. Globally optimal stitching of tiled 3D microscopic image acquisitions. *Bioinformatics* **2009**, *25*, 1463–1465. [CrossRef] [PubMed]
44. Schneider, C.A.; Rasband, W.S.; Eliceiri, K.W. NIH Image to ImageJ: 25 years of image analysis. *Nat. Methods* **2012**, *9*, 671–675. [CrossRef]
45. Buljac, A.; Hild, F.; Helfen, L.; Morgeneyer, T.F. On deformation and damage micromechanisms in strong work hardening 2198 T3 aluminium alloy. *Acta Mater.* **2018**, *149*, 29–45. [CrossRef]
46. Callister, W.; Rethwisch, D. *Materials Science and Engineering: An Introduction*, 7th ed.; John Wiley & Sons: Hoboken, NJ, USA, 2007; p. 290.
47. Westermann, I.; Hopperstad, O.S.; Marthinsen, K.; Holmedal, B. Ageing and work-hardening behaviour of a commercial AA7108 aluminium alloy. *Mater. Sci. Eng. A* **2009**, *524*, 151–157. [CrossRef]
48. Maire, E.; Bouaziz, O.; Di Michiel, M.; Verdu, C. Initiation and growth of damage in a dual-phase steel observed by X-ray microtomography. *Acta Mater.* **2008**, *56*, 4954–4964. [CrossRef]
49. Anderson, T.L. *Solutions Manual: Fracture Mechanics: Fundamentals and Applications*; CRC Press: Boca Raton, FL, USA, 1995.
50. Kleindiek Nanotechnik. LT12830 Substage. Available online: <https://www.kleindiek.com/fileadmin/public/brochures/Lt12830.pdf> (accessed on 20 June 2019).
51. Haltom, S.S.; Kyriakides, S.; Ravi-Chandar, K. Ductile failure under combined shear and tension. *Int. J. Solids Struct.* **2013**, *50*, 1507–1522. [CrossRef]







## Appendix B

Christian Oen Paulsen, Runar Larsen Broks, Morten Karlsen, Jarle Hjelen, Ida Westermann

**Microstructure evolution in super duplex stainless steels containing  $\sigma$ -phase investigated at low-temperature using in situ SEM/EBSD tensile testing**

Metals 8 (2018) 478.





## Article

# Microstructure Evolution in Super Duplex Stainless Steels Containing $\sigma$ -Phase Investigated at Low-Temperature Using In Situ SEM/EBSD Tensile Testing

Christian Oen Paulsen <sup>1,2,\*</sup>, Runar Larsen Broks <sup>1,†</sup>, Morten Karlsen <sup>1,3,†</sup>, Jarle Hjelen <sup>1,4,†</sup> and Ida Westermann <sup>1,2,†</sup>

<sup>1</sup> Department of Materials Science and Engineering, Norwegian University of Science and Technology (NTNU), NO-7491 Trondheim, Norway; runarbro@stud.ntnu.no (R.L.B.); mortenka@statoil.com (M.K.); jarle.hjelen@ntnu.no (J.H.); ida.westermann@ntnu.no (I.W.)

<sup>2</sup> Centre for Advanced Structural Analysis (CASA), Norwegian University of Science and Technology (NTNU), NO-7491 Trondheim, Norway

<sup>3</sup> Equinor ASA, NO-7053 Trondheim, Norway

<sup>4</sup> Department of Geoscience and Petroleum, Norwegian University of Science and Technology (NTNU), NO-7491 Trondheim, Norway

\* Correspondence: christian.o.paulsen@ntnu.no; Tel.: +47-73-59-49-21

† These authors contributed equally to this work.

Received: 25 May 2018; Accepted: 19 June 2018; Published: 22 June 2018



**Abstract:** An in situ scanning electron microscope (SEM) study was conducted on a super duplex stainless steel (SDSS) containing 0%, 5% and 10%  $\sigma$ -phase. The material was heat treated at 850 °C for 12 min and 15 min, respectively, to achieve the different amounts of  $\sigma$ -phase. The specimens were investigated at room temperature and at −40 °C. The microstructure evolution during the deformation process was recorded using electron backscatter diffraction (EBSD) at different strain levels. Both  $\sigma$ -phase and  $\chi$ -phase were observed along the grain boundaries in the microstructure in all heat treated specimens. Cracks started to form after 3–4% strain and were always oriented perpendicular to the tensile direction. After the cracks formed, they were initially arrested by the matrix. At later stages of the deformation process, cracks in larger  $\sigma$ -phase constituents started to coalesce. When the tensile test was conducted at −40 °C, the ductility increased for the specimen without  $\sigma$ -phase, but with  $\sigma$ -phase present, the ductility was slightly reduced. With larger amounts of  $\sigma$ -phase present, however, an increase in tensile strength was also observed. With  $\chi$ -phase present along the grain boundaries, a reduction of tensile strength was observed. This reduction seems to be related to  $\chi$ -phase precipitating at the grain boundaries, creating imperfections, but not contributing towards the increase in strength. Compared to the effect of  $\sigma$ -phase, the low temperature is not as influential on the materials performance.

**Keywords:** in situ tensile testing; super duplex stainless steel; SDSS; low-temperature;  $\sigma$ -phase; SEM; EBSD; microstructure analysis

## 1. Introduction

Duplex stainless steels (DSS) consist of two phases: austenite and ferrite. The two phases, in combination with the alloying elements, result in a steel with superior mechanical properties and corrosion resistance compared to steels with similar cost. DSS was first developed by the oil and gas industry for use in the North Sea. Here, it is typically used in process pipe systems and fittings

exposed to corrosive environments at elevated temperature (up to 150 °C in H<sub>2</sub>S atmosphere) [1]. DSS typically contains 22% Cr, 5% Ni and 0.18% N, to achieve the desired phase composition and corrosion properties. If better corrosion properties are required, super duplex stainless steel (SDSS) can be used instead. This alloy contains a higher amount of Cr, Ni and N typically 25%, 7% and 0.3%, respectively. In order to achieve the desired phase composition, it is annealed at 1050 °C, and left there until a 50-50 phase balance between ferrite and austenite is obtained. During cooling after the heat treatment, precipitation of intermetallic phases ( $\sigma$ ,  $\chi$ ,  $\pi$  and  $R$ ) may occur. These intermetallics have been found to considerably reduce the mechanical properties and corrosion resistance of the material [2–13]. The most common of these phases is the  $\sigma$ -phase. Even small amounts (<0.5%) of  $\sigma$ -phase will significantly reduce the fracture toughness [2,14]. This reduction, combined with the short time it takes for the phase to form and the deteriorating effect on corrosion properties, is what makes  $\sigma$ -phase a dangerous and strongly unwanted intermetallic.

The  $\chi$  precipitates on ferrite/ferrite grain boundaries and occurs before the  $\sigma$ -phase [13,15]. In addition, the  $\chi$ -phase is a metastable phase, consumed during  $\sigma$ -phase precipitation [13].  $\sigma$ -phase typically forms on austenite/ferrite boundaries, but can also form on ferrite/ferrite boundaries. The  $\sigma$ -phase forms in the temperature range 675 °C–900 °C. After 10 min at 850 °C, small amounts of  $\sigma$ -phase will start to precipitate [6,16,17].  $\sigma$ -phase has a body centered tetragonal crystal structure with the lattice parameters  $a = 8.8$  Å and  $c = 4.55$  Å, while the  $\chi$ -phase has a body centered cubic crystal structure with lattice parameter  $a = 8.8$  Å [18]. The lattice parameters of both are significantly larger than the 2.87 Å and 3.65 Å for ferrites and austenite, respectively [19,20]. The chemical composition of  $\sigma$ -phase includes, in addition to Fe, approximately 30–60% Cr and 4–10% Mo. The  $\chi$ -phase differs from  $\sigma$ -phase with a higher Mo content and a lower content of Cr [15]. As a result, since  $\chi$ -phase has a higher atomic weight, it is possible to distinguish it from  $\sigma$ -phase in a scanning electron microscope (SEM) using Z-contrast. In such an image, the  $\chi$ -phase will appear brighter. Since Cr and Mo are stabilizing elements for ferrite, the  $\sigma$  and  $\chi$ -phase will form at the expense of ferrite. Following the eutectoid reaction  $\alpha \rightarrow \sigma + \gamma$  or  $\alpha \rightarrow \chi + \gamma$ , an increase in the austenite phase will also occur [15,17]. The surrounding area will be depleted of Cr and Mo, which are important elements for corrosion protection and, as a consequence, leaving the material exposed. This is especially troublesome in SDSS since these are mostly selected to operate in areas requiring a corrosion resistance superior to DSS.

A study by Børvik et al. [2] looked into the low-temperature effect on  $\sigma$ -phase in DSS. It was found that the temperature had a minor effect on the tensile ductility, while increasing amounts of  $\sigma$ -phase in the structure considerably reduced the ductility. Another study by Kim et al. [21] investigated the low-temperature mechanical behavior of SDSS containing  $\sigma$ -phase. Here, the material was tested in a universal tensile test machine, equipped with a sub-zero chamber. After the specimens were tested, the microstructure was investigated, comparing the amount of  $\sigma$ -phase present with microcrack length. Microcracks were found to have propagated through the entire  $\sigma$ -phase, relating the crack length to the size of  $\sigma$ -phase inclusions. As in Børvik et al. [2], the influence of temperature was observed to be minor. In addition, in the tensile tests performed at  $-50$  °C, no strain-induced martensite was produced.

In the present study, in situ SEM tensile tests have been conducted on an SDSS with 0%, 5% and 10%  $\sigma$ -phase present in the microstructure. The tensile tests were carried out at both room temperature and sub-zero temperature ( $-40$  °C). The microstructure was monitored with secondary electron imaging and electron backscatter diffraction (EBSD). Images were acquired at different loading steps. From these results, it is possible to observe the microstructure evolution and study the effects of  $\chi$ -phase and  $\sigma$ -phase on the microstructure during the deformation process.

## 2. Materials and Methods

### 2.1. Material and Heat Treatments

The investigated material in this study was a 2507 SDSS, with the chemical composition listed in Table 1. This pipe was manufactured by welding a rolled plate along the length of the pipe.

The microstructure of the steel investigated here contained more ferrite than austenite, 56.3% and 43.7%, respectively. The grain size in the two phases is also different, with ferrite having larger grains compared with austenite grains. These results have been summarized in Table 2. In addition, the grains have different morphology in different directions. Figure 1 gives a phase map of the pipe in three different directions. Here, LD, RD, and TD are abbreviations for longitudinal direction, radial direction, and transverse directions, respectively. The meaning of these are illustrated in Figure 2a.

**Table 1.** Chemical composition of 2507 SDSS.

Element	C	Si	Mn	P	S	Cr	Mo	Ni	Cu	W	N
wt%	0.018	0.42	0.52	0.017	0.001	25.55	3.46	8.28	0.72	0.52	0.25

**Table 2.** Microstructure statistics summarized. The data was collected from EBSD scans.

Average	Ferrite	Austenite	Overall
Composition	56.3%	43.7%	100%
Grain size	9 $\mu\text{m}$	6.5 $\mu\text{m}$	7.9 $\mu\text{m}$

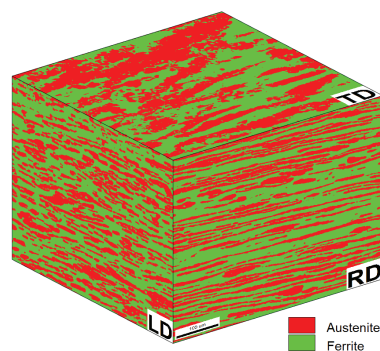


**Figure 1.** An illustration of the microstructure with the phases illustrated. The dimensions of the cube are 500  $\mu\text{m}$   $\times$  500  $\mu\text{m}$   $\times$  500  $\mu\text{m}$ , green representing ferrite and red representing austenite. In the bottom right corner of each side, the plane normal is given. LD, RD, and TD are illustrated in Figure 2a.

Specimens being used for EBSD analysis need a completely smooth surface, where the deformation layer at the surface has to be removed. For SDSS this was done by grinding and polishing down to 1  $\mu\text{m}$ , followed by electropolishing. The settings used are summarized in Table 3. Specimens were spark eroded from a 10 mm thick pipe to the dimensions in Figure 2b. All specimens were parallel to the length of the pipe, as illustrated in Figure 2a. The observed plane in the specimen during an in situ experiment has TD as plane normal.

**Table 3.** Parameters used during the electropolishing.

Electrolyte	Struers A2
Voltage [V]	20
Time [s]	15
Temperature [ $^{\circ}\text{C}$ ]	22

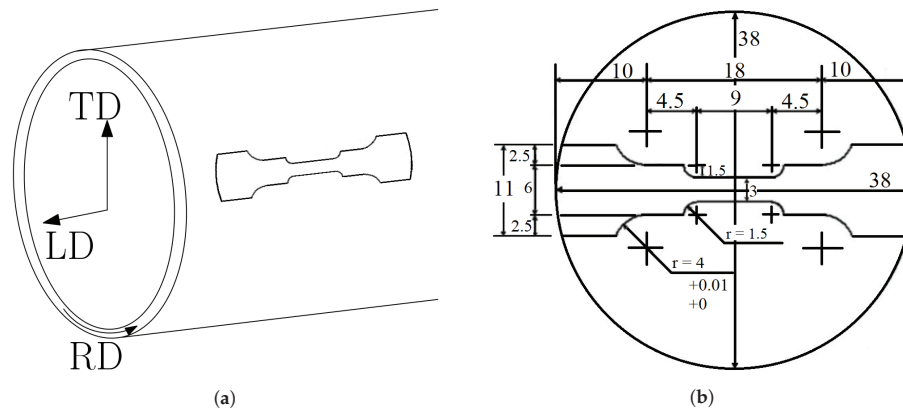


**Figure 2.** (a) an illustration on how the specimens were taken from the SDSS pipe and gives the definition of LD, RD and TD. The specimen dimensions is magnified compared to the pipe for illustration purpose; (b) specimen geometry, with all measurements in mm. The specimen had an original thickness of 2 mm before grinding and polishing.

The material was heat treated to achieve different amounts of  $\sigma$ -phase in the structure. Specimens were placed in a pre-heated oven at 850 °C for 12 min, 15 min, 20 min and 25 min. Cooling was performed by quenching in a water bath at room temperature. The heat treatment and the resulting amount of  $\sigma$ -phase achieved are summarized in Table 4. Phase maps from EBSD scans were used to quantify amounts of  $\sigma$ -phase present. These will not be exact measurements since they were only taken from the surface. The results from Elstad [16] was used to determine the heat treatment procedures used in this work. However,  $\sigma$ -phase precipitation was not constant with the same heat treatment being performed. Resulting in significant variation in  $\sigma$ -phase content during the heat treatment. All specimens in this work are heat treated as described in Table 4, but only specimens with amounts roughly in the region indicated in the third column were used for the in situ tests. However, the deviation was less than 1% for the 5% specimen, measured by EBSD. For the specimens with larger amounts of  $\sigma$ -phase present, the deviation was 1–2%.

**Table 4.** Heat treatment and resulting amount of  $\sigma$ -phase in the specimens tested.

Temperature [°C]	Time [min]	Amount $\sigma$ -Phase [%]
-	-	0
850	12	5
850	15	10
850	20	15
850	25	20

## 2.2. Materials Characterization

During this experiment, the microstructure was monitored using secondary electron imaging and EBSD. Images were acquired at different loading steps. At each step, the same area (350  $\mu\text{m} \times 350 \mu\text{m}$ ) was recorded with EBSD, using a step size of 1  $\mu\text{m}$ . From these results, it is possible to observe the microstructure evolution and study the effects of  $\sigma$ -phase and  $\chi$ -phase on the microstructure during the deformation process. The microscope used was a Field Emission SEM Zeiss Ultra 55 Limited Edition (Jena, Germany) with a NORDIF UF-1100 EBSD detector (Trondheim, Norway), with the microscope



settings given in Table 5. Z-contrast imaging mode was used in order to distinguish  $\sigma$ -phase from  $\chi$ -phase during the experiments.

**Table 5.** SEM parameters used during EBSD acquisition.

<b>Acceleration Voltage [kV]</b>	<b>20</b>
<i>Working distance [mm]</i>	24.6–25.4
<i>Tilt angle [°]</i>	70
<i>Aperture size [μm]</i>	300
<i>Probe current [nA]</i>	65–70

### 2.3. Tensile Testing

The specimen was deformed using a spindle-driven in situ tensile device. This device was placed inside the vacuum chamber of the SEM to monitor the microstructure. In situ tensile tests were carried out at both room temperature and at  $-40\text{ }^{\circ}\text{C}$  for specimens containing 0%, 5% and 10%  $\sigma$ -phase. Tensile tests were also performed on specimens containing 15% and 20% of  $\sigma$ -phase, however, no in situ investigation or low-temperature testing was carried out on these specimens, due to their purely brittle behavior. The in situ tensile tests were carried out with a constant ramp speed of  $1\text{ }\mu\text{m/s}$ . This corresponds to a strain rate of  $1.11 \times 10^{-4}\text{ s}^{-1}$ . For further reading and previous use of the in situ device, the reader is referred to [22,23]. When performing the sub-zero experiments, a cold finger was attached to the specimen as shown in Figure 3. This cold finger is made from 99.99% Cu. It goes from the specimen, through the microscope door, into a dewar filled with liquid N. The blue and white wire seen in Figure 3 is a thermocouple. It was placed between the screw-head and specimen throughout the experiment. The temperature was measured to be in the interval  $-35\text{ }^{\circ}\text{C}$  and  $-45\text{ }^{\circ}\text{C}$  for all specimens. However, the fluctuations in temperature are assumed to be due to the variable thermal resistance between the thermocouple and specimen. This variation is a result of the thermocouple shifting position during straining. The temperature is assumed constant and reported as  $-40\text{ }^{\circ}\text{C}$  in this paper.

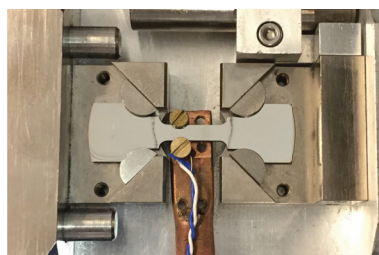


**Figure 3.** Cold finger attached to the specimen with a thermocouple placed between the screw-head and specimen.

## 3. Results

### 3.1. Tensile Properties and Fracture Surfaces

The tensile test curves for the specimens tested in this work are shown in Figure 4. As seen from these curves, the specimens with more than 10%  $\sigma$ -phase present exhibit a purely brittle behavior at room temperature and do not deform plastically before fracture. For that reason, these specimens are not suitable for in situ and low-temperature investigations. Hence, only specimens containing roughly 5% and 10%  $\sigma$ -phase are further investigated. The specimens containing 0%  $\sigma$ -phase are included as a reference.

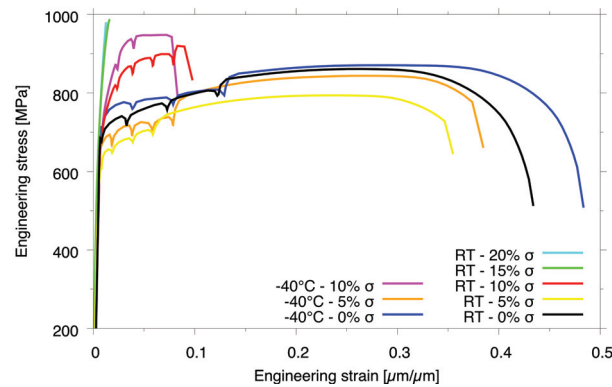


**Figure 4.** Tensile test curves obtained during the in situ tensile tests. The drops in the curves are when the test is paused for acquiring EBSD data.

The stress–strain curves in Figure 4 show that small amounts of  $\sigma$ -phase greatly affect the tensile properties of the material. Another observation is the short time at the critical temperature it takes before the material is completely brittle (cf. Table 4). Specimens containing 15% and 20%  $\sigma$ -phase only deforms elastically before fracture. A general remark is that the yield strength increases at low temperature and the strain at fracture decrease with an increasing amount of intermetallic phases. Conversely, for the material not heat treated, there is an increase of fracture strain. In addition, the drops in the curves are from when the tensile test is paused for EBSD acquisition. A curious observation from the tensile test curve is that the tests containing 5%  $\sigma$ -phase have a lower yield strength and ultimate tensile strength (UTS). In Figure 5, the microstructure of one of these specimens can be seen. Along the grain boundaries, the  $\chi$ -phase has precipitated as a thin continuous layer of approximately 200 nm thickness. This image was acquired during the test at room temperature, after 4% strain. In the center of the image is a  $\sigma$ -phase island, with two cracks marked with white circles. The  $\chi$ -phase also contains numerous small cracks, seen in the black circles in Figure 5, which seem to contribute towards a reduction in strength. When the amount of  $\sigma$ -phase increases, it also adds towards increased tensile strength.

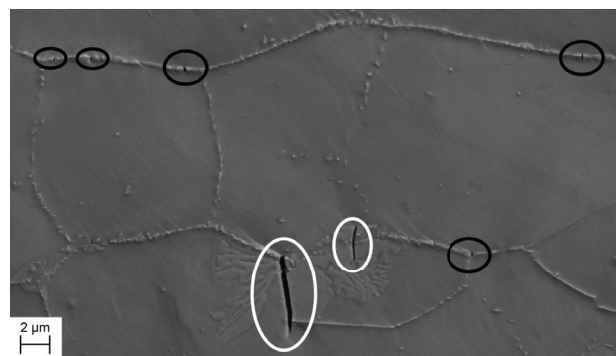


**Figure 5.** A close up micrograph from the specimen containing 5%  $\sigma$ -phase, after 4% strain, tested at room temperature. Along the grain boundaries, the  $\chi$ -phase can be found, and, in the center, a larger island of  $\sigma$ -Phase is seen. The white circles show cracks in the  $\sigma$ -phase and the black circles show the cracks in the  $\chi$ -phase.

In Figure 6, the fracture surfaces of the specimens tested at room temperature with 0%, 5% and 10%  $\sigma$ -phase are presented. To the left is an overview of the total surface area and to the right is a close-up image showing the fracture surface at a higher magnification. The reference sample exhibits classic ductile fracture features, with a large reduction of area and the typical cup and cone dimpled structure at the surface. This is also expected when compared to the tensile test curve (Figure 4). In the specimen with 5%  $\sigma$ -phase present, Figure 6b, some reduction in area is observed—however, not as great as in the test with 0%  $\sigma$ -phase present. In addition, here the fracture surface appears to be mixed between a ductile dimpled structure and a brittle faceted structure. Conversely, the specimen containing 10%  $\sigma$ -phase, Figure 6c, has all the characteristics of a brittle fracture. There is little to no reduction in area and completely faceted fracture surface, despite having a 10% fracture strain.

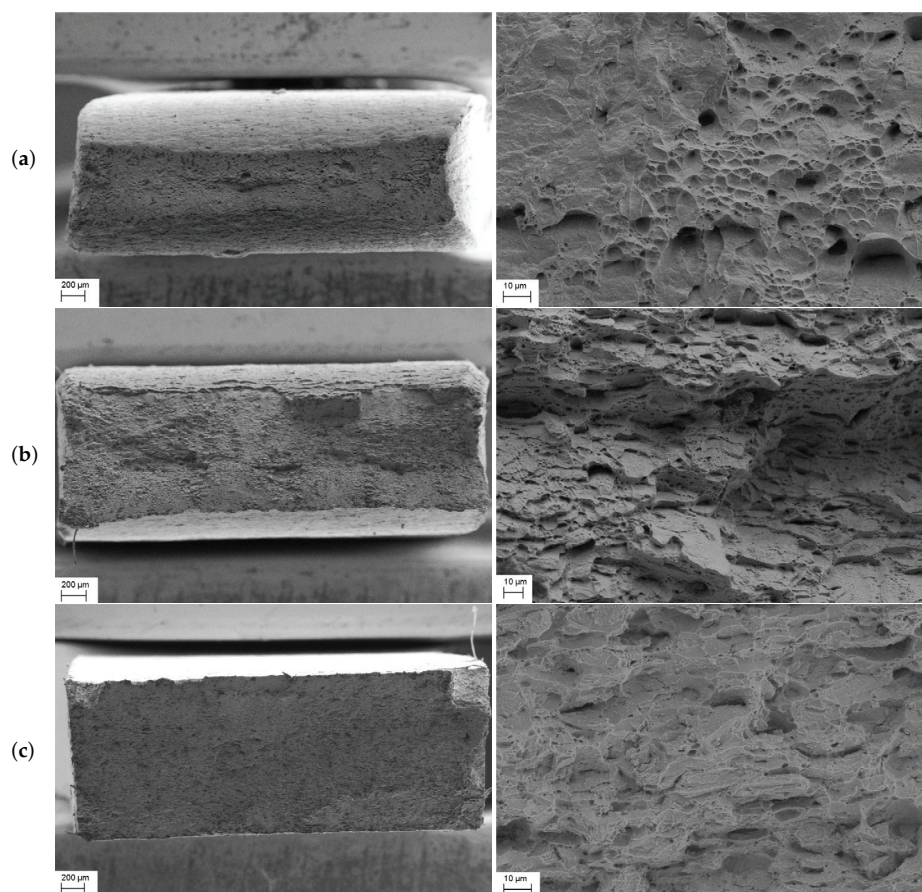


**Figure 6.** Fracture surfaces for the tensile test specimens with (a) 0%, (b) 5% and (c) 10%  $\sigma$ -phase, tested at room temperature. To the left is the total fracture area and to the right is a close-up of the fracture surface.

### 3.2. Microstructure Evolution

During the tensile tests, specimens containing different amounts of  $\sigma$ -phase were recorded using secondary electron imaging and EBSD to observe the microstructure throughout the deformation process. EBSD scans were obtained at the same area at approximately 0%, 2% and 6% strain of

all tested specimens. Each of the tensile test curves in Figure 4 showed a drop when the test was paused for the acquisition of EBSD scans and secondary electron imaging. An observation is that the specimen with 0%  $\sigma$ -phase, tested at  $-40\text{ }^{\circ}\text{C}$ , has a greater fracture strain than the specimen tested at room temperature.

In all specimens containing  $\sigma$ -phase, cracks were observed throughout the microstructure. These were observed to form after 3–4% strain in all the specimens, initiating in the  $\sigma$ -phase. Typical size of the cracks is seen in Figure 7. In Figure 8, two micrographs acquired at 6% and 10% strain show several micro-sized cracks in the  $\sigma$ -phase. During further straining, these cracks widen and appears to propagate deeper into the specimen. The ferrite and austenite grain boundaries act as a barrier for the cracks to propagate further. However, the larger constituents of  $\sigma$ -phase in the matrix contain large cracks, which eventually will propagate through the matrix. This is seen in the center of both frames in Figure 8. The microcracks in Figure 8a grow, and, in Figure 8b (black circle), they have coalesced, forming one large crack. A close-up of this crack is shown in Figure 9. This is a phase map superimposed on to an image quality (IQ) map from EBSD, acquired with a step size of 50 nm. From this map, it can be seen that the crack propagates along grain boundaries when it is moving through the matrix. When the cracks start to coalesce, the material is close to fracturing, as the volume fraction of cracks is increasing fast. The micrograph in Figure 8b was acquired after 10% strain. The specimen fractured after being strained less than 1% further. It is possible to see how the cracks in the white circles widen from Figure 8a to Figure 8b. Presumably, they are propagating through the thickness of the material.

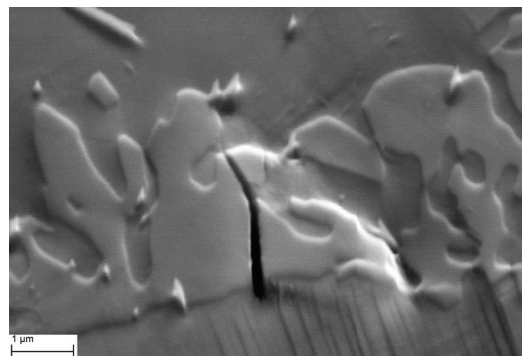


**Figure 7.** Micro-crack formed in the  $\sigma$ -phase during the initial stages of deformation. This frame is acquired after 6% strain, during the low temperature test with 5%  $\sigma$ -phase.

In Figure 10, the grain orientation spread (GOS) in the different tests are shown. All curves are obtained after 6% global strain. The GOS gives a quantitative description of the crystallographic orientation gradients in individual grains [24,25]. It is found by calculating the average orientation deviation of all points in a grain from the average grain orientation. A higher spread would indicate that those grains are accommodating a larger deformation compared to a lower spread. However, as seen from the graphs, there is, in general, a low spread, with peaks for all tests around  $1\text{--}2^{\circ}$ . One notable deviation is the curves from the experiment at  $-40\text{ }^{\circ}\text{C}$  with 0%  $\sigma$ -phase present in Figure 10b. These grains seem to accommodate more deformation, with a larger GOS distribution compared to other curves in Figure 10. Another observation is that the ferrite and austenite phases have nearly identical curves in the low-temperature test in Figure 10b, while the phases are behaving differently at room temperature (Figure 10a). During the room temperature tests, all curves for ferrite grains have a taller peak compared to austenite grains. In addition, the specimen with 5%  $\sigma$  has a higher GOS peak-value compared to the specimen containing 10%  $\sigma$ -phase when tested at  $-40\text{ }^{\circ}\text{C}$ .



At room temperature, the austenite for both tests is fairly similar, while the ferrite is accommodating more deformation in the specimen with 5%  $\sigma$ -phase.

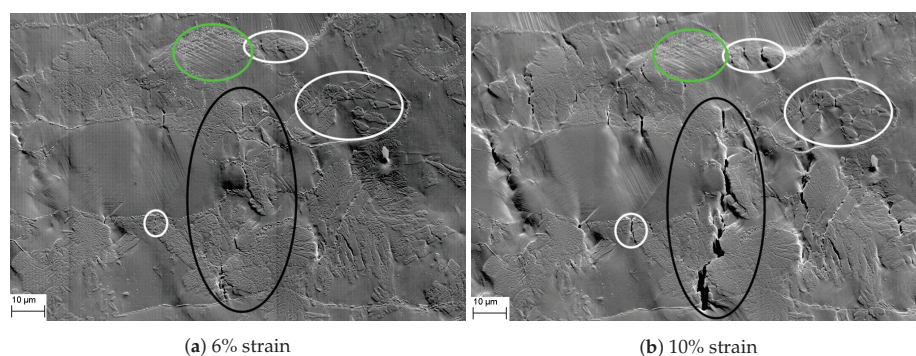


**Figure 8.** Micrographs of cracks formed in the  $\sigma$ -phase, taken from the test carried out at room temperature with 10%  $\sigma$ -phase present. Some cracks are restricted by the matrix while some propagate and coalesce. In the green circle, a heavily deformed austenite grain with cross-slip is seen. The white circles show microcracks restrained by the matrix and the large crack in the black circle was formed when many smaller cracks coalesce. A close-up of this crack is shown in Figure 9.

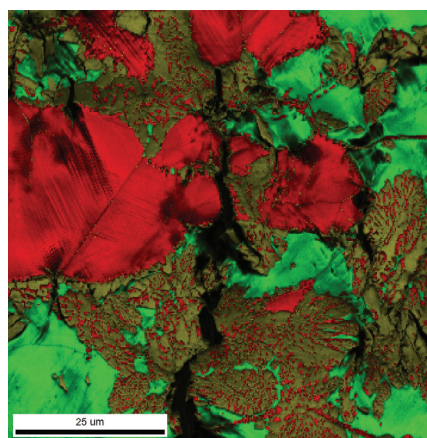


**Figure 9.** A close-up of the crack shown in the black circle in Figure 8b. This is a phase map with an IQ map overlay, acquired by EBSD. The red is austenite, green is ferrite and mustard yellow is  $\sigma$ -phase. The EBSD-scan of this area was acquired with a step size of 50 nm.

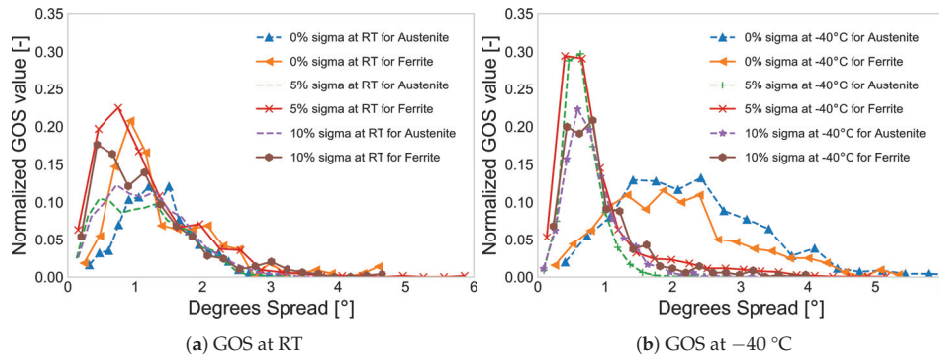


**Figure 10.** The grain orientation spread curves for the different specimens. (a) are the specimens tested at room temperature and (b) are the specimens tested at  $-40\text{ }^{\circ}\text{C}$ . All curves were taken after 6% strain. The solid lines are ferrite and the dashed lines are austenite.

#### 4. Discussion

During this work, different specimens of super duplex stainless steel, containing varying amounts of  $\sigma$ -phase have been investigated, during an in situ SEM tensile test. Each specimen was taken from a pipe segment and heat treated to get different amounts of  $\sigma$ -phase present. In general, it took roughly 10 min for the intermetallic phases to start forming at  $850\text{ }^{\circ}\text{C}$ . During the next 10 min, approximately 15% of  $\sigma$ -phase had precipitated, and the material had changed to an utterly brittle behavior, as seen in Figure 4. It proved hard to meet our targets of 5% and 10%  $\sigma$ -phase, sometimes achieving 0% after 13 min and other times 15% after 15 min at  $850\text{ }^{\circ}\text{C}$ . However, when the  $\sigma$ -phase starts to precipitate, it forms fast. Since duplex steels are being heat treated, typically at  $1050\text{ }^{\circ}\text{C}$ , to achieve its final microstructure and often goes through other heat treatment, e.g., welding, a thorough control of the cooling rate is crucial. In addition, no ductile-to-brittle transition was observed in this work. This was also the case in the work of Børvik et al. [2] and Kim et al. [21]. In these works, DSS and SDSS, respectively, were tested at  $-50\text{ }^{\circ}\text{C}$  and no transition was observed. This means that, if the material has a ductile-to-brittle transition temperature, it is lower than  $-50\text{ }^{\circ}\text{C}$ .

As seen from Figure 4, additions of  $\sigma$ -phase significantly reduce the ductility. This phenomenon is also well documented by others in previous studies [2,3,5,7,9]. However, in this study, the microstructure has been closely monitored during the tensile test to elucidate how it is accommodating the  $\sigma$ -phase in relation to deformation. The GOS in grains from the austenite and ferrite (shown in Figure 10) suggests that the presence of  $\sigma$ -phase and low temperature ( $-40\text{ }^{\circ}\text{C}$ ) is influencing the deformation behavior of the matrix. A consequence of presence of  $\sigma$ -phase is a lower fraction of ferrite. This altered phase balance, in combination with much harder particles containing numerous cracks explains this difference in behavior between specimens with and without  $\sigma$ -phase present. However, the primary concern is the brittle nature of  $\sigma$ -phase. Cracks were observed in the  $\sigma$ -phase at 3–4% strain in all specimens, and all cracks were oriented perpendicular to the tensile direction. During the initial stages, the surrounding matrix restricts the growth of the crack. As the material is strained further, the cracks continues to widen. Eventually, the cracks start to propagate and coalesce. In specimens with higher amounts of  $\sigma$ -phase, the propagation occurs earlier, following the shorter distance to the nearest  $\sigma$ -phase inclusion. In addition, the  $\sigma$ -phase particles are larger and the cracks, therefore, grow to a larger size.

The influence of temperature seems to make the  $\sigma$ -phase somewhat more brittle, resulting in a higher UTS and lower ductility. Austenite and ferrite grains seem to behave similarly during the low-temperature tests with  $\sigma$ -phase present when studying Figure 10b. However, during the test at

room temperature, the ferrite accommodates more deformation compared to the austenite. This is seen from the curves in Figure 10a. The reason for the ferrite being more active is believed to be due to the fact that ferrite has 48 active slip systems at room temperature. Conversely, austenite has 12 slip systems and they are not dependent on temperature. With more slip systems available, there are more ways for the dislocations to propagate. In addition, the specimens without any  $\sigma$ -phase present have a larger GOS compared to the specimens containing  $\sigma$ -phase. This indicates that the presence of  $\sigma$ -phase in the structure is retarding the deformation of ferrite and austenite. This is also observed through visual inspection of micrographs. There are more slip lines present, at equal strain level, in specimens without  $\sigma$ -phase present.

An observation of a specimen with 0%  $\sigma$ -phase, tested at  $-40\text{ }^{\circ}\text{C}$ , has a greater fracture strain than the specimen tested at room temperature. It could be expected that the ferrite would have a brittle behavior at this temperature. A reason for this behavior might be due to the fact that SDSS is a highly alloyed material, containing elements improving the low-temperature performance of ferrite. In addition, the presence of austenite will improve low-temperature performance. It has been reported in several studies that austenitic steels have increased ductility at  $-50\text{ }^{\circ}\text{C}$  in static uniaxial tensile tests [26–28].

Looking at the tensile test curve in Figure 4 for the tests with 5%  $\sigma$ -phase, a lower tensile strength compared to the curve without any  $\sigma$ -phase present is observed. Conversely, a greater amount of  $\sigma$ -phase gives a contribution towards increased strength. An explanation for this can be the relative amount of  $\chi$ -phase present. As seen from the black circles in Figure 5, the  $\chi$ -phase precipitates along grain boundaries and is very brittle containing many cracks. These cracks result in the observed reduction of tensile strength. However, the size of the cracks in  $\chi$ -phase are subcritical and does not contribute towards a large reduction in ductility. The specimen containing 5%  $\sigma$ -phase is still a very ductile material, with a fracture strain of 35%–38%. This is in contrast to previously reported literature. As mentioned in the Introduction, it has been reported that specimens with only 0.5%  $\sigma$ -phase have significantly reduced fracture toughness. However, as discussed in Børvik et al. [2] and Børvik et al. [3], DSS are more sensitive towards  $\sigma$ -phase with respect to fracture toughness than to tensile ductility. In this work, all specimens were tested strain rate of  $1.11 \times 10^{-4}\text{ s}^{-1}$ . In addition, the tensile tests were paused at certain intervals to acquire images and EBSD scans. In Børvik et al. [2], an increase in flow stress of about 30% was found for DSS when the strain rate was increased from  $5 \times 10^{-4}\text{ s}^{-1}$  to  $50\text{ s}^{-1}$  based on tensile tests.

No strain-induced martensite was observed in any of the specimens investigated in this work. This indicates a very stable austenitic phase. However, this is not unexpected, since the  $\sigma$ -phase is formed at the expense of ferrite, not austenite. The alloying elements added to stabilize the austenitic phase are still present in the matrix. In the work by Kim et al. [21], there was also no martensite observed.

## 5. Conclusions

- The cracks in  $\chi$ -phase contribute towards a lower flow stress but were not of critical size concerning a large reduction in tensile ductility. The specimens with small amounts of  $\chi$ -phase and  $\sigma$ -phase still retained a ductility of 35%.
- Visible cracks start to form after 3–4% strain, regardless of  $\sigma$ -phase content and they all form perpendicular to the tensile direction.
- During the initial stages of deformation, the cracks are constrained by the ferrite/austenite matrix. However, during the later stages, these cracks start to propagate through the material and coalesce. This occurs moments before fracture.
- The ferrite accommodates more deformation than austenite at room temperature tests; however, during low-temperature tests, both phases have a more equal behavior during deformation.
- At low temperature, with  $\sigma$ -present, the material had slightly higher flow stress and lower ductility. However, the amount of  $\sigma$ -phase present is the most important aspect when it



comes to duplex steels. It alters the phase balance of ferrite and austenite and deteriorates the mechanical properties.

**Author Contributions:** C.O.P. is the first author and analyzed the data and wrote the paper. The experiments were performed by C.O.P. and R.L.B. I.W., M.K., and J.H. conceived, designed and supervised the experiments. In addition, they contributed to the interpretation of data and editing the paper.

**Funding:** This research received no external funding

**Conflicts of Interest:** The authors declare no conflict of interest.

### Abbreviations

The following abbreviations are used in this manuscript:

CASA	Centre for Advanced Structural Analysis
DSS	Duplex Stainless Steel
EBS	Electron Backscatter Diffraction
GOS	Grain Orientation Spread
IQ	Image Quality
LD	Longitudinal Direction
NTNU	Norwegian University of Science and Technology
RD	Radial Direction
RT	Room Temperature
SDSS	Super Duplex Stainless Steel
SEM	Scanning Electron Microscope
TD	Transverse Direction
UTS	Ultimate Tensile Strength

### References

1. NORSOK Standard. Materials Selection. 2004. Available online: <http://www.standard.no/pagefiles/1174/m-dp-001r1.pdf> (accessed on 11 June 2018).
2. Børvik, T.; Lange, H.; Marken, L.A.; Langseth, M.; Hopperstad, O.S.; Aursand, M.; Rørvik, G. Pipe fittings in duplex stainless steel with deviation in quality caused by sigma phase precipitation. *Mater. Sci. Eng. A* **2010**, *527*, 6945–6955, doi:10.1016/j.msea.2010.06.087. [[CrossRef](#)]
3. Børvik, T.; Marken, L.A.; Langseth, M.; Rørvik, G.; Hopperstad, O.S. Influence of sigma-phase precipitation on the impact behaviour of duplex stainless steel pipe fittings. *Ships Offshore Struct.* **2016**, *11*, 25–37, doi:10.1080/17445302.2014.954303. [[CrossRef](#)]
4. Lee, Y.H.; Kim, K.T.; Lee, Y.D.; Kim, K.Y. Effects of W substitution on  $\zeta$  and  $\chi$  phase precipitation and toughness in duplex stainless steels. *Mater. Sci. Technol.* **1998**, *14*, 757–764, doi:10.1179/mst.1998.14.8.757. [[CrossRef](#)]
5. Kim, S.B.; Paik, K.W.; Kim, Y.G. Effect of Mo substitution by W on high temperature embrittlement characteristics in duplex stainless steels. *Mater. Sci. Eng. A* **1998**, *247*, 67–74, doi:10.1016/S0921-5093(98)00473-0. [[CrossRef](#)]
6. Lopez, N.; Cid, M.; Puiggali, M. Influence of  $\sigma$ -phase on mechanical properties and corrosion resistance of duplex stainless steels. *Corros. Sci.* **1999**, *41*, 1615–1631, doi:10.1016/S0010-938X(99)00009-8. [[CrossRef](#)]
7. Chen, T.H.; Yang, J.R. Effects of solution treatment and continuous cooling on  $\sigma$ -phase precipitation in a 2205 duplex stainless steel. *Mater. Sci. Eng. A* **2001**, *311*, 28–41, doi:10.1016/S0921-5093(01)00911-X. [[CrossRef](#)]
8. Chen, T.H.; Weng, K.L.; Yang, J.R. The effect of high-temperature exposure on the microstructural stability and toughness property in a 2205 duplex stainless steel. *Mater. Sci. Eng. A* **2002**, *338*, 259–270, doi:10.1016/S0921-5093(02)00093-X. [[CrossRef](#)]
9. Zucato, I.; Moreira, M.C.; Machado, I.F.; Lebrão, S.M.G. Microstructural characterization and the effect of phase transformations on toughness of the UNS S31803 duplex stainless steel aged treated at 850 °C. *Mater. Res.* **2002**, *5*, 385–389, doi:10.1590/S1516-14392002000300026. [[CrossRef](#)]
10. Cvijović, Z.; Radenković, G. Microstructure and pitting corrosion resistance of annealed duplex stainless steel. *Corros. Sci.* **2006**, *48*, 3887–3906, doi:10.1016/j.corsci.2006.04.003. [[CrossRef](#)]

11. Michalska, J.; Sozańska, M. Qualitative and quantitative analysis of  $\sigma$  and  $\chi$  phases in 2205 duplex stainless steel. *Mater. Charact.* **2006**, *56*, 355–362, doi:10.1016/j.matchar.2005.11.003. [CrossRef]
12. Souza, C.M.; Abreu, H.F.G.; Tavares, S.S.M.; Rebello, J.M.A. The  $\sigma$  phase formation in annealed UNS S31803 duplex stainless steel: Texture aspects. *Mater. Charact.* **2008**, *59*, 1301–1306, doi:10.1016/j.matchar.2007.11.005. [CrossRef]
13. Pohl, M.; Storz, O.; Glogowski, T. Effect of intermetallic precipitations on the properties of duplex stainless steel. *Mater. Charact.* **2007**, *58*, 65–71, doi:10.1016/j.matchar.2006.03.015. [CrossRef]
14. Calliari, I.; Zanesco, M.; Ramous, E. Influence of isothermal aging on secondary phases precipitation and toughness of a duplex stainless steel SAF 2205. *J. Mater. Sci.* **2006**, *41*, 7643–7649, doi:10.1007/s10853-006-0857-2. [CrossRef]
15. Escriba, D.; Materna-Morris, E.; Plaut, R.; Padilha, A. Chi-phase precipitation in a duplex stainless steel. *Mater. Charact.* **2009**, *60*, 1214–1219, doi:10.1016/J.MATCHAR.2009.04.013. [CrossRef]
16. Elstad, K.R. In Situ Tensile Testing During Continuous EBSD Mapping of Super Duplex Stainless Steel Containing Sigma Phase. 2016. Available online: <http://hdl.handle.net/11250/2418016> (accessed on 25 May 2018).
17. Stradomski, Z.; Dyja, D. Sigma Phase Precipitation in Duplex Phase Stainless Steels. 2009. Available online: <http://www.yseem.ing.unibo.it/Abstract/57Dyja.pdf> (accessed on 25 May 2018).
18. Padilha, A.F.; Rios, P.R. Decomposition of Austenite in Austenitic Stainless Steels. *ISIJ Int.* **2002**, *42*, 325–327, doi:10.2355/isijinternational.42.325. [CrossRef]
19. Cahn, R.W.; Haasen, P.; Kramer, E.J. *Materials Science and Technology: A Comprehensive Treatment—Volume 1: Structure of Solids*; Wiley-VCH: Weinheim, Germany, 2005.
20. Cahn, R.W.; Haasen, P.; Kramer, E.J. *Materials Science and Technology: A Comprehensive Treatment—Volume 7: Constitution and Properties of Steel*; Wiley-VCH: Weinheim, Germany, 2005.
21. Kim, S.K.; Kang, K.Y.; Kim, M.S.; Lee, J.M. Low-temperature mechanical behavior of super duplex stainless steel with sigma precipitation. *Metals* **2015**, *5*, 1732–1745, doi:10.3390/met5031732. [CrossRef]
22. Karlsen, M.; Hjelen, J.; Grong, Ø.; Rørvik, G.; Chiron, R.; Schubert, U.; Nilsen, E. SEM/EBSD based in situ studies of deformation induced phase transformations in supermartensitic stainless steels. *Mater. Sci. Technol.* **2008**, *24*, 64–72, doi:10.1179/174328407X245797. [CrossRef]
23. Karlsen, M.; Grong, Ø.; Søfferud, M.; Hjelen, J.; Rørvik, G.; Chiron, R. Scanning Electron Microscopy/Electron Backscatter Diffraction—Based Observations of Martensite Variant Selection and Slip Plane Activity in Supermartensitic Stainless Steels during Plastic Deformation at Elevated, Ambient, and Subzero Temperatures. *Metall. Mater. Trans. A* **2009**, *40*, 310–320, doi:10.1007/s11661-008-9729-5. [CrossRef]
24. Jorge-Badiola, D.; Iza-Mendia, A.; Gutiérrez, I. Study by EBSD of the development of the substructure in a hot deformed 304 stainless steel. *Mater. Sci. Eng. A* **2005**, *394*, 445–454, doi:10.1016/j.msea.2004.11.049. [CrossRef]
25. Mitsche, S.; Poelt, P.; Sommitsch, C. Recrystallization behaviour of the nickel-based alloy 80 A during hot forming. *J. Microsc.* **2007**, *227*, 267–274, doi:10.1111/j.1365-2818.2007.01810.x. [CrossRef] [PubMed]
26. Byun, T.; Hashimoto, N.; Farrell, K. Temperature dependence of strain hardening and plastic instability behaviors in austenitic stainless steels. *Acta Mater.* **2004**, *52*, 3889–3899, doi:10.1016/J.ACTAMAT.2004.05.003. [CrossRef]
27. Lee, K.J.; Chun, M.S.; Kim, M.H.; Lee, J.M. A new constitutive model of austenitic stainless steel for cryogenic applications. *Comput. Mater. Sci.* **2009**, *46*, 1152–1162, doi:10.1016/J.COMMATSCI.2009.06.003. [CrossRef]
28. Park, W.S.; Yoo, S.W.; Kim, M.H.; Lee, J.M. Strain-rate effects on the mechanical behavior of the AISI 300 series of austenitic stainless steel under cryogenic environments. *Mater. Des.* **2010**, *31*, 3630–3640, doi:10.1016/j.matdes.2010.02.041. [CrossRef]

